LEABHARLANN CHOLÁISTE NA TRÍONÓIDE, BAILE ÁTHA CLIATH | TRINITY COLLEGE LIBRARY DUBLIN
Ollscoil Átha Cliath | The University of Dublin

Terms and Conditions of Use of Digitised Theses from Trinity College Library Dublin

Copyright statement

All material supplied by Trinity College Library is protected by copyright (under the Copyright and Related Rights Act, 2000 as amended) and other relevant Intellectual Property Rights. By accessing and using a Digitised Thesis from Trinity College Library you acknowledge that all Intellectual Property Rights in any Works supplied are the sole and exclusive property of the copyright and/or other IPR holder. Specific copyright holders may not be explicitly identified. Use of materials from other sources within a thesis should not be construed as a claim over them.

A non-exclusive, non-transferable licence is hereby granted to those using or reproducing, in whole or in part, the material for valid purposes, providing the copyright owners are acknowledged using the normal conventions. Where specific permission to use material is required, this is identified and such permission must be sought from the copyright holder or agency cited.

Liability statement

By using a Digitised Thesis, I accept that Trinity College Dublin bears no legal responsibility for the accuracy, legality or comprehensiveness of materials contained within the thesis, and that Trinity College Dublin accepts no liability for indirect, consequential, or incidental, damages or losses arising from use of the thesis for whatever reason. Information located in a thesis may be subject to specific use constraints, details of which may not be explicitly described. It is the responsibility of potential and actual users to be aware of such constraints and to abide by them. By making use of material from a digitised thesis, you accept these copyright and disclaimer provisions. Where it is brought to the attention of Trinity College Library that there may be a breach of copyright or other restraint, it is the policy to withdraw or take down access to a thesis while the issue is being resolved.

Access Agreement

By using a Digitised Thesis from Trinity College Library you are bound by the following Terms & Conditions. Please read them carefully.

I have read and I understand the following statement: All material supplied via a Digitised Thesis from Trinity College Library is protected by copyright and other intellectual property rights, and duplication or sale of all or part of any of a thesis is not permitted, except that material may be duplicated by you for your research use or for educational purposes in electronic or print form providing the copyright owners are acknowledged using the normal conventions. You must obtain permission for any other use. Electronic or print copies may not be offered, whether for sale or otherwise to anyone. This copy has been supplied on the understanding that it is copyright material and that no quotation from the thesis may be published without proper acknowledgement.

A computational approach to understanding the *de*NO_x properties of Rhodium metal



A thesis submitted in partial fulfilment of the requirements for the degree of

Doctor of Philosophy

February, 2015

John J. Carey B.A. (Mod.)

School of Chemistry and CRANN

Trinity College Dublin

Under the supervision of Professors Graeme W. Watson and Michael E. Bridge

TRINITY COLLEGE
1 4 MAY 2015
LIBRARY DUBLIN
Thesis 10498

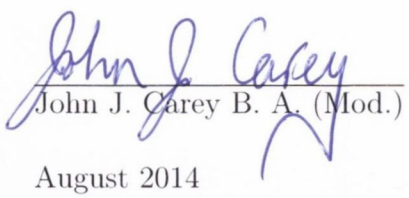
Declaration

I hereby declare that;

(a) This thesis has not been submitted as an exercise for a degree at this, or any other University.

(b) The work contained herein is entirely my own work, except where otherwise cited, referenced, or acknowledged in the text.

(c) I agree that the library of the University of Dublin may at their discretion lend or copy the thesis upon request.



John J. Carey B. A. (Mod.)

August 2014

Trinity College Dublin

Thesis Summary

The emission of nitrogen oxides (NO_x, $x = 1, 2$) from combustion engines is a significant contributor to acid rain, smog and the enhanced greenhouse effect. The environmental damage these pollutants have caused, as well as human health concerns, has led to governmental regulations aimed at reducing NO_x emissions. As the decomposition of NO_x gases ($de NO_x$) is difficult due to a high activation barrier, and catalytic technologies have been developed to assist in their subsequent breakdown. These technologies use rhodium, palladium and platinum precious metals employed on oxide supports, where 111 facets are the dominant surface on the metal clusters. Rhodium is known to be the most effective metal for NO_x reduction due to facile breaking of the NO bond; however, it is becoming increasingly scarce and thus progressively more expensive to use. This has led to significant interest in rhodium free technologies, motivating research to develop alternative, more cost effective catalysts that emulate the reductive properties of rhodium.

The need to understand the properties of rhodium metal takes initial precedence before investigating the development of novel catalysts. Firstly, density functional theory (DFT) will be used to investigate the adsorption of N, O, N_2, O_2 and NO_x to determine the most stable adsorption modes on the {111} surface of rhodium. Their electronic structure on interaction with the rhodium surface will be investigated using partial (ion and l-quantum number decomposed) electronic density of states (PEDOS), charge density and Bader analysis, and compared to the calculated electronic structure of their gaseous species. The energetics of the most stable adsorption modes, and of their gaseous species, will then be used to develop a $de NO_x$ profile

for rhodium. A similar procedure will be carried out on palladium and platinum metals to contrast their reductive properties for NO_x abatement to rhodium, to provide a clear insight to $de NO_x$ on rhodium.

The low index {100} and {110} surfaces will also be investigated in a similar manner to the {111} surface to compare their catalytic ability for $de NO_x$ and determine which surface is the most reactive for the reduction of NO_x. The flat crystalline surfaces are not perfect structures and can posses defects such as steps and kinks. The presence of a step on the {111} surface of rhodium will also be investigated in a similar manner to the other low index surface, and its ability to reduce NO_x will also be compared to the other surfaces. This will provide a more extensive description for $de NO_x$ on rhodium metal by examining and contrasting the most common exposed surfaces and their defects.

The precious metal catalysts contained within the $de NO_x$ technologies, exist as metal cluster particles of varying size, distributed across the oxide supports. The effect of varying the cluster size of rhodium metal particles on the $de NO_x$ chemistry will also be investigated. This is carried out by varying the size of the {111} surface expressed on the rhodium clusters from particle size from 10 metal atoms up to 56 atoms. The most stable N, O and NO_x adsorbates and their electronic structures will be determined in a similar manner to the extended metal surfaces. The energetics will be used to investigate the $de NO_x$ profile on the expose {111} surface of each metal particle and show the effect of size on the reduction profile. The energy barriers for the breakdown of NO_x will also be investigated on the most catalytically active rhodium cluster for $de NO_x$.

The complete $de NO_x$ mechanism on rhodium metal is in contentious debate in the current literature and remains uncertain. The breakdown of NO is known to be the rate determining step for $de NO_x$ due to the higher energy

barrier to break its bond. Investigation of the breakdown of NO to N_2 has indicated that the low temperature pathway proceeds through an N_2O intermediate; however the formation of the intermediate is unclear. Initially the proposed mechanism involved two NO molecules adsorbing on the surface with one NO breaking to N and O, producing a surface bound N-NO complex. Studies on other metal surfaces, and more recently on rhodium, have aluded to the existence of a $(NO)_2$ dimer formation on the metal surface which weakens the NO bond and is a precursor to N_2O formation during the process. The precursor leading to N_2O formation needs to be understood to fully elucidate the complete $de NO_x$ mechanism on rhodium, and the climbing nudged elastic band method will be used to determine the reaction mechanisms involving both intermediates to elucidate the lowest energy pathway.

Acknowledgements

Firstly, and most importantly, I would like to thank my supervisors for their continued help and support over the past four years. Their supervision has encouraged me to think critically about my research, and to fully enjoy the experience to date. The work of this thesis and my postgraduate experience would not be possible without the School studentship funding, awarded to me by the School of Chemistry. I also wish to acknowledge ICHEC (Irish Centre for High-End Computing), TCHPC (Trinity Centre for High Performance Computing), and the PRACE DECI-11 programme (Lindgren computer in Sweden) for the use of their HPC facilities.

I would like to express special thanks to Dr. Jeremy Allen who has read countless drafts of my work and helped me whenever possible over the course of my PhD studies. My gratitude goes towards the members of the Watson research group, Aoife K., Doug, Paddy, Kalle, Aoife L., and Alibhe who have made the lab an enjoyable place to be, and also to Dr. David Scanlon (now at UCL). Additionally, I would like to thank the other postgraduate students in the School of Chemistry, in particular Ian, Bryan, Michelle and Andy for their fun nights out and support.

I want to express my sincerest and heartfelt thanks to my family for their support and understanding throughout the years, a PhD is difficult to complete, and without them this would not be possible. Finally, I would like to express my gratitude to my dearest friend Clare, her cherished support, optimism, guidance and loving friendship over the years helped me through this difficult time in my life and we survived this adventure together.

Contents

Contents ix

List of Figures xv

List of Tables xxxiii

Nomenclature xl

1 Introduction 1

1.1 The Environment and Pollution Control 1

1.2 NO_x abatement and technologies 5

1.2.1 Automobile: Three-Way Catalytic Converter 6

1.2.2 Diesel Engine: Selective Catalytic Reduction 10

1.2.3 Diesel Engine: NO_x Storage/Reduction Catalyst 15

1.3 Understanding the $De NO_x$ pathway 18

1.3.1 The Rh {111} surface 19

1.3.2 The Pt and Pd {111} surfaces 22

1.3.3 The Rh {100} and {110} surfaces 25

1.3.4 Rh stepped surfaces 30

1.3.5 Rh clusters for $de NO_x$ applications 33

1.3.6 Intermediates leading to N_2O formation 38

1.4 Thesis Outline 42

2 Computational Theory 45

2.1 Introduction 45
2.2 Schrödinger Equation 46
2.2.1 The Born-Oppenheimer Approximation 48
2.2.2 The Variational Principle 49
2.3 Hartree and the Self-consistent Field Method 50
2.3.1 Roothan-Hall equations 54
2.3.2 Hartree-Fock Limitations 56
2.4 Density Functional Theory 57
2.4.1 The Hohenberg-Kohn Theorems 58
2.4.2 Kohn-Sham Self-consistent Field 60
2.4.3 Exchange-correlation functionals 65
2.4.4 Limitations of DFT 67
2.5 Solid State Simulations 68
2.5.1 Crystal lattices 68
2.5.2 Periodic Potential and Bloch's Theorem 70
2.5.3 Plane Waves and Pseudopotentials 72
2.5.4 Band theory and Orbital Based Approaches 76
2.6 Force and Geometry Optimisation 78
2.6.1 Hellmann-Feynman Theorem 78
2.6.2 Energy Minimisation Methods 79
2.6.3 First-order minimisation methods 80
2.6.4 Second-order Minimisation Methods 82

3 Computational Methodology **85**

3.1 Introduction 85
3.2 Vienna *ab-initio* Simulation Package (VASP) 86
3.3 Structural Optimisation and Convergence 86
3.4 Surface Generation and Slab Model 87
3.4.1 Surface Structure 89

3.5 Adsorption on Metal Surfaces 92
3.6 Bader charge analysis 93
3.7 Charge Difference Plots 95
3.8 Electronic Density of States 95
3.9 Vibrational Frequencies 96
3.10 Climbing Nudged Elastic Band Calculations 97

4 *De*NO$_x$ chemistry on the Rh, Pd and Pt {111} surfaces 101

4.1 Introduction 101
4.2 *De*NO$_x$ chemistry on the Rh {111} surface 102
4.2.1 Rh bulk and {111} surface 102
4.2.2 The electronic structure of the Rh {111} surface 103
4.2.3 Nitrogen adsorption on the Rh {111} surface 104
4.2.4 Oxygen adsorption on the Rh {111} surface 107
4.2.5 NO adsorption on the Rh {111} surface 109
4.2.6 NO_2 adsorption modes on the Rh {111} surface 115
4.2.7 N_2 and O_2 adsorption on the Rh {111} surface 126
4.2.8 Decomposition profile 131
4.3 Discussion 133
4.4 *De*NO$_x$ chemistry on the Pd and Pt {111} surfaces 136
4.4.1 Pd/Pt metal bulks and {111} surfaces 136
4.4.2 Pd/Pt {111} surfaces 136
4.4.3 Nitrogen adsorption modes and analysis 137
4.4.4 Oxygen adsorption modes and analysis 140
4.4.5 NO adsorption modes and analysis 143
4.4.6 NO_2 adsorption modes and analysis 151
4.4.7 Decomposition profile 158
4.4.8 Discussion 162
4.5 Conclusion 164

5 Comparative DFT study of the *de*NO_x chemistry on the Rh low index and stepped surfaces **167**

5.1 Introduction 167

5.2 Rh {100} and {110} surfaces 168

5.2.1 N adsorption and analysis 170

5.2.2 O adsorption and analysis 173

5.2.3 NO adsorption and analysis 176

5.2.4 NO_2 adsorption 184

5.2.5 N_2 and O_2 adsorption on the Rh {100} and {110} surfaces . . . 192

5.2.6 Decomposition Profile 193

5.2.7 Discussion 195

5.3 Rh {443} stepped surface 198

5.3.1 N adsorption and analysis 199

5.3.2 O adsorption and analysis 202

5.3.3 NO adsorption and analysis 205

5.3.4 NO_2 adsorption and analysis 212

5.3.5 Decomposition Profile 218

5.3.6 Discussion 219

5.4 Conclusion 221

6 Effect of Rh cluster size on *de*NO_x **225**

6.1 Introduction 225

6.2 Rh_n clusters (n = 10, 20, 35, 56) 226

6.3 N, O and NO adsorption on Rh_n clusters 228

6.3.1 N adsorption 228

6.3.2 O adsorption 231

6.3.3 NO adsorption 234

6.3.4 Decomposition Profile 241

6.4 NO barrier on the Rh_{20} cluster 243

6.4.1 Co-adsorption 244
6.5 Conclusion 246

7 Preliminary results for the chemical reduction of NO_x on the Rh {111} surface **249**

7.1 Introduction 249
7.2 NO_x adsorption and bond dissociation on the Rh {111} surface 250
7.2.1 NO_2 bond breaking 250
7.2.2 NO bond breaking 252
7.2.3 Discussion 257
7.3 Atomic and molecular diffusion on the Rh, Pd and Pt {111} surfaces . 258
7.3.1 N diffusion 259
7.3.2 O diffusion 260
7.3.3 NO diffusion 261
7.3.4 Discussion 262
7.4 Reaction pathways and intermediates 265
7.4.1 The adsorption of N_2O, N_2O_2 on the Rh {111} surface 265
7.4.2 Preliminary results for the intermediate formation during deNO$_x$ 267
7.5 Discussion 270
7.6 The energy barriers to N_2 and O_2 bond formation 271
7.6.1 Energy barrier to forming the N_2 bond 271
7.6.2 The energy barrier for O_2 bond formation 273
7.6.3 Discussion 274
7.7 Conclusion 275

8 Conclusions **277**

8.1 Conclusion 277
8.2 Future research 282

References **283**

List of Figures

1.1 A schematic diagram showing the harmful SO_x, NO_x and CO_x gases from automobiles and industry emissions into the atmosphere. SO_x and NO_x gases cause acid rain, and the gases also contribute to smog and ozone at ground level. 2

1.2 A schematic diagram showing the redox reactions that occur in a three-way catalytic converter. 9

1.3 A schematic diagram showing the layout and flow of an industrial SCR-NH_3 process. 14

1.4 A schematic diagram showing the layout and flow of a mobile SCR convertor. 15

1.5 A schematic diagram showing the (a) storage of NO_x under lean conditions and (b) the reduction of NO_x under rich conditions for the NSR technology. 17

2.1 A flow chart of the KS-SCF optimisation procedure. 64

2.2 The parameters **a**, **b**, **c**, α, β, and γ which characterise the unit cell. . . 68

2.3 The Bravais lattice for (a) simple cubic and (b) a face centred cubic (FCC) unit cell. 69

2.4 A 3x3 expansion of a unit cell under periodic boundary conditions. The symmetric movement of atoms in and out of the unit cell are shown by arrows. 70

2.5 A diagram showing the periodicity of the Brillouin zone in **k**-space . . . 71

2.6 A schematic showing the relationship between the all-electron wavefunction ($\Psi_{\text{all-electron}}$) indicated by the dashed black line, and a pseudopotential wavefunction (Ψ_{pseudo}) indicated by the solid red line. The Coulombic potential $V_{\text{all-electron}}$ related to the all-electron wavefunction is shown by the dashed black line, and the pseudopotential (V_{pseudo}) related to the pseudopotential wavefunction is shown by the solid red line. For both wavefunctions, the potentials are matched beyond the radius cut-off (r_c).[1] 74

2.7 A schematic showing the formation of a band continuum from discrete energy levels. The digram shows the valence and conduction bands for metals, semi-conductors and insulators, where they are separated by a distinct band gap for semi-conductors and insulators. 77

3.1 A schematic plot of energy versus volume at different k-point densities. 87

3.2 A schematic of the three-dimensional surface slab model of a periodic simulation cell. 88

3.3 The different Miller indices for the cubic set of Bravais lattices. 89

3.4 An example of a two dimensional p-$\{111\}$ metal surface. The black lines outline the unit cell of the p-$\{111\}$ metal surface which is extended in the xy plane by four unit cells. 91

3.5 A schematic illustrating the structure of a metal surface with labelled common surface defects. 92

3.6 A schematic for the (a) the position of a species above and below the slab of a periodic simulation cell, and (b) its subsequent adsorption onto the metal slab. 93

3.7 The calculated charge density difference of an adsorbed oxygen atom on a rhodium metal surface. The charge difference ranges from -0.3 (blue) to +0.3 (red) electrons/Å^3, as indicated by the scale. The plot is visualised using the Accelrys Materials Studio Software package. 96

3.8 (a) A schematic of a MEP between initial and final state configurations. (b) A plot showing the differences between NEB and CI-NEB calculations. 99

4.1 (a) The FCC lattice of the Rh bulk metal, and (b) the energies of the bulk metal at different lattice constants using different k-point sampling densities. The black, blue, red, yellow, red, green and purple lines are the 11x11x11, 13x13x13, 15x15x15, 17x17x17, 19x19x19 and 21x21x21 k-point sampling, respectively, that were tested on the rhodium bulk metal. 103

4.2 (a) The structure of the 7-layered Rh {111} p-(2x2) surface. The A-B-C type stacking in the fcc metal is highlighted by the coloured layers, where the top layer (A) is white, the second hcp layer (B) is yellow and the third fcc layer (C) is green. The four possible binding sites are labelled top, bridge, hcp and fcc. (b) The PEDOS of the Rh surface atoms and the bulk atoms within the slab. The dotted line indicates the position of the Fermi Level (E_F) and the vacuum energy is aligned 0 eV. The s, p and d states are shown by the blue, red and green lines, respectively. 104

4.3 The calculated adsorption sites for N on the (a) top, (b) hcp and (c) fcc sites of the Rh {111} surface. The N adsorbates are the blue spheres, while the {111} surface layers are coloured white (top), yellow (second) and green (third) for clarity. 104

4.4 (a) The calculated charge density difference of an adsorbed nitrogen atom on the hcp site, from -0.3 (blue) to +0.3 (red) electrons/Å^3, as indicated by the scale. (b) The PEDOS for a nitrogen atom on the hcp site. The Rh PEDOS is shown for surface atoms of the top layer. The blue, red and green lines are the s, p and d states, respectively. The Fermi level (E_{F}) is indicated by the dotted line and the vacuum energy (E_{vac}) is aligned to 0 eV. 106

4.5 The calculated adsorption sites for O on the (a) top, (b) bridge, (c) hcp and (d) fcc sites of the Rh {111} surface. The O adsorbates are the red spheres, while the {111} surface layers are coloured white (top), yellow (second) and green (third) for clarity. 107

4.6 (a) The calculated charge density difference of an adsorbed oxygen atom on the fcc site. The charge difference ranges from -0.3 (blue) to +0.3 (red) electrons/Å^3, as indicated by the scale. (b) The PEDOS for an oxygen adsorbate on the fcc site and the PEDOS of the top layer Rh surface atoms. The blue, red and green lines are the *s*, *p* and *d* states, respectively. The E_F is indicated by the dotted line and the E_{vac} is aligned to 0 eV. 109

4.7 The calculated adsorption sites for NO on the (a) top, (b) bridge, (c) hcp and (d) fcc sites of the Rh {111} surface. The N and O atoms of the NO adsorbates are the blue and red spheres, respectively, while the {111} surface layers are coloured white (top), yellow (second) and green (third) for clarity. 109

4.8 The charge density difference (electrons/Å^3) between NO adsorbed on the hcp site of Rh{111} and an unbound NO molecule and Rh{111} surface. 112

4.9 Electronic structure of NO. (a) Molecular orbital diagram for NO, (b) PEDOS of gas phase NO and (c) PEDOS of NO adsorbed on the hcp site of the Rh{111} surface. The blue, red and green lines indicate the s, *p* and *d* states, respectively. The dotted line indicates the position of the E_F on the hcp adsorption mode and the highest occupied state on the gas phase species. The graph of the hcp adsorption mode is aligned to the E_{vac} at 0 eV. 114

4.10 The relaxed structures of the (a)-(e) μ-nitrito, (f)-(h) O-O'-nitrito, and (i)-(j) O-nitrito adsorption modes on the Rh {111} surface. In each case, the top and side views of the adsorption modes are shown in (i) and (ii), respectively. The nitrogen and oxygen atoms are the blue and red spheres, respectively with the different Rh {111} surface layers coloured, white (top surface layer), yellow (sub-surface layer) and green (third surface layer) for clarity. 118

4.11 The calculated charge density difference of the most stable (a) μ-nitrito and (b) O-O'-nitrito adsorption modes. 120

4.12 (a) The molecular orbital diagram for NO_2. (b) The calculated PEDOS for gaseous NO_2. The calculated PEDOS for the most stable (c) μ-nitrito and (d) O-O'-nitrito adsorption modes on the Rh {111} surface. The N/O PEDOS shown is the single atom species for the adsorbates while the Rh PEDOS is for the top surface atoms. The subscript 's' indicates an atom bound directly to the surface. The blue, red and green lines are the s, p and d states. The E_F is indicated by the dotted line for the adsorption modes and the highest occupied state of the gaseous species. The E_{vac} for the adsorbates on the Rh surface is aligned to 0eV. 122

4.13 The calculated most stable adsorption modes for (a) N_2 and (b) O_2 on the Rh {111} surface. 127

4.14 The calculated charge difference plots (electrons $Å^{-3}$) for the most stable adsorption modes of (a) N_2 and (b) O_2 on the Rh {111} surface. 128

4.15 The calculated PEDOS for the most stable adsorption modes for (a) N_2 and (b) O_2 adsorption on the Rh {111} surface.(i) The molecular orbital diagram, (ii) PEDOS of the gaseous species and (iii) PEDOS of the adsorbate. The blue, red and green lines indicate the s, p and d states, respectively. The dotted line indicates the position of the E_F on the hcp adsorption mode and the highest occupied state on the gas phase species. The graph of the hcp adsorption mode is aligned to the E_{vac} at 0 eV. The 't' and 'b' subscripts indicate the top and bridge adsorption sites that the atoms are bound to. 130

4.16 The calculated step-wise reaction pathways for the dissociation of (a) NO_2 and (b) NO on the Rh {111} surface. The labels (i) - (vii) relate to the different steps of the profiles outlined in Table 4.9. 133

4.17 The structure of the (a) Pd and (b) Pt {111} surfaces with the adsorption sites labelled. The PEDOS for the top layer atoms of the {111} surface and bulks for Pd and Pt are shown in (c) and (d), respectively. The PEDOS plots are aligned to the vacuum energy at 0 eV and the Fermi level is indicated by the dotted line. The blue, red and green lines are the *s*, *p* and *d* states, respectively. 137

4.18 The calculated charge density difference of an adsorbed nitrogen atom on the (a) Pd and (b) Pt {111} surfaces. The charge difference ranges from -0.3 (blue) to +0.3 (red) electrons $Å^{-3}$, as indicated by the scale. . 139

4.19 The PEDOS for a single N atom on the fcc site of (a) Pd and (b) Pt {111} surfaces. The Pd and Pt PEDOS shows the mixing of states for the topmost layer of each surface. The blue, red and green lines are the *s*, *p* and *d* states, respectively. The Fermi level (E_F) is indicated by the dotted line and the vacuum energy (E_{vac}) is aligned to 0 eV. 140

4.20 The calculated charge density difference of an adsorbed oxygen atom on the (a) Pd and (b) Pt {111} surfaces. The charge difference ranges from -0.3 (blue) to +0.3 (red) electrons $Å^{-3}$, as indicated by the scale. 142

4.21 The PEDOS for oxygen adsorption on the fcc site of the (a) Pd and (b) Pt {111} surfaces. The blue, red and green lines are the *s*, *p* and *d* states, respectively. The E_F is indicated by the dotted line and E_{vac} is aligned to 0 eV. 143

4.22 The calculated charge difference between the adsorbed NO species on the (a) Pd and (b) Pt {111} surfaces. The charge difference ranges from -0.3 (blue) to +0.3 (red) electrons $Å^{-3}$, as indicated by the scale. 147

4.23 The calculated PEDOS for the most stable NO adsorption modes at the fcc site of the (a) Pd and (b) Pt {111} surfaces. The blue, red and green lines indicate the s, *p* and *d* states, respectively. The dotted line indicates the position of E_F and the highest occupied molecular orbital. The *E*vac of each graph is aligned to 0 eV. 148

4.24 The most stable μ-nitrito mode on the (a) Pd and (b) Pt {111} surface. Both the (i) top and (ii) side view are shown for clarity. 152

4.25 The calculated charge density difference of the most stable NO_2 adsorption mode on the (a) Pd and (b) Pt {111} surfaces. The charge difference ranges from -0.3 (blue) to +0.3 (red) electrons $Å^{-3}$ as indicated by the scale. 155

4.26 The calculated PEDOS for the most stable μ-nitrito on the (a) Pd and (b) Pt {111} surfaces. The N/O PEDOS shown is for the single atom species of the adsorbates while the Pd and Pt PEDOS is for the top surface atoms. The subscript 's' indicates an atom bound directly to the surface. The blue, red and green lines are the s, p and d states. The E_F is indicated by the dotted line for the adsorption modes and the highest occupied state of the gaseous species. The E_{vac} for the adsorbates on both surfaces is aligned to 0eV. 156

4.27 The calculated energies for the dissociation profile of (a) NO_2 and (b) NO on the Pd and Pt {111} surfaces. The red and green lines indicate the Pd and Pt dissociation pathways, respectively. The labels (i) - (vi) relate to the different steps of the profiles outlined in Table 4.18. 161

4.28 The calculated energies for the dissociation profile of (a) NO_2 and (b) NO on the Rh, Pd and Pt {111} surfaces. The blue, red and green lines indicate the Rh, Pd and Pt dissociation pathways, respectively. The labels (i) - (vi) relate to the different steps of the profiles outlined in Tables 4.9 and 4.18. 165

5.1 The structure of the Rh (a) {100} and (b) {110} surfaces with the high symmetry sites labelled. The top (white) and second (yellow) layers are coloured for clarity. 169

5.2 The PEDOS of the Rh (a) {100} and (b) {110} surfaces and the inner bulk layers. The dotted line indicates the position of E_F and the graphs are aligned to E_{vac} at 0 eV. The *s*, *p* and *d* states are indicated by the blue, red and green lines, respectively. 170

5.3 (a) The adsorption of N on the Rh {100} surface, at the (i) top, (ii) bridge and (iii) hcp sites. (b) N adsorption is also shown for {110} surface, on the (i) top, (ii) short bridge, (iii) long bridge and (iv) hcp sites. The blue sphere shows the N adsorbate, while the Rh surface layers are coloured for clarity. 172

5.4 The charge difference plot for the most stable N adsorption site on the Rh (a) {100} and (b) {110} surfaces. The charge difference ranges from -0.3 (blue) to +0.3 (red) electrons $Å^{-3}$, as indicated by the scale. 172

5.5 The PEDOS for N adsorption on the Rh (a) {100} and (b) {110} surfaces. The dotted line indicates the position of E_F and the graphs are aligned to E_{vac}. The *s*, *p* and *d* states are indicated by the blue, red and green lines, respectively. 173

5.6 (a) The adsorption of O on the Rh {100} surface, at the (i) top, (ii) bridge and (iii) hcp sites. (b) O adsorption is also shown for {110} surface, on the (i) top, (ii) short bridge, (iii) long bridge and (iv) hcp sites. The red sphere shows the O adsorbate, while the Rh surface layers are coloured for clarity. 175

5.7 The charge difference plot for the most stable O adsorption mode on the Rh (a) {100} and (b) {110} surfaces. The charge difference ranges from -0.3 (blue) to +0.3 (red) electrons $Å^{-3}$, as indicated by the scale. 175

5.8 The PEDOS for O adsorption on the Rh (a) {100} and (b) {110} surfaces. The dotted line indicates the position of E_F and the graphs are aligned to E_{vac}. The *s*, *p* and *d* states are indicated by the blue, red and green lines, respectively. 176

5.9 The adsorption of NO on the top, bridge and hcp sites of the Rh (a) {100} and (b) {110} surfaces. The (i) top view looking down the c-vector and (ii) side view looking along the a-vector are provided. The blue and red spheres show the N and O atoms, respectively, while the Rh surface layers are coloured for clarity. 180

5.10 The charge difference plot for the most stable NO adsorption mode on the Rh (a) {100} and (b) {110} surfaces. The charge difference ranges from -0.3 (blue) to +0.3 (red) electrons $Å^{-3}$, as indicated by the scale. . 181

5.11 The calculated PEDOS for NO adsorption on the Rh (a) {100} and (b) {110} surfaces. The dotted line indicates the position of E_F and the graphs are aligned to E_{vac}. The s, p and d states are indicated by the blue, red and green lines, respectively. 181

5.12 The most stable adsorption modes of NO_2 on the Rh (a) {100} and (b) {110} surfaces. The (i) top view looking down the c-vector and (ii) side view looking along the a-vector are provided. The blue and red spheres show the N and O atoms, respectively, while the Rh surface layers are coloured for clarity. 185

5.13 The charge difference plot for the most stable NO_2 adsorption mode on the Rh (a) {100} and (b) {110} surfaces. The charge difference ranges from -0.3 (blue) to +0.3 (red) electrons $Å^{-3}$, as indicated by the scale. . 187

5.14 (a) Molecular orbital diagram for NO_{2g}. The PEDOS for (b) gaseous NO_2 and the most stable NO_2 adsorption modes on the Rh (c) {100} and (d) {110} surfaces. The dotted line indicates the position of E_F and the graphs are aligned to E_{vac}. The s, p and d states are indicated by the blue, red and green lines, respectively. 189

5.15 The calculated most stable adsorption modes on the Rh (a) {100} and (b) {110} surfaces for (i) N_2 and (ii) O_2. The blue and red spheres are the nitrogen and oxygen atoms, respectively, with the top (white) and second (yellow) layers coloured for clarity. 193

5.16 The calculated energies for the dissociation profile of (a) NO_2 and (b) NO on the Rh {100} and {110} surfaces. The purple and orange lines indicate the {100} and {110} dissociation pathways, respectively. . . . 195

5.17 The structure of the Rh stepped {443} surface, along the (a) *b*-vector and (b) *c*-vector is indicate the position of all possible high symmetry sites that are labelled. The top (white) and second (yellow) layers are coloured for clarity. (c) The PEDOS of the Rh stepped {443} surface and the inner bulk layers. The dotted line indicates the position of E_F and the graph is aligned to E_{vac}. The *s*, *p* and *d* states are indicated by the blue, red and green lines, respectively. 199

5.18 The most stable adsorption modes of N (a) above and (b) below the step, and on the (c) terrace of the Rh {443} stepped surface, at the (i) top, (ii) bridge, (iii) hcp, and (iv) fcc sites, along the *c* and *a* vectors. The blue sphere shows the N adsorbate, while the Rh surface layers are coloured for clarity. 200

5.19 (a) The charge difference plot for the most stable N adsorption site on the Rh {443} stepped surface. The charge difference ranges from -0.3 (blue) to +0.3 (red) electrons $Å^{-3}$, as indicated by the scale. (b) The PEDOS for the most stable N adsorption mode on the Rh {443} stepped surface. The dotted line indicates the position of E_F and the graphs are aligned to E_{vac}. The *s*, *p* and *d* states are indicated by the blue, red and green lines, respectively. 203

5.20 The most stable adsorption modes of O (a) above and (b) below the step, and on the (c) terrace of the Rh {443} stepped surface, at the (i) top, (ii) bridge, (iii) hcp, and (iv) fcc sites, along the *c* and *a* vectors. The red sphere shows the O adsorbate, while the Rh surface layers are coloured for clarity. 204

5.21 (a) The charge difference plot for the most stable O adsorption site on the Rh {443} stepped surface. The charge difference ranges from -0.3 (blue) to +0.3 (red) electrons $Å^{-3}$, as indicated by the scale. (b) The PEDOS for the most stable O adsorption mode on the Rh {443} stepped surface. The dotted line indicates the position of E_F and the graphs are aligned to E_{vac}. The *s*, *p* and *d* states are indicated by the blue, red and green lines, respectively. 206

5.22 The most stable adsorption modes of NO (a) above and (b) below the step, and on the (c) terrace of the Rh {443} stepped surface, at the (i) top, (ii) bridge, (iii) hcp, and (iv) fcc sites, along the *c* and *a* vectors. The blue and red spheres show the N and O atoms, respectively, while the Rh surface layers are coloured for clarity. 207

5.23 (a) The charge difference plot for the most stable NO adsorption site on the Rh {443} stepped surface. The charge difference ranges from -0.3 (blue) to +0.3 (red) electrons $Å^{-3}$, as indicated by the scale. (b) The PEDOS for the most stable NO adsorption mode on the Rh {443} stepped surface. The dotted line indicates the position of E_F and the graphs are aligned to E_{vac}. The *s*, *p* and *d* states are indicated by the blue, red and green lines, respectively. 210

5.24 The most stable adsorption modes (a) μ-nitrito, (b) O-O'-nitrito and (c) O-nitrito adsorption modes on the Rh {443} stepped surface, along the (i) *c* and (ii) *a* vectors. The blue and red spheres show the N and O atoms, respectively, while the Rh surface layers are coloured for clarity. 212

5.25 (a) The charge difference plot for the most stable NO_2 adsorption site on the Rh {443} stepped surface. The charge difference ranges from -0.3 (blue) to +0.3 (red) electrons $Å^{-3}$, as indicated by the scale. (b) The PEDOS for the most stable NO_2 adsorption mode on the Rh {443} stepped surface. The dotted line indicates the position of E_F and the graphs are aligned to E_{vac}. The *s*, *p* and *d* states are indicated by the blue, red and green lines, respectively. 215

5.26 The calculated energies for the dissociation profile of (a) NO_2 and (b) NO on the Rh {443} stepped surface. 220

6.1 The relaxed structures of the Rh clusters with varying the size of the {111} surface for (a) Rh_{10}, (b) Rh_{20}, (c) Rh_{35} and (d) Rh_{56} metal clusters. The top (white), second (yellow) and third (green) layers are coloured for clarity allowing identification of top/bridge (white), hcp (yellow) and fcc (green) high symmetry adsorption sites. 226

6.2 The energies for the different spins of the Rh_n (n = 20, 35, 56) metal clusters. 227

6.3 The calculated PEDOS of the lowest energy electronic configuration for the (a) Rh_{10}, (b) Rh_{20}, (c) Rh_{35} and (d) Rh_{56} metal clusters. The graphs are scaled relative to to the largest Rh cluster, with E_F indicated by the dotted line and each graph aligned to their respective E_{vac}'s. The *s*, *p* and *d* states are indicated by the blue, red and green lines, respectively. 229

6.4 The most stable N adsorption modes on the (a) Rh_{10} (b) Rh_{20} (c) Rh_{35} and (d) Rh_{56} clusters. The nitrogen atoms are the blue spheres with the Rh atoms coloured by the different layers. 230

6.5 The charge difference plot for the most stable N adsorption modes on the (a) Rh_{10} (b) Rh_{20} (c) Rh_{35} and (d) Rh_{56} clusters. The charge difference ranges from -0.3 (blue) electrons/$Å^3$ to +0.3 (red) electrons/$Å^3$. 231

6.6 The calculated PEDOS for the most stable N adsorption modes on the (a) Rh_{10} (b) Rh_{20} (c) Rh_{35} and (d) Rh_{56} clusters. The PEDOS for the top Rh surface layer is shown in each plot with the *s*, *p* and *d* states shown by the blue, red and green lines, respectively. Each plot is aligned to E_{vac} at 0 eV with the position of E_F indicated by the dotted line. The Rh_{10-35} surface PEDOS are scaled relative to the Rh_{56} PEDOS, while the N PEDOS are all on the same scale. 232

6.7 The most stable oxygen adsorption modes on the (a) Rh_{10} (b) Rh_{20} (c) Rh_{35} and (d) Rh_{56} clusters. The oxygen atoms are the red spheres with the Rh atoms coloured by the different layers, similarly to the clean clusters. 233

6.8 The charge difference plot for the most stable oxygen adsorption modes on the (a) Rh_{10} (b) Rh_{20} (c) Rh_{35} and (d) Rh_{56} clusters. The charge difference ranges from -0.3 (blue) electrons/Å^3 to +0.3 (red) electrons/Å^3. 234

6.9 The calculated PEDOS for the most stable O adsorption modes on the (a) Rh_{10} (b) Rh_{20} (c) Rh_{35} and (d) Rh_{56} clusters. The PEDOS for the top Rh surface layer is shown in each plot with the *s*, *p* and *d* states shown by the blue, red and green lines, respectively. Each plot is aligned to the vacuum energy at 0 eV with the position of the fermi level indicated by the dotted line. 235

6.10 The most stable NO adsorption modes on the (a) Rh_{10} (b) Rh_{20} (c) Rh_{35} and (d) Rh_{56} clusters, along the (i) *c*- and (ii) the *b*-vectors. The N and O atoms are the blue and red spheres, respectively, with the Rh atoms coloured by the different layers, similarly to the bare clusters. 236

6.11 The charge difference plot for the most stable NO adsorption modes on the (a) Rh_{10} (b) Rh_{20} (c) Rh_{35} and (d) Rh_{56} nanoparticles. The charge difference ranges from -0.3 (blue) electrons/Å^3 to +0.3 (red) electrons/Å^3. 238

6.12 The calculated PEDOS for the most stable NO adsorption modes on the (a) Rh_{10} (b) Rh_{20} (c) Rh_{35} and (d) Rh_{56} clusters. The PEDOS for the top Rh surface layer is shown in each plot with the *s*, *p* and *d* states shown by the blue, red and green lines, respectively. Each plot is aligned to E_{vac} at 0 eV with the position of E_F indicated by the dotted line. . . 240

6.13 The calculated energies for the dissociation profile of (a) NO_2 and (b) NO on the Rh_n (n = 10, 20, 35, 56) clusters. The blue, red, purple and green lines show the dissociation pathways for the Rh_{10}, Rh_{20}, Rh_{35} and Rh_{56} clusters, respectively. 243

6.14 The most stable adsorption configuration for the co-adsorption of N+O on the Rh_{20} cluster, along the (a) *c*- and (b) *b*- vectors. The blue and red spheres are the N and O atoms, respectively, with the top layers of the Rh_{20} cluster coloured for clarity. 244

6.15 The reaction pathway for the decomposition of NO → N+O on the Rh_{20} cluster. The blue and red spheres are the N and O atoms, respectively, with the top layers of the Rh_{20} cluster coloured for clarity. The energy profile for the breakdown of NO is also shown. 246

6.16 The trends for the adsorption energies of the N (blue), O (red) and NO (green) species on the Rh_n clusters. 247

7.1 The reaction pathway from NO_2 in the gas phase above the surface leading to NO_2 bond dissociation on the {111} surface of rhodium, leading to the (a) NO_{hcp}+O_{fcc} and (b) NO_{fcc}+O_{fcc} combinations. The energy for each step is shown relative to $NO_{(2ads)}$, and the energy profile is also shown. The blue and red spheres are the N and O atoms, respectively, and the layers of the rhodium metal slab are coloured for clarity. 252

7.2 The most stable configurations for the co-adsorption of N and O atoms at the (a) fcc + fcc, (b) hcp + hcp, (c) hcp + fcc and (d) fcc + fcc sites on the {111} surface of Rhodium. The E_{ads} associated with each configuration is also shown relative to gaseous NO. The blue and red spheres are the N and O atoms, respectively, and the layers of the Rhodium surface are coloured for clarity. 253

7.3 The reaction pathway from the gas phase leading to NO bond dissociation on the {111} surface of rhodium. The energy for each step is shown relative to the energy of gaseous NO above the metal surface. The blue and red spheres are the N and O atoms for NO, and the layers of the rhodium metal slab are coloured for clarity. 254

7.4 The reaction pathway from NO in the gas phase above the surface leading to NO bond dissociation on the {111} surface of rhodium, across the (a) bridge site and (b) the top site. The energy for each step is shown relative to gaseous NO. The blue and red spheres are the N and O atoms for NO, and the layers of the rhodium metal slab are coloured for clarity. 256

7.5 The reaction pathway for the dissociation of NO + O → N + 2O. The energy for each step is shown relative to gaseous NO_2. The blue and red spheres are the N and O atoms, respectively, and the layers of the rhodium metal slab are coloured for clarity. 257

7.6 The structure of the Rh {111} surfaces with the diffusion pathways to be tested for N, O and NO across the high symmetry adsorption sites which are labelled. The top (white) and second (yellow) layers are coloured for clarity. 259

7.7 The energy versus reaction coordinate profile of N diffusion across adsorption sites on the Rh, Pt and Pd {111} surfaces. The red, blue and green lines are the profiles for N diffusion on Rh, Pd and Pt, respectively. The energies are relative to the starting fcc site of their respective surfaces. 260

7.8 The energy versus reaction coordinate profile of O diffusion across adsorption sites on the Rh, Pt and Pd {111} surfaces. The red, blue and green lines are the profiles for O diffusion on Rh, Pd and Pt, respectively. The energies are relative to the starting fcc site of their respective surfaces. 261

7.9 The energy versus reaction coordinate profile of NO diffusion across adsorption sites on the Rh, Pt and Pd {111} surfaces. The red, blue and green lines are the profiles for O diffusion on Rh, Pd and Pt, respectively. The energies are relative to the starting fcc site of their respective surfaces. 263

7.10 The possible orientations for (a) N_2O_2 and (b) N_2O to be examined on the Rh {111} surface. (c) The most stable adsorption modes for (i)-(ii) N_2O and (iii) N_2O_2 with the E_{ads} also shown. The blue and red spheres are the N and O atoms, respectively, and the layers of the rhodium metal slab are coloured for clarity. 266

7.11 The most stable adsorption co-adsorption configurations for (a) NO + N + O, (b)/(c) N_2O + O, (d) N_2 + 2O, and (e)/(f) N_2 + O_2 on the {111} surface of rhodium. The blue and red spheres are the N and O atoms, respectively, and the layers of the rhodium metal slab are coloured for clarity. 267

7.12 The reaction mechanism for the formation of N_2O_2 leading to N_2O formation and subsequent decomposition to N_2. The blue and red spheres are the N and O atoms, respectively, and the layers of the rhodium metal slab are coloured for clarity. 269

7.13 The reaction mechanism for the N-NO precursor to N_2O formation and subsequent decomposition to N_2. (a) The pathway for the breaking of the NO bond leading to the flat stable N_2O configuration and (b) the pathway leading to the straight down N-top site N_2O configuration. The blue and red spheres are the N and O atoms, respectively, and the layers of the rhodium metal slab are coloured for clarity. 270

7.14 The most stable configurations for the co-adsorption of two N atoms at the (a) hcp + fcc, (b) hcp + hcp-nn, (c) hcp + hcp-nnn and (d) fcc + fcc sites on the {111} surface of Rhodium. The E_{ads} associated with each configuration is also shown relative to gaseous N_2. The blue spheres are the N atoms and the layers of the Rhodium surface are coloured for clarity. 272

7.15 The reaction pathway for the N_2 bond dissociation from the most stable N_2 adsorption mode to the stable configuration for the co-adsorption of N atoms at the (a) hcp + fcc, (b) hcp + hcp-nn, and (c) hcp + hcp-nnn site combinations. The energy (eV) for each step and end point is labelled, and are calculated relative to the energy of the N_2 adsorption mode. 273

7.16 The most stable configurations for the co-adsorption of two O atoms at the (a) hcp + fcc, (b) fcc + fcc-nn, (c) fcc + fcc-nnn and (d) hcp + hcp sites on the {111} surface of Rhodium. The E_{ads} associated with each configuration is also shown relative to gaseous N_2. The blue spheres are the N atoms and the layers of the Rhodium surface are coloured for clarity. 274

7.17 The reaction pathway for the O_2 bond formation from the most stable O_2 adsorption mode to the stable configuration for the co-adsorption of O atoms at the (a) fcc + fcc-nn, and (b) fcc + fcc-nnn site combinations. The energy (eV) for each step and end point is labelled, and are calculated relative to the energy of the O_2 adsorption mode. 275

List of Tables

4.1 The adsorption energies (E_{ads}), Rh-N bond length, bader charges for the N adsorbate and bound Rh metal atoms. The number of Rh bonds are indicated for each adsorption site. 105

4.2 The adsorption energies of O (E_{ads}) Rh-O bond length, the bader charges for O adsorbates and the bound rhodium metal atoms. The number of Rh bonds are indicated for each adsorption site. 107

4.3 The adsorption energies (E_{ads}), Rh-N and N-O bond lengths and N-O vibrational frequencies (vib) of NO for the gas phase and high symmetry adsorption sites of NO on the {111} surface of rhodium. 110

4.4 The calculated Bader charges for NO in the gas phase and the surface atoms of the pure Rh {111} surface (upper) and NO adsorbed onto high symmetry adsorption sites on the Rh {111} surface and the directly coordinated surface Rh atoms (lower). 111

4.5 The approximate percentage contributions of N $2s$, N $2p$, O $2s$ and O $2p$ states to the molecular orbitals of gas phase NO and NO adsorbed at the hcp site on the Rh{111} surface. 115

4.6 The calculated bond distance and angle of gaseous $NO_{2\,(g)}$. The adsorption energies (E_{ads}), the calculated N-O bonds and angles for the most stable (a-e) μ-nitrito, (f-h) O-O'-nitrito and (i-j) O-nitrito adsorption modes on the Rh {111} surface. The subscript 's' denotes the surface bound atom on the Rh {111} surface. 117

4.7 (a) The calculated Bader charges (a) for gaseous NO_2 and the Rh surface atoms of the pure surface, and (b) for adsorbed NO_2 on the Rh {111} surface, and the Rh atoms they are bound to. 119

4.8 The approximate percentage contributions of N $2s$, N $2p$, O $2s$ and O $2p$ states to the molecular orbitals of gaseous NO_2 and the μ-nitrito and O-O'-nitrito adsorption modes on the Rh{111} surface. 125

4.9 The calculated energies for (a) the overall breakdown of NO_x, and each step of the (b) NO_2 and (c) NO decomposition pathways on the Rh {111} surface. 132

4.10 The adsorption energies calculated realtive to $N_{2(g)}$ (E_{ads}), coordination number (CN), M-N bond lengths and Bader charges for the different nitrogen adsorption modes on the Pd and Pt {111} surfaces. The number of bonds for each adsorbate on a high symmetry site is also included. . 138

4.11 The adsorption energies calculated realtive to $O_{2(g)}$ (E_{ads}), coordination number (CN), M-O bond length and Bader charges for the different oxygen adsorption modes on the Pd and Pt {111} surfaces. The number of bonds for each site is also indicated for the bond lengths and M charges in the Table. 141

4.12 The adsorption energies (E_{ads}), coordination number (CN), M-O and N-O bond lengths, and vibrational frequencies of NO for the gas phase and high symmetry sites of NO on the {111} surface of Pd and Pt. . . 144

4.13 The calculated Bader charges for NO in the gas phase and (b) adsorption site on the Pd and Pt {111} surface. The Bader charges for the Pd and Pt surface atoms of the adsorption sites are also included. 146

4.14 The percentage contributions of N_s, N_p, O_s and O_p states to the molecular orbitals of gas phase NO and NO adsorbed on the fcc site of the Pd and Pt {111} surfaces. The $2\pi^*_{occ}$ and $2\pi^*_{unocc}$ refers to the occupied and unoccupied states, respectively, for the $2\pi^*$ orbital of the NO molecule. 150

4.15 The calculated bond lengths and angles for gaseous NO_2. The E_{ads}, adsorption site for N and O, the calculated bond connected to the surface (O_s-N_s), the N-O bond away from the surface (N_s-O) and the adsorbed NO_2 bond angle for most stable μ-nitrito adsorption mode on the Pd and Pt {111} surfaces. The subscript 's' donates the atom bound to the surface. 152

4.16 The calculated Bader charges for NO_2 in the (a) gas phase and the pure Pd and Pt surfaces. (b) The Bader charges for the μ nitrito adsorption mode on the Pd and Pt {111} surfaces, along with the charge of the metal surface atoms bonded to the adsorbates. 154

4.17 The approximate percentage contributions of N $2s$, N $2p$, O $2s$ and O $2p$ states to the molecular orbitals of gas phase NO_2 and the μ-nitrito adsorption modes on the Pd and Pt {111} surfaces. 157

4.18 The calculated energies for each step of the (a) NO_2 and (b) NO decomposition pathways on the Pd and Pt {111} surfaces. 159

5.1 The adsorption energies (E_{ads}), coordination number (CN), M-N bond lengths and Bader charges for the different nitrogen adsorption modes on the Rh {100} and {110} surfaces. The number of bonds for each adsorbate on a high symmetry site is also included. 171

5.2 The adsorption energies (E_{ads}), coordination number (CN), Rh-O bond lengths and Bader charges for the different oxygen adsorption modes on the Rh {100} and {110} surfaces. The number of bonds for each adsorbate on a high symmetry site is also included. 174

5.3 The E_{ads}, CN, Rh-O and N-O bond lengths, and vibrational frequencies of NO for the gas phase and high symmetry sites of NO on the Rh {100} and {110} surfaces. 177

5.4 The calculated Bader charges for NO in the gas phase and (b) adsorption site on the Rh {100} and {110} surfaces. The Bader charges for the Pd and Pt surface atoms of the adsorption sites are also included. 178

5.5 The approximate percentage contributions of N $2s$, N $2p$, O $2s$ and O $2p$ states to the molecular orbitals of gas phase NO and NO adsorbed at the most stable sites of the Rh{100} and {110} surface. 183

5.6 The calculated bond lengths and angles for gaseous NO_2. The E_{ads}, adsorption site for N and O, the calculated bond connected to the surface (O_s-N_s), the N-O bond away from the surface (N_s-O) and the adsorbed NO_2 bond angle for most stable μ-nitrito adsorption mode on the Rh {100} and {110} surfaces. The subscript 's' donates the atom bound to the surface. 184

5.7 (a) The calculated Bader charges for gaseous NO_2 and the Rh surface atoms of the pure surface, and (b) for adsorbed NO_2 on the Rh {100} and {110} surfaces, and the Rh atoms they are bound to. 186

5.8 The approximate percentage contributions of N $2s$, N $2p$, O $2s$ and O $2p$ states to the molecular orbitals of gas phase NO_2 and the μ-nitrito adsorption modes on the Rh {100} and {110} surfaces. 190

5.9 The calculated energies for each step of the (a) NO_2 and (b) NO decomposition pathways on the Rh {100} and {110} surfaces. 194

5.10 The adsorption energies (E_{ads}), coordination number (CN), *Rh*-N bond lengths and Bader charges for the most stable nitrogen adsorption modes (a) above and (b) below the step, and on the (c) terrace of the Rh {443} stepped surface. The number of bonds for each adsorbate on a high symmetry site is also included. 201

5.11 The adsorption energies (E_{ads}), coordination number (CN), *Rh*-O bond lengths and Bader charges for the most stable oxygen adsorption modes (a) above and (b) below the step, and on the (c) terrace of the Rh {443} stepped surface. The number of bonds for each adsorbate on a high symmetry site is also included. 205

5.12 The adsorption energies (E_{ads}), coordination number (CN), *Rh*-N and N-O bond lengths, and vibrational frequencies of NO for the gas phase and high symmetry sites of NO (a) above and (b) below the step, and the (c) terrace of the Rh {443} stepped surface. 208

5.13 The calculated Bader charges for NO in the gas phase and the adsorption sites (a) above and (b) below the step, and on (c) the terrace of the Rh {443} stepped surface. The Bader charges for the Rh surface atoms of the adsorption sites are also included. 209

5.14 The approximate percentage contributions of N 2*s*, N 2*p*, O 2*s* and O 2*p* states to the molecular orbitals of gas phase NO and NO adsorbed at the most stable sites of the Rh{443} stepped surface. 211

5.15 The calculated bond distance and angle of gaseous $NO_{2\,(g)}$. The E_{ads}, the calculated N-O bonds and angles for the most stable (a) μ-nitrito, (b) O-O'-nitrito and (c) O-nitrito adsorption modes on the Rh {443} stepped surface. The subscript 's' denotes the surface bound atom on the Rh {111} surface. 213

5.16 (a) The calculated Bader charges for gaseous NO_2 and the Rh surface atoms of the pure step and terrace, and (b) for adsorbed NO_2 on the Rh {443} step, and the Rh step atoms it is bound to. 214

5.17 The approximate percentage contributions of N 2*s*, N 2*p*, O 2*s* and O 2*p* states to the molecular orbitals of gas phase NO_2 and the μ-nitrito adsorption mode on the Rh {443} stepped surface. 217

5.18 The energies for each step of the (a) NO_2 and (b) NO decomposition pathways on the Rh {443} stepped surface. 219

6.1 The most stable adsorption site, CN, E_{ads}, spin, Rh-N bond length, and N and Rh charges for the N adsorption on the Rh_n clusters. 230

6.2 The adsorption site, CN, E_{ads}, spin, Rh-N bond length, and N and Rh charges for the most stable O adsorption modes on the Rh_n clusters. . . 233

6.3 The adsorption site, CN, E_{ads}, spin, Rh-N and N-O bond lengths, and vibrational data for the most stable NO adsorption modes on the Rh_n clusters. 236

6.4 The calculated Bader charges for NO in the (a) gas phase and (b) adsorption site on the Rh_n clusters. 237

6.5 The approximate percentage contributions of N $2s$, N $2p$, O $2s$ and O $2p$ states to the molecular orbitals of NO adsorbed at the most stable sites of the (a) Rh_{10}, (b) Rh_{20}, (c) Rh_{35} and (d) Rh_{10} clusters. 241

6.6 The calculated energies for the dissociation profile of NO on the Rh_n (n = 10, 20, 35, 56) clusters, and the extended Rh {111} surface with all values given in eV. 242

6.7 The calculated E_{ads}, Spin, and bond distances for the most stable co-adsorption configurations of N+O on the Rh_{20} cluster. 245

Nomenclature

Roman Symbols

$de\mathrm{NO}_x$ Decomposition of nitrogen oxides

AIM Atoms in molecules

DFT Density functional theory

E_{xc} Exchange-correlation functional

FCC Face centred cubic

GGA Generalised gradient approximation

HF-SCF Hartree-Fock self consistent field model

HK Hohenberg and Kohn theorem

HREELS High resolution electron energy loss studies

KS Kohn-Sham theorem

LDA Local density approximation

LSDA Local spin density approximation

LTN Lean trap NO_x

METADISE Minimum energy techniques applied to dislocation, interface and surface energies

NO_x Nitrogen oxide emissions

NSR NO_x storage-reduction catalyst

PAW Projector-augmented wave method

PBE Perdew-Burke-Ernzerhof exchange-correlation functional

PEDOS Partial (ion and l-quantum number decomposed) electron density of states

PW91 Perdew-Wang 91 exchange-correlation functional

SCR Selective catalytic reduction of NO_x

SD Slater determinant

TPSSIMS temperature programmed static secondary ion mass spectrometry

TWC Three-way catalytic converter

VASP Vienna *ab-initio* simulation package

Chapter 1

Introduction

1.1 The Environment and Pollution Control

The 'industrial revolution' (1760-1840) sparked the transition from using man made tools and equipment to machinery based transport, roads, canals, chemical manufacturing industries and iron production plants. During the industrial revolution a lot of work was carried out in the development of the internal combustion engine, and the change over from the use of wood as a fuel source to coal. The first half of the 19th century saw the widespread use of the steam powered engine primarily fuelled by coal, and with the discovery of gasoline and diesel fuels in the later half of the 19th century, there was a surge in the use and development of the combustion engine. The continuously increasing global population and the emergence of large scale manufacturing industries with the excessive consumption of coal, created large urban areas that generated considerable volumes of carbon soot and smoke causing significant air pollution. The effects of pollution on the urban areas was noticeable; however the primary focus was on manufacturing and the damage of pollution on the environment was of no concern. The invention of the automobile further added to the issues associated with air pollution in urban areas, and concern over the effects of pollution on the environment only took precedence in the later half of the 20th century.

Modern awareness of air pollution became a popular topic across the world after the

radioactive fall-out from World War II and the great smog of 1952 in London killing at least 4000 people.[2, 3] The presence of urban smog and acid rain was linked to the voluminous increase in automobiles and industrial plants in the past 50 years.[4] This prompted substantial global research into the sources of air pollution in the atmosphere and the adverse effects they have on the environment. Primary air pollutants from the exhaust systems of automobiles and manufacturing industries include sulphur oxides (SO_x), nitrogen oxides (NO_x), carbon oxides (CO_x), volatile organic compounds (VOCs), and particulate matter (PM), as shown in Figure 1.1, in particular from the extensive use of coal.[5] These pollutants can cause environmental damage by forming acid rain in the atmosphere, damage the ozone layer, and can also form smog and ozone at ground level in urban areas.[6, 7] SO_x and NO_x pollutants combine with atmospheric water to form acid rain which can damage crops and buildings. CO is a harmful toxic emission and CO_2 is a strong greenhouse gas. VOCs, PM and NO_x all contribute to forming smog and ozone at ground level, which have been linked to damaging human health.[8–10]

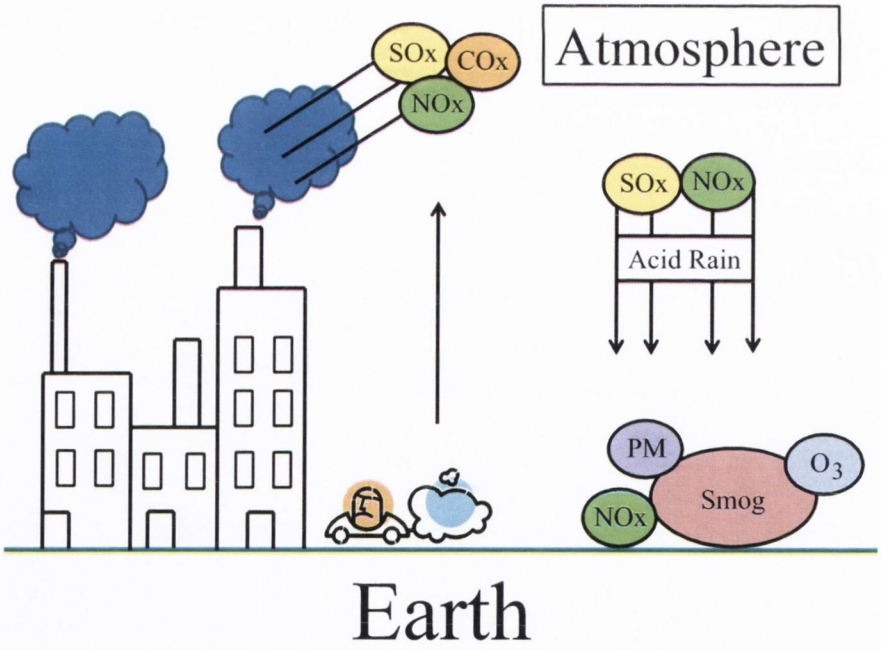


Figure 1.1: A schematic diagram showing the harmful SO_x, NO_x and CO_x gases from automobiles and industry emissions into the atmosphere. SO_x and NO_x gases cause acid rain, and the gases also contribute to smog and ozone at ground level.

Air pollution has been strongly linked to damaging human health causing respiratory diseases, cardiovascular issues, and lung cancer.[9] The human respiratory diseases associated with air pollutants include severe coughing and wheezing, reduced lung function, asthma, and chronic obstructive pulmonary diseases (COPD) such as chronic bronchitis and emphysema. These result in increase use of medication and hospitalisation, even resulting in premature death.[11] The reactions of individuals to poor air quality depend on the type of pollutant the person is exposed to, the degree of exposure, and the individuals health. The risk of developing asthma and COPD is related to increased traffic air pollution, while cardiovascular disease and stroke is also an emerging risk factor with high concentration of pollutants in urban areas, particularly in developing countries.[12] Long term exposure to SO_x and NO_x pollutants in busy traffic areas has also been linked to the development of lung cancer and early mortality among urban dwellers. Increased output of modern industries and vehicular emissions from traffic congestion results in the creation of modern urban smog.[13] This kind of smog reacts in the atmosphere with sunlight to form secondary pollutants, which in turn react with primary emissions to form photochemical smog that is highly toxic.[14, 15] Photochemical smog is a chemical reaction of sunlight, NO_x, and VOCs in the atmosphere, which produces PM and ozone at ground level and is considered a problem of modern industrialisation present in all modern cities.[16, 17] Many people living in large urban areas are therefore more at risk of developing the aforementioned diseases and health issues; however in areas of low air pollution, health effects have also been significant which is attributed to air pollutants being carried by the wind.[18] The dangers of air pollution on the environment and the affect it has on human health prompted governments to bring in legislation to reduce the concentration of primary pollutants from industrial and automobile emissions.

The severity of smog on urban areas and its affect on human health forced governments to address the issues associated with air pollution. In 1933 the United States promoted the use of smokeless fuels as an alternative to coal, and in London the Clean air act (1956) was introduced as a way of legally enforcing the use of smokeless fuels

across the capital.[19] These were the first steps in attempting to address air pollution in large urban areas; however these government acts only reduced the smoke pollution from industry and house-holds while automobile emissions were still uncontrolled. The US Environmental Protection Agency (EPA) was established in 1970 to deal with the effects air pollution has on the environment, both industrial and vehicle emissions, and similar agencies were also set up across Western Europe, Australia and Japan. The first attempt at dealing with automobile emissions was the development of the positive crankcase ventilation system (PCV),[20] which takes heavy unburned hydrocarbons into the tract of the engine so that they were re-burn rather than released into the atmosphere. The PCV system was required by law and implement globally in all automobiles. With the establishment of the EPA across the world, heavy legislation was introduced in 1975 and research into automobile emissions provided the development of the catalytic converter for after-treatment of exhaust gas.[21] In the same year leaded fuels were eliminated and distribution of unleaded fuel was a requirement by government law. In 1982 the two-way catalytic converter became obsolete with the development of the 'three-way' catalytic converter which is used in all automobiles across the world. For industrial sources, emission performance standards set out by the world EPAs lead to the development of scrubbing and absorber technologies for the exhaust streams to reduce the concentration of primary pollutants released into the atmosphere. These technologies deal with limiting SO_x and NO_x pollutants that are prevalent with industrial diesel engines, and also to reduce greenhouse gases.

Although there has been significant advances in awareness, government legislation and scientific research into atmospheric pollution and emissions control, there are still many improvements to be made and issues to be addressed. The three-way catalytic converter for automobiles does not fully remove harmful emissions from the exhaust system, with problems associated with NO_x, VOC and CO_2 emissions. For the industrial diesel engines, emission abatement is at 90%; however primary pollutants are still released into the atmosphere. The enforcement of the EPA on more stringent guidelines to further reduce automobile and industrial emissions is becoming more strict

across the world. This drives forward scientific research in 'green chemistry' to develop new technologies, or improve existing technologies in order to reduce primary pollutant concentrations from exhaust systems for a cleaner environment.

1.2 NO_x abatement and technologies

NO_x concentration refers to the mixture of nitrogen oxide (NO) and nitrogen dioxide (NO_2) gases that are formed from the reaction of nitrogen and oxygen during combustion. As nitrogen forms part of the gasoline mixture, and oxygen is introduced into the combustion chamber for more efficient combustion, it is difficult to remove NO_x before combustion occurs and it must be removed post-combustion. The amount of NO_x formed and emitted into the atmosphere as a pollutant is significant with NO having the largest contribution (100-1000 mg/m^3), NO_2 being the second largest contributor (10-100 mg/m^3) and other oxides of nitrogen such as nitrous oxide (N_2O) contributing lesser amounts (1-10 mg/m^3).[22] NO_x emissions from the combustion process are strongly oxidising gases that can damage the ozone layer and form acid rain in the atmosphere by the chemical reaction;

$$2NO_2 + H_2O \rightarrow HNO_2 + HNO_3 \tag{1.1}$$

the nitrous acid then decomposes to form nitric acid, nitrogen oxide and water;

$$3HNO_2 \rightarrow HNO_3 + 2NO + H_2O \tag{1.2}$$

the nitrogen oxide will then oxidise to form nitrogen dioxide that again reacts with more water to form nitric acid;

$$4NO + 3O_2 + 2H_2O \rightarrow 4HNO_3 \tag{1.3}$$

The nitric acid falls to earth damaging crops, buildings, and lakes and rivers which become acidic by alternating the pH of the water. NO_x can combine with VOCs to contribute to ozone and smog formation at ground level in urban areas, which affects human health and being linked to the cause of respiratory diseases such as asthma and COPD. The harmful effects NO_x pollution has on the environment and human health is a cause for concern, especially in the past 50 years with the significant increase in the automobile industry. The reduction of their emissions from the combustion engine is therefore a necessity to control the concentration of atmospheric NO_x.

The breakdown of NO_x to less harmful gases is governed by the overall equation;

$$NO_x \rightarrow \frac{1}{2} N_2 + \frac{x}{2} O_2 \tag{1.4}$$

The difficulty with the decomposition of NO_x ($de NO_x$) gases is the large energy required to break the NO bond (335kJ/mol), and a catalyst is thus required to address this issue.[23, 24] Catalytic technologies to reduce primary pollutants, in particular NO_x emissions from the combustion engine have been the forefront of heterogeneous catalysis research over the past 40 years. For automobile emissions this gave rise to the three-way catalytic converter, whereas a range of technologies have been innovated for stationary industrial diesel engines, including the selective catalytic reduction of NO_x and NO_x storage-reduction catalysts (lean-trap NO_x).[25] Although these technologies reduce NO_x emissions, they have not yet fully achieved a 100% conversion rate and further problems persist with the formation of nitrous oxide (N_2O), a greenhouse gas 300 times more potent than CO_2.[26]

1.2.1 Automobile: Three-Way Catalytic Converter

A catalytic converter was developed as a technology to combat the harmful emissions from exhaust gas of automobiles by converting the toxic gases to less harmful pollutants through a series of redox (reduction-oxidation) reactions. The catalytic converter lies between the combustion engine and the exhaust outlet and can be used by either

petrol or diesel engines. The first catalytic converter to be developed was the 'two-way' converter that combined carbon monoxide (CO) with hydrocarbons (HC) to produce carbon dioxide (CO_2) and water (H_2O) by the following reactions;

$$2CO + O_2 \rightarrow 2CO_2 \tag{1.5}$$

$$C_nH_m + \left(n + \frac{m}{4}\right) O_2 \rightarrow nCO_2 + \frac{1}{2} mH_2O \tag{1.6}$$

This kind of catalytic converter did not control the more harmful NO_x emissions, and a dual-bed catalyst was a first attempt at dealing with NO_x gases. The dual catalyst had two beds, the first catalysed the reduction of NO_x to N_2 and the second bed contained the oxidation catalyst. This system became redundant after the development of a single catalyst capable of simultaneously carrying out both reactions known as the 'three-way' catalytic (TWC) converter. These are implemented globally in all manufactured cars adhering to strict emissions control regulations, and are also used in forklifts, trucks, buses, motorcycles and aeroplanes.

The TWC adopts a monolithic type structure with strong porous walls in parallel channels and a ceramic base of cordierite ($2Mg.2Al_2O_3.5SiO_2$). This allows the gases to flow through the TWC at a high rate and large surface area to expose the catalyst to the exhaust gases. The internal surfaces of the monolith cover a large surface area ($400m^3$) for catalysis and covered with a thin film coating referred to as the washcoat. The washcoat consists mainly of γ-alumina (γ-Al_2O_3) as a support for metal oxide chemical promoters such as Ceria (CeO_2), Zirconia oxide (ZrO_2) or Barium oxide (BaO).[27–31] The precious metals such as Rh, Pd and Pt that act as the active metal catalysts are highly dispersed across the metal oxides but only make up 1-2% of the total TWC. The composition of some TWCs contains all three metals as active catalysts; however the majority of TWCs use Rh together with either Pd or Pt. Typically, TWCs use a Rh-Pt combination with 70-80% being Pt since Rh is scarce and expensive.[32, 33] Rh metal acts as the NO_x reductant aimed at carrying out the *de*NO_x reaction (Equation 1.4) while Pt (or Pd) carry out the oxidising reactions (Equations 1.5 and 1.6).

The objective of the TWC technology is to simultaneously remove CO, HC and NO_x gases from the exhaust gas mixture by a series of redox reactions. The removal of CO from the exhaust gas can be carried out by oxidising CO (Equation 1.5) and also by the water-gas shift reaction that occurs in the TWC cycle;[34]

$$CO + H_2O \rightarrow CO_2 + H_2 \tag{1.7}$$

As HCs are more harmful to the environment than CO_2 and H_2O, these are removed *via* hydrocarbon oxidation (Equation 1.6) and/or steam reforming reaction;

$$C_nH_m + nH_2O \rightarrow nCO + \left(n + \frac{m}{2}\right) H_2 \tag{1.8}$$

The advantages of using the TWC over the previous 'two-way' converter is the removal of NO_x gases by the following redox reactions with CO or hydrogen as the reductant;

$$2NO + 2CO \rightarrow N_2 + 2CO_2 \tag{1.9}$$

$$2NO + 2H_2 \rightarrow N_2 + 2H_2O \tag{1.10}$$

The redox reactions catalysing the toxic gases to less harmful ones are shown schematically in Figure 1.2 for a clearer overview of the reaction process. These redox reactions can occur simultaneously at any particular time during the TWC cycle and their efficiency depends on the ratio of air to fuel (A/F ratio). The redox reactions occur most efficiently just above the stoichiometric point (14.7:1) under fuel-lean, net oxidising conditions when there are low levels of HC and CO, and a higher concentration of NO_x. In theory, complete conversion should occur at the stoichiometric point with a balance of oxidising (O_2, NO_x) and reducing gases (HC, CO) to emit CO_2, H_2O and N_2. This is the objective of the TWC and ideally it should be operated in a narrow band around the stoichiometric point that will promote the reduction of NO_x to N_2 and oxidation of HC and CO to H_2O and CO_2, respectively. In practice however, complete conversion does not occur (around 80%) and the exhaust gas oscillates between rich (excess fuel)

and lean (excess oxygen) conditions. Under rich conditions the HCs consume all the available oxygen, while under lean conditions NO_x reduction is not favoured. An oxygen sensor is thus used to regulate the A/F ratio between to keep the exhaust composition within the window for optimum conversion. The multicomponent comercial catalyst is too difficult to study due to its complexity with Pt, Rh, Pd, Al_2O_3, BaO, CeO_2 etc present in the one catalyst. Model systems such as Rh/CeO_2 or Pt/BaO or Pd/Al_2O_3 *etc.* are studied to simply the catalyst components and examine their role at carrying out the redox reactions during the TWC cycle.

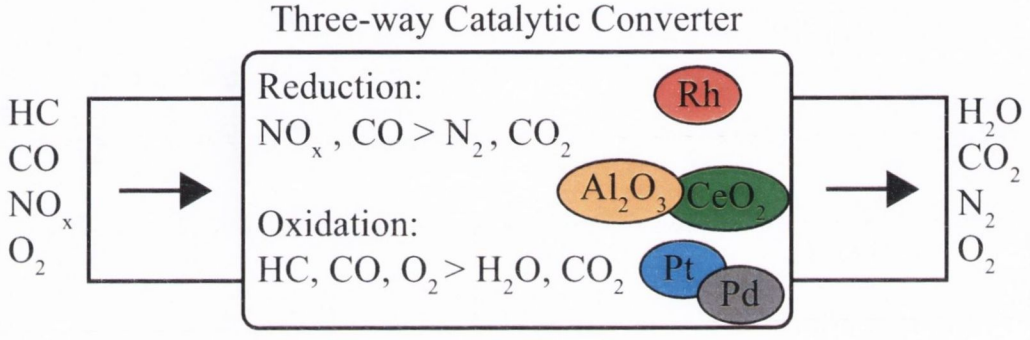


Figure 1.2: A schematic diagram showing the redox reactions that occur in a three-way catalytic converter.

Under lean conditions the oxidation of CO is mainly carried out on Pd or Pt metals; however all three metals used in the TWC are active for CO oxidation with Rh metal improving the low temperature activity.[34] Although Pt was used in first generation TWCs, Pd is becoming more of a viable alternative for next generation catalysts, as it has shown to be more efficient for CO oxidation, is cheaper and more widely available than Pt. Pt/CeO_2-Al_2O_3 and Rh/CeO_2-Al_2O_3 systems are found to be particularly active for CO oxidation under slightly fuel rich conditions *via* the water-gas shift reaction.[35–37] This reaction however, can also inhibit CO oxidation as the H_2 produced can combine with O_2 on the surface and form H_2O before CO_2.

Similarly to CO oxidation, hydrocarbon oxidation can occur on all three metals for A/F ratios at, or above, the stoichiometric value, with Pt being the most active. The mechanism of this reaction is more complicated than CO oxidation; however it

is thought that the process occurs by a steam reforming reaction (Equation 1.8). The combination of Rh-Pt/CeO_2-Al_2O_3 is found to be particularly active for this process.[38]

The removal of harmful NO_x gases is the most important reaction for the TWC. The *de*NO_x process (Equation 1.4) is carried out over the precious metals when the A/F ratio is stoichiometric or below stoichiometric in the presence of a reductant such as CO and/or HCs. The H_2 produced from the water-gas shift and steam reforming reactions can reduce NO_x to N_2, but also can form N_2O and NH_3 by-products from the side reactions;

$$2NO + H_2 \rightarrow N_2O + H_2O \tag{1.11}$$

$$2NO + 5H_2 \rightarrow 2NH_3 + 2H_2O \tag{1.12}$$

NO_x reduction examined on the three-metals used in the TWC, indicates that Rh is the most effective for carrying out *de*NO_x, particularly under net reducing conditions (low A/F ratio). The reason for Rh being a superior *de*NO_x catalyst is uncertain, with considerable focus on the reduction mechanism. Not only do Pd and Pt have lower activities for *de*NO_x but they are also less selective and produce considerable amounts of N_2O a harmful greenhouse gas, and NH_3. This indicates that Rh metal is an essential component of the TWC for NO_x control.

1.2.2 Diesel Engine: Selective Catalytic Reduction

The TWC is not a practical catalyst for industrial and mobile diesel engines as their operation is significantly different to the petrol engine. Diesel engines are a compression-ignition combustion engine and operate at high O_2 concentrations. Diesel engines therefore normally operate under lean conditions with an A/F ratio between (20:1) to (65:1) which is significantly higher than the stoichiometric value. The reduction of NO_x gases is thus not efficient using a TWC in the presence of excess oxygen. The diesel oxidation catalyst (DOC) is implemented that uses the high levels of O_2 to oxidise CO and HC to CO_2 and H_2O, respectively, having a 90% efficiency rate and also reducing PM (soot).

DOC catalysts however, are not active for NO_x reduction as any reductant would react with the high O_2 concetration before reduction NO_x gases. This was addressed by developing selective catalytic reduction (SCR) and NO_x storage reduction (NSR) technologies for NO_x abatement under lean conditions.[25, 39]

The SCR process reduces NO_x gases to N_2 in the presence of O_2 and a reducing agent such as anhydrous or aqueous ammonia (NH_3), HCs and urea ($CO(NH_2)_2$).[40–42] The use of NH_3 as the reducing agent for SCR (SCR-NH_3) was first introduced in the US in 1957, employing precious metals such as Rh, Pd and Pt as the active catalysts. These were not effective as the operating temperature required to reduce NO_x was in a similar range to the temperature at which explosive ammonium nitrate forms. Research into SCR-NH_3 continued in Japan in the 1960s that led to the development of vanadium/titanium oxide catalysts that proved successful and is still an active component of the current catalyst for NO_x abatement from stationary sources.[43] The SCR-NH_3 process using is well established to treat emissions from industrial and utility plants, chemical plants, waste incinerators, but the use of SCR with urea and HCs has not been commercially viable.

For stationary emissions, the SCR-NH_3 using vanadium-tungsten (V-W) oxides supported on titania (TiO_2) is the most used material;[44] however for nitric acid plants that have a large concentration of NO_x emissions, a copper-based zeolite is preferred.[45] The stationary SCR-NH_3 sources produces NO_x concentration primarily from NO with lesser contributions of NO_2, and $deNO_x$ is carried out in the presence of O_2 using NH_3 as a reductant added in the flue gas stream across the catalyst. The two main reactions for SCR-NH_3 are;

$$4NH_3 + 2NO + 2NO_2 \rightarrow 4N_2 + 6H_2O \tag{1.13}$$

$$2NH_3 + 2NO_2 \rightarrow NH_4NO_3 + N_2 + H_2O \tag{1.14}$$

and there is also a 'fast SCR reaction' that involves both NO and NO_2 which has a reaction rate 10 times faster than that of the standard SCR process (Equations 1.13

and 1.14);

$$4NH_3 + 4NO + O_2 \rightarrow 4N_2 + H_2O \tag{1.15}$$

which dominates at temperatures above 473K. At low temperatures the formation of the ammonium nitrate (Equation 1.14) is the main route for $de NO_x$, and at around 413K may responsible for complete NO_x conversion.[46] During the reduction process SO_2 can be produced from the oxidation of sulfur in the fuel, which can be further oxidised to SO_3 over the SCR catalyst.[47] This can cause deactivation of the catalyst by depositing ammonium sulphate ($(NH_4)_2SO_4$) and ammonium bisulphate (NH_4HSO_4) on the catalyst bed by the following side reactions;

$$2SO_2 + O_2 \rightarrow 2SO_3 \tag{1.16}$$

$$2NH_3 + SO_3 + H_2O \rightarrow (NH_4)_2SO_4 \tag{1.17}$$

$$NH_3 + SO_3 + H_2O \rightarrow NH_4HSO_4 \tag{1.18}$$

These sulphates can cause corrosion and plugging downstream which is avoided by adding excess NH_3. It is therefore necessary to prevent the early oxidation of SO_2 which is temperature sensitive. Additionally to avoid the direct oxidation of NH_3 before $de NO_x$, the NH_3/NO ratio is typically maintained below the stoichiometric values to between 0.90 and 0.95.

The catalyst adopts a monolithic porous structure in a similar manner to that found in a TWC, allowing exhaust gas to flow through. The washcoat contain the V-W-oxide catalyst is deposited on the ceramic or metallic honeycomb structure. The operating temperature for a typical monolithic SCR-NH_3 catalyst is around 453K, and Cu-zeolite catalyst operate at 423K which is ideal for nitric acid treatment plants.[48] Low temperature (413K - 523K) vanadium oxide catalysts were developed to reduce over 90% of NO_x emissions; however they are susceptible to SO_2 oxidation and can only be used in the absence of suplhur.[49] Many other various classes of catalyst have been trialled, in particular metal based catalysts, layer materials and micro- or meso- porous materials; however for SCR-NH_3 their performance does not match the V-W-oxide

supported TiO_2 catalyst that is used in many stationary sources. At higher reaction temperatures ($< 573K$) however, micro- and meso-porous materials containing precious metals (Rh, Pd, Pt) are preferred for greater thermal stability and durability. These materials are also used in industries with a large NO_2 output, as they are more reactive towards NO_x than the widely used V-W-oxide supported on TiO_2.

A schematic diagram showing the layout and flow of an industrial SCR process is provided in Figure 1.3. The exhaust flue gases flow into an economiser to regulate the temperature of the exhaust gas passing into the reactor. This ensures that the catalyst bed is operating at the desired temperature to minimise the rate of SO_2 oxidation, maximise space velocity and minimise the catalyst volume. The operating temperature of the SCR process is 653K - 753K using V-W oxide/TiO_2 catalyst. The exhaust gas is mixed with the vaporised form of the reducing agent, that is supplied from an external reservoir. The mixture proceeds into the SCR chamber containing a multi-bed layered catalyst and flows through to carry out $de NO_x$. The reduction of NO_x is controlled by the diffusion of gas through the catalyst bed, and mainly depends on the external geometric surface area rather than the thickness of the catalyst. The filtered air is then passed to a chamber that regulates the air temperature before passing it to an electrostatic precipitator (ESP) which removes any remaining fine particles (dust and smoke).

As the SCR-NH_3 process to carry out $de NO_x$ was implemented successfully on a commercial industrial level, this technology was extended to be used for high-duty diesel (HDD) vehicles such as trains, buses, trucks etc. For mobile source applications, the preferred choice of reductant is urea which is hydrolysed to form ammonia in the exhaust stream. SCR for HDD vehicles reduces NO_x emissions by around 80%, HC emissions by 90% and PM emissions by 40%, and EU testing shows excellent $de NO_x$ behaviour in HDD vehicles for over 500,000 km. The combination of SCR with a pre-oxidation catalyst (DOC), diesel particulate filter (DPF), a hydrolysis catalyst using a diesel exhaust fluid (DEF) such as urea, and a SCR catalyst enables a higher reduction of NO_x under low-load and low temperatures (Figure 1.4). The DOC and DPF reduces

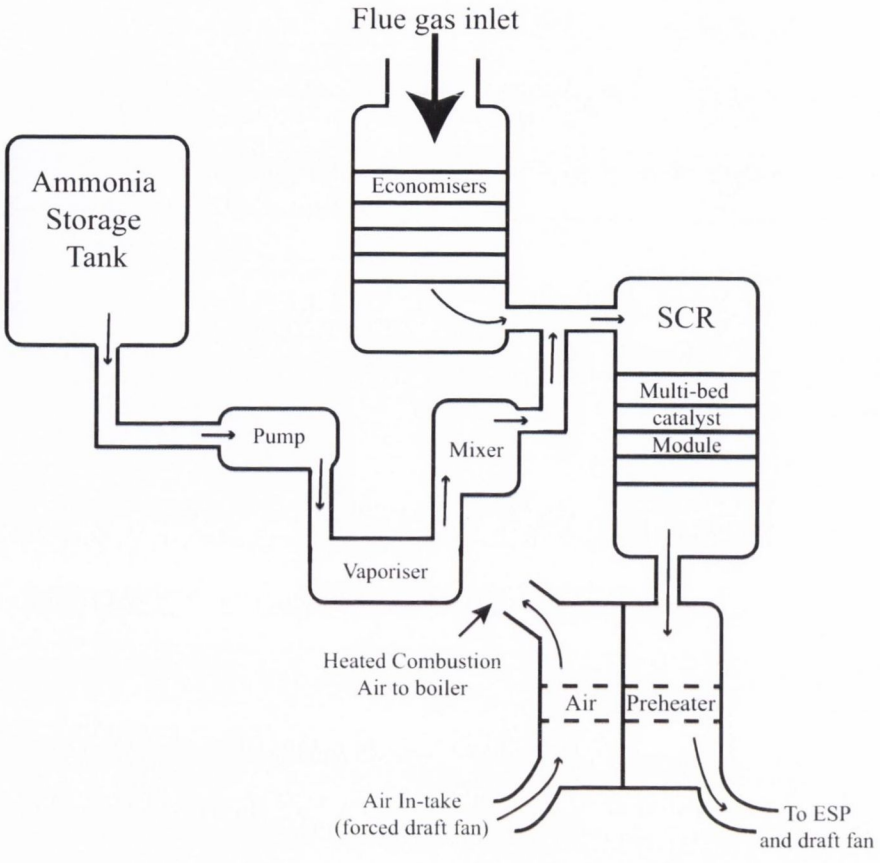


Figure 1.3: A schematic diagram showing the layout and flow of an industrial SCR-NH_3 process.

the HC, CO and PM emissions from the engine, while the DEF mixes with NO_x gases before entering the SCR catalyst. The hydrolysis of urea to ammonia then reduces the NO_x to N_2, with H_2O also formed. The SCR catalyst is based on a high loading supported metals to operate at low temperatures on a V-TiO_2 support that works in a similar manner to SCR-NH_3.

The mobile SCR (mSCR) catalyst is similar to the SCR-NH_3 catalyst with the exception of the hydrolysis of urea step. The mSCR was developed to operate under lean conditions, high velocities and at a low temperature as the HDD engine works at a lower temperature (393K - 473K) than stationary sources, and also resistant to sulphur deactivation. There are however, issues with the mSCR technology as; NO_x concentration requires a fast sensor which are not sufficiently fast enough, the size of the mSCR catalyst is significant and only suitable for large trucks and buses, and

the requirement to prevent the emission of ammonia based toxic by-products. The operation of the mSCR catalyst is heavily based on precise calibration of the in-flow of urea injected as a function of the quantity of NO_x emitted by the engine, and the exhaust temperature and catalyst characteristics.

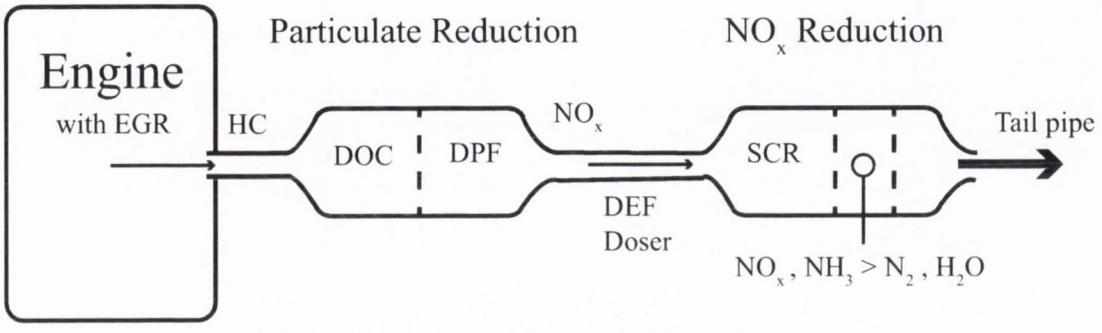


Figure 1.4: A schematic diagram showing the layout and flow of a mobile SCR convertor.

1.2.3 Diesel Engine: NO_x Storage/Reduction Catalyst

The NO_x storage/reduction catalyst (NSR) technology, often referred to as lean-trap NO_x, was developed by Toyota in 1995 as a viable alternative to SCR due to the difficulties associated with SCR.[50] NSR has the advantage over SCR that it does not require an ammonia/urea reductant, and is also more efficient for $de\mathrm{NO}_x$ than SCR. The principle of NSR is two-fold; (a) the NO_x emissions are oxidised and trapped on the absorber in nitrate form under lean conditions, and (b) the NO_x molecules are then released and reduced by the reductant under rich conditions (Figure 1.5). The A/F ratio needs to be controlled by oxygen sensors to create lean and rich conditions. To reduce NO_x and release N_2, the oxygen content needs to be greatly lowered to less than a factor of 1 which is unusual for the diesel engines. A priority of NSR technology is therefore to optimise the lean and rich conditions in order to optimise $de\mathrm{NO}_x$ while maintaining an economic fuel consumption. These conditions under which regeneration occurs regulate the duration and efficiency of $de\mathrm{NO}_x$, and it is better to tune the A/F ratio to favour CO emissions over HCs.

For an NSR catalyst, the structure is generally comprised of precious metals, a NO_x

storage component and a metal-oxide support. NSR catalysts are typically composed of Barium monoxide (BaO) as a NO_x storage component, and Pt metal deposited on the Al_2O_3 support, as shown in Figure 1.5. The BaO is mainly present for the storage of NO_x, while the oxidation of NO and reduction of NO_x is carried out on Pt.[51] The high concentration of O_2 during lean-burn conditions oxidises some of the BaO to a peroxide (BaO_2), which can also oxidise some NO gas to NO_2. Al_2O_3 acts as a support for the NSR catalyst due to its high surface area to disperse the precious metals and adsorbers for more efficient $de NO_x$, and also its high thermal stability.[52]

The Ba-Pt interface plays a significant role in the storage of NO_x, as the NO_2 gases formed from NO oxidation, or directly from the exhaust, are trapped/stored as nitrites (NO_2^-) or nitrates (NO_3^-), forming $Ba(NO_3)_2$ complexes.[53, 54] The oxidation of NO is an important step during NSR as the BaO is more effective at adsorbing NO_2 compared to NO. The reducing agents (CO, HC, H_2) are then introduced under rich conditions, and the NO_x is released from the storage sites onto the Pt metal and then reduced to N_2 on the metal surface. The mechanism by which this is carried out is different for varying types of HCs and it is difficult to distinguish between the different NO_x reduction mechanisms. The subtle changes in the operating conditions would also effect the $de NO_x$ process. Large Pt particles were found to be more efficient for NO_x reduction than smaller Pt particles as there is a greater surface area exposed for NO oxidation or NO_2 adsorption; however Pt-O can form on the particles and deactivating the metal.

The most commonly used metal for NSR technologies is Pt metal as it plays a key role in the NO_x storage/reduction cycle. More recently Pd metal has been widely used in the TWC as it has shown efficient oxidation of CO and reduction of NO_x, and therefore considered an alternative to Pt for NSR.[55, 56] Pd has shown an improvement over Pt for NSR under specific conditions, and a good candidate as it is less expensive and widely available, reducing manufacturing costs. $Pd/BaO/Al_2O_3$ catalysts were also developed and show promising NO_x reduction over the traditional $Pt/BaO/Al_2O_3$ NSR catalyst; however, during the NSR cycle over a period of time, the Pd based catalyst

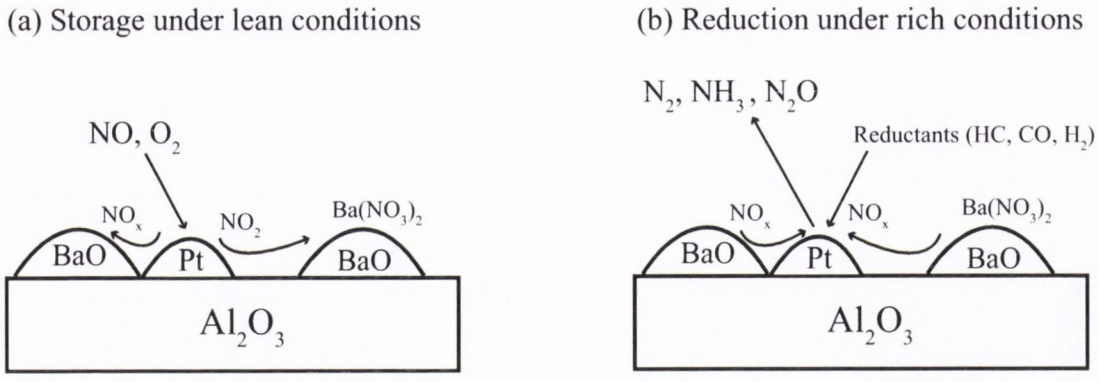


Figure 1.5: A schematic diagram showing the (a) storage of NO_x under lean conditions and (b) the reduction of NO_x under rich conditions for the NSR technology.

shows diminishing NO_x reduction at 673K while the Pt based catalyst is not effected. This has been attributed to the Pd catalyst becoming significantly deactivated by sulfur poisoning, as Pd is known to suffer from this attribute. At relatively low operating temperatures, the Pd catalyst also shows low NO_x conversion when using HCs as reducing agents. Rh metal was also investigated as an NSR catalyst since it has the highest NO_x reduction properties among platinum group metals. It did however, demonstrate low NSR activity due to its low NO_x storage capacity and low NO oxidation activity. Since Pd and Rh show better NO_x reduction than Pt, while Pt exhibits better NO oxidation performance than Rh or Pd, bimetallic combinations of Rh, Pd and Pt have been investigated. A Pt-Rh/BaO/Al_2O_3 catalyst exhibits poorer NO oxidation while having stronger NO_x reduction properties than the traditional Pt/BaO/Al_2O_3 catalyst,[57–60] indicating it as a stronger alternative. The cost of fabrication is however, much higher and this limits the use of bimetallic systems. The Pt based catalyst is therefore still used for NSR technologies, although recently Co has been suggested as a possible alternative candidate.

The impact the A/F ratio has on both storage and reduction of NO_x indicates that optimum regeneration occurs at high levels of richness; however under rich conditions, HC and CO can be emitted so there is also an oxidation catalyst introduced downstream. Optimisation of the system leads to 80% reduction of NO_x for only a 2-5% fuel consumption. Similarly to SCR, NSR can suffer from deactivation of by sulfur poisoning

as the trap becomes saturated by sulphates which are more stable than nitrates. This can be overcome/supressed by optimising the acidity of the support by using a combination of TiO_2 and Al_2O_3. This maintains NO_x storage while limiting the adsorption of SO_x. To enhance this effect, a monolithic substrate was used, resulting in a uniform washcoat thinkness. Rh/ZrO_2 was added to promote *in situ* hydrogen regeneration on the catalyst via steam reforming.[61, 62] The hyrdogen can bind to the sulphur forming hydrogen suphide (H_2S), which is easier to remove from the catalyst.[63, 64]

1.3 Understanding the *De*NO_x pathway

The reduction of NO_x gases from the exhaust is a crucial process for pollution control due to their adverse effects on the environment. The development of *de*NO_x technologies such as the TWC, SCR and NSR, the continuous scientific research into these technologies and stricter government regulations have reflected the need for NO_x abatement. The key to understanding these technologies for *de*NO_x is to investigate the mechanism for the reduction pathways of the NO_x gases on the Rh, Pd and Pt metals.[65–69] In particular Rh metal since this is known to be the most effective of the three metals to carry out NO_x reduction. The general breakdown of NO_2 (including NO) on the precious metals is given as;

$$NO_{2(g)} \rightarrow NO_{2(ads)} \tag{1.19}$$

$$NO_{2(ads)} \rightarrow NO_{(ads)} + O_{(ads)} \tag{1.20}$$

$$NO_{(ads)} + O_{(ads)} \rightarrow N_{(ads)} + 2O_{(ads)} \tag{1.21}$$

$$N_{(ads)} + 2O_{(ads)} \rightarrow \frac{1}{2}N_{2(ads)} + O_{2(ads)} \tag{1.22}$$

$$\frac{1}{2}N_{2(ads)} + O_{2(ads)} \rightarrow \frac{1}{2}N_{2(g)} + O_{2(g)} \tag{1.23}$$

which shows the associative adsorption, subsequent dissociation and removal of dissociative products on the metal surface. The *de*NO_x process on the Rh metal has attracted considerable interest in heterogeneous surface catalysis, as Rh metal is known

to be efficient as it breaks the N=O bond more easily,[70] and has greater selectivity for N_2, rather than harmful NH_3 in the presence of hydrocarbons.[71, 72] The U.S geological survey in 2012 reported that 81% of the world's production of Rh metal went into the fabrication of auto-catalysts, depleting ores and making it an expensive metal to use.[73] Pd and Pt metals are also used in these technologies to carry out the oxidation processes and can also perform *de*NO_x to reduce the concentration of Rh, albeit with a reduced efficiency. More recently, however, the use of Pt for these purposes and the general worldwide consumption of Pt has made it more expensive than Rh. Pd has been suggested to be a candidate to replace Rh; however it suffers from sulfur poisoning, and produces large quantities of N_2O as a by-product, which is 300 times more harmful to the environment than CO_2. This has prompted significant interest in these three metals, in particular their {111} surfaces since they are the most thermodynamically stable surfaces, with a view to understanding their *de*NO_x properties; however the exact mechanism for the *de*NO_x process on the three metals is unclear and in considerable debate. The exact mechanism by which NO_x are reduced on Rh by considering all possible pathways, is still lacking in the current literature and this needs to be understood to understand Rh's effectiveness for *de*NO_x.

1.3.1 The Rh {111} surface

The adsorption of NO and its subsequent breakdown to N and O ad-atoms have been examined by experimental studies. At low coverages ($\theta_{NO} < 0.25$ML), high-resolution electron energy loss spectroscopy (HREELS) and low-energy electron diffraction (LEED) techniques have assigned the preferred site for NO adsorption on the Rh surface as the three-fold hollow site,[74–78] which has been further identified as the hcp hollow site by computational studies.[79–82] Early infrared (IR) studies have used vibrational data to alude to the co-existence of a mixture of cationic (NO^+) ($1920\,cm^{-1}$), neutral ($1838\,cm^{-1}$) and anionic (NO^-) ($1740\,cm^{-1}$) NO on Rh/Al_2O_3.[83, 84] The NO^+ species can be formed by donation of electron density from the NO $2\pi^*$ anti-bonding orbital to the Rh $4d$ orbitals, while the NO^- species can be formed by the opposite pro-

cess. The assignment of vibrational data to the charged nature of the NO adsorbate on the Rh surface is in much debate as interpretation of the assignments can be ambiguous. A Fourier Transform IR study (FTIR) by Liang *et al.*[85] challenged this by assigning bands at 1838 cm^{-1} and 1740 cm^{-1} to the symmetric and anti-symmetric vibrations of a di-nitrosyl complex on the Rh surface, while indicating that a cationic Rh-$NO^{\delta+}$ species (1912 cm^{-1}) and a neutral tilted NO species (1648 cm^{-1}), were present at low temperatures on Rh/Al_2O_3. This was in agreement with an IR study[86]; however, they also identified the existence of an anionic surface species, that highlights the uncertainty with assigning the IR data for NO on Rh. An electron energy loss (EELS) study[87] identified two NO stretching modes on Rh {111} at 1500 cm^{-1} and 1610 cm^{-1} at low coverage, that were assigned to two-fold bridge bonded sites by comparing to IR data for NO on Pt {111}, rather than to $Rh(NO)_x$ complexes as previously carried out.[88, 89] The authors also further suggested that the bridge bonded NO adsorption is observed for all coverages up to a saturation coverage of 0.75ML. The low frequency band first observed on adsorption (1500 cm^{-1}) experienced an IR shift down to 1480cm^{-1} for small exposures of NO (<0.1L), which was attributed to the back-donation of charge from the metal *d* band into the $2\pi^*$ orbital of the NO adsorbate, resulting in a strengthening of the metal-NO bond and a weakening of the N-O bond.

The vibrational assignment for the surface site and charge of the NO molecule on the Rh surface is uncertain. Subsequent IR studies disputed previous work by assigning vibrational bands to an anionic NO^- species (1642 cm^{-1}) at low coverages on the Rh surface, while at higher coverages the cationic species was observed to form from the presence of multiple NO adsorbates.[90, 91] As the experimental IR assignment is ambiguous, a density functional theory (DFT) study using the Perdew-Wang 91 (PW91) exchange-correlation functional was used to calculate the vibrational frequencies for NO adsorption on the Rh surface at 0.33ML, 0.5ML and 0.75ML coverages;[80] however the coverages that were used in this study are surprising, as experimental findings indicate that NO adsorption ranges from 0.25ML to 0.75ML coverages.[75] The DFT calculations indicated that the most favourable adsorption site for NO at a low coverage (in

this case 0.33ML) is the three-fold hcp hollow site with a calculated harmonic vibrational frequency of 1629 cm^{-1} and an anharmonic frequency of 1544 cm^{-1} in contrast to previously assigned bands to a bridge site.[87] The DFT study[80] then compares the calculated vibrational frequencies with that of the experimental assignments for the three-fold hollow sites, indicating that the lowest energy NO adsorption is a three-fold site.[92] Although this study examines the assignment of the adsorption sites by vibrational data, it did not however, discuss on the electronic structure or any charge interactions between the NO adsorbates and metal surface.

The adsorption of a molecule on a metal surface is generally described by the interaction of the molecular frontier orbitals, namely the highest occupied molecular orbital (HOMO) and the lowest unoccupied molecular orbital (LUMO). A bond is formed between the HOMO of the adsorbate with the metal states leading to charge donation into the metal which is balanced by back-donation from the metal to the LUMO. This is known as the Blyholder model for unsaturated π accepting molecules on metal surfaces[93] and has been used to describe the electronic structure of an NO adsorbate on a metal surface for the platinum group metals,[94–98] in particular for NO on the Rh {111} surface[99]. X-ray emission spectroscopy (XES) studies for CO and N_2 on metal surfaces by Nilsson *et al.*[100–104] have, however, shown that this model is an over-simplification, and alude to the existence of a more complicated mechanism referred to as the 'allylic configuration' for these systems, which has recently been supported by DFT studies for NO on Pt {100}[105]. This is characterised by the NO 5σ orbital being stabilised by the metal surface, and mixing between the 1π and $2\pi^*$ NO orbitals with the metal d states at the top of the valence band. This interaction is described as a non-bonding interaction, where the electron density is localised as a 'lone pair' situated on the non-bound atom directed away from the metal surface. The interaction between the metal d band and the mixed 1π-$2\pi^*$ states of the adsorbate is said to from a $\widetilde{d}_\pi$ band. The σ interactions for these adsorbates have shown strong orbital mixing, where the adsorbate-substrate complex is stabilised by the π interaction but destabilised by the σ interaction. These recent revelations have brought into question

the charge interactions for molecules such as NO with metal surfaces, and thus their electronic structure on metal surfaces needs to be re-examined.

Temperature-programmed desorption (TPD) and X-ray photoelectron spectroscopy (XPS) studies indicated that the low temperature adsorption of NO on the Rh {111} surface is found to occur molecularly at a temperature of 120K and a coverage of <0.3ML.[106] Upon heating it dissociates to N and O ad-atoms with a barrier for dissociation around 65 kJ/mol.[75] The N_{ads} and O_{ads} dissociation products were found to prefer hcp and fcc hollow sites, respectively.[107] At higher coverages, NO dissociation does not occur and around 455K NO desorbs from the Rh surface.[87, 106] Temperature-programmed static secondary ion mass spectrometry (TPSSIMS) has shown that the activation energy for the desorption of dissociated products to both N_2 and O_2 requires 118±10 kJ/mol, with no provided breakdown for the individual contributions.[75]

In contrast to NO, the adsorption, decomposition and electronic structure of NO_2 on the Rh {111} surface has received little attention. The adsorption of NO_2 on the Rh {111} surface occurs at temperatures below 150K[108] and at a 0.25ML coverage. Through vibrational analysis, NO_2 is thought to dissociate to surface adsorbed NO^+ and O^- species,[109] where the breakdown of NO_2 increases the concentration of adsorbed O species, thus hindering further dissociation of NO to N_2 and O_2 gases. These studies, or any to our knowledge, have not fully established the coordination of NO_2 adsorption on the Rh {111} surface, and furthermore have not examined the energetics for the decompositions steps on the Rh {111} surface, which need to be investigated.

From the previous studies detailed above, a number of issues with $de\mathrm{NO}_x$ on the Rh {111} surface still needs to be addressed: (1) the exact charge and electronic interaction of the adsorbates, (2) the adsorption mode of NO_2 and (3) the decomposition energies for NO_x to N_2 and O_2 gases.

1.3.2 The Pt and Pd {111} surfaces

The adsorption and decomposition of NO_2 on the Pd and Pt {111} surfaces has received little attention in the current literature. High resolution electron energy loss (HREELS)

studies have characterised the NO_2 adsorption mode as a μ-nitrito configuration (N and O atoms bonded to surface top sites and the other O atom directed away from the surface) by assigning vibrational frequencies of 790 cm^{-1}, 1170 cm^{-1} and 1545 cm^{-1} for Pd[110], and 795cm^{-1}, 1180 cm^{-1}, and 1560 cm^{-1} for Pt[111] to the bending, asymmetric and symmetric modes, respectively, which has also been supported by density functional theory (DFT) studies.[94, 97] NO_2 adsorbs on the Pd and Pt {111} surfaces at 110K and 100K, respectively, up to a saturation coverage of 0.5ML of which, it no longer decomposes, and competition to desorb from the surface occurs[94, 111, 112]. At a surface coverage of $\leq$ 0.25ML, NO_2 completely dissociates to NO, with two vibrational bands observed at 1735cm^{-1} and 1575cm^{-1} assigned to NO top and bridge sites respectively, and O species at 180K and 285K on Pd and Pt, respectively [110, 111]. For the Pt {111} surface, it is suggested that NO and O species do not recombine[113] and NO desorbs, leaving the O atoms bound to the surface[114, 115]. The flat Pt {111} surface is thus weak at decomposing NO, and O ad-atoms are seen to inhibit further decomposition of NO_2 due to site blocking.[116] To our knowledge, the decomposition of NO_2 has not been investigated on the Pd {111} surface.

In comparison to NO_2, the adsorption of NO on the Pd and Pt {111} surfaces has received considerably more attention, with the adsorption sites and surface structure being characterised at different coverages.[80, 88, 89, 117–132] HREELS study showed that NO adsorbs with an N-down orientation between 100-373K on the Pd surface with the vibrational bands (1535 cm^{-1}) of the low temperature adsorption at 100K assigned to a three-fold hollow site.[133, 134] NO adsorption on the Pt {111} surface initially occurs at 120K up to 300K[88, 117]. Experimental[123, 126, 127, 130–132, 135] and computational[80, 128] studies are in agreement that the low temperature adsorption of NO occurs at a coverage of 0.25ML with a (2x2) structure[136], and using the assignment of vibrational data, was found to adsorb onto the fcc three-fold hollow site on both the Pd (1543 cm^{-1}) and Pt (1490 cm^{-1}) {111} surfaces. The surface-adsorbate charge transfer for the adsorption of NO on the Pd and Pt surfaces was thought to occur by direct donation of the metal d states to the anti-bonding $2\pi^*$ of the NO molecule forming

an NO^- species.[89, 95, 124, 128] This charge donation process is generally described by the interaction of the molecular frontier orbitals, namely the highest occupied molecular orbital (HOMO) and the lowest unoccupied molecular orbital (LUMO). A bond is formed between the HOMO of the adsorbate with the metal states leading to charge donation into the metal which is balanced by back-donation from the metal to the LUMO. This is known as the Blyholder model for unsaturated π accepting molecules on metal surfaces[93] and has been used to describe the electronic structure of an NO adsorbate on a metal surface for the platinum group metals.[94–98] More recent X-ray spectroscopy studies for CO and N_2 on metal surfaces have, however, shown that direct donation from the surface d states to the anti-bonding orbital of the adsorbate is a simplified model, and show that it is a more complicated mechanism called the 'allylic configuration'.[100–104] This has been supported by DFT studies for NO on Pt {100}[105]. The 'allylic configuration' is characterised by a stabilised 5σ orbital with the metal surface, and mixing between the 1π and $2\pi^*$ orbitals with the metal d states at the top of the valence band. This metal d band and $1\pi/2\pi^*$ interaction at the top of the valance band is suggest to be a non-bonding interaction with 'lone pair' states situated on the non-adsorbed atom directed away from the surface, which is referred to as a $\widetilde{d_\pi}$ band. These recent findings have brought into question the charge interactions for molecules such as NO with metal surfaces, and thus their electronic structure on metal surfaces needs to be re-examined.

In order to rationalise the different abilities of the metals for $de\mathrm{NO}_x$ chemistry, NO decomposition was investigated by molecular beam and vibrational studies.[134, 137, 138] NO was observed to dissociate on the Pd {111} surface, as evidenced by the detection of N_2 and N_2O around 425K. As temperatures increases so too does the surface coverage of the dissociation products and NO adsorbates up to a saturation coverage, and at 500K, NO was predominantly found to desorb from the Pd {111} surface[139]. This appears to free up surface sites and thus further dissociates any remaining NO molecules.[133] The oxygen surface atoms resulting from the decomposition are reported to form a p(2x2) structure at a surface coverage of 0.25ML, with

the oxygen atoms occupying three-fold hollow sites[140, 141]. These O ad-atoms consequently block surface sites on the Pd {111} surface, inhibiting further NO dissociation at saturation coverages[134]. On the Pt {111} surface, NO fully desorbs at 320K with no clear evidence for dissociation[142–144]. Overall, NO dissociation is observed on the Pd {111} surface while it simply desorbs on the equivalent Pt surface, with the cause of this difference being unknown.

Previous studies have all focused on identifying the adsorption mode of NO_x on the Pd and Pt {111} surfaces rather than building a complete understanding of the electronic interactions of the adsorbates with the clean metal surfaces. In addition, the stepwise decomposition profile of NO_x to N_2 and O_2 gases has not been studied in detail. Understanding this process on the two metals is essential for understanding the differences in their abilities for *de*NO_x chemistry.

1.3.3 The Rh {100} and {110} surfaces

Although the {111} surface is the most thermodynamically stable surface, a mixture of other low index surfaces such as the {100} and {110} may be present on the metal catalyst within the *de*NO_x technologies. The *de*NO_x chemistry of these lower index surfaces will need to be investigated in order to understand their ability to breaking down NO_x.

The adsorption and dissociation of NO_2 on the {100} and {110} surfaces of Rh, to our knowledge, lacks any extensive attention in the current literature. The absence of experimental detection for NO_2 on the low index surfaces, and the presence of NO and O on the {100}[145] and {110}[146], surfaces suggests evidence for fast dissociative adsorption of NO_2 to NO and O. To provide a clearer understanding of the *de*NO_x chemistry on the low index {100} and {110} surfaces of Rh, the adsorption and dissociation of NO_2 is important, and needs to be examined in detail.

The adsorption and dissociation of NO on the {100} and {110} surfaces of Rh has received much more attention than NO_2 since this is an important step in the *de*NO_x process due to the large activation barrier for NO dissociation.[23, 24] The NO molecule

was found to adsorb associatively at 100K on the Rh {100} surface.[147] For NO adsorption on the Rh {100} surface, experimental HREELs, SFEM, XPS and XPD studies have suggested the existence of two chemisorption modes; one is a molecular linear adsorption mode bonded perpendicular to the surface, while the other is a highly inclined NO adsorption mode with both N and O atoms bonded to the surface, possessing a weak N-O bond.[145, 147–149] The HREELS vibrational data eluded to the preference of a bridge site for both adsorption modes, with an adsorption band of $920\,\mathrm{cm}^{-1}$ assigned to the tilted species, while a frequency band of $1580\,\mathrm{cm}^{-1}$ was assigned to the upright NO adsorption mode.[150] The upright NO adsorption mode is observed experimentally for coverages up to 0.25ML, while the tilted adsorption mode is observed at coverage of 0.1-0.2ML[149] and LEED studies indicate these form a p(2x2) structure.[151] Any other species that may contribute to low energy bands such as N_2O, NO_2, N_2O_2 were ruled out to verify the existence of the tilted species and its vibrational data assignment,[150] as originally suggested to exist on the {100} surface of Rh.[147] The adsorption of NO at the bridge site for a 0.25ML coverage was supported by DFT calculations,[79, 152–154] and a calculated vibrational frequency of $1605\,\mathrm{cm}^{-1}$ providing a link to experiment.[154] The DFT calculations by Loffreda *et al.*[154] examined the upright and tilted NO adsorption modes, indicating that the upright NO mode is a more stable adsorption mode that the tilted NO with N and O atoms bonded to the surface by 0.07 eV at the dissociation coverage of 0.25ML, in contrast to the previous combined experimental and theoretical study by Bondino *et al.*[149] The difference in energy between the two configurations is too small to rule out the existence of the highly tilted NO mode on the {100} surface; however a more recent DFT study by Tian *et al.*[155] clarified this by using the nudged elastic band method to show that the tilted NO with N and O atoms bonded to the surface is a stable transition state precursor to NO dissociation.

For the Rh {110} surface, NO adsorbs associatively at 100K and prefers the bridge site at a coverage of 0.25ML,[156] in a similar manner to the {100} surface. At this coverage, a p(1x1) structure is observed, which changes to a disordered c(2x8) structure up

to a saturation coverage of 0.9ML at 120K, evaluated by XPS[157] and TPD.[158] This structure converts to a (2x1)*pg* after being heated up to 200K, and the NO adsorbates are speculated to form zig zag patterns, but lacked any experimental evidence.[158] Unlike the {100} surface where two different adsorption modes were observed experimentally, only one adsorption mode was detected on the {110} surface of Rh with a N-O vibrational stretching range of 1560-1710 cm^{-1} depending on NO coverage.[156] There is no direct evidence to suggest that the NO molecule is upright on the {110} surface; however the assignment of vibrational data falls in a similar range to the {100} surface. Near edge X-ray adsorption spectroscopy (NEXAFS) by Morgante *et al.*[159] indicated that the molecular axis of NO is close to the surface normal at all coverages. The adsorption of NO molecule being the most stable mode in an upright position at the bridge site was supported by DFT calculations.[160] The DFT-LDA study by Liao *et al.*[160] also tested a tilted NO adsorption mode with both N and O atoms bonded to the surface that is observed on the {100} surface, finding that it is less stable than the upright molecule. This study suggested that the tilted adsorption mode could be a precursor for NO dissociation, which was later identified in a recent study by Tian *et al.*[155] in a similar manner to NO adsorption on the {100} surface of Rh. Although the adsorption mode for NO on the {100} and {110} surfaces of Rh has been identified by both experiment and theory, the electronic interactions between the NO and metal surface still needs to be elucidated. This will provide a clearer understanding of the NO-Rh bonding on the {100} and {110} surfaces, and also the charge transfer mechanism that is uncertain in a similar fashion to the {111} surface.

The dissociation of NO is detected between 120-250K on the {100} surface using TPD and SSIMS measurements[161], and around 300K on the {110} surface of Rh identified by TPD,[146] with N_2 and N_2O gas products seen to evolve from both surfaces. The dissociation of NO on the {100} surface reaches a maximum rate around 0.25ML coverage,[162] and the rate becomes progressively slower with increasing coverage of NO up to a temperature of 450K where the NO begins to desorb from the surface.[163] The dissociation of NO to N and O atomic species is the crucial step for *de*NO_x on the

{100} surface, having an activation barrier of 37kJ/mol.[164] At higher coverages the dissociation is significantly effected by the N and O dissociation products as these are also found to occupy bridge sites on the {100} surface.[155, 164, 165] The O surface atoms are found to form a p(2x2) structure at a coverage of 0.25ML[166], which is found to change to a (2x2)$p4g$ structure at a coverage of 0.5ML, identified by STM and LEED.[167, 168] The symmetry of the structure pattern was contended by Norris *et al.*[169] suggesting that it is a (2x2)$p2gg$ in support of an earlier study by Oed *et al.*[166] The preferred adsorption site for N on the {100} surface has been calculated to be the four-fold hollow site by DFT calculations,[79, 155] which is the suggested adsorption site by experiment.[164] The N atoms are found to combine on the surface to form N_2 and desorb from the surface with a barrier of 225kJ/mol at a temperature range of 600-800K, whereas the combination of O ad-atoms and desorption of O_2 occurs at a much higher temperature range of 1200-1400K.[147, 164] This indicates that O_2 is much more difficult to remove from the {100} surface, and it has been suggested that O saturates the surface at high coverages, reducing the dissociation rate of NO.[167] Since the desorption of O_2 occurs at a higher temperature range, a TPRS and RAIRS study by Jansen *et al.*[162] has been suggested that the surface bound O ad-atoms are removed from the surface by CO, oxidising to CO_2 and regenerating the surface for further NO dissociation, which was earlier suggested by a theoretical study by Vučković.[170]

NO dissociation on the {110} surface to atomic N and O ad-atoms occurs between 170-400K[146, 156, 157], and an activation energy of 15kJ/mol was measured by TPSSIMS experiments assuming first order kinetics.[171] The dissociation of NO increases with increasing temperature but decreases with increasing surface coverage of NO adsorbates, in a similar manner to the {100} surface.[156] The dissociation of NO was found to occur more rapidly on the {110} surface than on the {111} surface,[172] while the reactivity of the {100} surface was found to lie between these two surfaces.[173] A comparative DFT study[155] examining dissociation pathways on the three surfaces indicated that the barrier is lowest on the {100} surface, suggesting that NO dissociation is more facile on this surface and questioning the previous experimental results.

At low concentrations of N and O dissociation products on the {110} surface, the surface is enriched by N ad-atoms forming (nx1)-N reconstructions, where n is 2 or 3, at coverages less than 0.2ML.[174] The N layers form a (2x2)*pg* pattern at coverages below 0.4ML at temperatures <400K, while above 440K the surface reconstructions are removed and the (2x2)*pg* pattern remains.[175] The fractions of N and O on the top layer change with surface concentrations, and LEED measurements indicate that N atoms tend to sink subsurface.[157] The adsorption of O on the {110} surface forms a (2x2)*p2mg* structure at 0.5ML[176] above 470K, which consists of O ad-atoms adopting zig-zag patterns in three-fold hollow sites observed by LEED experiment,[177] which are suggested to diffuse below the surface in a similar manner to N ad-atoms.[178] At higher coverages above 0.2ML, the O atoms occupying the three-fold hollow sites displace the (2x1)-N structure causing structural transformations with a transition from separate (2x1)-N and (1x2)-O islands to a mixed (2x2) N and O structure.[179, 180] The N atoms on the surface were found to form N_2 and multi-directional desorption occurs from the surfaces showing 5 different TPD peaks up to 160K.[181, 182] The peaks indicate different species of N_2 present from recombination of N on the surface, and also varied kinetics from possible decomposition of N_2O forming N_2 which is evolved from the surface.[183] The evolution of gaseous O_2 was not experimentally observed from the {110} surface; however for the NO+CO reaction, CO_2 is detected suggesting that the CO molecule removes O ad-atoms from the surface.

The dissociation of NO_x on the low index {100} and {110} needs further investigation as the full description of *de*NO_x on their surfaces remains unclear. Electronic structure studies between the atomic and molecular species and the metal surfaces is lacking in the current literature, requiring full examination to describe their mechanism for charge interactions. The energies for the different steps of the *de*NO_x profile on these surfaces has also not been examined, which is important to show their differences at breaking down NO_x, forming N_2 and desorption from the surfaces. The different adsorption modes for NO_2, N_2 and O_2 have also not been characterised. These points need to be addressed to fully explain and show the *de*NO_x behaviour of the {100} and

{110} surfaces of Rh metal.

1.3.4 Rh stepped surfaces

The exposed metal surfaces with low index {111}, {100} and {110} facets are not entirely flat, possessing defects such as steps and kinks that act as active sites to enhance the ability of the surface to interact with the gaseous species. The steps are generally more active for molecular dissociation than on the flat terrace as their presence on the surface perturbs the local electronic structure due to the lower coordination of the atoms than on the flat terrace.[184–186] Understanding the surface morphology such as steps on the metal surface provides more of an insight into reaction mechanisms that occur on actual metal catalysts.

The enhanced activity of metal catalysts for bond dissociation has been the subject of rigorous investigation by both experiment[187–189] and theoretical calculations[190–192] in recent years. Step defects on metallic surfaces such as Rh and Pd favour bond breaking mechanisms which were shown to be 10 times more reactive to NO_x dissociation than the flat {111} surface.[190, 193, 194] Experimental work has been carried out to investigate the effect of steps on the adsorption of NO on Rh. The adsorption of NO and CO has been characterised using LEED and thermal desorption spectroscopy (TDS) measurements on Rh{755} and {331} surfaces,[195] while XPS has been used to study NO on Rh{553} and {311} surfaces.[196, 197] Scanning field emission probe-hole microscopy (SFEPHM) has also been used to study the adsorption of NO on the Rh{211} and {321} surfaces, and the effect of the steps on the kinetics for NO dissociation on these surfaces and the Rh{911}, {711}, {511} and {311}.[194] The dissociation of NO on the stepped Rh{211} surface was examined using scanning field electron emission microscopy (SFEM)[148], and also on the Rh{711}, {410}, {533} and {311} using TDS.[188] An FEM study by Hendrickx *et al.*[198] carried out for several stepped surfaces showed that NO adsorption occurs at around 300K on all surfaces of Rh, and the work function due to NO adsorption increases as the surface becomes rougher (more step defects are present). This FEM study also shows

that the ability of the surfaces for N-O bond scission increasing in the following order; $\{111\}, \{110\} < \{100\}, \{511\} < \{650\} < \{410\} < \{210\} < \{331\}, \{533\} < \{321\}$. The dissociation of NO to N and O was found to occur at <450K on the step, and at saturation coverage found to desorb around 420K.[188] The presence of steps on Rh was found not to effect the stability of N ad-atoms, and at a saturation exposure of NO, N_2 desorbs from the {100} terraces at 750K and between 450 to 750K on the {111} terraces. The presence of O ad-atoms however, destabilises the N atoms and the N+O $\rightarrow$ NO reaction is favoured over the N+N $\rightarrow$ N_2 reaction.[188] Although the experimental studies have shown that the adsorption of NO and its dissociation occurs at the step edge and at a faster rate than on the flat terrace, they have not fully investigated the steps for the breakdown of NO_x, the formation of N_2 and O_2, and also the removal from the step edge.

Theoretical studies have investigated the adsorption and dissociation of NO at the step edge. A DFT study by Loffreda *et al.*[81] investigating the dissociation of NO on the stepped and flat Rh{100} surface, indicated that favourable dissociation occurs on the step of the Rh{511} surface (a Rh{100} stepped surface) but has a higher activation energy than the flat {100} surface, while it has a lower dissociation barrier to the close packed Rh{111} surface. Another study by Inderwildi *et al.*[199] found that a lower barrier for NO dissociation occurred on the step edge of a Rh{311} surface (a stepped Rh{111} surface with {111} terraces) than on the flat Rh {111} surface, while a the stepped Rh {211} surface was also found to have a lower activation energy than the flat {111} surface.[200] The lower activation energy for NO bond breaking on the step edge was also found to be lower that on the flat {111} surfaces of Ru and Pd metals;[190, 191] however Rh is generally found to have lower activation energies.[81] The NO dissociation to N and O were found to inhibit any further NO dissociation at high saturation coverages, and in the presence of excess O recombination of N and O occurs to form NO which desorbs from the step.[188] The preferred site for the N and O ad-atoms are the three-fold hollow site beside the step edge and the two-fold bridge site on the step edge, respectively, while the NO adsorbate was also found to adsorb directly

on the step edge. The N ad-atoms on the step were found to be more stable than on the flat {111} surface, and also more stable than either O or NO adsorbates with the order of the calculated DFT(PW91) chemisorption energies listed with the most stable first; $N_{211} > N_{111} > O_{211} > O_{111} > NO_{211} > NO_{111} >$.[201] The combination of N atoms to form N_2 is suggested to occur at the step since N_2 is weakly bound to the Rh{111} surface;[107] however the formation of N_2 was not examined in detail. The dissociation of N_2 was found to be dominated by steps for the Ru {0001} surface, indicating that the reverse reaction could possibly be difficult on the step.[202] Experiments have lead to questioning the formation of N_2 and facile desorption from the step edge on the Rh {111} surface. Additionally, the formation of O_2 was also left unexamined at the step edge, which is critical to remove O atoms from the step edge or poisoning and deactivation of the step could possible occur.

The adsorption and dissociation of NO on different stepped surfaces of Rh metal have been investigated by experimental and theoretical studies to date since the breakdown of NO is suggested to be the rate determining step.[67, 203–205] The presence of a step has shown to enhance the rate of NO dissociation on Rh{100} and {111} surfaces, and surfaces with a {111} step structure are found to be more active than those with a {100} step structure.[148] Theoretical studies have however found that the dissociation of NO is easier on a stepped Rh{511} surface than on stepped Rh{111} surface, questioning previous experimental results.[81] To date, the complete *de*NO_x profile for the breakdown of NO_x gases on the step of a Rh{111} surface and the elucidation of their electronic structure on the stepped Rh surface have not been investigated, in particular the investigation of NO_2 on step which has not been examined. A clearer understanding on formation and removal of N_2 and O_2 from the step edge is also lacking in the current literature. In order to further understand the properties of Rh metal for *de*NO_x, a complete profile for the breakdown of NO_x and subsequent removal of $N + O \rightarrow N_2 + O_2$ on a step of the Rh{111} surface needs to be fully examined.

1.3.5 Rh clusters for *de*NO_x applications

Atoms and small molecules react with transition metal nanoparticles in a similar manner to physisorption and chemisorption reactions observed on extended metal surfaces. Small metal nanoparticles, however, better reflect the surface defects present in catalytic materials than perfect crystalline surfaces and therefore an understanding of their catalytic properties will allow a more accurate description of conditions in catalytic technologies.

DeNO_x technologies contain Rh, Pd and Pt metal clusters dispersed across metal oxide supports and promoters. The study of these metal clusters is imperative to provide further insights into their *de*NO_x chemistry, as the presence of small clusters can perhaps interact with NO_x molecules in a different manner to extended low index surfaces of Rh, Pd and Pt metals. Examining the reactivity and unique properties of metal clusters will therefore allow an interesting opportunity to investigate any differences that may exist between cluster and extended metal surfaces.

Typical surface science experimental techniques for heterogeneous catalysis that characterise surface structure are difficult to use on transition metal clusters due to their complexity and relatively small size compared to extended surfaces. Laser-based spectroscopic techniques have been used to provide information on small metal clusters, resonant two-photon ionisation spectroscopy for a number of transition metal dimers, and zero electron kinetic energy photoelectron spectroscopy to obtain structures for species containing up to three metal atoms.[206] Raman spectroscopy provided structural information on silver clusters up to 5 atoms;[207] however these techniques can only be used for small metal clusters and in practice transition metal clusters are much larger. As larger transition metal clusters have large numbers of vibrational degrees of freedom, and low lying electronic states, traditional spectroscopic techniques can not be used and their structures are determined from their physical and chemical properties. Detailed measurements of the physical and chemical properties of transition metal clusters such as ionisation energies,[208–214] electron affinities,[215–219]

and magnetic properties[220–223] at thermal energies can be carried out by using fast flow tube reactors,[224–229] ion cyclotron resonance mass spectrometers,[230–235] and drift cells.[236] For most of these experimental methods, mass selection techniques are employed to examine the size of the clusters and fragmentation during reactions and ionisation.

Theoretical calculations on transition metal clusters are difficult to carry out due to the large number of electrons and open d-shells for the atomic species under consideration. The complexity of the issue and the computational difficulty of modelling these clusters meant that less sophisticated approaches were used such as Hartree-Fock,[237] extended Hückel theory,[238, 239] and potential scattering models.[239, 240] These approaches can provide qualitative information and identify trends about the systems of interest; however they are not accurate enough to provide sufficient geometrical and electronic data about the transition metal clusters. More modern theoretical approaches developed for sophisticated electronic structure analysis such as DFT, and increased computational power have allowed the prediction of transition metal cluster structures. DFT calculations have provided more accurate description of the ground state electronic structures, finding low lying isomers for metal clusters up to 10 atoms that are in close agreement with experimental results.[241–245] High level electronic structure calculations for metal clusters with more than 10 atoms were computationally demanding, and semi-empirical potentials, molecular dynamics and gradient based methods were thus used previously to predict the structure for larger metal clusters of nickel, palladium, copper, silver and gold.[246–250] The structural sensitivity and rates of reactions with gaseous species are cluster size dependent for many transition metals, therefore examining the metal cluster size and structure is crucial to determining the properties of transition metal clusters for chemical reactions. More recent advances in computational power and electronic structure methods have allowed these calculations to model larger cluster systems which provides a more accurate description of surface reactions with gaseous species on the transition metal clusters. These can work closely with experimental results on reactivity and thermodynamics to examine their

underlined chemistry.

Gas phase studies of transition metal clusters has shown that there is a strong size dependence on their structures and reactivity, and as the cluster size increases, their reactivity reaches a limiting behaviour similar to bulk metal properties. Small metal clusters exhibit greater reactivities towards gaseous species than surfaces of bulk metals demonstrating that they behave in a different manner to, and are not just small pieces of the bulk metal.[225, 251–253] For copper, silver and gold metal clusters, the ground electronic structure appeared to influence the stability of the cluster and relative size. These metal clusters with odd numbers of atoms have even numbers of electrons and are thus closed shell species, which are more stable than clusters with even numbers of atoms that have open shell electronic configurations. The metal clusters with even numbers of atoms thus tended to lose atoms to form stable closed shell species.[254–256] A similar dependence of the structure and behaviour of anionic vanadium trimers was attributed to the local electronic configuration of the $3d$ orbitals, supported by experiment and theoretical calculations.[257, 258] The copper, silver and gold metals have atoms with a ground state configuration of $s^1\ d^{10}$, and cationic, neutral or anionic metal clusters of these metals have strong stabilities, showing strong odd-even oscillations. The charged metal cluster, either cationic or anionic, exhibit strong binding energies for odd sized clusters while even-sized clusters have the strongest binding for neutral species. The variations are related to the number of valence s electrons, with the clusters having an even number of s electrons being the most stable. For small clusters, this predicts that the most stable are M_3^+, M_9^+, M_8 and M_7^- which is consistent with the predicted electron shell models.[259, 260]

Similar behaviour and stability is expected for transition metal clusters with 18 and 20 valence electrons, consistent with large binding energies associated with Ag_{19}^+ and Ag_{21}^+.[261] The stable cationic clusters of chromium metal have odd numbers of atoms with a ground state electronic configuration of $4s^0\,3d^5$, while Cr clusters with even numbers of atoms are more stable for the neutral Cr cluster ($4s^1\,3d^5$) suggesting their stability is dominated by the interaction of the $4s$ electrons.[262] For other transition

metal clusters the number of electrons does not greatly impact the stability of the clusters, but for these transition metals their compact and symmetric geometry has more of an impact on their relative stabilities.[206, 243, 263] The stability and behaviour of transition metal clusters appears be 'special' around clusters with 8, 18, 20, 34, 40, etc. valence electrons due to the local electronic configuration of these electrons being delocalised across degenerate levels.[259, 260, 264, 265] The unique properties and stabilities of metal clusters with around 20 atoms can also be examined using the cluster cohesive energy (E_c(n)) and heat of vaporisation at 0K ($\Delta_{vap}H_0^\circ$). The thermodynamics indicate that these size clusters have a E_c(n) about 70% of $\Delta_{vap}H_0^\circ$ which suggest that these clusters, have not arrirved at, but are approaching bulk phase behaviour as nearly all the atoms in these clusters are surface atoms. The study of these 'special' clusters is therefore necessary to understand their electronic structure and applications for surface chemistry.

The reaction of NO_x on rhodium clusters has received little attention in the current literature, in particular the adsorption and interaction of NO_2 which is lacking any considerable understanding on rhodium clusters. Theoretical calculations[266–275] have examined the magnetic and electronic properties, and also the structure of small $Rh^{\pm}$ clusters, reporting the different isomers and minimum energy structures for different cluster sizes; however the adsorption or interaction of small molecules on these clusters for catalytic purposes was not investigated. The adsorption and reaction of nitrogen oxides has been studied on small $Rh_n^{\pm}$ clusters (n < 30) by mass spectrometry techniques,[276–278] that showed a dramatic cluster size dependence on the interaction with NO. The rate of reaction of NO increases monotonically with increasing Rh cluster size in line with the rates predicted by collision theories,[279] with biexponential kinetics being observed for Rh_5^+ and Rh_6^+ clusters.[276] The reactivity of the rhodium clusters is dominated by electronic effects, and even in systems with smooth size dependence, the mechanism of reaction changes significantly with cluster size and structure, observed for the dehydrogenation of benzene,[280] interaction with azidoacetonitrile,[281] small alkanes,[282–284] and decomposition of nitrogen oxide. For the breakdown of NO the

Rh clusters have significant different reactivities with varying cluster size, even though the metal clusters have similar sticking probabilities.[277] $Rh^{\pm}$ clusters decompose NO at cluster sizes below 17 with the exception of the Rh_{13}^{+} cluster, which adsorbs multiple NO molecules without any evolution of NO. The interaction and breakdown of N_2O on the Rh_n clusters is also size dependent, with maxima in reactivity observed at cluster sizes of $n = 16$, 20,[278] which shows a similar size dependence to other transition metal clusters whose bonding is dominated by metal s valence electrons.[259, 260, 264, 265]

The structure and size sensitivity of $Rh^{\pm}$ clusters on the reactivity to decompose NO adsorbates is typical of transition metal clusters. For small clusters (n < 16) two NO adsorbates need to adsorb on the cluster before any N_2 evolution is observed.[277] The mechanism for decomposition is in much debate, similar to extended surface studies of Rh metal; however recombination of the N atoms are thought to lead to N_2 formation with the O atoms saturating the cluster. There is no evidence for N_2O or NO_2 formation on the Rh clusters to suggest this recombination mechanism.[277] As the concentration of NO increases, the Rh clusters become further saturated with O atoms forming $[Rh_xO_y]^{+}$ rhodium oxide clusters where the O atoms are found to inhibit any further NO decomposition.[276] DFT calculations on the adsorption of NO and dissociation are also very limited to date. NO was found to adsorb on the bridge site of Rh and Pd dimers, while this was found to be a tetrahedral site for NO on Rh_4 clusters. A DFT study by Piotrowski *et al.*[285] examined the adsorption of NO on Rh_{13} clusters finding that the low coordinated top and bridge sites are preferred on the different geometries of the Rh_{13} clusters. The study also investigates the electronic structure for NO interacting with the Rh cluster, reporting that there is no occupation of the $2\pi^*$ orbital for NO and that the general d-band model for metal-adsorbate interactions does not hold. The DFT studies to date have not examined larger metal clusters due to previous limitations in computer power and electronic structure theories; however the study by Piotrowski *et al.*[285] is more recent and size dependence was not the subject of their study. Examining larger clusters and also cluster size dependence on the adsorption and decomposition of NO is of technological importance to crucially understand their

behaviour for $de\mathrm{NO}_x$ chemistry.

The size of the metal clusters varies, and it is difficult to control their size when impregnated on the metal oxide surface. As the {111} surface is the most thermodynamically stable surface, it is the most express on the metal clusters and also varies with varying cluster size. It is therefore necessary to examine the variation of the {111} surface on the metal clusters to carry out $de\mathrm{NO}_x$ chemistry.

1.3.6 Intermediates leading to N_2O formation

The removal of NO from the exhaust stream is environmentally and catalytically important, as the breakdown of NO is considered the critical rate determining step for $de\mathrm{NO}_x$.[70, 71] Rh is known to be the best possible candidate to achieve the catalytic reduction of NO to N_2; however during this reaction, significant amounts of undesirable nitrous oxide (N_2O) are formed as a by-product.[172] The crucial property of Rh metal is thought to be the breaking of the N-O bond, so any other viable alternative catalyst for NO_x reduction will need to emulate this property. According to this mechanism the resulting surface N atoms would recombine to form N_2 and the formation of N_2O occurs via an interaction between a N atom and molecular NO. If this was the case, then the formation of N_2O could be controlled kinetically by maintaining a low concentration of NO in the reaction mixture;[286] however the desorption of N_2 at low temperatures did not follow first or second order reaction kinetics, suggesting a different mechanism is occurring.[287]

On the Rh{111} surface, NO dissociation to N and O atoms is followed by N_2 desorption above 350K,[87, 106, 288–292] TPD experiments for the reduction of NO on Rh indicated that two N_2 desorption peaks are detected at temperatures of 470K and above 500K on the {111} surface,[87, 106, 288] between 60 and 140K on the {100} surface,[293] and between 60 and 190K on the {110} surface.[182] The high temperature route for N_2 desorption can be described by simple second-order kinetics by assuming

the recombination of N atoms on the surface;

$$N + N \rightarrow N_2 \tag{1.24}$$

since there is sufficient thermal and kinetic energy to allow this reaction to occur.[87, 106, 288, 294] The kinetics for the low temperature route to N_2 formation should follow first order kinetics; however the reaction does not fit well to the first-order rate law, bringing the mechanism into question and there is thus considerable debate. Experimental studies[205, 294–303] using various surface science techniques suggested the formation of a N-NO surface intermediate during the production of N_2 at low temperatures, as opposed to the recombination of N atoms on the surface. These studies indicated that N_2O is in fact an intermediate step in the reduction of NO at low temperatures, and therefore the selectivity of N_2 versus N_2O cannot be controlled. The proposed mechanism leading to the formation of N_2O is given by;

$$2NO \rightarrow NO + N + O \rightarrow N_2O + O \rightarrow N_2 + 2O \tag{1.25}$$

The mechanism by Equation 1.25 indicates the breaking of one NO molecule on the surface, where a N and NO surface species combine forming the N-NO intermediate (N_2O). The N-NO intermediate formed on the Rh surface, is found to be relatively unstable on the surface and decomposes to form N_2(g) and $O_{(ads)}$ at the reaction temperature.[205, 297, 298, 302] Under realistic conditions both reactions (Equations 1.24 and 1.25) are simultaneously occurring on the surface, with the N-NO formation suggested to be the dominant mechanism, which can be enhanced by co-adsorbed NO.[302] The structure of the N_2O intermediate on the Rh {111} surface was characterised using DFT calculations by Paul *et al.*[304] as a linear N-terminal adsorbate on a single Rh atom top site. This adsorption mode is said to be weakly binding (0.39 eV), and an activation energy of 0.11 eV for dissociation of N_2O to N_2 and O. On the {100} and {110} surfaces of Rh, the adsorption of N_2O is suggested to be a mixture of a lying down linear species and a tilted species with terminating N and O bonds to the

surface.[305–307] The reaction between N and NO occurring at low temperatures to form N_2O was first studied by Belton *et al.*[308] whom examined this interaction by covering the Rh {111} surface with N atoms and subsequently exposing the ad-layer to NO at 200K. They only observed NO desorption, and recombinative desorption of N_2 from the {111} surface (Equation 1.24), and only a small amount of N_2O was detected from the reaction mixture. The low concentration of N_2O formed and evolved from the N+NO reaction was attributed to the weak binding of N_2O and its unstable nature which readily dissociates to N_2. The formation of N_2O via the N+NO mechanism was questioned, and a recent near-edge X-ray adsorption fine structure spectroscopy by Nakai *et al.*[309] revealed that the N atoms of the ad-layer do not interact with NO molecules but with a weak NO dimer weakly bound on the nitrogen layer. This has brought into question and reasonable doubt the mechanism for the N+NO reaction to form N_2O.

The NO dimer ($(NO)_2$) has been suggested to be an important intermediate in various NO-related biochemical and surface reactions.[310–314] The NO dimer precursor to the formation of N_2O is governed by the following mechanism;

$$2NO \rightarrow (NO)_2 \rightarrow N_2O + O \rightarrow N_2 + 2O \tag{1.26}$$

The mechanism outline by Equation 1.26 is in contention to the mechanism for N_2O formation proposed by Equation 1.25. As the breaking of a single NO adsorbate on the metal surface is difficult to achieve, the formation of a $(NO)_2$ (or N_2O_2) dimer species by two NO molecules is suggested to weaken the NO bonds, leading to a more facile breaking of one NO bond and forming the N-NO intermediate.[309, 315–318] The $(NO)_2$ dimer can exist from two NO molecules as they have one unpaired electron in their $2\pi^*$ orbitals which can accept another electron to become half filled, and thus have the ability to form a bond. The NO dimer is thus stable in the solid phase,[319] in the gas phase at low temperatures,[320] in rare gas matrices,[321] and on inert surfaces of graphite.[322, 323] The examination and elucidation of the NO dimer on a metal

surface will provide a more in-depth understanding of the reactions for NO reduction on metal surfaces.

The complete mechanism for the formation of $(NO)_2$, and decomposition to N_2O on the clean Rh {111} surface has not been fully characterised in the current literature by either experimental or theoretical studies, to the best of our knowledge. The presence of the N_2O_2 species has however, been characterised by DFT studies and detected by experimental techniques on the low index surfaces of Cu[324–326] and the {111} surface of Ag.[72, 314, 327–330] The $(NO)_2$ dimer was found to be unstable on the flat {111} surface of Pt; however it was found to exist on the step of the Pt {111} surface.[316, 331] These studies used RAIRS, STM, and photoelectron techniques to show that the low temperature pathway (below 90K) to N_2O formation goes via the $(NO)_2$ dimer as outlined by Equation 1.26, while DFT was used to characterise the stable structures of the dimer on the metal surfaces. In the gas phase, the ground state stable structure was determined by theoretical calculations to be a singlet A^1 *cis*(ON-NO) geometry with a long and weak N-N bond.[332–335] On adsorption the *cis*-$(NO)_2$ geometry was found to remain the same when interacting with the Cu{100} surface, as a (O_{ads}N-N-O_{ads}) adsorption mode was found to be the most stable from DFT calculations.[326] For the $(NO)_2$ dimer on the Ag and Pt surfaces, the most stable adsorption mode was found to change from the ground state geometry of the gaseous species to a (O=N_{ads}-N_{ads}=O) geometry, where both N atoms are bonded to the surface in an upright configuration.[316, 330] The mechanism for the breakdown of the $(NO)_2$ dimer on the Ag surface to the N_2O species was calculated using DFT, and it was found that the dissociation proceeds via an inverted (O_{ads}N-N-O_{ads}) dimer species, which assists in the facile breakdown to N_2O at very low temperatures, as observed experimentally.[336] The difficulty of Pt breaking down the $(NO)_2$ dimer species is that it must occur at a step edge, where the step pulls off an O atom leaving behind N_2O on the flat {111} surface of Pt.[316] These studies indicate that the $(NO)_2$ dimers exist on the Cu, Ag, and Pt surfaces as precursors to N_2O formation, and perhaps maybe an indication that they can also occur on other transition metal surfaces. This may

motivate further research into the mechanism of NO reduction through a $(NO)_2$ dimer as a possible weak intermediate to N_2O formation.

For the {111} surface of Rh, the interaction of NO with layers of N atoms was examined using NEXAFS and *ab initio* calculations.[309, 317, 318] These studies suggest that the $(NO)_2$ dimer forms as a second layer, interacting with the first layer of N adatoms as a precursor to N_2O formation on Rh; however this is unrealistic as at low temperatures below 100K, the dissociation of NO does not occur so that N atoms should not be already saturating the Rh surface. The formation of the $(NO)_2$ dimer as a possible weak precursor has been eluded to as a possible weak step for the reduction of NO on the clean {111} surface of Rh, but further investigation is required to fully understand this mechanism.

The mechanism for the reduction of NO on Rh metal is difficult to ascertain and in much controversy, as the two mechanisms to the formation of N_2O are possible; (1) by the N+NO interaction or (2) through a weak $(NO)_2$ precursor. No single study has examined all possible mechanisms to fully rule out the possibility of either mechanism occurring. In order to fully understand the mechanism of NO reduction on Rh, these need to be determined and compared to show the most favourable pathway leading to the N_2O intermediate. It is also necessary to understand the formation of both N_2 and N_2O, as the formation of N_2O is an undesirable by-product that is a harmful greenhouse gas.

1.4 Thesis Outline

Although rhodium metal is considered the most effective platinum group metal to carry out *de*NO_x, there are a number of unknown properties that have not been fully explained. These omissions in the current literature regarding an understanding of the full electronic structure, interactions and profile for the breakdown of NO_x molecules on the low index surfaces of Rh metal needs to be addressed. The complete mechanism for NO reduction via the pathways outlined in Equations 1.25 and 1.26 needs to be

considered and trialled on the Rh {111} surface in order to confirm the low energy route. The main purpose and motivation for the body of work presented in this thesis is to fully understand these issues mentioned previously, so that the enhanced reductive properties of Rhodium metal to carry out *de*NO_x chemistry can be understood. This may lead to development of alternative catalysts that are more cost effective and can emulate the properties of Rhodium metal.

Chapter 1 provided a description of the harmful effects of NO_x gases on the atmosphere, and why their reduction form the atmosphere is essential for a cleaner environment. The chapter also provided the catalytic processes and the components of *de*NO_x technologies, and the current research undertaken to elucidate NO_x reduction on Rh, Pt and Pd precious metals.

In Chapter 2, the theoretical methods that are used on the systems in this thesis are discussed, underlining the main quantum chemical approaches that are used, along with their advantages and limitations. Chapter 3 introduces the computationally methodology to generate the metal surfaces, using the slab model within the unit cell and the procedure to adsorb the molecular and atomic species on the metal surface slab. Details of the electronic structure analysis that is carried out on the most stable adsorbate of each species on the metal surface is outline, and the climbing nudged elastic band method that is used to calculate the reaction mechanisms on the metal surface slab.

The first chapter of results, Chapter 4, introduces the most stable adsorbates for N, O, N_2, O_2, and NO_x on the {111} surface of Rh, Pd and Pt metals, and details on the electronic structure for their interaction with these metals. The calculated energies for the most stable species, and the gas phase species are used to build a decomposition profile on each of the metal surfaces. These are developed to compare and contrast the differences in their abilities to carry out *de*NO_x and understand why Rh is a more effective *de*NO_x catalyst. A similar procedure is carried out in Chapter 5, to investigate the *de*NO_x profiles on the {100} and {110} surfaces of Rh, and compared to a step on the {111} surface to elucidate which surface is most effective for *de*NO_x on Rhodium metal.

Chapter 6 investigates the variation of the {111} surface to carry out $de\mathrm{NO}_x$ chemistry on different sized rhodium metal clusters. A similar procedure to investigate the most stable adsorption modes of N, O and NO_x on the different size Rh_n clusters (n = 10 - 56) will be used to develop a $de\mathrm{NO}_x$ profile on each, providing an understanding and comparison of the different rhodium metal clusters that have exposed {111} facets. The optimum size for a rhodium cluster to efficiently carry out $de\mathrm{NO}_x$ will be determined, and reaction barriers to the breaking of NO_x bonds will also be provided.

The climbing nudged elastic band method will be used in Chapter 7 to examine activation barriers for the breaking of the N_2, O_2 and NO_x bonds on the clean {111} surface of Rh. This method will also be used to describe the atomic and molecular diffusion on this surface and compare to the activity of the {111} surface of Pd and Pt metals. All possible reaction mechanisms for the reduction of NO on the Rh {111} surface will be carried out to investigate the intermediate to $\mathrm{N}_2\mathrm{O}$ formation by determining the lowest energy pathway on the metal surface.

Chapter 2

Computational Theory

2.1 Introduction

The increasing power of high performance computers, and the modern resources accessible for large parallel processes have paved the way for the development and utilisation of more sophisticated theoretical models to study chemical systems. This has allowed more accurate descriptions of the interactions between atoms and molecules to investigate larger systems than previously examined, in order to more closely model experiment. Theoretical models are used alongside experiment to explain a number of properties of chemical systems such as bonding between molecules, surface-adsorbate interactions, and thermal and optical properties of solid state systems. Understanding these properties has led to insight into these systems that experiments have not or cannot elucidate, allowing the prediction of novel materials with improved properties. Such insights and predictions have led computational tools to become more relevant and have an increased importance in modern scientific research.

Quantum mechanical approaches calculate the energy of a system through solving the Schrödinger equation by minimising the interaction of the electrons in a given field around atomic cores. The Schrödinger equation can be solved exactly for one-electron systems, but approximated for larger multi-electronic systems. Approximations such as Hartree-Fock theory have dealt with solving the Schrödinger equation using one-

electron operators to treat electrons individually, but this has its short comings. Other approaches such as configuration interaction and density functional theory have built on Hartree-Fock through consideration of electron correlation, which is a more realistic way of describing the electronic interactions between ions.

This chapter outlines the details of the Schrödinger equation, and approximations made to describe the Hamiltonian operator. The electron-electron interactions contained in the Hamiltonian are difficult to calculate, and the description of their interaction based on the Hartree-Fock method, are discussed. Density functional theory is an alternative approach that uses the electron density as method of determining the Hamiltonian, and this is the chosen method to study the systems in this work.

2.2 Schrödinger Equation

The fundamental aim of quantum mechanical calculations is the determination of the ground state energy of a wavefunction for a given system. The Hamiltonian operator is applied to the wavefunction of a system under consideration and will return the system energy as an eigenvalue, solving the time-independent Schrödinger equation:

$$\hat{H}\Psi = \mathrm{E}\Psi \tag{2.1}$$

where $\hat{H}$ is the Hamiltonian operator, Ψ is the wavefunction and E is the energy of the system. The Hamiltonian operator takes the form:

$$\hat{H} = -\sum_{i} \frac{\hbar^2}{2m_e}\nabla_i^2 - \sum_{A} \frac{\hbar^2}{2M_A}\nabla_A^2 + \mathrm{V}(r) \tag{2.2}$$

where i and A are the electrons and the nuclei, respectively, $\hbar$ is Planck's constant divided by 2π, m_e is the electron mass, M_A is the nuclear mass of A, ∇^2 is the Laplacian operator, and V(r) is the potential energy of the system as a function of its coordinates. The constants appearing in Equation 2.2 are equal to 1 when atomic units are used,

and when using Cartesian coordinates, the Laplacian takes the form;

$$\nabla = \left(\frac{\partial^2}{\partial x_i^2} + \frac{\partial^2}{\partial y_i^2} + \frac{\partial^2}{\partial z_i^2} \right) \tag{2.3}$$

The Hamiltonian operator in Equation 2.2 is composed of the kinetic energy and potential energy components. These can be broken down into contributions from the kinetic energy from the electrons ($\hat{T}_e$) and nuclei ($\hat{T}_n$), with the potential energy interactions separated into contributions from the nuclei-nuclei ($\hat{V}_{NN}$), electron-nuclei ($\hat{V}_{eN}$) and the electron-electron ($\hat{V}_{ee}$) interactions:

$$\hat{H} = \hat{T}_e + \hat{T}_n + \hat{V}_{eN} + \hat{V}_{ee} + \hat{V}_{NN} \tag{2.4}$$

In general terms, the Schrödinger equation (Equation 2.1) contains the Hamiltonian operator that is applied to the eigenfunction Ψ (wavefunction) for a given system, with each being characterised by an associated eigenvalue E (energy). The energy of the wavefunction for the system of interest can be computed by taking Equation 2.2 for a specific wavefunction Ψ, and hence multiply both sides by the complex conjugate Ψ^*, and integrating over the volume:

$$\int \Psi \hat{H} \Psi^* \, d\tau = \int \Psi E \Psi^* \, d\tau \tag{2.5}$$

As the energy (E) is a scalar value, it can be removed from the integral and thus Equation 2.5 becomes:

$$\begin{aligned} \int \Psi \hat{H} \Psi^* \, d\tau &= E \int \Psi \Psi^* \, d\tau \\ \frac{\int \Psi \hat{H} \Psi^* \, d\tau}{\int \Psi \Psi^* \, d\tau} &= E \end{aligned} \tag{2.6}$$

An exact solution of the Schrödinger equation would therefore yield the ground state energy of a wavefunction by solving the integral on the left when the wavefunction is normalised. For more complicated systems the integral is much more difficult to solve.

The wavefunction produced by the Schrödinger equation has no physical meaning, and only the square of the wavefunction provides the probability of finding an electron in space (i.e. the electron density). The difficulty with this model is that as the electron-electron interactions can not be solved analytically, only the energy of a one electron system (e.g. H, He^{+}, Li^{2+}) can be solved exactly. It is therefore difficult to obtain the energy of an electronic wavefunction for a system with more than one electron and approximations are required to solve it for more complex systems.

2.2.1 The Born-Oppenheimer Approximation

The individual kinetic and potential contributions to the Hamiltonian operator for a given system are provided in a general sense in Equation 2.2. The Born-Oppenheimer approximation is applied to simplify the determination of the wavefunction for a system of interest, by separating out the nuclear and electronic contributions to the Hamiltonian operator;

$$\hat{H} = (\hat{T}_N + \hat{V}_{NN}) + \hat{V}_{eN} + \hat{T}_e + \hat{V}_{ee} \tag{2.7}$$

The nuclear motion is significantly slower than the motion of electrons from the differences in inertia between the nuclei and electrons. As a result, electronic relaxation with respect to nuclear motion is instantaneous, and it is convenient to decouple these motions and calculate the electronic energies with respect to fixed nuclear positions.[337] The nuclear kinetic term ($\hat{T}_N$) is thus taken to be independent of the electrons, correlation in the attractive electron-nuclear potential energy term ($\hat{V}_{eN}$) is eliminated, and the repulsive nuclear-nuclear potential energy term ($\hat{V}_{NN}$) becomes a simplified constant by geometry. The simplification using the Born-Oppenheimer approximation leaves the Hamiltonian with just electronic components:

$$\hat{H}_{el} = \hat{T}_e + \hat{V}_{eN} + \hat{V}_{ee} \tag{2.8}$$

where the kinetic energy term is simplified to;

$$\hat{T}_e = -\sum_{i}^{N} \frac{1}{2}\nabla_i^2 \tag{2.9}$$

and the nuclear-electron interaction, $\hat{V}_{eN}$ given as:

$$\hat{V}_{eN} = \sum_{i}\sum_{k} \frac{e^2 Z_k}{r_{ik}} \tag{2.10}$$

The electronic Schrödinger equation therefore becomes:

$$\hat{H}_{el}\Psi_{el}(q_i; q_k) = E_{el}\Psi_{el}(q_i; q_k) \tag{2.11}$$

where the electronic coordinates q_i are independent variables but the nuclear coordinates q_k are parameters.

The eigenvalue of the electronic Schrödinger equation is the referred to as the 'electronic energy'. The $\hat{H}_{el}$ term becomes easier to solve as the $\hat{T}_e$ and $\hat{V}_{eN}$ terms are simple to calculate; however, the electron-electron term $\hat{V}_{ee}$ remains the most difficult part of the Schrödinger equation to determine, and must be further approximated. The Born-Oppenheimer approximation is successfully applied to the majority of modern ground state electronic structure methods.

2.2.2 The Variational Principle

The energy of a chemical system can be calculated by the Hamiltonian operating on a wavefunction in Equation 2.6; however, the Hamiltonian does not provide a way of obtaining the set of wavefunctions that provide the lowest energy. The variational principle states that the expectation energy associated with a wavefunction will always be higher than the true ground state energy E_0, calculated from the ground state wavefunction Ψ_0;

$$\frac{\int \Psi \hat{H} \Psi^* \, dr}{\int \Psi \Psi^* \, dr} \geq E_0 \tag{2.12}$$

This indicates that any expectation energy (E_i) obtain from a set of wavefunctions (Ψ_i) will always be higher in energy than the true ground state. If a new set of wavefunctions provides a lower energy than the previous set, these are considered to be a more accurate description than the previous set. The quality of the calculation can therefore be improved by varying the wavefunction until the lowest energy solution is obtained or a certain convergence criteria between two sets of wavefunctions is reached.

2.3 Hartree and the Self-consistent Field Method

This section outlines the Hartree product wavefunction and the approach to simplifying the solution of the Schrödinger equation. The Hartree wavefunction violates the Pauli principle, and the introduction of Slater determinants by Fock into the Hamiltonian to alleviate this problem is also discussed. This results in the Hartree-Fock method which is a solution of the Schrödinger equation by a self-consistent field approach. The self consistent field approach is carried out using the Roothan-Hall equations which is discussed in the next section, and also applicable to density functional theory that is the methods used in this body of work.

The determination of the electron-electron interaction component contained within the electronic Hamiltonian is difficult. Hartree divided up the wavefunction of a multi-electron system into the product of one-electron Hamiltonians, so that the operator can be separated and expressed as;

$$\hat{H} = \sum_{i=1}^{N} h_i \tag{2.13}$$

where N is the total number of electrons. The one-electron Hartree hamiltonian ignores electron-electron interactions, and is only composed of kinetic and potential terms for

one electron and the nucleus so h_i is defined as;

$$h_i = -\frac{1}{2}\nabla_i^2 + \sum_{A=1}^{M} \frac{Z_A}{r_{iA}} \tag{2.14}$$

where M is the total number of nuclei and the equation is expressed in atomic units. This allows a one-electron Schrödinger equation to be solvable, where the one-electron Hamiltonian above (Equation 2.14) must be satisfied by corresponding one-electron eigenvalues;

$$h_i\psi_i = \epsilon_i\psi_i \tag{2.15}$$

The Hamiltonian operator in Equation 2.13 equals the sum over all one-electron operators of a particular system, therefore the many-electron wavefunctions can be constructed as products of one-electron wavefunctions;[337]

$$\Psi_{HP} = \psi_1\psi_2....\psi_N \tag{2.16}$$

where Ψ_{HP} is referred to as the 'Hartree-product' wavefunction. The Schrödinger equation is solved for the initial set of wavefunctions, resulting in a new set of eigenvalues to test for a new set of wavefunctions. The one-electron Hamiltonian does not include electron-electron interactions, which are essential to model a more realistic system since electrons repel one anther. Hartree introduced interelectron repulsions by including an interaction potential V_i for each orbital ψ_i with all other electrons in the system occupying orbitals $\{j\}$;

$$h_i = -\frac{1}{2}\nabla_i^2 - \sum_{k=1}^{M} \frac{Z_k}{r_{ik}} + V_i(j) \tag{2.17}$$

where,

$$V_i\{j\} = \sum_{j\neq i} \int \frac{\rho_j}{r_{ij}}\, dr \tag{2.18}$$

where ρ_j is the probability density associated with electron j. To calculate the eigenvalues (ϵ_i) of the wavefunctions ψ_i using the one-electron Hamiltonian (h_i), Hartree (1928) proposed the 'self consistent field' (SCF) method. The wavefunction ψ for all molecular

orbitals are initially guessed, and a solution of Equation 2.15 provides a new set of ψ. The one-electron Hamiltonians are formed using the more accurate ψ and the process set is continuously repeated until the final set of ψ is converged to a certain criteria. The tighter the criteria of convergence, the more SCF cycles are required to produce the necessary degree of accuracy.

Equation 2.16 shows that the sum of the one-electron operators define a separable Hamiltonian operator for which Ψ_{HP} is an eigenfunction. The separable one-electron operator h (Equation 2.18) corresponds to a 'non-interaction' system of electrons where each electron only interacts with a constant potential (mean field approach), which is not a good approximation for the true Hamiltonian. The one electron operator h_i does include the repulsion of its associated electron i with another electron j, thus Ψ_{HP} treats electrons independently ignoring this repulsion.

Fock recognised that Ψ_{HP} treated electrons independently which is physically unrealistic. The Ψ_{HP} also does not satisfy the Pauli exclusion principle, that no two electrons can be characterised by the same set of quantum numbers. All electrons are characterised by a spin quantum number that is an eigenfunction of the operator S_z with two eigenvalues $\pm\frac{\hbar}{2}$, and spin eigenfunctions denoted α and β. For the Ψ_{HP}, there is thus only two possible choices α and β for electrons to be placed;

$$^3\Psi_{HP} = \psi_a(1)\alpha(1)\psi_b(2)\alpha(2) \tag{2.19}$$

where the superscript 3 indicates a triplet electronic state (2 electrons with parallel spin). The problem with this equation is that the electrons cannot be interchanged between α and β spin states and thus the Ψ_{HP} does not obey Pauli, the wavefunction must change sign. By combining two Ψ_{HP} with different electrons (1 and 2) in different wavefunctions functions (a and b), the resultant wavefunction is produced;[338]

$$^3\Psi = \frac{1}{\sqrt{2}}[\psi_a(1)\alpha(1)\psi_b(2)\alpha(2) - \psi_a(2)\alpha(2)\psi_b(1)\alpha(1)] \tag{2.20}$$

where $\frac{1}{\sqrt{2}}$ is a normalisation constant. Ψ_{HP} now satisfies the concept of an anti-

symmetric wavefunction as swapping electrons 1 and 2 produces -Ψ_{HP}. Slater determined that the anti-symmetry wavefunction in Equation 2.20 could be could be expressed as a determinant;

$$ {}^3\Psi_{SD} = \frac{1}{\sqrt{2}} \begin{vmatrix} \psi_a(1)\alpha(1) & \psi_b(1)\alpha(1) \\ \psi_a(2)\alpha(2) & \psi_b(2)\alpha(2) \end{vmatrix} \tag{2.21} $$

On a general basis for a system of N electrons and N spin orbitals, the Slater determinant is given as;

$$ {}^3\Psi_{SD} = \frac{1}{\sqrt{N!}} \begin{vmatrix} \chi_1(1) & \chi_2(1) & \cdots & \chi_N(1) \\ \chi_1(2) & \chi_2(2) & \cdots & \chi_N(2) \\ \vdots & \vdots & \ddots & \vdots \\ \chi_1(N) & \chi_2(N) & \cdots & \chi_N(N) \end{vmatrix} \tag{2.22} $$

where N is the total number of electrons and χ is a spin-orbit which is a product of a spatial orbital and an electron spin eigenfunction ($\chi_a(1) = \psi_a(1)\alpha(1)$). The Slater determinant allows every electron to appear in every spin orbital somewhere in the expansion, manifested from the indistinguishability of quantum particles, which is violated by the Hartree wavefunction.

The extension of Hartree's SCF procedure to include Slater determinants was proposed by Fock. The Hartree-fock (HF) SCF approach determines the eigenfunctions as of a set of one-electron operators, and obtains the set of wavefunctions by an iterative SCF method in a similar manner to the Hartree SCF approach. For the HF method however, the one-electron Hamiltonian is replace by the one-electron Fock operator defined as;

$$ \hat{f}_i = \hat{H}_{ii}^{core}(1) + V_i^{\mathrm{HF}}(j) \tag{2.23} $$

where the motion of a single electron in the field generated by the nuclei is given by $\hat{H}_{ii}^{core}$;

$$ \hat{H}_{ii}^{core}(1) = -\frac{1}{2}\nabla_i^2 - \sum_k^{nuclei} \frac{Z_k}{r_{ik}} \tag{2.24} $$

By replacing the Hamiltonian with the one-electron Fock operator the Schrödinger

equation becomes;

$$f_i \chi_i = \epsilon_i \chi_i \tag{2.25}$$

showing that the Fock operator on a set of wavefunctions produces the set of associated energies.

The HF electron potential determined during the SCF cycle for a given molecular orbital (j) is; $V_i^{\mathrm{HF}}(j) = 2J_i - K_i$, which includes the classical Coulombic (J_i) and exchange operators (K_i) for two electrons:

$$J_i = \int |\psi_a(1)|^2 \frac{1}{r_{12}} |\psi_b(2)|^2 \, dr_1 \, dr_2 \tag{2.26}$$

$$K_i = \int \psi_a(1)\psi_b(1) \frac{1}{r_{12}} \psi_b(2)\psi_a(2) \, dr_1 \, dr_2 \tag{2.27}$$

This equation indicates that the classical coulomb repulsion (J) between the electron cloud is reduced by the exchange of electrons K_i. The consequence of this is that the probability of finding two electrons of the same spin close to one another is reduced, and a 'Fermi-hole' is said to surround each atom. This property is a correlation effect unique to electrons of similar spin and if the Slater determinant wavefunction is evaluated for electrons of different spins, the exchange correlation reduces to 0 due to the orthogonality nature of α and β spin functions.

2.3.1 Roothan-Hall equations

The complexity of calculating the exchange and Coulombic electronic terms of the HF method meant that the solution for the complex multi-electronic systems was not practical. For such systems, Roothan noted that the HF calculations needed to be expressed in terms of basis functions by representing each spin molecular orbital (χ_i) as a linear combination of atomic orbitals (LCAO);

$$\chi_i = \sum_{v}^{K} c_{vi} \phi_v \tag{2.28}$$

where ϕ_v are the atomic orbital like basis functions, and c_{vi} are the weighted associated coefficients of the atomic orbitals v in molecular orbital i. Roothan and Hall developed a set of matrix equations that incorporates these orbitals into a secular equation;

$$FC = SCE \tag{2.29}$$

where C is a K x K matrix whose elements are the coefficients $(c_v i)$;

$$C = \begin{pmatrix} c_{11} & c_{12} & \cdots & c_{1K} \\ c_{21} & c_{22} & \cdots & c_{2K} \\ \vdots & \vdots & \ddots & \vdots \\ c_{K1} & c_{K2} & \cdots & c_{KK} \end{pmatrix} \tag{2.30}$$

and E is a diagonal matrix of the orbital energies;

$$E = \begin{pmatrix} \epsilon_1 & 0 & \cdots & 0 \\ 0 & \epsilon_2 & \cdots & 0 \\ \vdots & \vdots & \ddots & \vdots \\ 0 & 0 & \cdots & \epsilon_K \end{pmatrix} \tag{2.31}$$

The values of the matrix elements for F and S are implicitly calculated, where S is the overlap matrix elements and for arbitrary basis functions μ and ν, the Fock operator matrix (F) can be calculated by;

$$F_{\mu\nu} = \left\langle \mu \left| -\frac{1}{2}\nabla^2 \right| \nu \right\rangle - \sum_{k}^{nuclei} Z_k \left\langle \mu \left| -\frac{1}{r_k} \right| \nu \right\rangle + \sum_{\lambda\sigma} P_{\lambda\sigma} \left[(\mu\nu|\lambda\sigma) - \frac{1}{2}(\mu\lambda|\nu\sigma) \right] \tag{2.32}$$

In order to determine the molecular orbitals using this approach, the secular equa-

tion with N basis functions is solved to find is various roots E_j;

$$\begin{vmatrix} F_{11} - ES_{11} & F_{12} - ES_{12} & \cdots & F_{1N} - ES_{1N} \\ F_{21} - ES_{21} & F_{22} - ES_{22} & \cdots & F_{2N} - ES_{2N} \\ \vdots & \vdots & \ddots & \vdots \\ F_{N1} - ES_{N1} & F_{N2} - ES_{N2} & \cdots & F_{NN} - ES_{NN} \end{vmatrix} \tag{2.33}$$

The process for solving the HF secular determinant is to diagonalise F, finding the orbital energies, and the weighted coefficients in a similar manner to the Hartree method. The orbital coefficients are required to form the density matrix that is used in the Fock matrix, so the main purpose of solving the secular equation is to obtain the orbital coefficients using an SCF procedure; the coefficients are first guessed from the Hamiltonian and then iterated until the convergence criteria is achieved.

2.3.2 Hartree-Fock Limitations

The HF method using the Roothan-Hall approach is an approximate way of solving the Schrödinger equation for a multi-electronic system. The Hartree-product wavefunction calculated the energy by solving one electron hamiltonians that ignored electron-electron interactions. The interelectronic repulsion was introduced by accounting for the classical Coulombic interactions using a mean-field approach; however the exchange of electrons was not incorporated. Fock realised this, and using Slater determinants was able to describe the exact exchange of electrons. The classical Coulombic electron-electron repulsion however, does not describe the location of the electrons, since it is a mean field approach. The electrons are thus closer to one another than expected. The lack of consideration for the correlation of electrons in a multi-electronic system is a well-known shortcoming of the HF method. The lack of correlation in the HF method means that it is unsuited for the simulation of systems with delocalised states, such as metallic states for transition metals.

The HF methods has some advantages with Coulombic interactions and exact ex-

change; however, the lack of correlation places a important chemical flaw within its framework. The use of HF methods in modern computational chemistry is thus seldom implemented due to the lack of correlation. Post HF methods were therefore developed such as, Møller-Plesset perturbation theory and configuration interaction to account for the lack of electronic correlation in a variety of ways. Although the post HF methods are more sophisticated approaches, they are much more computationally demanding than standard HF, scaling by N^5 basis sets and beyond, depending on the level of theory chosen. This limits their applicability to only small systems, and other methods for simulating periodic systems at a level of theory beyond HF are sought after, which are not as computationally expensive. One such approach is density functional theory which is the level of theory utilised in this study.

2.4 Density Functional Theory

Quantum mechanical methods such as HF theory aim to accurately solve the Schrödinger equation (Equation 2.1) are limited in their application and beyond one electron systems, this is not a very intuitive approach. The wavefunction itself, is uninterpretable, and it is therefore easier to deal with some physical observable to determine the energy of a system.

The Hamiltonian depends on the positions of the nuclei and the total number of electrons, suggesting that a physical observable to use is the electron density (ρ). Integrated over space, it provides the total number of electrons (N);

$$N = \int \rho(r)\, dr \tag{2.34}$$

The Hamiltonian operator can thus be constructed in terms of the electron density to solve the Schrödinger equation, by producing the eigenvalues using the electron density. Density functional theory (DFT) therefore calculates the energy of a system as a function of the electron density (ρ), while the density itself is a function of three spatial coordinates. A function whose argument is also a function is described as being

a 'functional'. This simplifies the calculation of the energy by optimising ρ in contrast to solving Φ that is a function of 3N variables, with N being the number of electrons.

The approach of trying to relate the electron density to the energy of a system was first proposed by Thomas-Fermi as a way of dealing with electron-electron interactions within the Hamiltonian operator. Thomas-Fermi DFT was however, a first approximation with a number of shortcomings; it did not accurately describe the kinetic energy of electrons, approximated exchange, and did not include the approximated correlation of electrons. Hohenberg-Kohn used the basis of DFT to show that the ground state properties of a many body system.

2.4.1 The Hohenberg-Kohn Theorems

In DFT the electrons interact with each other, and an external potential from the nuclei. Hohenberg-Kohn (HK)[339] existence theorem calculates the energy of the system by employing the ground state electron density. As the density provides the number of electrons in the system (Equation 2.34), all that remains to define the Hamiltonian is the determination of the external potential for the charges and positions of the nuclei.

The kinetic and potential energy components of the Hamiltonian operator describe the electron and nuclear interactions for the system of interest. If two different external potential components (ν_a and ν_b) can be consistent with the same non degenerate ground state electron density ρ_0, then two different Hamiltonian operators ($\hat{H}_a$ and $\hat{H}_b$) can be related to a ground-state wavefunction Ψ_0 and its associated energy E_0. The variational theorem dictates that the expectation value of $\hat{H}_a$ over Ψ_b must be higher than the ground-state energy of E_a;

$$E_{0,a} < \left\langle \Psi_{0,b} \middle| \hat{H}_a \middle| \Psi_{0,b} \right\rangle$$

where $\Psi_{0,b}$ is the ground state wavefunction of system b and $E_{0,a}$ is the ground state

energy of system a. This can be re-written to include the external potentials;

$$E_{0,a} < \langle \Psi_{0,b} | \nu_a - \nu_b | \Psi_{0,b} \rangle + E_{0,b} \tag{2.35}$$

Since the external potentials are one-electron Hamiltonians, the integral above can be written in terms of the ground-state electron density;

$$E_{0,a} < \int [\nu_a(r) - \nu_b(r)] \rho_0(r)\, dr + E_{0,b} \tag{2.36}$$

HK existence theorem shows that, if the ground-state electron density of Ψ_a and Ψ_b are interchangeable, then ρ_0 must determine the external potential energies. The external potentials are related to the Hamiltonian, therefore the ground state electron density can determine the properties of the system, and thus the energy. The energy dependence for the electron density of the system on the external potentials can be written as;

$$E[\rho(r)] = \int \nu_{\text{ext}}(r) \rho(r)\, dr + F[\rho(r)] \tag{2.37}$$

where $\nu_{\text{ext}}(r)$ is the external potential, and $F[\rho(r)]$ is the HK universal functional that is the sum of the kinetic energy of the electrons and their interactions between one another. The minimum value of $E[\rho(r)]$ gives the true ground state electron density, which can be achieved by a variational approach.

Although the HK existence theorem is helpful in relating the electron density to the energy, it provides no indication on how to predict the density of a system or calculate the energy. The HK variational theorem shows that the ground-state electron density upholds the variational principle (Section 2.2.2), which is important in determining the ground state energy of the system. Assuming the electron density of the system integrates to the correct number of electrons (N), the HK variational theorem indicates that this density determines the wavefunction, and the Hamiltonian of the system. The

expectation energy must be greater than or equal to the true ground-state energy;

$$\left\langle \Psi_{\text{sys}} \middle| \hat{H}_{\text{sys}} \middle| \Psi_{\text{sys}} \right\rangle = E_{\text{sys}} \geq E_0 \tag{2.38}$$

Electron densities to achieve the closest energy to the true ground state energy are chosen using the variational principle. Similar to the choice of the initial trial wavefunction to produce the ground state energy, there is no rationale behind choosing the initial guess electron density. The use of the electron density in such a way is however, inaccurate and there is no mechanical means by which the electron density can be used in a general characteristic, variational way. Kohn-Sham further developed the HK formalism so that it could be introduced into a computational scheme.

2.4.2 Kohn-Sham Self-consistent Field

Kohn-Sham (KS)[340] showed that the HK formulaism could be developed for a computational scheme by reintroducing the wavefunction into the calculations. The difficulty with previous DFT schemes was the calculation of the electronic kinetic energy. They realised that this could be simplified if the Hamiltonian operator was constructed for a non-interacting system of electrons, developed from the wavefunction using SDs[341] which has the same ground state energy as a fully interacting system. The KS method considers a fictitious system of non-interacting electrons that have the same density for their ground-state as the real system of interest with interacting electrons;

$$\rho_s(r) = \sum_i \left| \rho_{\text{KS}}^2(r) \right| = \rho_{\text{exact}}(r) \tag{2.39}$$

As the electron density can indicate the relative positions and charge interactions of the nuclei, the non-interacting and real systems can be identical. To calculate the ground state energy of the system using the variational principle, the kinetic energy and electron-electron interactions can be separated to classical ($T_{ni}[\rho(r)]$, $V_{ne}[\rho(r)]$,

$V_{ee}[\rho(r)]$) and non-classical components ($\Delta T[\rho(r)]$, $\Delta V_{ee}[\rho(r)]$);

$$E[\rho(r)] = T_{ni}[\rho(r)] + V_{ne}[\rho(r)] + V_{ee}[\rho(r)] + \Delta T[\rho(r)] + \Delta V_{ee}[\rho(r)] \tag{2.40}$$

where $T_{ni}[\rho(r)]$ is the kinetic energy term for the non-interacting electrons;

$$T_{ni}[\rho(r)] = -\frac{1}{2}\sum_{i} \langle \chi_i | \nabla^2 | \chi_i \rangle \tag{2.41}$$

where χ_i is the spin molecular orbital. The potential for the classical nuclear-electron interaction term $V_{ne}[\rho(r)]$ is given as;

$$V_{ne}[\rho(r)] = \sum_{A}^{nuclei} \int \frac{Z_A}{|r - r_A|} \rho(r)\, dr \tag{2.42}$$

and the classical electron-electron interaction term $V_{ee}[\rho(r)]$ is;

$$V_{ee}[\rho(r)] = \frac{1}{2} \int \int \frac{\rho(r_1)\rho(r_2)}{|r_1 - r_2|}\, dr_1\, dr_2 \tag{2.43}$$

The $\Delta T[\rho(r)]$ term is the correction to the kinetic energy deriving from the interacting nature of the electrons, the $\Delta V_{ee}[\rho(r)]$ term is the non-classical correction to the electron-electron repulsion energy ($V_{ee}[\rho(r)]$), and χ_i is the set of orbitals that provide the minimum energy for Equation 2.40 which are selected by the variational principle. The electron-electron interactions between two different densities can be dealt with by adding a non-classical correction term ($E_{\mathrm{xc}}[\rho(r)]$) that deals with the exchange and correlation energies to the classical electron-electron repulsion term. $E_{\mathrm{xc}}[\rho(r)]$ contains the corrections to the kinetic and electron-electron interactions, ΔT and ΔV_{ee} respectively, and are grouped together as the non-classical exchange-correlation energy. $E_{\mathrm{xc}}[\rho(r)]$ not only includes the effects of quantum mechanical exchange and correlation, but also accounts for the correction for the classical self-interaction energy along with the difference in kinetic energy between the fictitious non-interacting system and the real one.

The HK functional can thus take the form;

$$F[\rho(r)] = T_{ni}[\rho(r)] + J[\rho(r)] + E_{\mathrm{xc}}[\rho(r)] \tag{2.44}$$

where $J[\rho(r)]$ is the classical Coulombic interactions and $E_{xc}[\rho(r)]$ is the exchange-correlation functional. This allows the exchange and correlation of electrons to be built into the DFT formulaism as opposed to HF where they are separate. The total energy for the KS equations can be expressed as a function of the electron density, including the orbital contributions, given as;

$$\begin{aligned} E[\rho(r)] \;=\; & \sum_{i}^{N} \left(\left\langle \chi_i \left| -\frac{1}{2}\nabla_i^2 \right| \chi_i \right\rangle - \left\langle \chi_i \left| \sum_{k}^{nuclei} \frac{Z_k}{|r_i - r_k|} \right| \chi_i \right\rangle \right) \\ & + \sum_{i}^{N} \left\langle \chi_i \left| \frac{1}{2} \int \frac{\rho(r')}{|r_i - r'|}\, dr' \right| \chi_i \right\rangle + E_{\mathrm{xc}}[\rho(r)] \end{aligned} \tag{2.45}$$

where N is the number of electrons, and a Slater determinant-type wavefunction is used for the density, which is an exact eigenfunction for the non-interacting system so that;

$$\rho = \sum_{i=1}^{N} \langle \chi_i | \chi_i \rangle \tag{2.46}$$

The total energy for the system can be evaluated using the KS equations, in an approach to solving the Schrödinger equation. The set of orbitals (χ_i) that provide the minimum energy for Equation 2.45 are obtained by the variational principle under the constraint that all orbitals are orthonormal. This procedure is similar to the HF method and χ_i that are required to minimise the energy of the system (E), are found using an eigenfunction equation;

$$h_i^{KS} \chi_i = \epsilon_i \chi_i \tag{2.47}$$

where the Kohn-Sham (KS) one-electron operator (h_i^{KS}) is defined as;

$$h_i^{KS} = -\frac{1}{2}\nabla_i^2 - \sum_k^{nuclei} \frac{Z_k}{|r_i - r_k|} + \int \frac{\rho(r')}{|r_i - r'|}\, dr' + V_{xc} \tag{2.48}$$

and

$$V_{xc} = \frac{\partial E_{xc}}{\partial \rho} \tag{2.49}$$

V_{xc} is known as the exchange-correlation potential that describes the one-electron operator for which the expectation value of the wavefunction is $E_{\mathrm{xc}}[\rho(r)]$. The KS approach allows the density of the non-interacting system to be identical to that of a real system. The energy determined from the sum of the one electron operators can be used to determine the kinetic energy of the non-interacting system, which is a large proportion of a real system.

To include orbitals within the KS approach, the orbitals are expressed as a set of basis functions (ϕ), and the individual orbital coefficients are determined by diagonalising the Fock matrix similar to HF theory through the Roothan-Hall approach. As the set of orbital to minimise the energy are required, and obtained by using the variational principle, then the KS approach must be carried out using an iterative SCF procedure similar to HF.

The steps involved in carrying out the KS-SCF procedure are outlined in Figure 2.1. The KS-SCF procedure starts with the choice of a basis set for the system of interest from which the KS orbitals are formed. Once the initial density and wavefunction are determined, V_{xc} can be constructed from the initial guess of the density, and the overlap, kinetic energy, nuclear attraction integrals are computed. The KS matrix is diagonalised to evaluate the components and determine a new charge density and wavefunction. The new set of orbitals obtained from the solution of the secular equations, provide an energy for the set of orbitals. This energy is compared to the energy of the initial set of orbitals used to construct the KS matrix or the energy from the preceding iteration. If the resultant energy for the obtained set of orbitals is not within the specified electronic convergence criteria, then the set of obtained orbitals are used to construct the new KS

matrix. Once the electronic convergence criteria is achieved, the energy is computed by placing the final density into Equation 2.40. The geometry optimisation of the system is carried out, and the atomic forces are evaluated to update the positions of the ions as to whether the forces on the ions are minimised. If not, the procedure is repeated until this is achieved.

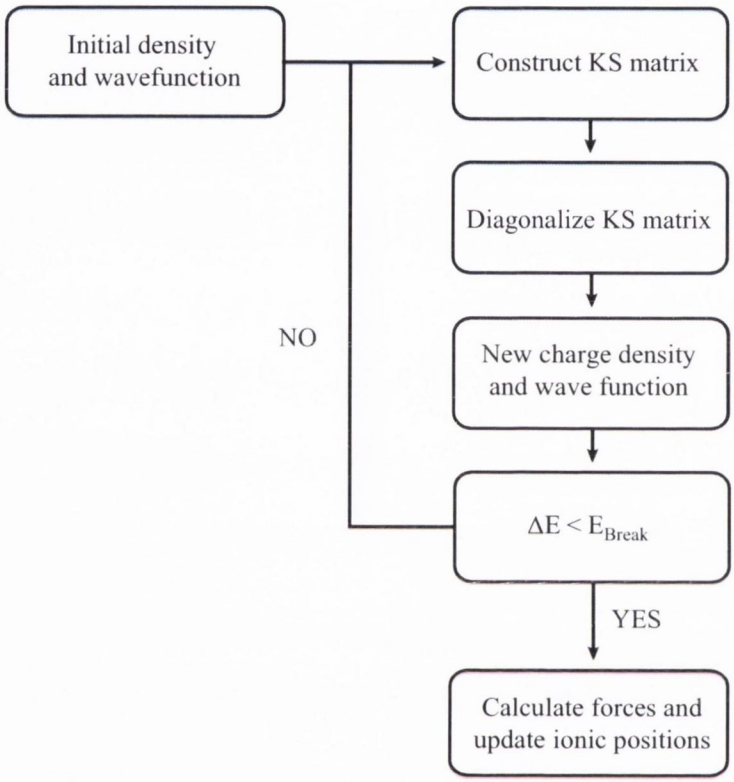


Figure 2.1: A flow chart of the KS-SCF optimisation procedure.

The main difference between HF and DFT, is that DFT could be an exact method to calculating the ground state energy of a system but the relevant equations must be solved approximately, whereas for HF the equations are solved exactly. For DFT, the exchange and correlation components are not known and the evaluation of $E_{\mathrm{xc}}[\rho(r)]$ as a function of ρ is approximated. DFT therefore approximates the electronic exchange and correlation, while HF calculates exact exchange but does not consider correlation. The $E_{\mathrm{xc}}[\rho(r)]$ functional is an important component of DFT which contains the description of electronic exchange and correlation, and there have been many functionals developed and continuously updated over the years to improve the accuracy of DFT.

2.4.3 Exchange-correlation functionals

The E_{xc} functional accounts for the difference between classical and quantum mechanical electron-electron repulsion, and it also includes the difference in kinetic energy between the fictitious non-interacting system and the real system. For many E_{xc} functionals empirical parameters are used to introduce some correction to the kinetic energy based on experiment. The dependence of E_{xc} on the electron density is expressed as the interaction between the electron density and an 'energy density' (ϵ_{xc}) that is dependent on the electron density, defined as;

$$E_{xc}[\rho(r)] = \int \rho(r)\epsilon_{xc}[\rho(r)]\, dr \tag{2.50}$$

The local density approximation (LDA) determines the exchange-correlational function using the 'local' density at specific points. The value of ϵ_{xc} is determined from the value of the local density ρ to provide the exchange correlational energy as given in Equation 2.50. The only requirement on ρ is that it will be single-valued at every position and because of this, LDA can poorly describe the cusps in the density at the nucleus. The prediction of LDA E_{xc} functionals are based on the uniform electron gas (UEG), which is a hypothetical system where the electrons are free to move in an electrically neutral environment. The benefit of using UEG is that the model has very accurate exchange and correlation energies from in depth Monte Carlo simulations. Systems that require spin polarisation (open shell systems) use a spin-polarised formalism which includes spin contributions to the exchange energy and referred to as the local spin density approximation (LSDA).

The main issue with determining ϵ_{xc} is the approximation of the correlation energy, as it has no analytical derivation. Ceperley and Alder[342] used Monte Carlo techniques to calculate the correlation energy by computing the total energy of UEG for several different densities, and subtracted the exchange energy for each case. Vosko, Wilk and Nusair (VWN)[343] designed the equations for the LDA functionals by fitting to these results. LDA works reasonably well for most systems were the density does not

dramatically change; however it is known to suffer from a number of issues, including the overbinding of electrons, overestimation of atomisation and ionisation energies, and underestimated bond lengths.

For a molecular system, the electron density is not spatially uniform, limiting the use of the LDA functional as they only calculate the local density and not the change in density over space. In account for this, the correlation functional is adjusted to depend not only on the local value of the density but also on the extent to which the density is locally changing; the gradient of the density. The gradient is expanded with respect to $\rho(r)$ using a Taylor series which varies the density at more than one single position. The term for a functional that depends on both the density and the gradient of the density is the 'generalised gradient approximation' (GGA). This approach has more flexibility and accuracy in determining the electron structure of molecules and solid structures as the density is allowed to vary over distance. Most GGA functionals are 'gradient corrected' functionals which are constructed by adding a gradient correction term to the LDA functional;

$$\epsilon_{\mathrm{xc}}^{\mathrm{GGA}}[\rho(r)] = \epsilon_{\mathrm{xc}}^{\mathrm{LSDA}}[\rho(r)] + \Delta\epsilon_{\mathrm{x/c}}\left[\frac{|\nabla\rho(r)|}{\rho^{\frac{4}{3}}(r)}\right] \tag{2.51}$$

The dependence of the correction term is on a dimensionless reduce gradient, rather than the absolute gradient. The first GGA exchange functional was developed by Becke[344] that incorporates empirical parameters which are optimised by fitting the exactly known exchange energies of the six noble elements. The Lee Yang Parr (LYP) correlational functional is also based on fitting to experimental data from the noble elements, and linked together with Beckes exchange functional describes the commonly used BLYP GGA functional. As these functionals are based on noble elements, there should be caution when using this functional for heavier periodic elements. Other GGA functionals do not depend on empirical parameters, and should be more applicable to a wider range of chemical compounds. These functionals have been developed are based on rational function expansions of the reduced gradient. Examples of these are the

Perdew and Wang (PW91),[345] and the popular Perdew-Burke-Ernzerhof (PBE)[346] functionals. The PBE functional has been used for all the DFT calculations presented in this thesis.

2.4.4 Limitations of DFT

DFT is preferred choice in computational solid state chemistry over other molecular orbital (MO) theory approaches, as it is simple and accurate in its approach. Modern DFT functionals are problematic as the energy is a function of the local density and possibly the gradient. They are therefore incapable of describing London dispersion forces, and thus poorly describe these forces for gases such as H_2 and N_2. Along with problems associated with intra-molecular bonding, DFT also has issues with inter-molecular bonding. DFT functionals have a tendency to predict charge transfer interactions to be stronger than they should be, and for LDA functionals bonds are normally underestimated, while for GGA bonds are usually overestimated compared to bonds measured experimentally.

Another major problem with DFT is $E_{\mathrm{xc}}[\rho(r)]$ is only approximated, even when the exact density for a system is known. The formulation of the Coulombic term ($J_[\rho(r)]$) allows electrons to self interact, which would not occur if the $E_{\mathrm{xc}}[\rho(r)]$ was exact. This error is known as the self interaction error (SIE) of electrons. The problems associated with many functionals occurs for systems having highly delocalised densities that are over stablised compared to more localised systems, when trying to correct for the SIE. This imbalance can lead to errors in prediction of higher symmetry structures preferred over lower symmetry ones. Although electron correlation stabilises delocalised electronic structure, hybrid functionals show improved performance by cancelising the SIE to an extent. A number of different approaches to introduce a self interaction correction have been developed.

2.5 Solid State Simulations

2.5.1 Crystal lattices

The quantum mechanical methods employed to study the behaviour of solid state systems differs to those of individual or isolated molecules. A perfect crystalline system can be constructed from a series of repeating motifs, referred to as a *unit cell*. The structure of a crystal can be defined by the size and shape of the unit cell and the arrangement of atoms within it. The unit cell is thus characterised by three vectors along the different Cartesian directions, x, y and z, labelled **a**, **b**, and **c**, respectively, separated by angles α, β, and γ as shown in Figure 2.2.

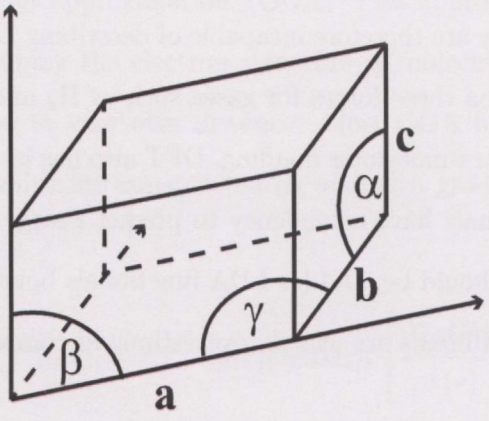


Figure 2.2: The parameters **a**, **b**, **c**, α, β, and γ which characterise the unit cell.

There are fourteen different types of unit cell known as Bravais lattices, each defined by an infinite array of discrete points with a unique set of unit cell parameters (Figure 2.2). This gives each of the unit cells different orientations and atomic arrangements, where the coordinates of the atoms in the unit cell may be expressed as fractional coordinates with a general vector;

$$\mathbf{R} = (\lambda\mathbf{a}, \zeta\mathbf{b}, \xi\mathbf{c}) \tag{2.52}$$

where **R** is the general vector with **a**, **b**, **c** being the atomic coordinates, and λ, ζ, ξ

being the partial positions along the vector. The cubic set of Bravais lattices contain a simple cubic structure where atoms are positioned on the corners (Figure 2.3 (a)). When the atoms are also located on the 'face' of the cubic unit cell it is referred to as a face centred cubic (fcc) structure (Figure 2.3 b). Not only does the general unit cell have to posses translational symmetry, but have symmetry for the atomic positions within it. The particular combination of symmetry elements in a crystal defines its space group, of which there are 230 different space groups. If there is symmetry within the unit cell, then it is only necessary to specify the asymmetric unit; the positions of the other atoms within the cell can be generated using the appropriate symmetry operators.

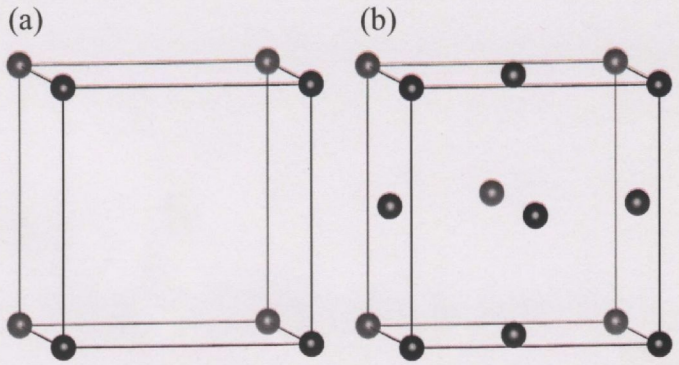


Figure 2.3: The Bravais lattice for (a) simple cubic and (b) a face centred cubic (FCC) unit cell.

In practice, the simulation of an infinite crystal lattice is difficult due to the large number of atoms and electrons. Periodicity of the unit cell is thus employed in three dimensions to simulate an infinite crystal lattice of the material. The unit cell is the focus of the optimisation and solution to the Schrödinger equation, which is repeated in three dimensions to represent the infinite crystal lattice (Figure 2.4). If atoms move outside of the unit cell, the symmetrically equivalent atom from an image cell will move into the opposite side of the unit cell, which is indicated by the arrows on atoms in Figure 2.4.

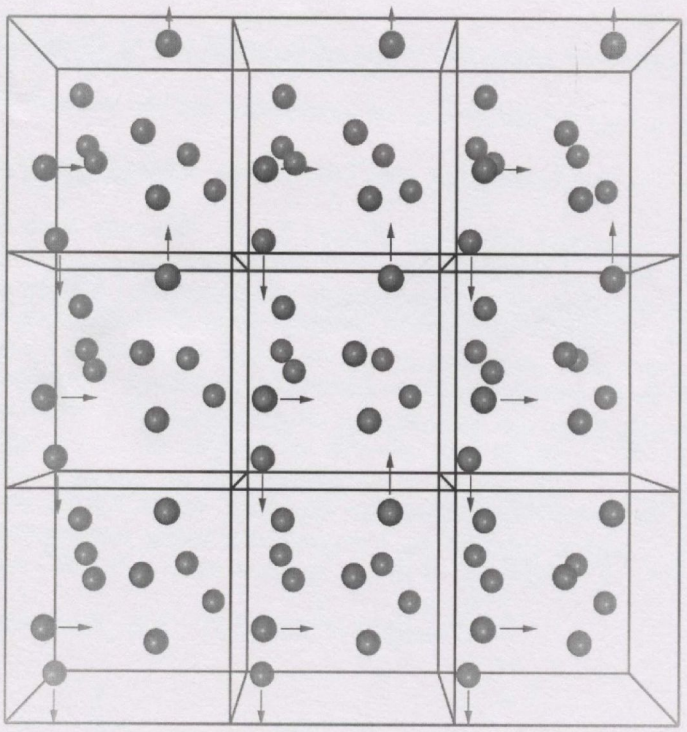


Figure 2.4: A 3x3 expansion of a unit cell under periodic boundary conditions. The symmetric movement of atoms in and out of the unit cell are shown by arrows.

2.5.2 Periodic Potential and Bloch's Theorem

The solution of the Schrödinger equation is implemented for the unit cell under periodic boundary conditions, rather than for the infinite crystal system which would be difficult. The Hamiltonian treats the electrons in the unit cell as non-interacting particles that adopt a static one-electron effective potential ($V(r)$);

$$\hat{H}\Psi = \left(-\frac{1}{2}\nabla^2 + V(r)\right)\Psi = E\Psi \tag{2.53}$$

The effective potential comes from the periodic array of nuclei in the crystal, so that the same potential of the unit cell can be expressed periodically in three dimensions as a periodic potential;

$$V(r + \mathbf{R}) = V(r) \tag{2.54}$$

where $\mathbf{R}$ corresponds to primitive vectors from Equation 2.52.

The periodicity of the unit cell allows a relationship between the values of the wavefunction in the unit cell, and at equivalent points on the lattice. Bloch's theorem identifies that the electronic wavefunction Ψ of the one-electron Hamiltonian in a periodic potential (Equation 2.53) can be written as a function of an expanded plane wave basis set with the periodicity of the Bravais lattice;

$$\Psi(r) = u_{n\mathbf{k}}(r)\exp(i\mathbf{k}\cdot r) \tag{2.55}$$

where the periodic function is described by $u_{n\mathbf{k}}(r+\mathbf{R}) = u_{n\mathbf{k}}(r)$ with $\mathbf{k}$ being the wave vector that represents the phase relationship of the wavefunction between repeated cells, and n is the band index. The band index corresponds to independent wavefunctions of different energies with the same $\mathbf{k}$ value. The Brillouin zone is the region of 'k-space' in which all the eigenstates of the Hamiltonian as shown in Figure 2.5 which periodically ranges from $-\frac{\pi}{R}$ to $+\frac{\pi}{R}$ along the $\mathbf{k}$ axis.[347] Allowing any values of $\mathbf{k}$ to

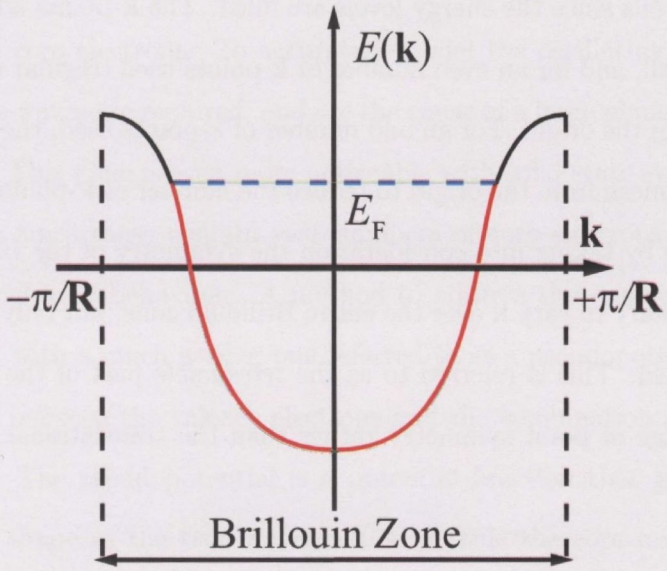


Figure 2.5: A diagram showing the periodicity of the Brillouin zone in $\mathbf{k}$-space

be located outside the Brillouin zone is unnecessary due to the periodic nature of the wavefunction within the Brillouin zone, as they can be reduced to the first zone by the

following relationship;

$$\Psi(r + \mathbf{R}) = \exp(i\mathbf{k} \cdot \mathbf{R})\Psi(r) \tag{2.56}$$

This equation identifies the wavefunction with label $\mathbf{k}$, while Figure 2.5 shows the periodicity of the wavefunction within the Brillouin zone.

The wavefunctions at certain points that are close together in $\mathbf{k}$ space will be almost identical. The denser the $\mathbf{k}$ vector sampling, the smaller the error in the calculation. Selecting a suitable set of $\mathbf{k}$ vectors to provide accurate energies and properties such as the charge density of a system, is carried out in a systematic way. The selection of $\mathbf{k}$ vectors is determined by the size and shape of the system, and is inversely proportional to the size of the unit cell so that the larger the unit cell the less number of $\mathbf{k}$ points that are required for sufficient sampling. The nature of the material is also considered when selecting the number of $\mathbf{k}$ vectors, as metallic systems need a more dense set of $\mathbf{k}$ vector sampling to accurately obtain the energies of the partially occupied bands and accurately define the Fermi level. For semi-conductors and insulators this does not need to be as rigorous since the energy levels are filled. The $\mathbf{k}$-points adopt a sampling mesh in the unit cell, and for an even number of $\mathbf{k}$-points used (regular mesh), they are equally spaced from the origin. For an odd number of k-points used, the sampling mesh offsets the regular mesh from the origin to reduce the number of $\mathbf{k}$-points required. The mesh achieves this by taking into consideration the symmetry of the Brillouin zone so that it is not necessary to vary $\mathbf{k}$ over the entire Brillouin zone, but only a small section needs to be sampled. This is referred to as the *irreducible* part of the Brillouin zone, and takes advantage of point symmetry rather than the translational symmetry of a lattice.

2.5.3 Plane Waves and Pseudopotentials

The description of the wavefunction within the unit cell for the system is instrumental in determining the accuracy of the calculation. The mathematical representations of the wavefunction is important for this, which are constructed from basis functions. Plane

waves are implemented as the choice of basis set for calculations of periodic systems, as they are a periodic function. Each orbital wavefunction is expressed as a linear combination of plane waves which differ by reciprocal vectors;

$$\Psi_i^{\mathbf{k}}(r) = \sum_{\mathbf{G}} c_{i,\mathbf{k}}(\mathbf{G}) \exp(i(\mathbf{k}+\mathbf{G}) \cdot r) \tag{2.57}$$

where $\mathbf{G}$ is the reciprocal lattice vector, and $c_{i,\mathbf{k}}$ are the plane wave coefficients that must be optimised.

The valence electrons involved in bonding are important, since these are responsible for the chemical bonding and most physical properties. The core electrons are the least affected by the atomic environment. The valence electrons are thus considered explicitly in the calculation, and the core electrons are incorporated into the nuclear core. A potential drawback of expressing the valence electrons using a plane wave basis set, is that near to the atomic nuclei the wavefunctions for the valence electrons experience rapid oscillations. This occurs as the wavefunctions must be orthogonal to those of the core electrons. To accurately model the oscillating behaviour, a high frequency plane waves are required, and are the cause of a large plane wave expansion of Equation 2.57. This issue is even more noticeable with solid state systems that contain heavy elements since these contain vast numbers of core electrons producing a more pronounced oscillatory behaviour. A method to address these issues is to replace the 'true' potential with a much weaker one referred to as a pseudopotential. This models the interaction between the valence electrons and the combination of the nucleus plus core electrons. The pseudopotential is a potential function that gives wavefunctions with the same shape as the true wavefunction outside the core region (r_c), but with fewer nodes inside the core region as shown in Figure 2.6. This reduces the number of plane waves required for the expansion of the wavefunction, which in turn reduces the scale of the computational problem.

Pseudopotentials are derived from all-electron atomic calculations and are used to avoid the need for the explicit treatment of strongly bound core electrons that are not

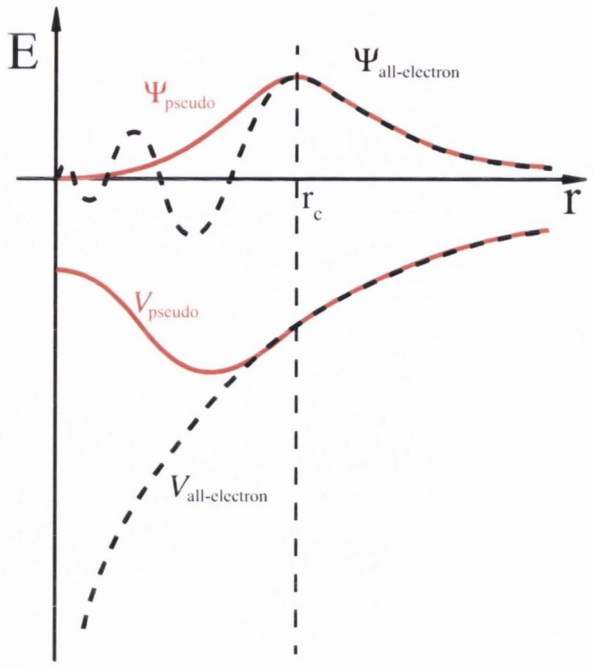


Figure 2.6: A schematic showing the relationship between the all-electron wavefunction ($\Psi_{\text{all-electron}}$) indicated by the dashed black line, and a pseudopotential wavefunction (Ψ_{pseudo}) indicated by the solid red line. The Coulombic potential $V_{\text{all-electron}}$ related to the all-electron wavefunction is shown by the dashed black line, and the pseudopotential (V_{pseudo}) related to the pseudopotential wavefunction is shown by the solid red line. For both wavefunctions, the potentials are matched beyond the radius cut-off (r_c).[1]

involved in bonding. The construction of an accurate, transferable and efficient pseudopotential is difficult. The valence electron pseudopotential is required to reproduce the behaviour and properties of the valence electrons in the full calculation, therefore the pseudopotential should be the same as the all-electron calculation. The pseudopotential will also depend on the orbital angular momentum of the wavefunction and requires the total valence electron density within the core radius to be similar to the all-electron case. The development of 'norm-conserving' pseudopotentials ensures that the function agrees with all the chosen reference energies and cut-off radii. The advantage of these norm-conserving wavefunctions is that relativistic effects can be considered in the model for heavier elements.

A number of functional forms of the pseudopotential are possible with varying parameters, that differ in the number of required plane waves and in the transferability between different atomic environments. Pseudopotentials that require fewer plane waves

are referred to as being 'soft' and are computationally less demanding; however, there is a trade off between their transferability and softness. '*Ultrasoft*' pseudopotentials drop the norm-conserving criteria and their logarithmic derivatives span the entire range of eigenvalues of the valence electrons. These pseudopotentials allow calculations of d and f valence electrons to be more feasible, and reproduce the results of accurate all-electron calculations. A drawback of using *ultrasoft* pseudopotentials is that due to the non-linearity of the exchange interaction between valence and core electrons, sophisticated non-linear core corrections are required for systems where the overlap between valence and core electron densities is not completely negligible. The 'non- local norm-conserving' plane waves were built on by Blochl with the introduction of the Projected Augmented Wave (PAW)[348] approach.

The PAW method simultaneously achieves the computational efficiency of the pseudopotential methods as well as the accuracy of a full-potential augmented plane wave method, which is regarded as the benchmark for solid state calculations using DFT. Unlike the pseudopotential approach, PAW accounts for the nodal behaviour of valence orbitals and ensures orthogonality between the valence and core wavefunctions. In the PAW method, the all-electron valence wavefunctions (Ψ_n^{AE}) are reconstructed from pseudo wavefunctions *via* a linear transformation;

$$|\Psi_n^{AE}\rangle = |\Psi_n^{PS}\rangle + \sum_l \left(|\phi_i^{AE}\rangle - |\phi_i^{PS}\rangle\right) p_i^{PS} |\Psi_n^{PS}\rangle \tag{2.58}$$

The pseudo wavefunctions Ψ_n^{PS} (n being the band index) are variational quantities expanded by plane waves, accurately and efficiently calculating the electronic structure of materials within the framework of DFT. The PAW approach uses localised basis sets to represent the core electrons, with the effect of the core states being projected on to the valence electrons. This retains the numerical advantage of pseudopotential calculations while maintaining the physics of the all-electron calculation, including the correct nodal behaviour of the valence electron wavefunctions.

In practice a pseudopotential is employed only with plane waves that have a kinetic

energy ($\left(\frac{\hbar^2}{2m}\right)|\mathbf{k}+\mathbf{G}|^2$) less than a certain cut-off, which is dependent on the system. Elements with higher energy valence states will have softer pseudopotentials than those with lower valences states close to the nucleus, such as the $2p$ states of oxygen and carbon. A higher cut-off is required for elements with valence states close to the nucleus, and hence more plane waves. The basis functions for the plane wave expansion are not associated with particular atoms but defined over the entire cell, removing the problem of basis set superposition errors normally associated with Gaussian or Slater type basis functions; however this also introduces Paulay Stress, a common issue with periodic calculations.

2.5.4 Band theory and Orbital Based Approaches

To calculate the ground state energy of a chemical system, the **k**-points are sampled over the Brillouin zone, and at each value of **k**, the energy of each band is determined. A band is comprised of basis sets to produce molecular orbitals, and is based on the assumption that the effect of orbital overlap is to modulate the atomic levels. The more basis functions that are present in the unit cell, the more discrete energy levels that are present in the system of interest. The energy levels will eventually merge into a continuum and form a band, as shown in Figure 2.7. Each atom will contribute electrons to fill the energy levels according to Hund's Rule of Maximum Multiplicity, and the Pauli exclusion principle allows the occupation of two electrons for each energy level at a particular value of **k** depending if the calculation is spin polarised or spin paired.

The energy levels or bands are filled until all electrons within the system occupy an energy level. The continuum of bands that are filled make up the valence band (VB) of the system, whereas bands that are not filled make up the conduction band (CB). The presence of unoccupied bands allows excitation of electrons from the highest filled band of the VB to the lowest unoccupied band of the CB, giving rise to special properties of the materials such as conduction, optical, and thermal properties. For semi-conductors a band gap forms between the VB and CB, thus energy is required to

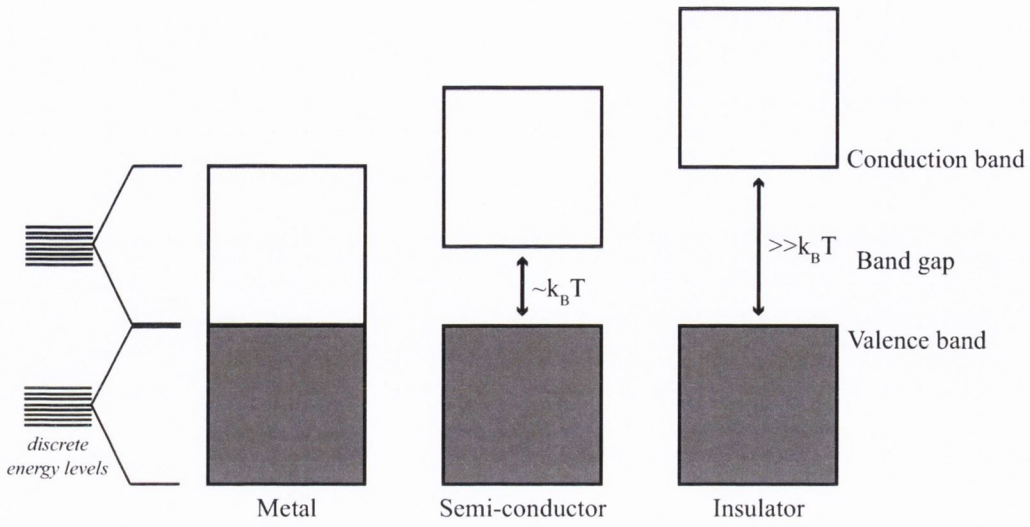


Figure 2.7: A schematic showing the formation of a band continuum from discrete energy levels. The digram shows the valence and conduction bands for metals, semi-conductors and insulators, where they are separated by a distinct band gap for semi-conductors and insulators.

excite electrons from the top of the VB to the bottom of the CB The size of the band gap is greatly increased for an insulator so that a large amount of energy is required to excite electrons from the VB to the CB. Typically conduction of electrons is not common within insulators, unless a great amount of energy is supplied or defects are added to the system.

The Fermi Energy (E_F) lies half way between the occupied and unoccupied levels of the system, where for a metallic system this is located within the partially filled band between the VB and CB, and located inside the band gap for semi-conductors and insulators. When one or two more bands are partially filled (as in the case of a metallic system), a surface in **k** space is considered that separates the occupied bands and the unoccupied bands, defined by the Fermi energy. This surface is known as the Fermi surface, and defines a separation between the VB and CB. Normally, the Fermi surface is contained within a single band, if this does not occur, then branches of the Fermi surface may be across the partially filled bands. For metallic systems, a more rigorous **k** space sampling is thus required in contrast to semi-conductor or insulating systems, to accurately define the Fermi surface. The Fermi surface shows the same periodicity

as the reciprocal lattice, and can be measured experimentally providing a link between experiment and theory.

2.6 Force and Geometry Optimisation

2.6.1 Hellmann-Feynman Theorem

The DFT-SCF method employed to determine the low energy ground state wavefunction is a complicated process, which includes the nuclear coordinates, basis functions, and basis function coefficients. The calculation for the total energy and the derivatives of both nuclei and electronic wavefunctions are even more difficult and computationally expensive. In order to simplify the calculation of forces, the Hellmann-Feynman theorem is used.[349] This theorem allows the separation of the force (derivative) calculations on the nuclei and electronic wavefunction by calculating the force on every atom within the system using the classical electrostatics, once the spatial distribution of the electrons with respect to the nuclei are determined from solving the Schrödinger equation. The force on all ions can be thus calculated after the force directly related to the wavefunction is determined, with only one call to the energy subroutine.

There are however, issues with this approach as the derivative of the basis set with respect to the volume of a cell is ignore, introducing an extra force to the pressure identified as the Pulay Stress.[350] This is not a major concern for plane wave basis sets since they are not atom specific; however the pressure is wrongly calculated at any given volume. The change in the volume of the cell would affect the plane wave cut off parameters and therefore care must be taken when accounting for Pulay stress. Once the forces are accounted for, they are used for atomic relaxation and their optimisation techniques are discussed in the next section.

2.6.2 Energy Minimisation Methods

The objective of static lattice calculations is to determine the configuration which provides the minimum energy for the system. This is achieved by optimising the forces on the atoms, and adjusting their coordinates to locate the minimum energy configuration of the system. The derivatives of the potential energy with respect to nuclear coordinates for the multi-atomic system can be expressed using a Taylor series;

$$V(x_k + \partial x) = V(x_k) + (\partial x)V'(x_k) + \frac{(\partial x)^2 V''(x_k)}{2} \tag{2.59}$$

where the gradient $\frac{\partial E}{\partial q_k}$ is derivatives of the potential energy with respect to the atomic coordinates (x) which provides a direction to the minimum. The magnitude of the gradient indicates the 'steepness' of the slope, which is the force acting on the atoms. The minimum energy configuration is determined from first derivative methods when;

$$\frac{\partial V}{\partial x_k} = 0 \tag{2.60}$$

and for second derivative methods;

$$\frac{\partial^2 V}{\partial x_k^2} > 0 \tag{2.61}$$

where V is the potential energy and the variables x_k are the internal atomic coordinates in Cartesian space. The second derivative indicate the curvature of the function to predict the change in direction of the function and can be used to locate any stationary points (transition states) on the potential energy surface (PES).

The Taylor series uses vectors and matrices for various derivatives, so that for a system with a potential energy that is a function of $3N$ Cartesian coordinates, the vector $\mathbf{x}$ for the first derivative of the energy at a point k (gradient $\mathbf{g}_k$) will have $3N$ components. For second derivatives of the energy function ($\mathbf{V}''(\mathbf{x}_k)$) with respect to the coordinates of the current system (x_k) a dimensional matrix of $3N$ x $3N$ components

known as the *Hessian* or force constant matrix (**H**) is implemented.

Minimisation methods for static lattice calculations commonly use first and second derivative methods at efficiently finding an energy minimum; however they have a number of drawbacks. As the PES contains both local and global minima/maxima, these methods cannot distinguish between a local or global point, and the optimisation process may find a local minimum rather than a global minimum. As the static lattice calculations minimise the potential energy, they effectively calculate the energy of the system at 0K, and neglecting any vibrational and thermodynamic properties of the system. Despite this, the minimisation techniques can predict structures and properties to experimental results.

2.6.3 First-order minimisation methods

There are two first order methods for minimising the energy of a system of interest; 1) steepest descent and 2) conjugate gradient methods. These approaches gradually change the coordinates of the atoms within the crystalline lattice so that they move the energy closer and closer to the minimum point. The initial configuration of the crystalline lattice, in most cases the experimental structure, is taken as the starting point ($\mathbf{x}_1$) for calculation, with the first iteration (k) relaxing the structure in the direction of the minimum point on the PES.

Steepest descent approach moves in the direction along the gradient of the net force, and is represented as a $3N$-dimensional vector ($\mathbf{s}_k$) for $3N$ Cartesian coordinates;

$$\mathbf{s}_k = -\frac{\mathbf{g}_k}{|\mathbf{g}_k|} \tag{2.62}$$

This approach is carried out by selecting the direction of the gradient to optimise the starting structure. The energy minimum of the function is located by a line search or an arbitrary step size along the direction of force, along this direction such that the middle point lies in a minimum between two outer points. An iterative procedure is carried out to decrease the distance between the two outer points, gradually reducing the area

where the minimum is located, until the difference in energy is within the specified convergence criteria and the system is considered to be converged to a minimum energy structure.

As the line search approach may be computationally demanding, a arbitrary step approach takes a step length along the gradient vector $\mathbf{s}_k$ so that the new set of coordinates after a step k is given by;

$$\mathbf{x}_{k+1} = \mathbf{x}_k + \lambda \mathbf{s}_k \tag{2.63}$$

where λ is the step size which initially has a predetermined value. If the first iteration leads to a reduction in energy then the step size for the second iteration is increased by a multiplication factor. This is iterated until the minimum is reached within the specified convergence criteria. The step size is dependent on the nature of the PES, for a flat surface a large step size is appropriate while for a surface with many hills and troughs a smaller step size is used. The arbitrary step approach requires a larger number of steps to reach the minimum than the line search approach; however, the arbitrary step evaluates less functions.

For the steepest descent method, the direction of the step is based on the intermolecular forces and this method is useful for relieving high forces in the initial configuration. The method is robust even when the starting configuration is far from the minimum; however, many small steps may be required closed to the minimum and the method over corrects itself, introducing oscillations and errors.

To overcome the oscillatory nature and errors of the steepest descent approach close to the minimum, the conjugate gradient approach chooses a direction before proceeding to the minimum point. For the steepest descent the gradient and direction of steps are orthogonal, while for the conjugate gradient approach, the gradient at each point is orthogonal, but the direction is conjugate. The set of conjugate directions has a function of M variables so that the minimum is achieved in M steps, moving in a

direction $\mathbf{v}_k$ from point $\mathbf{x}_k$;

$$\mathbf{x}_k = -\mathbf{g}_k + \gamma \mathbf{x}_{k-1} \tag{2.64}$$

where $\mathbf{x}_k$ is computed from the gradient at point k, and the previous direction vector $\mathbf{x}_{k-1}$ with γ being a scalar given by;

$$\gamma_k = \frac{\mathbf{g}_k \cdot \mathbf{g}_k}{\mathbf{g}_{k-1} \cdot \mathbf{g}_{k-1}} \tag{2.65}$$

In order to efficiently implement the conjugate gradient approach, the steepest descent approach is used for the first step since there is no previous search direction to find the direction of the minimum on the PES. The conjugate gradient approach is then employed close to the minimum to evaluate the minimum energy configuration. Ideally, the line search approach is used to evaluate the minimum in all search directions to ensure that each gradient is orthogonal to all previous gradients, and the each direction is conjugate to all previous directions.

2.6.4 Second-order Minimisation Methods

Second-order methods use both the first derivatives (gradient) and the second derivative (curvature) of the function to locate the minimum. The Newton-Raphson approach is the simplest second-order minimisation method. At the minimum/maximum point the gradient is 0 $V'(x^*) = 0$ and so the Newton-Raphson equation is given as;

$$x_{k+1} = x_k - \frac{V'(x_k)}{V''(x_k)} \tag{2.66}$$

This calculates a new atomic position (x_{k+1}) based on the previous position (x_k), and the change in the curvature with respect to the gradient of the Taylor expansion. This is referred to as as the inverted Hessian matrix ($\mathbf{H}^{-1}$) of second derivatives employed for $V''^{-1}(x_k)$. Although for a pure quadratic equation this approach can find the minimum in one step at any point on the PES. In reality however, the function is only quadratic at a first approximation, and so a number of steps are required, with $\mathbf{H}^{-1}$ evaluated at each

step. The Hessian matrix must be positive in the Newton-Raphson approach, meaning that all eigenvalues contained in the matrix are positive. If one element is negative the Newton-Raphson approach moves to a point where the energy increases (saddle point). Far from the minimum this approach is unstable as the harmonic approximation is not appropriate and a more robust approach is required to ensure that the Hessian is positive before employing the Newton-Raphson method.

The calculation and inversion of the second derivatives of the inverse Hessian matrix is computationally expensive and time demanding, which is a significant drawback for second derivative methods. The quasi-Newton approach was developed, aiming to eliminate the calculation of the Hessian. This approach requires only the first derivatives, approximating the inverse Hessian matrix as the calculation proceeds. At each iteration k, the new positions $\mathbf{x}_{k+1}$ are obtained from the current (or initial) atomic positions $\mathbf{x}_k$, the gradient $\mathbf{g}_k$ and the current approximation to $\mathbf{H}_k^{-1}$;

$$\mathbf{x}_{k+1} = \mathbf{x}_k - \mathbf{H}_k^{-1}\mathbf{g}_k \tag{2.67}$$

This formula is exact for a quadratic function, and for static lattice calculations the vector $-\mathbf{H}_k^{-1}\mathbf{g}_k$ is used for the line search approach. For quantum mechanics calculations, the additional energy evaluations required by the line search approach may prove to be computationally demanding, forcing approximations to be employed. An effective approximation is to fit a function to the energy and gradient at the initial point $\mathbf{x}_k$ and at the point $\mathbf{x}_{k+1}$, determining the minimum of the fitted function between the two points. The inverse Hessian matrix is thus updated after moving to the new positions at $\mathbf{x}_{k+1}$, which is dependent on the formula of the specific method used. Examples of such methods are Davidon-Fletcher-Powell (DFP), Broyden-Fletcher-Goldfarb-Shanno (BFGS) and Murtaugh-Sargent (MS) methods which converge to the minimum for a quadratic function of M variables in M steps. These approaches all use current and new positions to update the Hessian matrix.

The choice of minimisation method is based on a number of factors: the storage and

computational requirements of the calculation, the relative speed of the calculations at various points, the availability of analytical derivatives and functions. The calculation of the inverse Hessian matrix present problems with memory storage for large systems of atoms such as static lattice calculations. Steepest descent and conjugate gradient approaches are preferred for such systems, whereas for small molecule calculations the Newton-Raphson approach is used. For the work outlined in this thesis, the conjugate gradient approach is preferred for the optimisation of the adsorption and interaction of N, O and NO_x species on the metal surfaces, and the methodology to carry out the adsorptions is detailed in the next chapter.

Chapter 3

Computational Methodology

3.1 Introduction

This chapter outlines the methods used to implement the theory discussed in Chapter 2 for the systems of study in this body of work. The method to optimise the bulk metals, and to generate the surface orientation using the slab model from the optimised metals will be discussed. The procedure to calculate the most stable adsorption modes for N, O and NO_x species on the metal surfaces, and analysis of their interactions and electronic structure with the metal surfaces within the framework of the Vienna *ab-initio* Simulation Package (VASP),[350–352] will also be outlined. The detailed analysis will then be carried out on the most stable adsorption mode using partial (ion and *l*-quantum number decomposed) electronic density of states (PEDOS), charge density and Bader analysis[353–356] in order to resolve the charge interactions between adsorbates and metal surfaces. The approach to calculation energy barriers between the different reaction steps, in addition to the diffusion of N, O and NO will also be discussed, using the climbing nudged elastic band method (cNEB) developed by Henkelman *et al.*[357, 358]

3.2 Vienna *ab-initio* Simulation Package (VASP)

All calculations in this thesis were performed using the Vienna *ab-initio* Simulation Package (VASP).[350–352] This code is used in computational chemistry and physics for electronic structure calculations for a wide range of materials. VASP having its own set of optimised PAW pseudopotentials for each element and a range of implemented DFT functionals, makes it a popular choice and flexible to use. The unit cell is repeated in all three directions under periodic boundary conditions to represent an infinite lattice, and full electronic and geometrical optimisations are carried out. Analysis of the relaxed unit cell can be carried out to provide a full description of the electronic structure.

3.3 Structural Optimisation and Convergence

The optimisation of the structures by using first or second derivative methods has a drawback, as they ignore the derivative of the basis set with respect to the ionic position. In plane wave basis set calculations, this error arises due to the basis set being incomplete and has the effect of getting the pressure wrong with respect to changes in volume. The volume for the calculation varies, resulting in an underestimation of the equilibrium volume, unless a very large plane wave cut-off is used. This issue is addressed by optimizing the unit cell at a series of volumes, where the atomic positions, lattice vectors and angles are allowed to relax within the constrained total volume. Typically the starting configuration is obtained from experimental and/or computational data for the system of interest. The ground state configuration of a system has the lowest energy according to the variational principle, hence the equilibrium value is the minimum energy obtained from the resulting energy-volume data fitted to the Murnaghan equation of state as shown below;

$$E(V) = E_0 + \frac{B_0 V}{B_1(B_1 - 1)} \left[B_1 \left(1 - \frac{V_0}{V_1} \right) - 1 + \left(\frac{V_0}{V} \right) B_1 \right] \tag{3.1}$$

where B_0 corresponds to the bulk modulus and B_1 is its pressure derivative, V_0 is the equilibrium cell volume and E_0 is the ground state energy.

The approach taken to test for convergence of the bulk metals in this work, is the use of a series of energy-volume curves that are plotted using different k-point sampling grids at a certain plane wave cut-off energy, and an example of this is shown schematically in Figure 3.1. The number of k-points are rounded to the nearest even number for

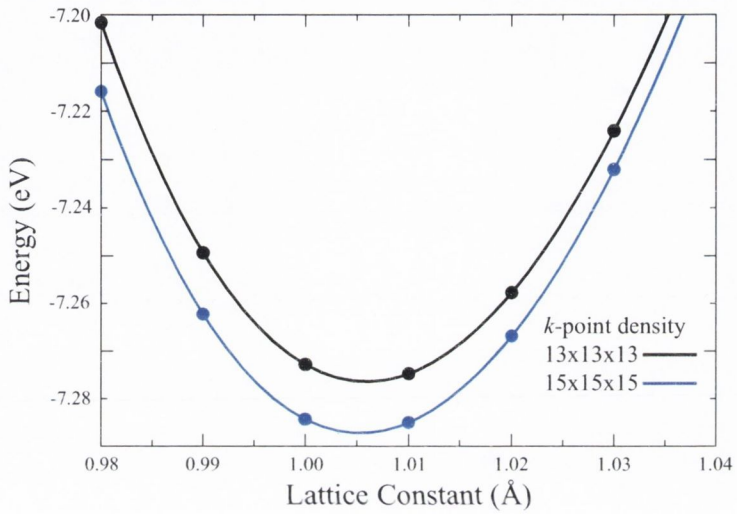


Figure 3.1: A schematic plot of energy versus volume at different k-point densities.

continuity in the convergence. Even numbers produce a distribution in which the zone centre is not included, while odd numbers give distributions that include the zone centre. Using all even numbers ensures equivalent distributions, varying only in the density of points. Once an equilibrium volume has been obtained from the fit to Equation 3.1, a final geometry relaxation is performed at this value, which results in the optimized structure for the material.

3.4 Surface Generation and Slab Model

The surface is generated by orientating the crystal in such a way that two of the three lattice vectors lie in the plane of the surface, with the third lattice vector expanded in the stacking direction. This creates a metal slab with two surfaces and a void or

vacuum gap either side of the slab within the periodic unit cell as shown in Figure 3.2. The vacuum gap must be large enough so that interactions between slab images in the stacking direction do not occur. To ensure the metal surface slab is representative of a surface, it must contain enough layers so that the middle layers behave the same way as the bulk metal, and that adsorbates above and below the slab do not interact. Once the surface is generated, the surface structure can be optimised by keeping the lattice vectors of the slab and vacuum fixed, to ensuring the surfaces do not collapse into the vacuum, while the metal surface atoms are allowed to relax.

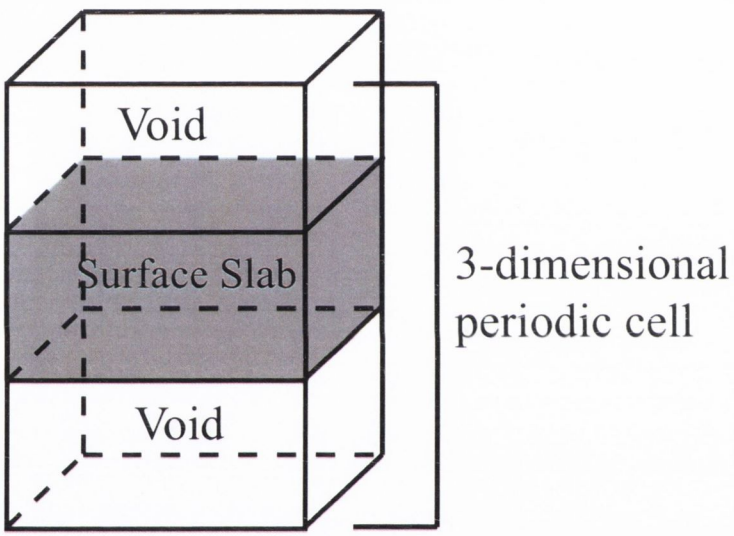


Figure 3.2: A schematic of the three-dimensional surface slab model of a periodic simulation cell.

The free energy for the lattice plane of interest is a measure of the surface stability. For the periodic slab model, the surface energy (γ) is obtained by;

$$\gamma = \frac{E_s - nE_{bulk}}{2\,Area} \tag{3.2}$$

where E_s is the energy of the surface unit cell, n is the number of atoms of the surface and E_{bulk} is the energy of the metal bulk.

3.4.1 Surface Structure

The METADISE code generates the surface from the optimised bulk metal, along the direction of a specific lattice plane in Cartesian space. The lattice plane is denoted by a set of integers h, k, and l known as Miller indices, and defined in two ways; 1) by the reciprocal lattice that is orthogonal to the reciprocal vector or 2) by its orientation that inversely intercepts along the **a**, **b**, and **c** vectors parallel to $\left(\frac{\mathbf{a}}{h}, \frac{\mathbf{b}}{k}, \frac{\mathbf{c}}{l}\right)$. The Miller indices are thus proportional to the inverse of the intercepts of the plane, in the basis of the lattice vectors, where a 0 indicates that the lattice plane does not intercept that axis. For the cubic set of Bravais lattices, the high symmetry low index planes are shown in Figure 3.3, where the Miller indices written with as $\overline{1}$ refer to negative directions. The Miller indices are usually written as integers and normally reduced to be divisible by 1.

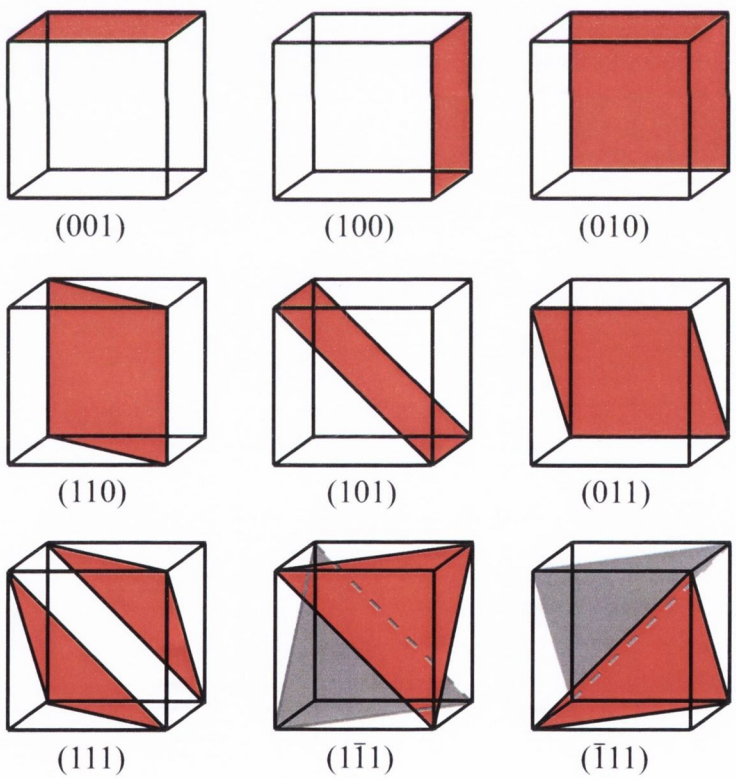


Figure 3.3: The different Miller indices for the cubic set of Bravais lattices.

The symmetry of the cubic set of Bravais lattices allows the planes to be symmetri-

cally equivalent in different directions. An example is that coordinates in curly brackets $\{100\}$ denotes a subset of planes that are equivalent due to symmetry operations; such as $(100), (010), (001)$, which can be seen in Figure 3.3. For the case of FCC unit cells of the metal bulks in this work, the primitive lattice vectors are not orthogonal and the Miller indices are conventionally defined relative to the lattice vectors of the cubic supercell in Cartesian directions.

The metal surface defined by the Miller index that is generated by METADISE is a two dimensional slab structure contained in a unit cell, and under periodic boundary conditions is effectively infinitely extended in the xy plane, with a vacuum in the third dimension (z direction). The two dimensional structures can be described by types of symmetry operations via translational, point operations and glide planes. Through such symmetry considerations, the unit cell for the two dimensional metal slab can be extended in the xy plane to increase the size of the surface under investigation. The notation used to describe the extended surface is given as;

$$R\{hkl\}p \times q \tag{3.3}$$

where R is the chemical symbol, h, k, l are the Miller indices of the surface, and p, q are the integers of the surface extension. Figure 3.4 shows an example for a $\{111\}$ surface of an FCC metal for which $p = q$ ranges from 1 to 4. In this case, the structure is characterised as being primitive as there is one atom per lattice point providing the notation for the unit cell as R $\{111\}$ p-1x1 which can be extended to R $\{111\}$ p-2x1 or R $\{111\}$ p-2x2 or R $\{111\}$ p-3x1 etc. by simple translation. The surfaces for the adsorption of N, O and NO_x species are extended to a 2x2 surface to give a surface adsorbate coverage of 0.25ML, that is observed experimentally. A larger 3x3 surface is used when two or more species are adsorbed on the metal surface so that the adsorbates of the periodic images are sufficiently far apart and do not interact. The larger surface is also used for the cNEB calculations for the same reasons.

Real crystalline low index surfaces terminated at the crystal edge are never com-

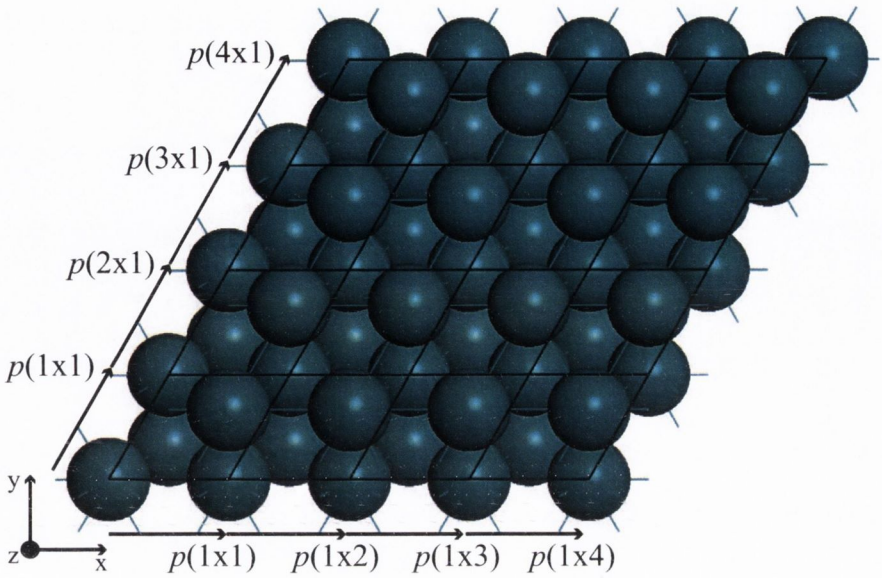


Figure 3.4: An example of a two dimensional p-{111} metal surface. The black lines outline the unit cell of the p-{111} metal surface which is extended in the xy plane by four unit cells.

pletely flat and may possess features or defects such as steps, kinks, ad-atoms and vacancies on the surface terrace. The presence of these defects is referred to as a terrace-kink-ledge (TLK) model, shown schematically in Figure 3.5, and used extensively to describe surface properties. The low index planes similar to that shown in Figure 3.3, are the exposed portions known as terraces which are bonded by atomic steps (ledges) whose length can contain kinks or ad-atoms. Step defects on the surface can act as active sites for chemical reactions due to their lower atomic surface coordination and greater affinity to bind with molecular species than flat surfaces. Stepped surfaces are therefore generated by METADISE in a similar manner to a flat surface using a Miller index that will provide a step on a flat low index surface. This will allow the examination for the effect of step defect on the $de\mathrm{NO}_x$ chemistry of the metal surfaces of interest.

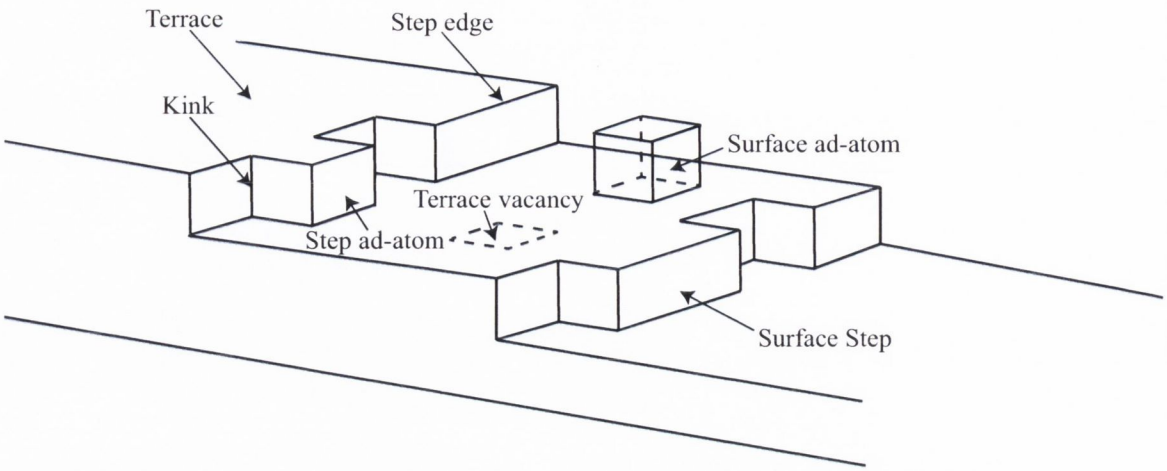


Figure 3.5: A schematic illustrating the structure of a metal surface with labelled common surface defects.

3.5 Adsorption on Metal Surfaces

To determine the surface adsorption energies of a species interacting with the metal slab, the desired species is placed above and below the slab at a certain distance from the surface, in symmetrically equivalent positions to remove any dipole effects that may arise during the calculation, as shown in Figure 3.6 (a). The entire simulation cell is then optimised, allowing the adsorbate and all the metal slab atoms to relax so that the adsorbate species interacts with the metal surface as shown in Figure 3.6 (b). The species may adsorb into the site it is placed above; however if this site is unstable for adsorption of the species, then the species will relax to the nearest, more stable adsorption site. This approach is in contrast to many other surface adsorption studies that adsorb the species on one side of the slab, while holding the bottom layers fixed rather than relaxing the entire slab. By adsorbing on one side of the slab, a dipole may arise in the calculation producing questionable energies, and keeping the layers fixed does not accurately represent a metal surface interface.

After the adsorbate species is optimised on the metal slab at a specific surface site,

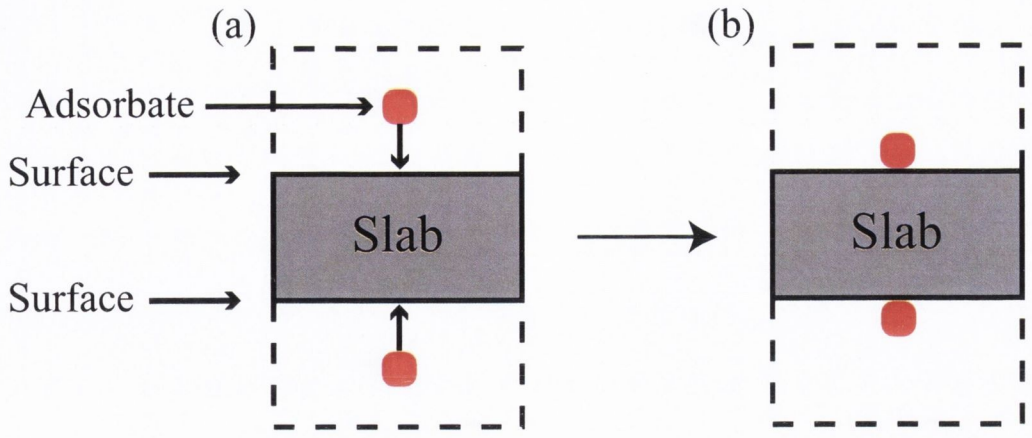


Figure 3.6: A schematic for the (a) the position of a species above and below the slab of a periodic simulation cell, and (b) its subsequent adsorption onto the metal slab.

the adsorption energy (E_{ads}) can be calculated by;

$$E_{\text{ads}} = \frac{E_{\text{SA}} - E_{\text{S}} - nE_{\text{A}}}{n} \tag{3.4}$$

where E_{SA}, E_{S} and E_{A} are the calculated energies of the adsorbate absorbed onto the slab, the clean metal slab and the gaseous species in vacuum (empty simulation cell), respectively, with n indicating the number of adsorbates in the system. The adsorption energies for the mono-atomic adsorbates are calculated with respect to their gaseous molecules.

The adsorption energies for all the possible high symmetry sites and molecular orientations of N, O, and NO_x on the metal slab surface are calculated to determine the most stable configuration of the adsorbate on the surface. Electronic structure analysis is then carried out on the most stable adsorption configuration to investigate its interactions with the metal surface.

3.6 Bader charge analysis

Quantum chemical calculations have difficulty with accurately describing the charge density of a particular atom within in a system, and thus can not be defined by quantum mechanics. The presence of a continuous electron density for solid state and molecular

systems, makes it difficult to describe the electron density within solids, and thus the partitioning of electrons can be unclear, especially when using plane wave basis sets as these are not associated with any particular atom in the system, or indeed the basis set assignment. Mulliken analysis is the most common way of approaching this issue, which allows partial charges to be determined from the charge density associated with the basis functions centred on the atoms. The problem with this approach is that the entire electron density of the system can be centred on one atom.

An alternative approach developed by Bader, focuses entirely on the charge density, so that the atomic charge is insensitive to the basis sets used to calculated the electronic wavefunction allowing it to be used for plane wave calculations. Bader's 'Atoms in Molecules' (AIM) approach partitions a system into atomic volumes so that the electron density is divided into regions on the charge density surface. AIM is implemented by finding maxima/minima on the charge density where $\nabla\rho = 0$, followed by the construction of the zero-flux surface which intersects these points, and then the integration of the electron density in the region. Integration of the region where the atomic nucleus is located, provides the number of electrons, or total charge, associated with the atom. This approach for AIM is computationally expensive and time consuming, and thus was later refined. The implementation of AIM was simplified by a grid based approach developed by Henkelman,[354, 355] and is the method implemented in VASP, and hence used exclusively in this study.

The calculated Bader charges in this work are used to determine the charge of each individual atom of the adsorbate on the metal surface and for the gaseous species. The Bader charges are compared to the absolute atomic values to assess any differences in their charge densities upon adsorption on the metal surface. Any differences between the calculated and atomic values, will quantify if there is any change in the charge distribution of the adsorbate and if any charge transfer between the adsorbate and the metal surface occurs. This approach determines if there has been a gain or loss of charge for each species, indicating the direction of electronic donation between the surface and adsorbate.

3.7 Charge Difference Plots

The Bader charges quantify any re-distribution of charge for the adsorbates, and the charge transfer process, charge difference plots are calculated to illustrated the charge transfer process. The charge difference plots were calculated by taking difference between the charge densities of the adsorbate on the metal surface, and the sum of the charge densities of the surface and adsorbate species in the same position in the simulation cell, according to the equation;

$$\Delta\rho = \rho_{\mathrm{SA}} - (\rho_{\mathrm{S}} + \rho_{\mathrm{A}}) \tag{3.5}$$

where ρ_{SA}, ρ_{S} and ρ_{A} are the charge densities of the adsorbate on the surface, the clean surface and the adsorbate, both in the same configuration as when adsorbed. The difference in the calculated electron density between the surface and the adsorbate provides a visual representation of the charge interactions between them. An example of this is shown in Figure 3.7, which shows an adsorbate (red atom) on a metal surface (white atoms). The red regions indicate increases in charge density, while the blue regions indicate decreases in charge density, as outlined in the figure. The figure shows that the adsorbate gains charge, while the metal surface looses charge.

3.8 Electronic Density of States

The electronic density of states (EDOS) displays the information about the electronic structure of the material under consideration. The total EDOS shows the density of eigenvalues as a function of energy, and can be integrated to provide the number of electrons per energy level. Although the total EDOS can provide information about the total electronic structure, it can not distinguish between ions or orbital to which the states belong to. In order to clarify this, and to show the individual contributions from the atomic orbitals at a particular energy, the partial (ion and l and m decomposed)

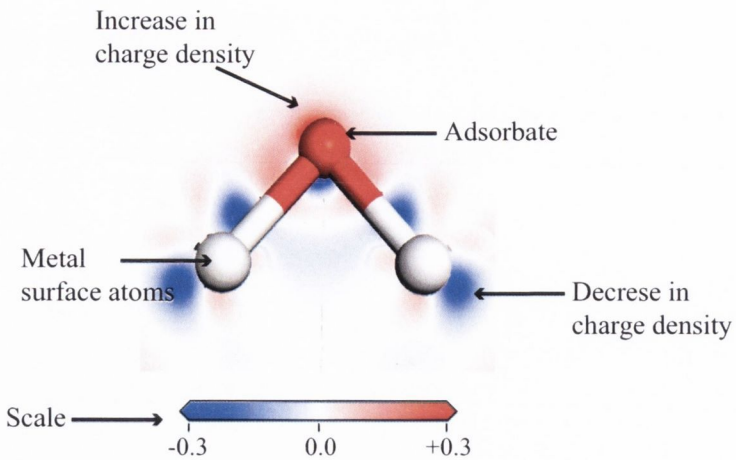


Figure 3.7: The calculated charge density difference of an adsorbed oxygen atom on a rhodium metal surface. The charge difference ranges from -0.3 (blue) to +0.3 (red) electrons/Å^3, as indicated by the scale. The plot is visualised using the Accelrys Materials Studio Software package.

electronic density of states are calculated. This is achieved by projecting the wavefunction onto spherical harmonics within spheres of a certain radius around each ion. In order to determine the density around each ion, the radius is examined using the charge density surrounding each atom. The ratio between the projected radii can be measured by plotting the charge density map and measuring the radius for the charge density sphere surrounding each atom. The ratio between the atomic radii is then calculated and the size of the radii is then varied, while keeping the ratio fixed until the correct number of electrons are calculated. For the calculations in this body of work, the PAW projection radii defined by the VASP pseudopotentials are implemented.

3.9 Vibrational Frequencies

The calculated vibrational frequencies for the adsorbates allows a comparison of the adsorbates on the metal surface with the experimental vibrational data to determine if they are observed experimentally, thus providing a link between theory and experiment. The calculated vibrational frequencies for the adsorbates in this study are static lattice calculations and carried out at OK. The frequencies for the normal modes of vibration

for the molecule on the surface can be calculated from the wavefunction using the Hessian matrix. The estimated Hessian matrix determined from the minimisation of the forces on the atoms must be explicitly calculated and converted to a force constant matrix in mass weighted coordinates, to calculated the vibrational modes. The mass weighted matrix (**F**), it is diagonalised giving the eigenvalues and eigenvectors. The frequency of each motion is calculated from the eigenvalues using the relationship;

$$v_i = \frac{\sqrt{\lambda_i}}{2\pi} \tag{3.6}$$

The frequencies obtained from this relationship provide normal modes relating to the symmetric, asymmetric and translational motions. (A more formal discussion is found in Leech[337])

The calculated vibrational frequencies for the molecules on the surface in this study are only considered along the direction of the molecular bonds. The atoms of the adsorbates are displaced from their equilibrium positions along the axis according to Hooke's law with the metal slab being held fixed to reduce the computational cost.

3.10 Climbing Nudged Elastic Band Calculations

The identification and calculation of the minimum energy path (MEP) and transition states for the rearrangement of a group of atoms from one stable state to another is difficult in solid state calculations. These quantities are useful when determining the most favourable pathway for chemical reactions, and diffusion on solid crystalline surfaces. This can be carried out by using harmonic approximation in locating the lowest saddle points on the potential energy surface (PES) of the system of interest. The search is carried out by estimating a path connecting the initial and final configurations along the minimum energy path (MEP), with the forces acting on the atoms only in the direction of the pathway. The maxima on the MEP are the saddle points on the PES, and is normally higher in energy than the initial and final configurations. A schematic is shown in Figure 3.8 (a) that illustrates the position of the saddle point between the

initial and final state configurations. By determining the saddle point the activation barrier (E_a) between the two states can be calculated.

The MEP normally has a number of minima along the path, including the initial and final states, which correspond to stable intermediate configurations. The MEP will thus have more than one maximum saddle point and the overall rate of the reaction is determined by the highest saddle point. A number of methods have been proposed to determine the MEP and transition states between initial and final states. The most widely used and efficient is the nudged elastic band method (NEB), employed for plane wave DFT calculations. The MEP is found by constructing a number of structures (images) between the initial and final states. A spring interaction between adjacent images is used to ensure continuity of the path, thus replicating an elastic band. The 'elastic band' is optimised to the MEP by minimising the forces acting on the images. The forces acting on the images are projected in a way that ensures the spring forces do not interfere with the convergence of the elastic band to the MEP, and that the images are evenly distributed across the MEP. The MEP is calculated by estimating the tangent to the path at each image at every iteration during the minimisation. The force projection is referred to as 'nudging'.

The NEB method provides an accurate description of the MEP; however the energy of the saddle point is calculated by interpolation. As a result, few images land close to the saddle point indicating that interpolation is inaccurate. The climbing image NEB (CI-NEB) method developed by Henkleman[357] overcomes this problem by maintaining the MEP with rigorous convergence to a saddle point with no extra computational effort. The CI-NEB method allows the initial few iterations of the calculation to use the conventional NEB method, with the highest energy image being identified and referred to as the 'climbing image'. The force on this image moves it up the PES along the elastic band. The images in the band converge to the MEP as previous with the NEB giving a good approximation of the saddle point, while the climbing image converges to the saddle point.[358] As all images are relaxed simultaneously, there is no additional effort to change one to a climbing image. A plot indicating the difference between the

NEB and CI-NEB approaches in finding the saddle point is shown in Figure 3.8 (b). The saddle point is shown to be converged to a maximum for the CI-NEB approach while it is absent for the NEB.

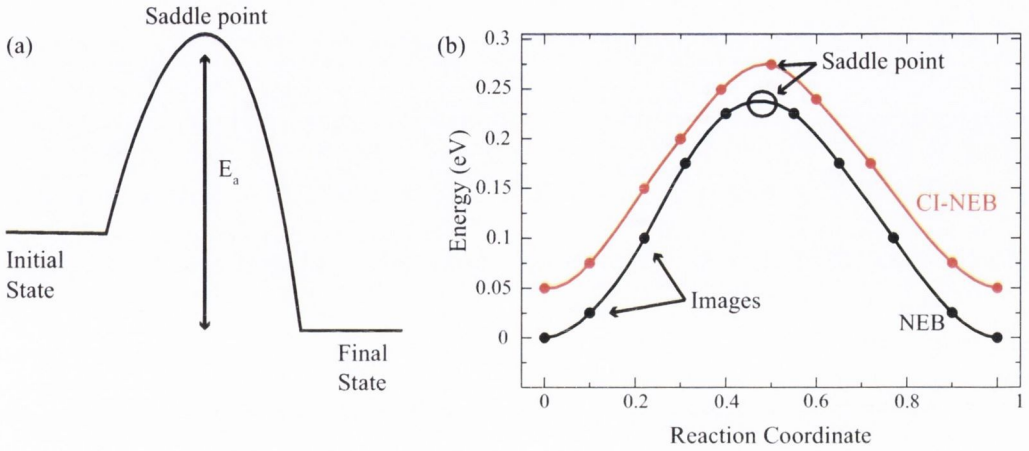


Figure 3.8: (a) A schematic of a MEP between initial and final state configurations. (b) A plot showing the differences between NEB and CI-NEB calculations.

The following chapters will outline the adsorption of N, O and NO_x on the Rh, Pd and Pt {111} surfaces with detailed analysis of their electronic structures using PEDOS, orbital integration, Bader analysis and charge difference plots. The decomposition profile will then be determined from the energies of the most stable adsorption modes and their respective gaseous species to understand their *de*NO_x chemistry. A similar methodology is used to investigate the *de*NO_x chemistry on the Rh low index and stepped surfaces, and Rh_n (n = 10, 20, 35, 56) clusters. The reaction pathways on the Rh {111} surface will then be investigated by using the most stable adsorption modes as initial and final configurations to determine the reaction intermediates and barriers using the CI-NEB method. This will allow the lowest energy pathway on the Rh {111} surface to be determined, and hence the mechanism for *de*NO_x chemistry.

Chapter 4

DeNO_x chemistry on the Rh, Pd and Pt {111} surfaces

4.1 Introduction

As NO_x gases are strongly oxidising gases that damage the atmosphere and environment, reducing their atmospheric concentration is important for a cleaner environment. *De*NO_x chemistry is therefore an important environmental topic to facilitate their removal from the emissions of automobiles and industrial factories. Rh, Pd and Pt metals are the activate catalysts used in *de*NO_x technologies, with their {111} surfaces being the most exposed surface to interact with the gases. Of these metals, Rh is known to be the most efficient metal for *de*NO_x due to its ease at breaking the NO bond and selectivity at producing N_2 over NH_3 under fuel rich conditions. More recently however, it has become overused, depleating its ore and making it a scarce and expensive metal to use. Pd and Pt are alternative metals that reduce the manufacturing costs of *de*NO_x technologies while exhibiting similar *de*NO_x characteristics to Rh metal, albeit at a reduced efficiency. Understanding the *de*NO_x chemistry of Rh, Pd and Pt metals is required to elucidate the behaviour of Rh and explain its efficieny over Pd and Pt metals. This will also provide an insight into the properties of Pd and Pt metals, and lead to the postulation of alternative catalysts that emanulate the propeties of Rh while

remaining cheaper to manufacture.

The *de*NO$_x$ chemsitry on Rh, Pd and Pt {111} surfaces will be investigated in this chapter by examining all the possible adsorption configurations of N, O, N_2, O_2, and NO$_x$ species on the metal surfaces. This will allow the identification of the most stable adsorption site for each species on each of the metal surfaces, and detailed analysis of its electronic structure and interaction with Rh, Pd and Pt will be carried out. The energies of the most stable adsorption modes along with the gaseous species will be used to build a *de*NO$_x$ profile on each of the metal surfaces, to contrast and compare the overall *de*NO$_x$ properties on Rh, Pd and Pt.

4.2 *De*NO$_x$ chemistry on the Rh {111} surface

4.2.1 Rh bulk and {111} surface

Rh bulk metal possess an FCC lattice as shown in Figure 4.1 (a), with the reduced unit cell containing one atom at the apex. The structural optimisations of the reduced unit cell were performed at a series of volumes, allowing the atomic positions to relax while the total volume was held constant. The equilibrium lattice parameters for the bulk Rh metal were determined using Γ-centred k-point sampling grids of 11x11x11, 13x13x13, 15x15x15, 17x17x17, 19x19x19 and 21x21x21 at an energy cut-off of 400 eV. The resulting energy volume curves at the different k-point densities shown in Figure 4.1 (b), and were fitted to the Murnaghan equation of state[359] to obtain the minimum energy structure. The minimum energy structure was obtained with a k-point grid of 15x15x15 and an energy cut-off of 400eV, gives an optimised lattice parameter of 3.824 Å, 0.53% larger than the experimental structure.[360] Sufficient convergence for the bulk Rh metal was found when the forces were relaxed to within 0.01 eV/Å

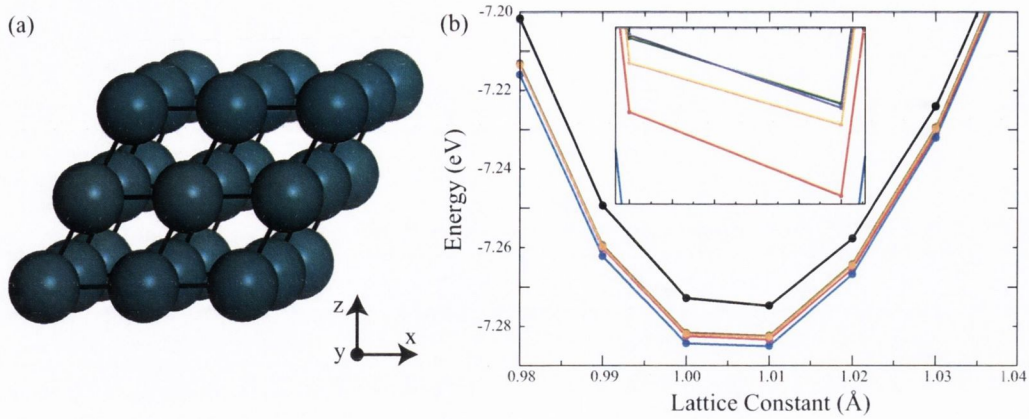


Figure 4.1: (a) The FCC lattice of the Rh bulk metal, and (b) the energies of the bulk metal at different lattice constants using different k-point sampling densities. The black, blue, red, yellow, red, green and purple lines are the 11x11x11, 13x13x13, 15x15x15, 17x17x17, 19x19x19 and 21x21x21 k-point sampling, respectively, that were tested on the rhodium bulk metal.

4.2.2 The electronic structure of the Rh {111} surface

The calculated structure of the Rh {111} p-(2x2) surface is shown in Figure 4.2 a. The surface Rh-Rh distance was calculated to be 2.70 Å and the bond distance between layers was determined to be 2.66 Å.

The calculated PEDOS for the Rh surface atoms of the top layer, and the Rh atoms contained in the centre of the slab (bulk), is shown in Figure 4.17 b. The PEDOS is aligned to the vacuum energy (E_{vac}) at 0 eV with the Fermi level (E_{F}) indicated by the dashed line. The valence and conduction bands are dominated by the Rh 4d states with a smaller contribution from the s/p states. The electronic structure for the Rh surface atoms is shown to be different to the bulk atoms, as there is a higher concentration of occupied Rh 4d states at the top of the VB compared to a similar region for the Rh bulk PEDOS. This is likely caused by the lower coordination of the Rh surface atoms. The position of E_{F} relative to E_{vac}, the workfunction, is located at -4.98 eV, in excellent agreement with the experimental value of -5 eV. The Bader charges for the Rh surface were calculated to be -0.04, which is balanced by sub surface layers with a charge of +0.04, and the middle of the slab (bulk) having a charge of 0.00 for each atom.

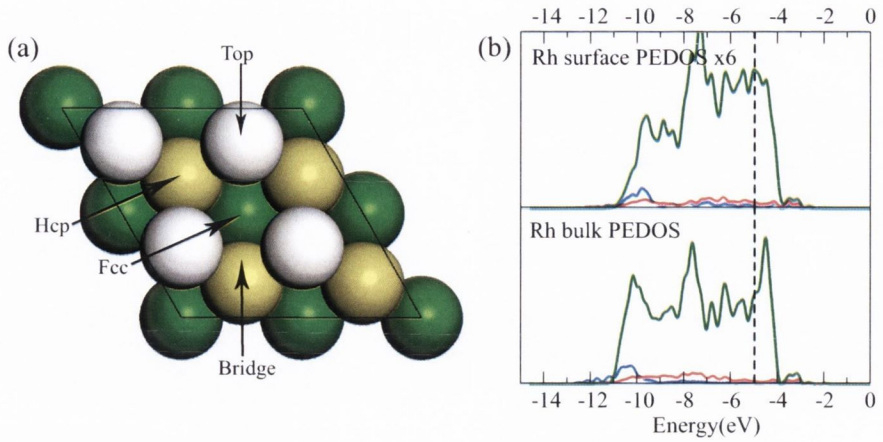


Figure 4.2: (a) The structure of the 7-layered Rh {111} p-(2x2) surface. The A-B-C type stacking in the fcc metal is highlighted by the coloured layers, where the top layer (A) is white, the second hcp layer (B) is yellow and the third fcc layer (C) is green. The four possible binding sites are labelled top, bridge, hcp and fcc. (b) The PEDOS of the Rh surface atoms and the bulk atoms within the slab. The dotted line indicates the position of the Fermi Level (E_F) and the vacuum energy is aligned 0 eV. The s, p and d states are shown by the blue, red and green lines, respectively.

4.2.3 Nitrogen adsorption on the Rh {111} surface

The adsorption of N was examined and relaxed on the four high symmetry sites (top, bridge, hcp, fcc) of the Rh {111} surface. The calculated structures for each of the different adsorption modes are shown in Figure 4.3, where the bridge site is not present as this was found to be unstable, relaxing to the hcp site. The adsorption energies (E_{ads}),

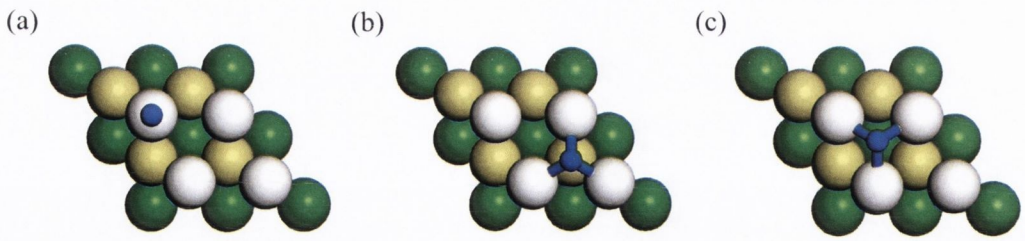


Figure 4.3: The calculated adsorption sites for N on the (a) top, (b) hcp and (c) fcc sites of the Rh {111} surface. The N adsorbates are the blue spheres, while the {111} surface layers are coloured white (top), yellow (second) and green (third) for clarity.

Rh-N bond lengths, and Bader charges for the different N adsorption sites are detailed in Table 4.1. Details for adsorption at the bridge site are absent as the mode was found

to be unstable, relaxing to the hcp configuration. The metal-N bond distances are seen to increase with increased coordination of the N adsorbate, and the adsorption energies (E_{ads}) follow a similar trend, with adsorption on the top site being endothermic but exothermic for the three-fold hollow sites. Of the two hollow sites, adsorption at the hcp site is more favourable than the fcc site. For all adsorption sites, the atomic spin is quenched to 0 by the Rh metal surface.

Site	E_{ads} (eV)	Rh-N (Å)	N charge	Rh charge
top	+1.64	1.66 x 1	-0.31	+0.30 x 1
bridge	(hcp site)	-	-	-
hcp	-0.33	1.91 x 3	-0.63	+0.20 x 3
fcc	-0.16	1.91 x 3	-0.63	+0.20 x 3

Table 4.1: The adsorption energies (E_{ads}), Rh-N bond length, bader charges for the N adsorbate and bound Rh metal atoms. The number of Rh bonds are indicated for each adsorption site.

The Bader charges for each of the adsorbates on the rhodium surface are provided in Table 4.1. The values given in the table are shown relative to the absoluted value of the neutral atomic species (in this case five for atomic N) and all values provided in subsquent tables are calculated in a similar manner. The Bader charges show that, regardless of site, the N adsorbate gains electron density from the Rh surface while the Rh surface atoms lose charge, forming a $Rh^{\delta+}$-$N^{\delta-}$ species. The charge transfer from the individual Rh surface atoms is seen to decrease with increased coordination of the N adsorbate; however, as there are 3 surface Rh atoms for the hollow site, there is greater donation from the three-fold hollow sites of 0.6 e. This charge transfer process is shown visually for the most stable N adsorbate on the Rh surface (hcp site), by the charge density difference plot in Figure 4.4 (a). The red regions show an increase in electron density while blue regions indicated a decrease. The plot shows that there is an increase in electron density around the N atoms, with a smaller decrease in density around the N adsorbate. There is a corresponding decrease for the Rh metal atoms along the bond axis with a p-orbital type shape, as seen in the figure. The plot thus

shows that charge is donated from the Rh surface atoms to the N adsorbate, confirming the Bader charges.

The electronic structure for the N adsorbate at the hcp site on the Rh surface is shown by the calculated PEDOS in Figure 4.4 (b). The valence and conduction band are primarily composed of N $2p$ states and Rh $4d$ states. The majority of N $2p$ states are observed at peaks between -12 and -10 eV in the valence band, with some minor $2s$ contribution. Corresponding peaks of Rh $4d$ states are observed at a similar energy, possibly indicating mixing. A significant change occurs in this range compared to the PEDOS of the pure surface, indicating a strong overlap of the Rh $4d$ states with the N $2p$ states. There is a range of N $2p$ states from -10 eV up to E_F that mix with the Rh $4d$ band. The presence of these states which continue into the bottom of the conduction band, are present from the Rh surface charge transfer, occupying additional $2p$ states compared to atomic N. The presence of N $2p$ states in the conduction band shows that the states are not fully occupied. The charge transfer is also reflected by a reduction in E_F, from -4.98 of the pure Rh surface to -5.39 for N adsorbed on Rh.

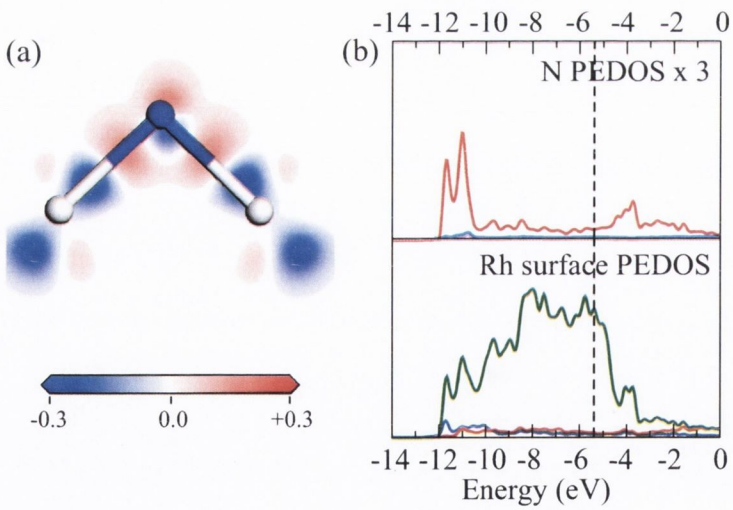


Figure 4.4: (a) The calculated charge density difference of an adsorbed nitrogen atom on the hcp site, from -0.3 (blue) to +0.3 (red) electrons/Å^3, as indicated by the scale. (b) The PEDOS for a nitrogen atom on the hcp site. The Rh PEDOS is shown for surface atoms of the top layer. The blue, red and green lines are the s, p and d states, respectively. The Fermi level (E_F) is indicated by the dotted line and the vacuum energy (E_{vac}) is aligned to 0 eV.

4.2.4 Oxygen adsorption on the Rh {111} surface

The adsorption of O was examined in a similar manner to N adsorption on the four high symmetry sites (top, bridge, hcp, fcc) of the Rh {111} surface. The calculated structures for each of the different adsorption modes are shown in Figure 4.5, where all four adsorption sites are found to be stable for O ad atoms. The E_{ads}, Rh-O bond

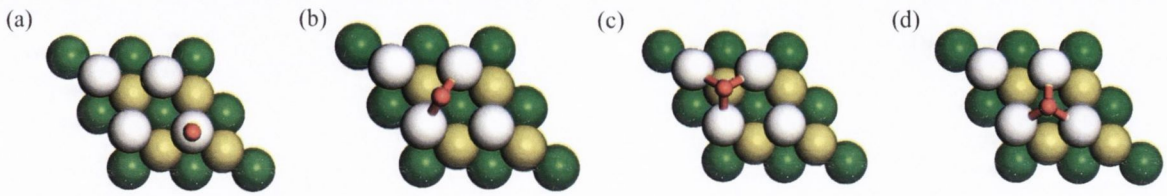


Figure 4.5: The calculated adsorption sites for O on the (a) top, (b) bridge, (c) hcp and (d) fcc sites of the Rh {111} surface. The O adsorbates are the red spheres, while the {111} surface layers are coloured white (top), yellow (second) and green (third) for clarity.

lengths, and Bader charges for oxygen adsorption at the different surface sites are detailed in Table 4.2. As seen for N adsorption, the E_{ads} increases with increasing coordination of the O adsorbate, where the top and bridge sites are found to be less stable than the three-fold hollow sites, with the fcc site being most stable. The Rh-O bond distance shows a similar trend, and the bridge, hcp and fcc sites all quench the atomic spin to 0. This is not true of the top site however, with an atomic spin of 1.84 for the O adsorbate.

Site	E_{ads} (eV)	Rh-O (Å)	O charge	Rh charge
top	-0.56	1.79 x1	-0.50	+0.31 x 1
bridge	-1.15	1.94 x 2	-0.67	+0.17 x 2
hcp	-1.95	2.01 x 3	-0.69	+0.21 x 3
fcc	-2.01	2.01 x 3	-0.72	+0.23 x 3

Table 4.2: The adsorption energies of O (E_{ads}) Rh-O bond length, the bader charges for O adsorbates and the bound rhodium metal atoms. The number of Rh bonds are indicated for each adsorption site.

The calculated Bader charges are detailed in Table 4.2, with the charge of the O adsorbate following a similar trend to E_{ads} and Rh-O bond lengths. Regardless of the adsorption site, charge is donated to the O adsorbates from the surface forming a $O^{\delta-}$ species on the surface, which increases with increase coordination of the adsorption site with the fcc site donating the greatest charge. The greater charge donation (associated with the fcc site) may suggest a stronger interaction between the O $2p$ states and the Rh surface, perhaps explaining its increased stability over the other adsorption sites. To visualise the change in electron density between the O adsorbate and the Rh {111} surface, the calculated charge density difference is shown in Figure 4.6 (a) for the fcc site. The plot shows that the O adsorbate gains density (red regions) with a small amount of charge lost (blue regions) and the Rh surface atoms losing charge along the bond axis. This indicates that charge is transferred from the Rh surface to the O adsorbate, supporting the calculated Bader charges.

The calculated PEDOS for the most stable adsorption mode, O on the fcc site, is shown in Figure 4.6 (b). The valence and conduction bands are predominantly a mixture of O $2p$ and Rh $4d$ states. A large O $2p$ peak is observed between -12 and -10 eV with a minor contribution from O $2s$ states, which mixes with Rh $5s$ and $4d$ states. There is a small contribution of O $2p$ states that are observed throughout the rest of the valence band, mixing with Rh $4d$ states up to E_F. The O $2p$ states up to E_{F} continue into the bottom of the conduction band, similar to N adsorption. These states are present in this region from the occupation of the O $2p$ states from the Rh surface charge donation as outlined by the Bader charges, thus increasing the occupation of the O $2p$ states. The presence of these states in the conduction band indicate that they are not fully occupied. The charge transfer from the Rh surface to the O adsorbate is also reflected by the lowering of E_{F} (-5.53 eV), relative to that of the pure surface (-4.98 eV).

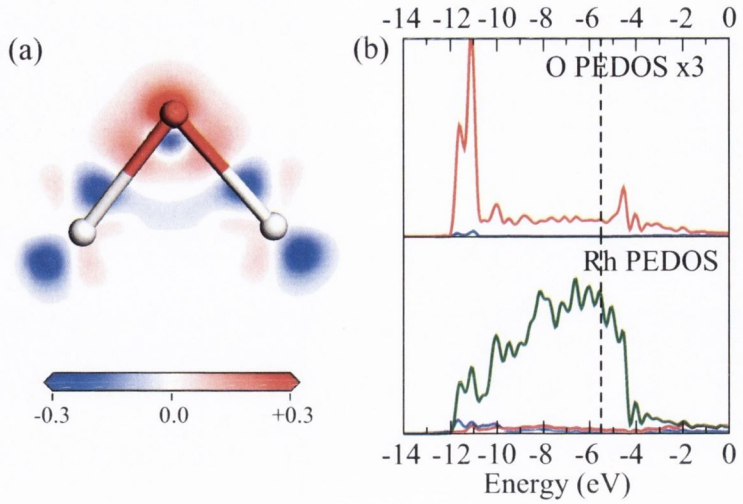


Figure 4.6: (a) The calculated charge density difference of an adsorbed oxygen atom on the fcc site. The charge difference ranges from -0.3 (blue) to +0.3 (red) electrons/Å^3, as indicated by the scale. (b) The PEDOS for an oxygen adsorbate on the fcc site and the PEDOS of the top layer Rh surface atoms. The blue, red and green lines are the s, p and d states, respectively. The E_{F} is indicated by the dotted line and the E_{vac} is aligned to 0 eV.

4.2.5 NO adsorption on the Rh {111} surface

The adsorption of NO was examined in a similar manner to N and O adsorption on the four high symmetry sites (top, bridge, hcp, fcc) of the Rh {111} surface. The calculated structures for each of the different adsorption modes are shown in Figure 4.7, where all four adsorption sites are found to be stable for NO. The adsorption

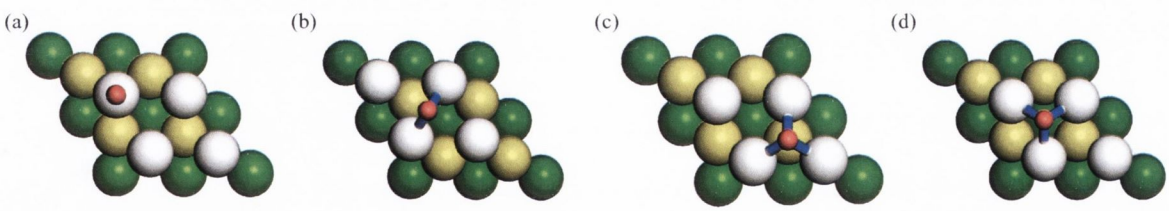


Figure 4.7: The calculated adsorption sites for NO on the (a) top, (b) bridge, (c) hcp and (d) fcc sites of the Rh {111} surface. The N and O atoms of the NO adsorbates are the blue and red spheres, respectively, while the {111} surface layers are coloured white (top), yellow (second) and green (third) for clarity.

energies (E_{ads}), Rh-N and N-O bond lengths and the N-O vibrational frequencies for the high symmetry NO adsorption modes on the Rh {111} surface are given in Table

4.3, with all structures giving rise to a complete quenching of the initial molecular spin. The adsorption energies are generally seen to increase with coordination number, with adsorption at the hcp site being the most stable, although the two coordinate bridge site is similar in energy to the three coordinate fcc site. The trend in the Rh-N bond distances also reflect the nitrogen coordination, with the singly coordinated top site giving rise to the shortest distance and the more stable three coordinate fcc and hcp sites showing the largest distances. The N-O bond expands on adsorption showing an increase of 0.03 Å (top), 0.05 Å (bridge), 0.07 Å (fcc) and 0.07 Å (hcp) over the gas phase bond length of 1.15 Å. Vibrational frequencies indicate that only the most stable hcp site (1550 cm^{-1}) is close to the experimental HREELS and dynamical LEED data with a value of 1515 cm^{-1}, assigned to a low energy hollow site of a p-(2x2) surface structure,[74] and a previous DFT:PW91 calculation.[80] The calculated vibrational frequency for the less stable bridge site (1647cm^{-1}) is similar to that observed for the IR bands at high coverages[87], and its calculated E_{ads} is close to the most stable hcp site. This suggests that the bridge site may exist at higher coverages along with a mixture of the hcp adsorption mode.

Site	E_{ads} (eV)	Rh-N (Å)	N-O (Å)	Vib (cm^{-1})
Gas Phase	—	—	1.15	1920
top	-2.01	1.76	1.18	1865
bridge	-2.30	1.96	1.20	1647
hcp	-2.46	2.04	1.22	1550
fcc	-2.31	2.05	1.22	1554

Table 4.3: The adsorption energies (E_{ads}), Rh-N and N-O bond lengths and N-O vibrational frequencies (vib) of NO for the gas phase and high symmetry adsorption sites of NO on the {111} surface of rhodium.

The Bader charges for gas phase (neutral, anionic and cationic) and adsorbed NO are given in Table 4.4. For all adsorption sites the overall charge on the molecule is negative, indicating charge transfer from the surface to the molecule, which increases as the coordination of the nitrogen atom increases. Transfer from each coordinated

surface metal atom decreases with the nitrogen coordination number, with the total transfer from the directly coordinated surface atoms representing approximately 75% of the overall charge transfer. For the top site however, the charge lost from the Rh surface atoms is greater by 0.05 e than the charge gained by the NO molecule, which may also be lost to surrounding Rh surface atoms.

Species/Site	NO	N	O	Rh
NO^+	+1.00	+1.21	-0.21	—
NO	+0.00	+0.53	-0.53	—
NO^-	-1.00	+0.10	-1.10	—
Rh{111}	—	—	—	-0.04
top	-0.21	+0.24	-0.45	+0.26 x 1
bridge	-0.33	+0.03	-0.38	+0.13 x 2
hcp	-0.43	+0.03	-0.46	+0.12 x 3
fcc	-0.43	-0.02	-0.41	+0.12 x 3

Table 4.4: The calculated Bader charges for NO in the gas phase and the surface atoms of the pure Rh {111} surface (upper) and NO adsorbed onto high symmetry adsorption sites on the Rh {111} surface and the directly coordinated surface Rh atoms (lower).

The largest charge transfer is for the hollow sites (-0.43), although comparison to the gas phase anion shows that this is clearly not a simple case of charge donation. The charge on the nitrogen atom is more negative on the bridge, hcp and fcc hollow sites than on the gas phase anion, gaining approximately 0.5 e compared with the neutral molecule. However, the overall charge transfer to the molecule is less than this, illustrating that the oxygen atom in fact loses charge density compared to the neutral molecule. This indicates a picture which is far from a simple charge transfer process with significant redistribution within the molecule. For the top site the gain of charge density on the nitrogen atom (-0.29) is again greater than the overall charge transfer (-0.21). From the Bader charges it is clear that there is significant charge donation from the surface to the molecule for all of the adsorption modes, coupled with a significant redistribution of charge within the molecule leading to charge transfer from the oxygen

to the nitrogen.

To illustrate the charge transfer process, Figure 4.8 shows the charge difference plot for NO adsorbed at the hcp adsorption site. The surface-bound nitrogen gains electron density (red regions), while the rhodium atoms show a decrease in electron density (blue regions). The oxygen atom gains electron density perpendicular to the bond axis and loses electron density along the bond axis towards the nitrogen atom, indicating changes to the σ and π bonding within the molecule and supporting the complex picture of transfer and redistribution indicated by the Bader charges.

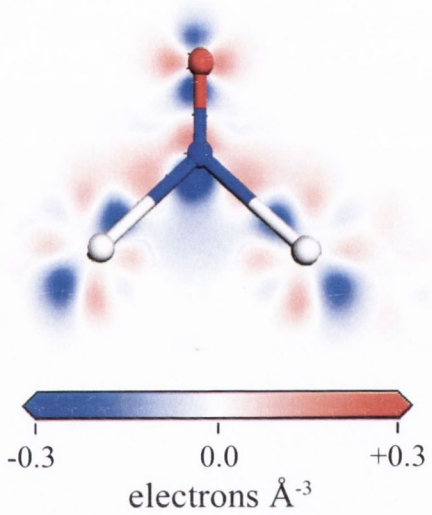


Figure 4.8: The charge density difference (electrons/Å^3) between NO adsorbed on the hcp site of Rh{111} and an unbound NO molecule and Rh{111} surface.

To further analyse the redistribution of charge on adsorption, the molecular orbital diagram and PEDOS for gas phase NO and NO adsorbed on the hcp site are shown in the Figure 4.9. The valence molecular orbitals of a NO molecule, in increasing energy, are usually labelled 3σ, $4\sigma^*$, 1π, 5σ, $2\pi^*$ and $6\sigma^*$, as shown in the molecular orbital diagram (Figure 4.9 (a)). The position of the occupied $4\sigma^*$, 5σ and 1π molecular orbitals in the PEDOS are shown in Figure 4.9(b) relative to the vacuum level, with the 3σ lower in energy (around -30 eV) and not shown. A neutral NO molecule contains 11 valence electrons, with the HOMO being a single electron in the doubly degenerate $2\pi^*$ molecular orbital, allowing NO to be a strong π acceptor. For the NO^+ species, there

are no unpaired electrons, with a HOMO of 5σ, and the NO^- species has two unpaired electrons in the $2\pi^*$ being iso-electronic with O_2. The nature of the molecular orbitals do not vary significantly with charge state. The $4\sigma^*$ has a strong contribution from N $2s$, O $2s$ and O $2p$ states, while the 5σ is composed of N $2p$ and O $2p$ with a small contribution from the N $2s$ states. The 1π and $2\pi^*$ are composed of a mixture of N $2p$ and O $2p$ states with a greater contribution from the O $2p$ to the 1π and a greater contribution from the N $2p$ to the $2\pi^*$.

On adsorption, there are significant changes to the energies and composition of the orbitals with all of the orbitals reducing in energy relative to the vacuum level. The $4\sigma^*$ orbital of the NO adsorbate gains N $2p$ states while losing O $2p$ contributions. The 5σ orbital, which lies above the 1π orbital in the molecule, is below the 1π for the adsorbate due to a large stabilisation in which it loses N $2s$ states while gaining O $2s$. The 1π orbitals are still composed of N $2p$ and O $2p$ states, however, the distribution has changed from being oxygen-dominated for the gas phase molecule to being nitrogen-dominated for the adsorbate. There are also significant changes in the $2\pi^*$ orbital due to its interaction with the Rh valance band. The $2\pi^*$ orbitals split into occupied states which are primarily located on the oxygen atom and unoccupied states which have a significant contribution from both the oxygen and the nitrogen. There is also a change in the position of E_F which is lowered to -5.76 eV relative to the pure surface (-4.98 eV). This indicates an increase in the workfunction for the system, suggesting charge transfer to the NO molecule.

To quantify these changes, the percentage contributions of the N s/p and O s/p states to the molecular orbitals of gas phase NO and NO adsorbed at the hcp site were obtained by integration of the PEDOS and are detailed in Table 4.5. Comparison is only made to $NO_{(g)}$ since only minor changes are seen in the orbital character between the neutral, cationic and anionic species. On adsorption, the contribution to the $4\sigma^*$ orbital from the N $2s$ and N $2p$ states increases by 9% and 19% respectively, while the O $2s/p$ contributions reduce by 7 % and 21 %. The 5σ orbital loses N $2s/p$ character (-11%, -8%), while gaining O $2s/p$ character (+12%, +7%). The 1π orbital gains N $2p$ character

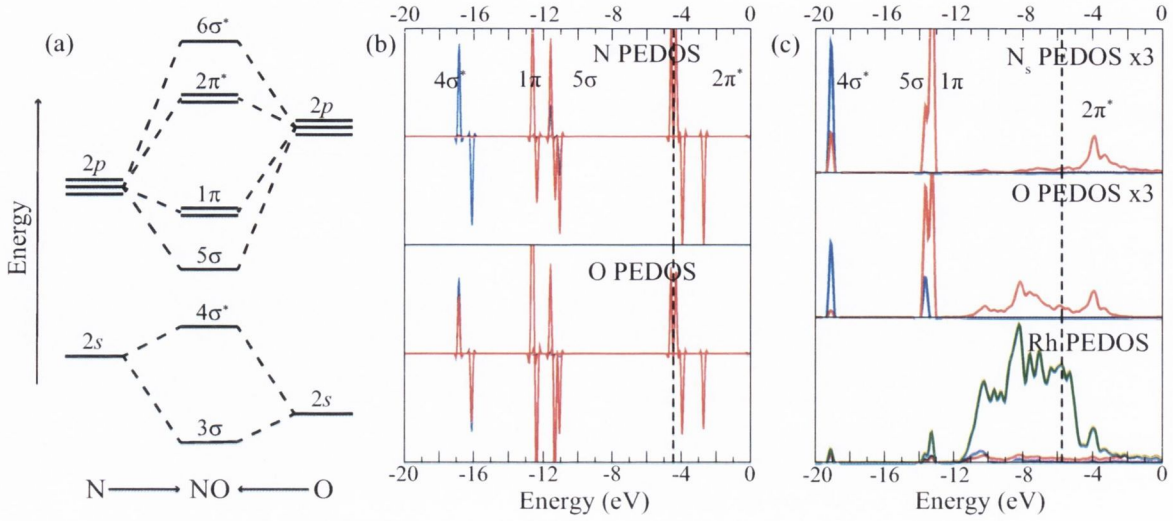


Figure 4.9: Electronic structure of NO. (a) Molecular orbital diagram for NO, (b) PEDOS of gas phase NO and (c) PEDOS of NO adsorbed on the hcp site of the Rh{111} surface. The blue, red and green lines indicate the s, p and d states, respectively. The dotted line indicates the position of the E_F on the hcp adsorption mode and the highest occupied state on the gas phase species. The graph of the hcp adsorption mode is aligned to the E_{vac} at 0 eV.

(+24%) while losing O $2p$ character (-24%). The situation is more complicated for the $2\pi^*$ orbitals. Taken as a whole they display the expected O $2p$ dominance to mirror the 1π orbital. However, the interaction with the surface causes the occupied $2\pi^*$ states to have an enhanced contribution from O $2p$ (+20%) and a reduction in N $2p$ (-20%) compared to that expected. The reverse trend is seen in the unoccupied $2\pi^*$ states.

From the analysis of the Bader charges, the charge density difference plots, the PEDOS and the changes in the orbital contributions, it is clear that there is a complex change to the electronic structure on NO adsorption. Analysis of the hcp site adsorption shows that the interaction of the molecule with the surface stabilises the atomic orbitals of the nitrogen atom, causing both a lowering of the energy of the molecular orbitals and a shift in the orbital contributions. For the adsorbate, the lower energy molecular orbitals contain a greater contribution from the nitrogen atom, while the higher energy orbitals have a greater contribution from the oxygen atom, reversing the effect of the greater electro-negativity of the oxygen in the gas phase. The $2\pi^*$ orbital would be expected to contain a greater contribution of oxygen states due to the above effect. The

	$NO_{(g)}$				
States	$4\sigma^*$	5σ	1π	$2\pi^*_{occ}$	$2\pi^*_{unocc}$
N $2s$	40	11	0	0	0
N $2p$	0	40	34	56	59
O $2s$	33	1	0	0	0
O $2p$	27	48	66	44	41
	$NO_{(ads)}$				
States	$4\sigma^*$	5σ	1π	$2\pi^*_{occ}$	$2\pi^*_{unocc}$
N $2s$	49	0	0	0	0
N $2p$	19	32	58	22	60
O $2s$	26	13	0	0	0
O $2p$	6	55	42	78	40

Table 4.5: The approximate percentage contributions of N $2s$, N $2p$, O $2s$ and O $2p$ states to the molecular orbitals of gas phase NO and NO adsorbed at the hcp site on the Rh{111} surface.

strong interaction of this orbital with the Rh valence band and splits it into an occupied and unoccupied parts. The $2\pi^*$ orbital is anti-bonding and the interaction with the surface reduces the nitrogen states in the occupied part, indicating that the mechanism of stabilisation is to reduced the anti-bonding interaction and transfer electron density onto the oxygen atom. These two effects together give rise to a charge transfer to the molecule, and a redistribution within the molecule giving rise to Bader charges which show that the nitrogen has greater charge density than the gas phase species while the oxygen has a charge state similar to that found in the molecule.

4.2.6 NO_2 adsorption modes on the Rh {111} surface

NO_2 can adsorb on the Rh surface in four different modes: μ-nitrito (N and O bound to the surface), O-O'nitrito (O and O bound to the surface), O-nitrito (single O bound to surface), and N-nitro (N bound to surface). The N-nitro adsorption mode was trialled and found to be unstable with each configuration relaxing to the μ-nitrito

adsorption mode. The N-nitrito has also been shown to be unstable is on the Pt {111} surface.[94] Only the first three of these adsorption modes are thus investigated, adsorbing in different configurations on the four high symmetry adsorption sites. All possible orientations of each mode on the different sites were tested, with the stable configurations shown in Figure 4.10, where other unstable structures relaxed to one of those seen in the figure. The E_{ads} and molecular bond distances and angles for the stable configurations are provided in Table 4.6. Molecular NO_2 is expected to have a spin due to its unpaired electron; however, for all NO_2 adsorption modes, the spin of the adsorbate is zero due to quenching by the metal surface. Overall, the results for both μ-nitrito and O-O'-nitrito modes indicate that N and O atoms prefer to be adsorbed at top and bridge positions over the three-fold hollow sites. Of the stable configurations, the most stable μ-nitrito and O-O'-nitrito adsorption modes are those shown in Figure 4.10 (a) and (f) respectively. As the most stable structure for the μ-nitrito and O-O'-nitrito modes are close in energy (0.09 eV difference), they are expected to be observed experimentally.

For the most stable μ-nitrito mode, Table 4.6 indicates that the bond parallel to the surface (N_s-O_s) has expanded and the bond perpendicular to the surface (N_s-O), which is similar to gaseous NO_2. For the most stable O-O'-nitrito mode, the N-O_s bonds have similar lengths and are both expanded relative to $NO_{2(g)}$. Both adsorption modes have a bond angle smaller than gaseous NO_2. The O-nitrito adsorption modes have an O_s-N bond perpendicular to the surface, and a N-O bond with N/O atoms away from the surface directed towards either a top site (Figure 4.10 (i)) or hcp site (Figure 4.10 (j)). For both O-nitrito adsorption modes, the perpendicular O_s-N bond is significantly expanded while the N-O bond contracts. The O-nitrito modes, both have similar values of E_{ads} but were found to be less stable than the other modes on the Rh {111} surface, and therefore analysis of this orientation is not presented.

The asymmetric, symmetric and bending vibrational modes for the μ-nitrito mode (O-O'-nitrito mode) were calculated to be 1566 (1205) cm^{-1}, 983 (1155) cm^{-1} and 732 (783) cm^{-1}. The vibrational frequencies for the NO_2 molecule have decreased on

Configuration	N_s	O_s	E_{ads} (eV)	O_s-N_s (Å)	N-O (Å)	O-N-O (°)
$NO_{2\,(g)}$	-	-	-	1.21	1.21	133.73
a	top	top[1]	-1.76	1.33	1.22	118.92
b	top	bridge[2]	-1.61	1.41	1.20	116.55
c	top	bridge[3]	-1.58	1.45	1.20	115.81
d	bridge	top[2]	-1.34	1.36	1.23	118.03
e	bridge	top[3]	-1.31	1.35	1.23	118.43
	O_s	O_s	E_{ads} (eV)	O_s-N (Å)	N-O_s (Å)	O-N-O (°)
f	top	top[1]	-1.67	1.30	1.30	119.54
g	bridge	top[2]	-1.41	1.26	1.29	117.36
h	bridge	top[3]	-1.44	1.27	1.29	117.14
	O_s	N-O	E_{ads} (eV)	O_s-N (Å)	N-O (Å)	O-N-O (°)
i	fcc	top	-1.08	1.78	1.16	110.13
j	fcc	hcp	-1.08	1.83	1.16	110.51

[1] molecule across bridge site
[2] molecule across hcp site
[3] molecule across fcc site

Table 4.6: The calculated bond distance and angle of gaseous $NO_{2\,(g)}$. The adsorption energies (E_{ads}), the calculated N-O bonds and angles for the most stable (a-e) μ-nitrito, (f-h) O-O'-nitrito and (i-j) O-nitrito adsorption modes on the Rh {111} surface. The subscript 's' denotes the surface bound atom on the Rh {111} surface.

interaction with the metal surface compared to the calculated values of 1682 cm^{-1}, 1348 cm^{-1} and 729 cm^{-1} for gaseous NO_2, which are close to the experimental values (1618 cm^{-1}, 1318 cm^{-1}, 750 cm^{-1}). There is little experimental vibrational data to directly compare to our calculated results on the Rh {111} surface. An IR study[109] of NO_2 adsorption on Rh/Al_2O_3 at low pressure and 300K, reported dominant IR bands at 1540 cm^{-1}, 1309 cm^{-1} and 1231 cm^{-1}. The latter two are quite different to those calculated for both adsorption modes which may be caused by the presence of the Al_2O_3 support, although the experimental symmetric vibrational band is close to the calculated values for the μ-nitrito mode. The mixture of vibrational bands detected

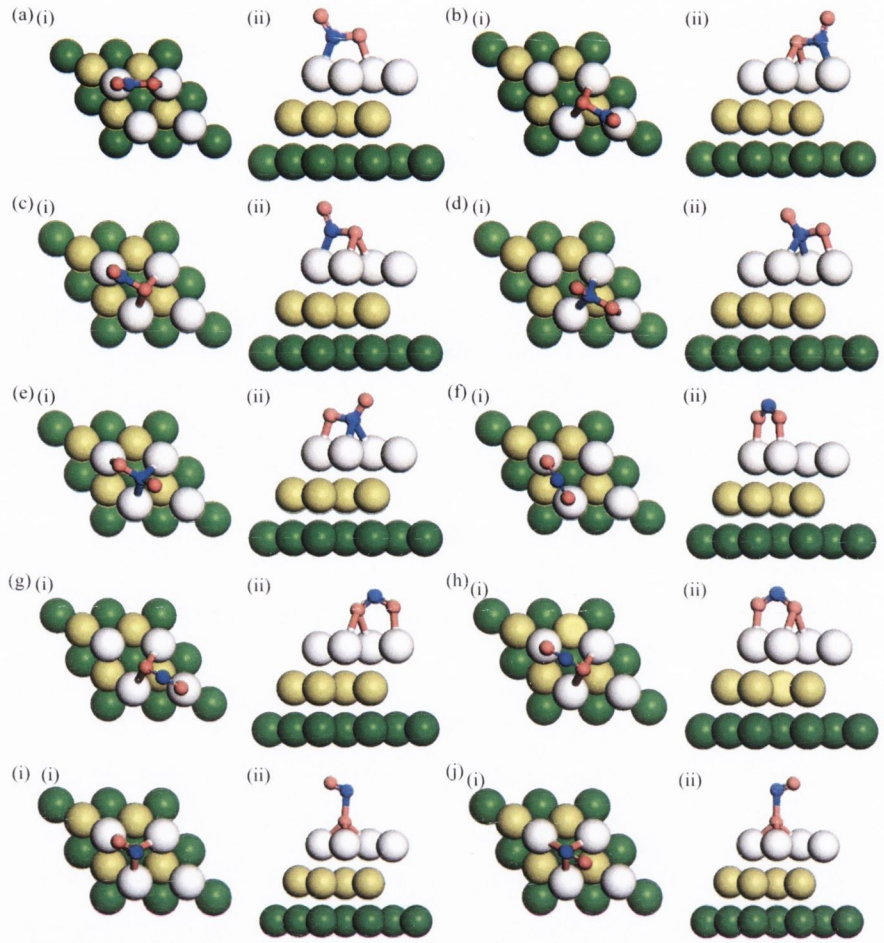


Figure 4.10: The relaxed structures of the (a)-(e) μ-nitrito, (f)-(h) O-O'-nitrito, and (i)-(j) O-nitrito adsorption modes on the Rh {111} surface. In each case, the top and side views of the adsorption modes are shown in (i) and (ii), respectively. The nitrogen and oxygen atoms are the blue and red spheres, respectively with the different Rh {111} surface layers coloured, white (top surface layer), yellow (sub-surface layer) and green (third surface layer) for clarity.

by IR measurements suggest that more than one adsorption mode is present on the Rh surface, which links well with the calculated bands for both adsorption modes. HREELS studies of NO_2 on the clean Pd (Pt) {111} surface have observed vibrational frequencies for a μ-nitrito bond modes of 1545 (1560) cm^{-1}, 1170 (1180) cm^{-1}, and 790 (795) cm^{-1},[110, 111] which has also been supported by density functional theory (DFT) studies.[94, 97] These vibrational bands for NO_2 on the clean Pd and Pt {111} surfaces are within the error for the calculated values of this study compared to gaseous NO_2, suggesting that the μ-nitrito mode and O-O'-nitrito modes are present on the Rh

surface.

Bader charges for the individual atoms of the μ-nitrito and the O-O'-nitrito adsorbates are shown in Table 4.7. The equivalent charges for the gas phase NO_2^+, NO_2 and NO_2^- molecules and the pure Rh {111} surface are also given in Table 4.7. The change in overall charge of the Rh surface atoms are positive, with the overall charge on the molecules being -0.43 for the μ-nitrito mode and -0.46 for the O-O'-nitrito mode, indicating charge transfer from the surface to the adsorbate. The discrepancy between the charge gained by the adsorbates and the charge lost from the Rh surface atoms that the molecules are bound to, is due to small amounts of charge being lost from surrounding Rh atoms on the surface and subsurface layers.

	Species	NO_2	N charge	O charge	O charge	Rh charge
(a)	NO_2^+	+1	+0.93	+0.03	+0.04	-
	NO_2	0	+0.73	-0.34	-0.39	-
	NO_2^-	-1	+0.38	-0.69	-0.69	-
	Rh {111}	-	-	-	-	-0.04
(b)	μ nitrito	-0.43	+0.42	-0.47*	-0.38	+0.15, +0.18
	O-O'-nitrito	-0.46	+0.57	-0.52*	-0.51*	+0.16 x2

* O atom bonded to surface

Table 4.7: (a) The calculated Bader charges (a) for gaseous NO_2 and the Rh surface atoms of the pure surface, and (b) for adsorbed NO_2 on the Rh {111} surface, and the Rh atoms they are bound to.

The Bader charges of the individual adsorbate atoms show that the N atom is less positive than the corresponding N atom of gaseous NO_2, gaining 0.31 e for the μ-nitrito mode and 0.16 e for the O-O'-nitrito. The O_s atoms of both adsorption modes are more negative than the O atoms for gaseous NO_2, also showing a gain in charge, with the two O_s atoms of the O-O'-nitrito mode being more negative than the O_s atom of the μ-nitrito mode. The unbound O atom of the μ-nitrito adsorption mode has a charge similar to the gaseous NO_2 species (a difference of 0.01 e). To visualise this charge transfer process, the charge difference is plotted for the μ-nitrito and O-O'-nitrito

adsorption modes in Figures 4.11 (a) and (b), respectively. The charge difference plots show that for both adsorbates, there are areas of charge loss (blue regions) and gain (red regions) around the individual atoms, while the Rh surface atoms predominantly lose charge in the direction of the bond axis. The surface bound atoms for both adsorption modes and the N atom of the O-O-nitrito mode have regions of strong charge density increase, as indicated by the Bader charges. For simple charge transfer, the charge lost from the surface Rh atoms would be expected to increase the charge of the adsorbate in a similar manner to the gaseous NO_2^- species. However as with NO adsorption, this is not the case, as there are both negative and positive regions surrounding the atoms of the adsorbates suggesting that there is a significant change in the σ and π systems of the adsorbate when interacting with the metal surface. This shows that there is considerable redistribution of electron density across the adsorbates upon adsorption on the Rh surface, indicating a more complex mechanism is occurring.

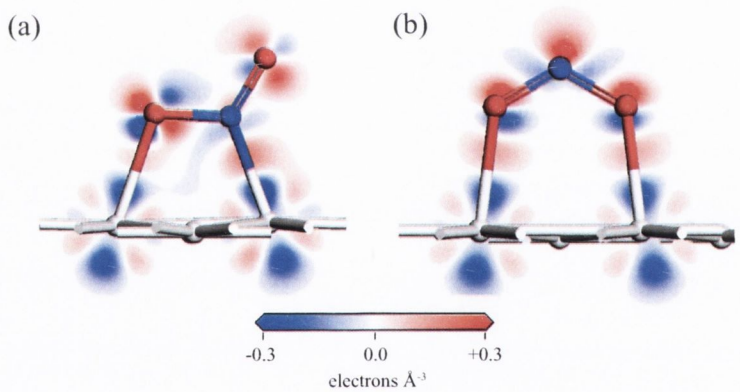


Figure 4.11: The calculated charge density difference of the most stable (a) μ-nitrito and (b) O-O'-nitrito adsorption modes.

In order to further analyse the charge distribution of the NO_2 adsorbates, the electronic structures are investigated. A molecular orbital (MO) diagram and PEDOS for the neutral gaseous NO_2 species and the PEDOS for the most stable μ-nitrito and O-O'-nitrito adsorption modes are shown in Figure 4.12. The MO diagram is simply labelled by the valence molecular orbitals for NO_2, in ascending order of energy are, $4\sigma^{nb}$, $5\sigma^{nb}$, 6σ, 7σ, 1π, $2\pi^{nb}$, $3\pi^*$, $8\sigma^*$ and $9\sigma^*$, where the 'nb' refers to a non-bonding orbital. The

specific labels for symmerty considerations for the bent gaseous NO_2 are omitted for a clearer representation and comparison between the MO diagram and calculated PEDOS plots. NO_2 has 17 valence electrons with one electron occupying the doubly degenerate $3\pi^*$ orbital (HOMO), allowing NO_2 to be a strong π-acceptor/donator similar to NO. The cationic NO_2^+ species thus has no unpaired electrons and the HOMO is the $2\pi^{nb}$ orbital, and for NO_2^- the $3\pi^*$ is half filled. In the PEDOS for gaseous NO_2, the 6σ, 7σ, 1π, $2\pi^{nb}$, $3\pi^*$, $8\sigma^*$ valence orbitals are shown relative to E_{vac} at 0eV, and the vertical dotted line is E_F, which splits the $3\pi^*$ orbital into occupied and unoccupied parts. The $4\sigma^{nb}$ and $5\sigma^{nb}$ orbitals are much lower in energy at -32 eV and -28 eV, respectively, and thus not shown. The 6σ orbital is made up of N $2s$ states mixed with O $2s/p$ states, while the 7σ and 1π orbitals are very close in energy, with their spin up components mixing into one peak at -14 eV. The $7\sigma/1\pi$ orbitals are a mixture of N $2p$ states with O 2 s/p states, and the $2\pi^{nb}$ orbital is composed purely of O $2p$ states. The half-filled $3\pi^*$ HOMO has contributions from the O $2p$ states and N $2p$ states, with the former being more dominant.

The electronic structure for the μ-nitrito and O-O'-nitrito adsorption modes are seen to be different to gaseous NO_2 due to the interaction with the Rh surface. All the orbitals of both adsorbates are stabilised, which for the μ-nitrito adsorbate, causes the 1π orbital to be lower in energy than the 7σ orbital. For the O-O'-nitrito mode the orbitals have the same order as gaseous NO_2 with the 1π orbital splitting into a doublet. The 6σ orbital of the μ-nitrito adsorbate gains N $2p$ states, while losing O $2p$ character from the O atom not bound to the surface. The major contribution to the 7σ orbital of the μ-nitrito mode comes from the N_s atom, and the O atom not bound to the surface, while the 7σ orbital of the O-O'-nitrito adsorbate loses O $2s$ contributions. The top of the valence band, from -12 eV to E_F for both adsorbates is a mixture of the $2\pi^{nb}$ and $3\pi^*$ orbitals, which smear across the energy range. For the gaseous species, these orbitals are dominated by O $2p$ states, with some N $2p$ contribution to the $3\pi^*$ orbital; however, the N $2p$ contribution to this region is absent for the μ-nitrito mode, while for the O-O-nitrito mode some N $2p$ states are present at the top of the VB. The conduction

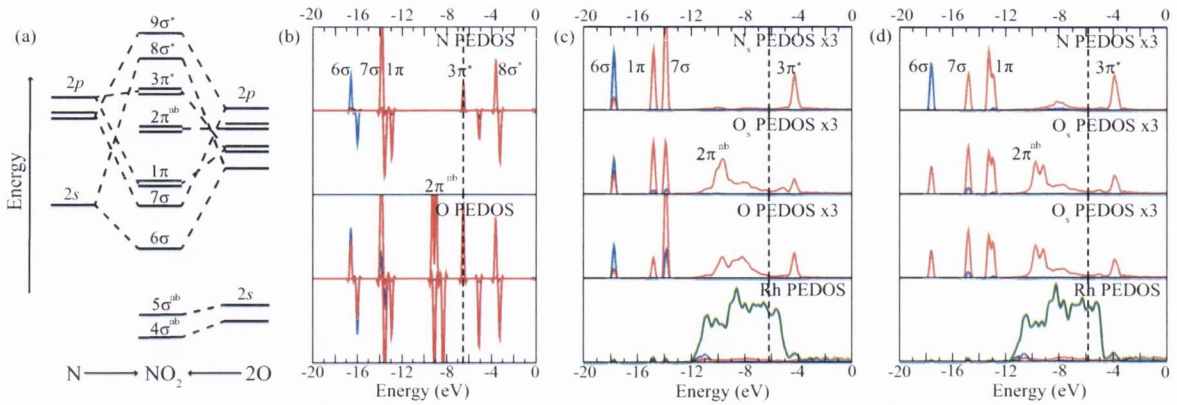


Figure 4.12: (a) The molecular orbital diagram for NO_2. (b) The calculated PEDOS for gaseous NO_2. The calculated PEDOS for the most stable (c) μ-nitrito and (d) O-O'-nitrito adsorption modes on the Rh {111} surface. The N/O PEDOS shown is the single atom species for the adsorbates while the Rh PEDOS is for the top surface atoms. The subscript 's' indicates an atom bound directly to the surface. The blue, red and green lines are the s, p and d states. The E_F is indicated by the dotted line for the adsorption modes and the highest occupied state of the gaseous species. The E_{vac} for the adsorbates on the Rh surface is aligned to 0eV.

band of both adsorbates is dominated by N $2p$ contribution to the unoccupied states of the $3\pi^*$ orbital, reversing the O $2p$ dominance from both O atoms, observed for gaseous NO_2. The position of E_F is reduced to -6.21 eV and -5.83 eV for the μ-nitrito and O-O'-nitrito adsorption modes, respectively, relative to the pure surface (-4.98 eV). This would indicate a increase in the workfunction for both adsorbates, supporting charge donation to both adsorbates; however a larger increase for the μ-nitrito mode would suggest that charge donation is easier than for the O-O'-nitrito mode.

To quantify the changes in the NO_2 electronic structure upon adsorption, the percentage contributions of the N and O $2s/p$ states to the molecular orbitals of gaseous and adsorbed NO_2 were obtained by integrating the PEDOS and are detailed in Table 4.8. The N/O $2s/p$ contributions to the 7σ and 1π orbitals are grouped together in the table, as the 7σ and 1π orbitals are so close in energy that it is hard to distinguish between them for the gaseous NO_2 species. For both adsorbates, the $2\pi^{nb}$ and $3\pi^*_{occ}$ orbitals are smeared together at the top of the valence band, making it difficult to distinguish between their N/O $2s/p$ contributions. The percentage contributions that appear in the table are thus approximated by integrating the states at a similar energy

range to that of gaseous NO_2.

The percentage contributions of the N/O $2s/p$ states to the molecular orbitals show a considerable change in the electronic structure of the μ-nitrito mode relative to gaseous NO_2. Upon adsorption, the increase in charge of the N_s and O_s atoms is reflected by the increase in the N_s and O_s $2s/p$ contributions to the 6σ (N: 14%, O: 3%) and $2\pi^{nb}$ (N: 4%, O: 5%) orbitals. A considerable loss of O $2p$ states to the 6σ (10%) orbital and $2\pi^{nb}$ (12%) is seen, which indicates transfer of density from the unbound O atom to the N_s atom from the electronic redistribution of the μ-nitrito mode interacting with Rh. The contributions to the $7\sigma/1\pi$ system of this adsorbate is relatively unaffected, indicating either small changes or that the redistribution of one orbital, are complimentary to the other. The $2\pi^{nb}$ orbital gains O_s $2p$ character while losing O $2p$ states. The change in the electronic structure from gaseous NO_2 to adsorption on the surface indicates a redistribution of electron density, and that the density donated from the surface is not evenly distributed to the NO_2 adsorbate. The $3\pi^*$ orbital is thus split into bonding and anti-bonding components from the interaction with the surface, causing a redistribution of the charge from the O atom not bound to the surface to the surface bound N_s and O_s atoms. The interaction of the NO_2 molecule with the Rh surface, stabilises the anti-bonding $3\pi^*$ orbital interaction between N_s and O, with a charge redistribution from N_s to O. The interaction reduces the N_s contribution to the $3\pi^*_{occ}$ and transfers the electron density donated from the surface to the unbound O atom of the adsorbate, in a similar manner to that observed for NO adsorption. This is balanced by the transfer of electron density back to the N_s atom through the 6σ orbital accounting for the increased charge of the N atom, and the charge of the O atom being similar to gaseous NO_2. The electronic redistribution of the μ-nitrito adsorption mode on the Rh surface, behaves in a similar manner to a NO adsorbate with an extended bond to an O atom. The orientation of the adsorption mode allows a stronger interaction with the N atom, donating more charge and facilitating breaking of the bond parallel to the surface to NO and O.

For the O-O'-nitrito mode, the change in the electronic structure is not as pro-

nounced as the μ-nitrito mode. The 6σ orbital is largely unaffected, with only small changes in its composition relative to gaseous NO_2. The N $2p$ contributions to the $7\sigma/1\pi$ system decreases (5%) with the O $2s$ states increasing (4% each) when interacting with the Rh surface. The $2\pi^{nb}$ orbital gains N $2p$ contribution (6%), and loses O $2p$ character (5% each), while the occupied states of the $3\pi^*$ orbital show only small deviations relative to gaseous NO_2. The direct interaction of the O_s atoms with the Rh surface through the $7\sigma/1\pi$ system accounts for their increase in charge, while the increased charge for the unbound N atom is reflected in the increase in N contributions to the 6σ and $2\pi^{nb}$ orbitals. The occupied states of the $3\pi^*$ orbital are relatively unaffected compared to the $3\pi^*_{occ}$ orbital contributions for gaseous NO_2. There are however, more significant changes to the unoccupied components of the $3\pi^*$ orbital, as there is a large increase in the N contribution to this orbital with lesser contributions from the O atoms, compared to gaseous NO_2. This indicates that on interaction, the surface charge density donation occupies the O $2p$ states reducing their contribution to the $3\pi^*_{unocc}$, and the electronic redistribution alters the N contribution to the $3\pi^*_{unocc}$ orbital, suggesting charge transfer from the N $2p$ states to the O atoms.

From the analysis of the Bader charges, the charge density difference plots, and the changes in the orbital contributions it is clear that there is a redistribution of the electron density for NO_2 adsorption on Rh. The overall Bader charges show that there is charge transfer from the Rh surface to both of the adsorbates; however the breakdown of the individual charges suggests that there is a rearrangement of the σ and π bonding within the adsorbate, which can also be seen on the charge difference plots.

The change in the electronic structure for the O-O'-nitrito mode is relatively straight forward. The orbitals are stabilised on adsorption with insignificant changes to the 6σ and $3\pi^*_{occ}$ orbitals. The increase in charge for the O_s atoms can be accounted for by the redistribution of density for the $7\sigma/1\pi$ system from direct interaction with Rh atoms, while the charge gained by the N atom is from the increase in contribution to the $2\pi^{nb}$ orbital. The redistribution of charge for the μ-nitrito mode is considerably greater than the O-O'-nitrito mode following interaction with the Rh surface, indicating

	$NO_{2\,(g)}$				
States	6σ	$7\sigma/1\pi$	$2\pi^{nb}$	$3\pi^*_{occ}$	$3\pi^*_{unocc}$
N $2s$	27	0	0	8	7
N $2p$	1	38	0	24	27
O $2s$	21	4	0	0	0
O $2p$	15	27	50	34	33
O $2s$	21	4	0	0	0
O $2p$	15	27	50	34	33
	μ-nitrito				
States	6σ	$7\sigma/1\pi$	$2\pi^{nb}$	$3\pi^*_{occ}$	$3\pi^*_{unocc}$
N_s $2s$	35	0	0	2	4
N_s $2p$	7	39	5	7	38
O_s $2s$	21	3	2	0	1
O_s $2p$	12	23	55	36	28
O $2s$	20	6	0	0	0
O $2p$	5	29	38	55	27
	O-O'-nitrito				
States	6σ	$7\sigma/1\pi$	$2\pi^{nb}$	$3\pi^*_{occ}$	$3\pi^*_{unocc}$
N $2s$	31	1	2	8	1
N $2p$	7	32	6	25	40
O_s $2s$	18	2	1	2	1
O_s $2p$	17	31	45	32	28
O_s $2s$	18	2	1	2	1
O_s $2p$	17	31	45	32	28

Table 4.8: The approximate percentage contributions of N $2s$, N $2p$, O $2s$ and O $2p$ states to the molecular orbitals of gaseous NO_2 and the μ-nitrito and O-O'-nitrito adsorption modes on the Rh{111} surface.

a more complex mechanism. The O atom of the μ-nitrito mode that is not bound to Rh has much less O $2p$ contribution to these orbitals than the O_s atoms of the O-O'-nitrito mode, with the exception of the $3\pi^*_{occ}$ where there is a significant increase (23%). The interaction of the Rh surface with the N atom allows the stabilisation of the $3\pi^*$ antibonding orbital in a similar manner to NO. This reduces the N contribution

and transfers the surface donation to the O atom not bound to the surface, explaining its significant increase in density over the O-O'-nitrito mode. The surface/adsorbate treatment of the μ-nitrito mode to behave like NO with an elongated bond to O may explain its increased stability over the O-O'-nitrito mode.

4.2.7 N_2 and O_2 adsorption on the Rh {111} surface

The most stable adsorption modes for N_2 and O_2 were explored on the Rh {111} surface by trialling the different molecular orientations, perpendicular and flat on the surface, across the four high symmetry adsorption sites. A number of configurations were thus examined and relaxed, with the most stable configuration for N_2 and O_2 adsorption shown in Figure 4.13. The N_2 molecule is shown to prefer adsorption perpendicular to the top site on the Rh surface, while the preferential adsorption mode for O_2 was calculated to be flat across a hcp hollow site to top and bridge sites. The E_{ads} for the most stable adsorption modes for N_2 and O_2 were calculated to be -0.58 eV and -1.49 eV, respectively, while the metal surface was found to quench the molecular spin of both adsorbates to zero. On adsorption, the molecular bonds for N_2 and O_2 were calculated to be 1.13 Å and 1.43 Å, respectively, showing a lengthening and weakening from the calculated bonds for gaseous N_2 (1.12 Å) and O_2 (1.23 Å). The N-Rh bond was calculated to be 1.91 Å while for the O_2 adsorbate, the bonds at the bridge site were calculated to be 2.11 Å and 1.97 Å at the top site. The calculated values indicate that the O-O bond is elongated further than the N-N bond on adsorption, indicating that the O-O bond of the adsorbate becomes much weaker than the N-N when interacting with the Rh surface. The calculated vibrational frequencies for the N_2 adsorption mode is 2231 cm^{-1} which has decreased from the calculated vibrational frequencies for gaseous N_2 (2425 cm^{-1}) and the experimental value of 2359 cm^{-1}. For the O_2 adsorption mode, the calculated vibrational frequencies are 723 cm^{-1}, 477 cm^{-1} and 384 cm^{-1}, while in the gas phase it has only one vibrational mode which was calculated to be 1566 cm^{-1} close to the experimental gaseous value (1580 cm^{-1}).

The Bader charges were calculated for the most stable adsorption modes of N_2 and

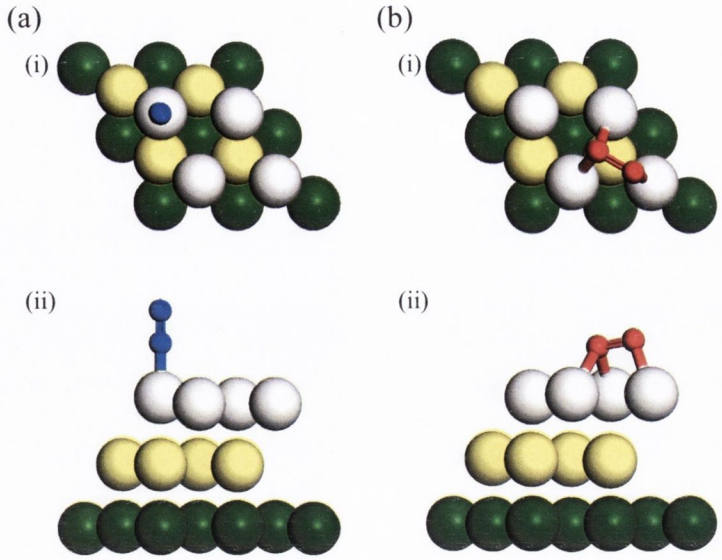


Figure 4.13: The calculated most stable adsorption modes for (a) N_2 and (b) O_2 on the Rh {111} surface.

O_2 on the Rh {111} surface. The overall Bader charges show that there is an increase in charge of -0.18 and -0.65 for the N_2 and O_2 adsorbates, respectively, forming anionic $N_2^{\delta-}$ and $O_2^{\delta-}$ species on the surface. The breakdown of the charges show that the surface bound N atom gains charge (-0.26 e) and the N atom not bound to the surface loses charge (+0.08 e), while the Rh surface atom also lose charge (+0.18 e). For the O_2 adsorption mode, both O atom bonded to the surface gain charge (-0.35 and -0.30 e) whereas the Rh atoms at the bridge site lose charge (+0.17 e x2) and also at the top site (+0.23 e). Both adsorbates gaining charge and the Rh surface atoms losing charge indicates a charge transfer process from the surface to each adsorbate, in a similar manner to the atomic species on the surface. The charge transfer mechanism however, appears to be different for each adsorbate. The N atom bound to the surface gains a greater charge than that donated by the surface, while the N atom not bound to the surface loses charge. This indicates that the N atom bound to the surface gains charge from both the Rh metal surface atom and the other N atom. The charge transfer mechanism for O_2 is not as complicated as the N_2 adsorbate, since the charge gained by both O is accounted for by the charge lost from the metal surface atoms they are bound to, and surrounding surface atoms (around 0.08 e).

The calculated charge difference plots for the most stable adsorption modes of N_2 and O_2 on the Rh {111} surface are shown in Figure 4.14. On adsorption, the charge difference plots show areas of increased charge (red regions) and decreased charge (blue regions) around the adsorbates and surfaces. This indicates that there is a change to the σ and π systems of the adsorbates, with a redistribution to their electronic structure through interaction with the Rh surface. For the N_2 adsorbate, there is charge donated from the surface to the N atom bound to the surface, while the N atom not bound to the surface is seen to lose charge along the direction of the bond (σ direction), supporting the Bader charges. The plot also indicates that there is a gain in charge for the π system that is perpendicular to the bond axis. The charge difference plot for O_2 shows that there is charge donated from the surface along the bonds to the O_2 adsorbate with some loss in charge along the bond axis.

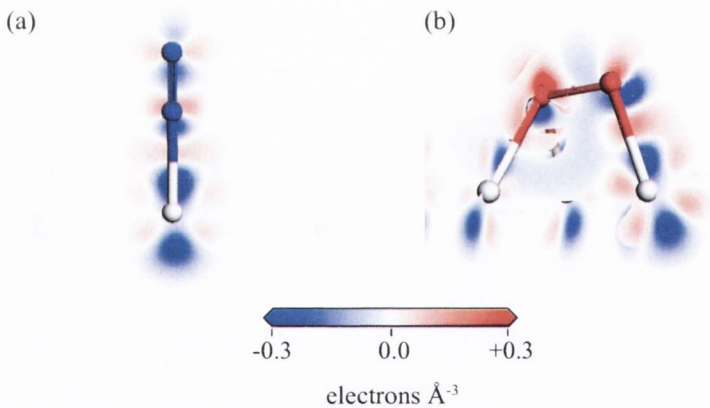


Figure 4.14: The calculated charge difference plots (electrons Å^{-3}) for the most stable adsorption modes of (a) N_2 and (b) O_2 on the Rh {111} surface.

To further asses the electronic structure for the interaction of the N_2 and O_2 molecules with the Rh surface, the molecular orbital (MO) diagram for the N_2 and O_2 species, the calculated PEDOS for the gaseous species and the most stable adsorption mode on the Rh surface, are shown in Figure 4.15. The valence MOs in increasing energy for N_2, are usually labelled 3σ, $4\sigma^*$, 1π, 5σ, $2\pi^*$ and $6\sigma^*$, as shown in the molecular orbital diagram (Figure 4.15 (i)); however for the MO diagram of O_2 the 1π orbital is lower in energy than the 5σ. The position of the occupied $4\sigma^*$, 5σ and 1π

molecular orbitals in the PEDOS for N_2 and O_2 are shown in Figures 4.15 (a) (ii) and (b) (ii), respectively, relative to the vacuum level, with the 3σ lower in energy (around -30 eV) and not shown. The HOMO for the N_2 adsorbate is the 5σ orbital being fully filled, while for O_2 the HOMO is the doubly degenerate $2\pi^*$ molecular orbital with two unpaired electrons. The difference in the nature of the HOMO orbital may explain the different geometries on the Rh surface, N_2 preferring a σ orientation whereas the O_2 species prefers a π bonded configuration. For the N_2 PEDOS, the $4\sigma^*$ has a strong contribution from N $2s$ and a minor amount of N $2p$ states, while the 1π is composed of N $2p$ and the 5σ has a major contribution from the N $2p$ with some N $2s$ states. A similar mixing of O $2s$ and $2p$ states and contributions to the different orbitals of O_2 is seen in the PEDOS.

On adsorption with the Rh surface, a shift in contributions to the orbitals is observed for the N_2 adsorbate can be seen on the PEDOS plot, indicating an electronic redistribution on interaction with the surface as shown in the charge different plots, and calculated Bader charges. All the orbitals appear to lower in energy when interacting with the Rh surface, in particular the $4\sigma^*$ orbital compared to the gasous species. The $4\sigma^*$ and 1π orbitals are seen to gain N $2p$ character from the N atom bound to the surface, while the main N $2s/p$ contribution to 5σ orbital is from the N atom not bound to the surface. The presence of unoccupied N $2p$ states contributing to the $2\pi^*$ orbital shows that the orbital is not fully filled. The charge donation from the surface to the adsorbate should occupy the 2π orbital, reflected in the presence of N $2p$ states below E_F interacting with the Rh $4d$ band; however the absence of N $2p$ states at the top of the VB suggests that a more complicated mechanism is occurring. This mechanism of interaction between N_2 and the Rh surface is similar to NO and NO_2 adsorbates, indicating that the N-N antibonding $2\pi^*$ orbital is stabilised, reducing the N states at the top of the valence band. This leads to charge donation from the surface to the unbound N atom, with a back donation through the σ bond to the N atom bound to the surface.

The interactions of O_2 with the Rh surface are not as complicated as N_2. The

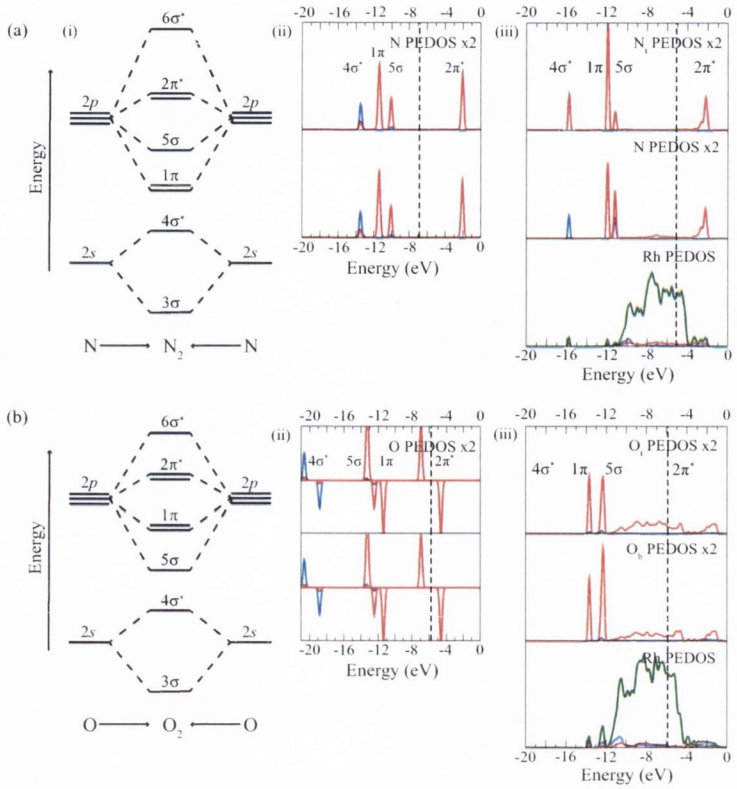


Figure 4.15: The calculated PEDOS for the most stable adsorption modes for (a) N_2 and (b) O_2 adsorption on the Rh {111} surface.(i) The molecular orbital diagram, (ii) PEDOS of the gaseous species and (iii) PEDOS of the adsorbate. The blue, red and green lines indicate the s, *p* and *d* states, respectively. The dotted line indicates the position of the E_F on the hcp adsorption mode and the highest occupied state on the gas phase species. The graph of the hcp adsorption mode is aligned to the E_{vac} at 0 eV. The 't' and 'b' subscripts indicate the top and bridge adsorption sites that the atoms are bound to.

orbitals are lowered in energy compared to gaseous O_2, in a similar manner to N_2 adsorption. The O $2s/p$ state contributions to the orbitals appear unchanged from the gaseous species. The presence of O $2p$ state contributions to the $2\pi^*$ orbital at the top of the valence band, are not only from the already half filled orbital but can also be attributed to the charge donation from the Rh surface as indicated by the Bader charges.

4.2.8 Decomposition profile

The calculated energy profile for the NO_x decomposition pathway on the Rh {111} surface are detailed in Table 4.9. The energetics of each step were calculated using the energies of the most stable adsorption modes for N, O, N_2, O_2, NO and NO_2 on Rh, and the energies of their respective gaseous species. The calculated energies for each step of the dissociation of NO_x on the Rh surface can also be summarised graphically in Figure 4.16. The values detailed in the table and figure relate to the change in enthalpy (ΔH) at 0K, without any entropic considerations. The contribution of entropy (S) to the overall change in gibbs free energy (ΔG) would be significant at higher temperatures (T) according to the following relationship; $\Delta G = \Delta H - T\Delta S$, so that increasing the entropy of the system decreases ΔG, allowing the reaction to more readily occur. The calculations are carried out at 0K so that the $-T\Delta S$ term is 0. The change in the energies presented can therefore be related to the gibbs free energy so that $\Delta G = \Delta H$, indicating that a negative change in energy is $-\Delta G$ and the reaction is spontaneous, while a positive change in energy is $+\Delta G$ indicating that the reaction step requires energy in order to proceed. All reaction profiles in subsequent sections are calculation in a similar manner.

The overall calculated energy for $NO_{(g)}$ and $NO_{2(g)}$ to $N_{2(g)} + O_{2(g)}$ was calculated to be -0.95 eV and +0.22 eV, respectively. The calculated energy for the NO process is very close to the experimental value of -0.94 eV; however for NO_2 this is not as accurate to the experimental value (-0.35 eV) due to the overestimated DFT-calculated binding energy of O_2 with respect to experiment.[361–365]

The adsorption and dissociation energies for NO_x on the Rh surface are found to be exothermic. The lower dissociation energy for NO_2 to NO and O on the Rh surface (-1.53 eV) indicates that this step is more thermodynamically favourable on Rh, than the dissociation of NO to N and O on the Rh surface (-0.81 eV). The breakdown of NO_2 has been observed to be facile on other metal surfaces including rhodium; however the subsequent breakdown of NO is suggested to be the more difficult step for the *de*NO_x

		Reaction Step	Energy (eV)
(a)		$NO_{2(g)} \rightarrow \frac{1}{2}N_{2(g)} + O_{2(g)}$	+0.22
		$NO_{(g)} \rightarrow \frac{1}{2}N_{2(g)} + \frac{1}{2}O_{2(g)}$	-0.96
(b)	(i)	$NO_{2(g)} \rightarrow NO_{2(ads)}$	-1.76
	(ii)	$NO_{2(ads)} \rightarrow NO_{(ads)} + O_{(ads)}$	-1.53
	(iii)	$NO_{(ads)} + O_{(ads)} \rightarrow N_{(ads)} + 2O_{(ads)}$	-0.84
	(iv)	$N_{(ads)} + 2O_{(ads)} \rightarrow \frac{1}{2}N_{2(ads)} + 2O_{(ads)}$	+0.04
	(v)	$\frac{1}{2}N_{2(ads)} + 2O_{(ads)} \rightarrow \frac{1}{2}N_{2(g)} + 2O_{(ads)}$	+0.29
	(vi)	$\frac{1}{2}N_{2(g)} + 2O_{(ads)} \rightarrow \frac{1}{2}N_{2(g)} + O_{2(ads)}$	+2.54
	(vii)	$\frac{1}{2}N_{2(g)} + O_{2(ads)} \rightarrow \frac{1}{2}N_{2(g)} + O_{2(g)}$	+1.49
(c)	(i)	$NO_{(g)} \rightarrow NO_{(ads)}$	-2.46
	(ii)	$NO_{(ads)} \rightarrow N_{(ads)} + O_{(ads)}$	-0.84
	(iii)	$N_{(ads)} + O_{(ads)} \rightarrow \frac{1}{2}N_{2(ads)} + O_{(ads)}$	+0.04
	(iv)	$\frac{1}{2}N_{2(ads)} + O_{(ads)} \rightarrow \frac{1}{2}N_{2(g)} + O_{(ads)}$	+0.29
	(v)	$\frac{1}{2}N_{2(g)} + O_{(ads)} \rightarrow \frac{1}{2}N_{2(g)} + \frac{1}{2}O_{2(ads)}$	+1.27
	(vi)	$\frac{1}{2}N_{2(g)} + \frac{1}{2}O_{2(ads)} \rightarrow \frac{1}{2}N_{2(g)} + \frac{1}{2}O_{2(g)}$	+0.75

Table 4.9: The calculated energies for (a) the overall breakdown of NO_x, and each step of the (b) NO_2 and (c) NO decomposition pathways on the Rh {111} surface.

process on metal surfaces. The superiority of rhodium over other metals has been reported to be the more facile breakdown of NO, which here we show to be exothermic, compared to the breakdown being endothermic and unfavourable on Pd and Pt.[366] The exothermic and favourable breakdown of NO on Rh can be explained by the greater stability of N atoms on Rh, driving forward the reaction to form N+O on the surface, whereas N adsorption on Pd and Pt is endothermic.

The formation of N_2 from the dissociation N+O products on the Rh surface, requires a small formation energy of only +0.04 eV and the energy required for its subsequent removal is also relatively low (+0.29 eV). This suggests that the difficulty in removing the N and O dissociation products from the Rh surface lies with the formation and removal of O_2 on Rh. The large energy required for these steps is caused by the large E_{ads} of O atoms on the Rh surface. The strong adsorption of O atoms on the Rh

surface also suggests that they are likely to saturate the surface at higher concentrations, hindering any further adsorption and dissociation of NO_x on the surface. This may explain the poor performance of Rh to carry out $de NO_x$ under oxidising conditions, and indicates that the removal of surface bound O atoms is important for the $de NO_x$ process on Rh metal, and indicates that alternative pathways, such as the inclusion of a reductant are required.

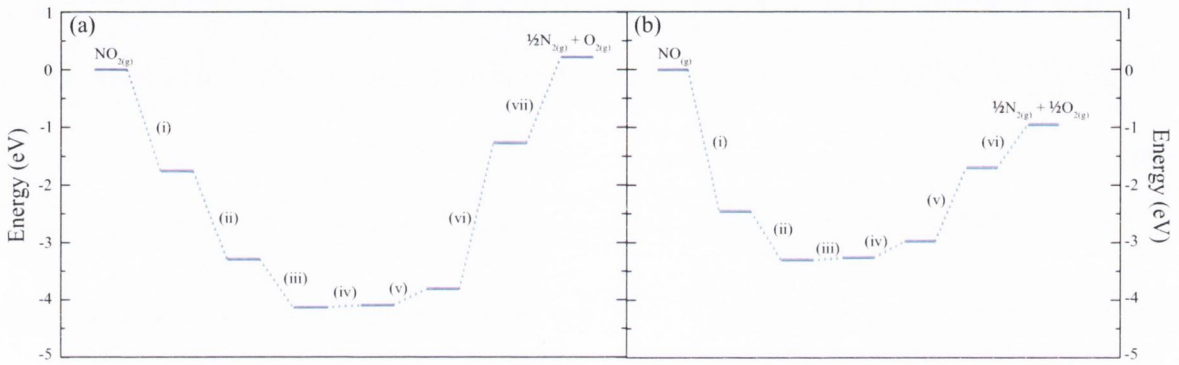


Figure 4.16: The calculated step-wise reaction pathways for the dissociation of (a) NO_2 and (b) NO on the Rh {111} surface. The labels (i) - (vii) relate to the different steps of the profiles outlined in Table 4.9.

4.3 Discussion

There are two proposed mechanisms for charge donation from a metal surface to an adsorbate; (1) the Blyholder model[93] and (2) the more recently proposed allylic configuration.[100–104] The Blyholder model suggests direct charge transfer from the metal surface to the LUMO of the adsorbate, while charge is transferred back from the HOMO of the adsorbate to the metal surface. The Blyholder model has been used to support charge interactions with NO adsorbates on metal surfaces;[94–98] however if direct donation to the anti-bonding $2\pi^*$ orbital is the mechanism as suggested previously,[95, 96] then both N and O $2p$ state contribution to this orbital should be observed for this orbital in the valence band. Previous studies have not separated out the N and O contributions to the $2\pi^*$ orbital. The allylic configuration established by XPS for CO and N_2 on metal surfaces, proposes that the σ interaction of the adsorbate with

the metal surface is stabilised in the bonding region, while the anti-bonding region is stabilised by reducing the interaction of the π^* orbital with the metal d band.[100–104] This is suggested to form a non-bonding state at the top of the valence band referred to as $\widetilde{d}_\pi$.

The electronic structure of the most stable NO and NO_2 adsorbates on the Rh {111} surface was characterised using Bader charge analysis, charge difference plots and PE-DOS. The Bader charge analysis indicates that there is an overall charge donation from the surface to both adsorbates, with the charge difference plots showing a considerable change to the σ and π systems upon interaction of the adsorbates with the Rh surface. The interaction of NO_x molecules with the Rh surface causes a redistribution of electron density within both adsorbates. For NO this interaction stabilises the N-O $2\pi^*$ anti-bonding orbital, reducing the N $2p$ contribution to this orbital, and transferring the donated electron density from Rh to the O atom. A similar stabilisation of the $3\pi^*$ orbital is observed for the interaction of μ-nitrito mode with the Rh surface, indicating that the NO_2 adsorbate behaves like an NO molecule with an elongated bond to an O ad-atom. The absence of N $2p$ contributions to this orbital can been seen at the top of the valence band. Direct donation to the π^* orbital is therefore shown not occur, suggesting that the Blyholder model does not hold for NO_x adsorption on the Rh {111} surface. The electronic rearrangement of the σ and π systems, along with the stabilisation of the anti-bonding orbitals would suggest that a more complicated mechanism is occurring, similarly to that proposed by the allylic configuration. The electronic structure for NO_x on Rh is closely related to the allylic configuration as; (1) the 5σ for NO, and 1π for NO_2 are greatly stabilised on the rhodium surface compared to gaseous NO_x, and (2) the $2/3\pi^*$ orbitals are stabilised and dominated by O $2p$ states at the top of the valence band. This can be linked to the non-bonding electron pair, which interacts with the Rh $4d$ states giving the $\widetilde{d}_\pi$ band, a filled state at the top of the VB similar to N_2 and CO.

The analysis of the adsorbates electronic structure, and the calculated *de*NO$_x$ profile in this study provides an insight into the use of Rh metal as a catalyst within *de*NO$_x$

technologies. The selectivity of the Rh surface for producing N_2 and other organo-nitro species under rich conditions (excess fuel) may be explained by the favourable interaction of the Rh surface with N atoms. The most important aspect of our study is that it finds the breaking of the NO bond is exothermic and favoured, supporting suggestions that this is the reason why Rh metal is efficient at $de\mathrm{NO}_x$.[70, 71] In order for alternative $de\mathrm{NO}_x$ catalysts to emulate the properties of Rh metal, they would therefore have to be exothermic and favour the breaking the NO bond, while also having a strong interaction with N and O atoms. This is an important attribute of Rh metal as under rich conditions it is difficult to form N_2 in the presence of excess hydrocarbons.[367]

The strong interaction of the O ad-atoms with the Rh surface will most likely cause the saturation of the surface with O atoms, when a high oxygen concentration is present. This will lead to deactivation of the catalyst, hindering any further $de\mathrm{NO}_x$; however this may also be beneficial to Rh as a three-way catalyst, as the O surface species are more likely to remain in their adsorption site and unlikely to form O_2. This will allow the easy oxidation of a reductant such as CO or H_2; however under lean conditions (excess oxygen) the excess O may inhibit NO_x breakdown, explaining why Rh can be inefficient under lean conditions.[25, 68, 367, 368] The facile removal of surface O ad-atoms from the Rh surface using a reductant such as CO or H_2 will allow regeneration of the catalyst and assist in further breakdown of NO_x. For NO_x storage-reduction catalysts, lean-trap NO_x and selective catalytic reduction of NO_x, the strong interaction of O with the surface would allow activation of fuel hydrocarbons, forming a $\mathrm{C}_x\mathrm{H}_y\mathrm{O}_z$ intermediate species, which has been suggested to assist in the $de\mathrm{NO}_x$ process.[369–371]

4.4 *De*NO$_x$ chemistry on the Pd and Pt {111} surfaces

4.4.1 Pd/Pt metal bulks and {111} surfaces

Similarly to Rh, Pd and Pt bulk metals adopt an fcc lattice, and the structural optimisation is carried out on the reduced unit cell. The structural optimisations were performed at a series of volumes, allowing the atomic positions to relax, while the total volume was held constant. The equilibrium lattice parameters for the bulk metals were determined using Γ-centred k-point sampling grids at an energy cut-off of 400 eV in a similar manner to bulk Rh metal. The resulting energy volume curves at the different k-point densities were fitted to the Murnaghan equation of state[359] to obtain the minimum energy structure. Sufficient convergence for the minimum bulk Pd and Pt metal structures was found when the forces were relaxed to within 0.01 eV/Å, using a Γ-centred k-point sampling grid of 15x15x15 and a plane wave energy cut-off of 400eV. The lattice parameters of the relaxed Pd and Pt structures were 3.939 and 3.968 Å, respectively, which are 1.23% and 1.11% larger than the experimental structures[372, 373]

4.4.2 Pd/Pt {111} surfaces

The relaxed structure of the Pd and Pt {111} surfaces, with the high symmetry adsorption sites labelled (top, bridge, fcc and hcp) are shown in Figure 4.17(a) and (b), respectively. The Pd-Pd distance for atoms in a metal layer and between layers, was calculated to be 2.79Å while for Pt this was calculated to be 2.81Å and 2.82Å , respectively. The PEDOS of the topmost surface layer and the middle of the metal slab (bulk) for Pd and Pt are shown in Figures 4.17(c) and (d), respectively. The PEDOS plots are aligned to the vacuum energy (E_{vac}) at 0 eV and the relative position of the Fermi level (E_F) is indicated by the dotted line. For both surfaces, all states lower than E_F are occupied while those states of energy higher than E_F are unoccupied. The higher E_F

for the Pd surface (-5.09 eV) suggests that donation to adsorbed species maybe easier than on the Pt surface (-5.54 eV) with the calculated position of E_F being similar to the experimental values. The PEDOS plots show that the Pd 4*d* band is narrower and has a large proportion of states close to E_F compared to the Pt 5*d* band. The higher concentration of metal *d* states at the top of the valence band for the Pd {111} surface may suggest that charge donation from the surface to an adsorbate is easier than for Pt.

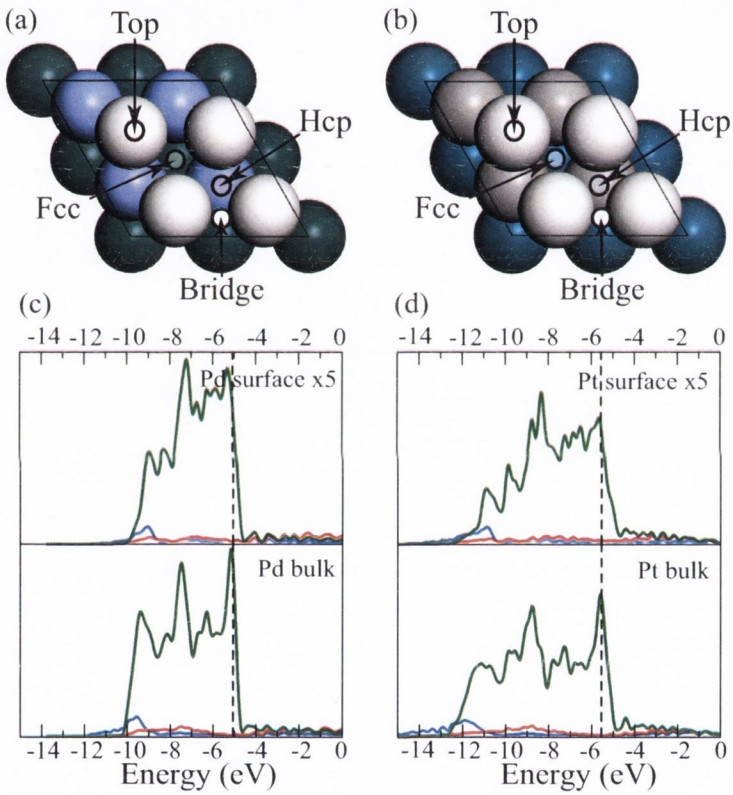


Figure 4.17: The structure of the (a) Pd and (b) Pt {111} surfaces with the adsorption sites labelled. The PEDOS for the top layer atoms of the {111} surface and bulks for Pd and Pt are shown in (c) and (d), respectively. The PEDOS plots are aligned to the vacuum energy at 0 eV and the Fermi level is indicated by the dotted line. The blue, red and green lines are the *s*, *p* and *d* states, respectively.

4.4.3 Nitrogen adsorption modes and analysis

Nitrogen adsorption was investigated on the four high symmetry sites (top, bridge, hcp, fcc) of the Pd and Pt {111} surfaces to determine the most stable adsorption mode.

The adsorption energies (E_{ads}), coordination number (CN), and bond distances for each of the adsorption modes are detailed in Table 4.10. The calculated E_{ads}, determined relative to N_2, indicate that N adsorption is endothermic on all sites for each metal, with the low coordinated top and bridge sites being less stable than the three-fold hollow sites, as detailed in Table 4.10. The positive adsorption energies indicates that N adsorption is endothermic on Pd and Pt, which is not surprising due to the large energy associated with a N_2 bond. Of these three-fold hollow sites, the fcc site was calculated to be the most stable, with a lower adsorption energy on Pt. The spin of the N adsorbates were quenched to 0 by the metal surfaces.

Surface	Site	CN	E_{ads} (eV)	M-N (Å)	N charge	M charge
Pd {111}	top	1	+3.62	1.79 (x1)	-0.34	+0.25 (x1)
	bridge	—	(fcc site)	—	—	—
	hcp	3	+1.12	2.01 (x3)	-0.52	+0.21 (x3)
	fcc	3	+1.02	2.01 (x3)	-0.56	+0.21 (x3)
Pt {111}	top	1	+3.35	1.79 (x1)	-0.28	+0.32 (x1)
	bridge	2	+1.82	1.94 (x2)	-0.47	+0.24 (x2)
	hcp	3	+1.14	2.01 (x3)	-0.53	+0.19 (x3)
	fcc	3	+0.91	2.01 (x3)	-0.56	+0.21 (x3)

Table 4.10: The adsorption energies calculated realtive to $N_{2(g)}$ (E_{ads}), coordination number (CN), M-N bond lengths and Bader charges for the different nitrogen adsorption modes on the Pd and Pt {111} surfaces. The number of bonds for each adsorbate on a high symmetry site is also included.

The calculated Bader charges for the adsorption sites of each metal are detailed in Table 4.10. The negative charges for the adsorbates indicate an increase in electron density, while the positive charges for the metal surface atoms coordinated to the N adsorbate shows a decrease in charge. This indicates that the N adsorbates on both surfaces gain electron density from the metal surfaces which increases with the increasing coordination of each adsorption site, and both surfaces are seen to donate similar charge to the adsorbates. The greatest charge donated is associated with the most stable site forming anionic $N^{\delta-}$ species on the Pd and Pt surfaces. The redistribution

of charge can be visualised by the calculated charge difference plots for the most stable N adsorption site (fcc) on the Pd and Pt surfaces, shown in Figure 4.18 (a) and (b), respectively. The plots are constructed by taking the difference in the charge density between the adsorbate on the metal surface and the charge density of the clean surface and gaseous adsorbate. The red regions show an increase in electron density, while the blue regions show a decrease in electron density, as indicated by the scale in Figure 4.19. These plots show that a positive increase in electron density is located around the N atoms while a decrease in electron density is seen on the surface metal atoms. The charge lost from the metal Pd and Pt atoms to the N adsorbates can been seen to occur along the bond axis. The N adsorbates gaining charge and the metal surface atoms losing charge is in support of the Bader charges.

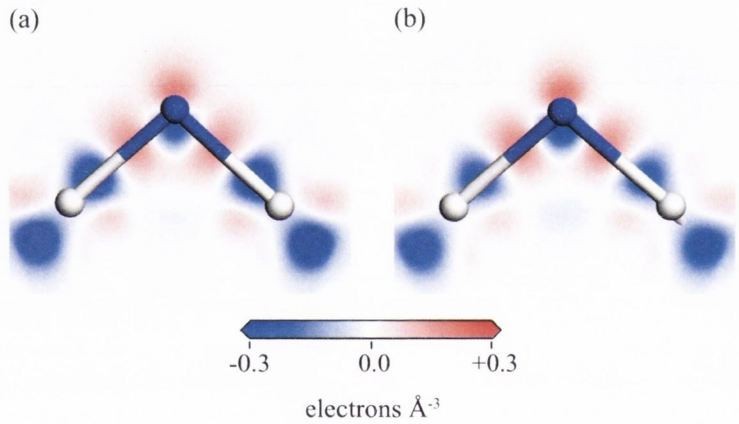


Figure 4.18: The calculated charge density difference of an adsorbed nitrogen atom on the (a) Pd and (b) Pt {111} surfaces. The charge difference ranges from -0.3 (blue) to +0.3 (red) electrons Å^{-3}, as indicated by the scale.

As adsorption at the fcc site was the most stable, a PEDOS was calculated to provide the electronic structure of the N adsorbate interacting with the metal surface given in Figure 4.19 (a) and (b) for Pd and Pt, respectively. The primary difference between the two systems appears at the bottom of the valence band, between -12 to -10 eV. The PEDOS for the N adsorbate on the Pd surface has three distinct peaks, while only one peak is observed for the corresponding range on Pt. This may be caused by the structure of the metal d band as the Pt metal d band is dispersed over a larger energy

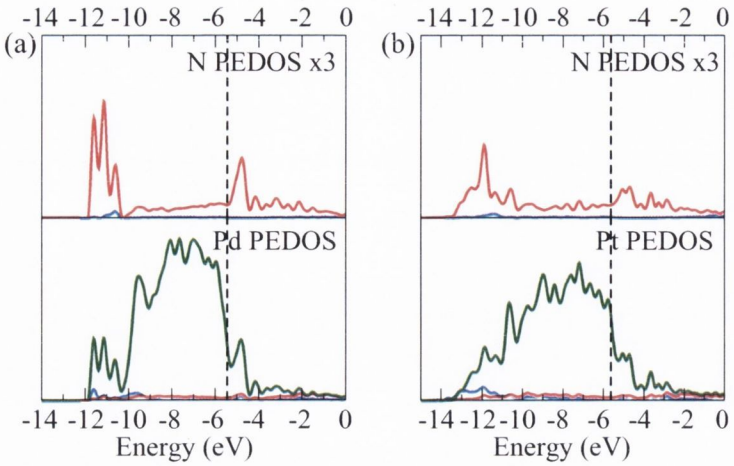


Figure 4.19: The PEDOS for a single N atom on the fcc site of (a) Pd and (b) Pt {111} surfaces. The Pd and Pt PEDOS shows the mixing of states for the topmost layer of each surface. The blue, red and green lines are the *s*, *p* and *d* states, respectively. The Fermi level (E_{F}) is indicated by the dotted line and the vacuum energy (E_{vac}) is aligned to 0 eV.

range, while the Pd *d* band is narrower. The interaction between the N adsorbate and Pt surface will thus disperse the states across the energy range while the peaks are sharp for the narrow Pd interaction. Both systems have occupied N $2p$ states mixing with metal *d* states up to E_F, possibly from the charge transfer from the surface to the N adsorbate. The presence of N $2p$ states in the conduction band indicates that they are not fully occupied with a single large peak for N on the Pd near E_F, while for N on the Pt surface this is a split doublet peak. The E_{F} of the adsorbed system can be seen to decrease on both metal surfaces compared to the pure surface, from -5.09 eV to -5.55 eV on Pd and -5.54 eV to -5.64 eV on Pt. The decrease in the E_{F} indicates charge transfer from the surface to the N adsorbate, with the lowest E_F associated with N on Pt. This may indicate that charge donation is easier on Pt and suggesting a reason for the greater stability of N on Pt than Pd.

4.4.4 Oxygen adsorption modes and analysis

Oxygen adsorption was also simulated on the high symmetry sites on the Pd and Pt {111} surfaces to determine the lowest energy adsorption mode in a similar manner to

N adsorption. The E_{ads}, coordination number (CN), bond distances and Bader charges for O adsorption on each of the sites on the Pd and Pt surfaces are detailed in Table 4.11. Oxygen was found to adsorb endothermically and thus requires energy to adsorb on the top sites of both surfaces and the bridge site of Pt. The details for O adsorption on the bridge site for Pd is absent, as this was found to be unstable, relaxing to the fcc site. The top and bridge sites on each surface are less stable than the more highly coordinated three-fold hollow sites, with O adsorbing exothermically on these sites as detailed in Table 4.11. Of the three-fold hollow sites, the fcc site was found to possess the greatest stability on both the Pd and Pt surfaces, with the greater stability for O on Pd. The metal-oxygen bond distance are seen to increase with the increased coordination of the adsorption site. All adsorption modes were found to favour an overall spin of 0, as the atomic spin was quenched by the metal surfaces.

Surface	Site	CN	E_{ads} (eV)	M-O (Å)	O charge	M charge
Pd {111}	top	1	+0.33	1.79 (x1)	-0.54	+0.33 (x1)
	bridge	—	(fcc site)	—	—	—
	hcp	3	-1.17	2.01 (x3)	-0.65	+0.22 (x3)
	fcc	3	-1.36	2.01 (x3)	-0.65	+0.23 (x3)
Pt {111}	top	1	+0.88	1.79 (x1)	-0.50	+0.37 (x1)
	bridge	2	+0.01	1.94 (x2)	-0.60	+0.25 (x2)
	hcp	3	-0.20	2.01 (x3)	-0.63	+0.21 (x3)
	fcc	3	-0.64	2.01 (x3)	-0.65	+0.22 (x3)

Table 4.11: The adsorption energies calculated realtive to $O_{2(g)}$ (E_{ads}), coordination number (CN), M-O bond length and Bader charges for the different oxygen adsorption modes on the Pd and Pt {111} surfaces. The number of bonds for each site is also indicated for the bond lengths and M charges in the Table.

The Bader charges indicated in Table 4.11 are calculated relative to atomic O, with the charge increasing for the adsorbate and decreasing per metal surface atom for the increasing coordination of the adsorption site. The Bader charges indicate that the O atoms are negative, gaining charge, while the metal surface atoms are positive, loosing charge, for all adsorption modes on both surfaces. This shows that both surfaces

donate electronic density to the O adsorbates, forming $O^{\delta-}$ species on Pd and Pt, with the greatest amount of charge donated from the most stable fcc site. This explains its increased stability over the other adsorption modes. To show the redistribution of charge for the O adsorbates on the metal surfaces, the charge difference plots were calculated and are shown in Figures 4.21 (a) and (b), respectively. These plots show that positive (red) regions are located around the O atoms and negative (blue) regions are located on the metal surface atoms, indicating that electron density is donated from the metal surface atoms to the O adsorbate, supporting the Bader charges, similarly to N adsorption.

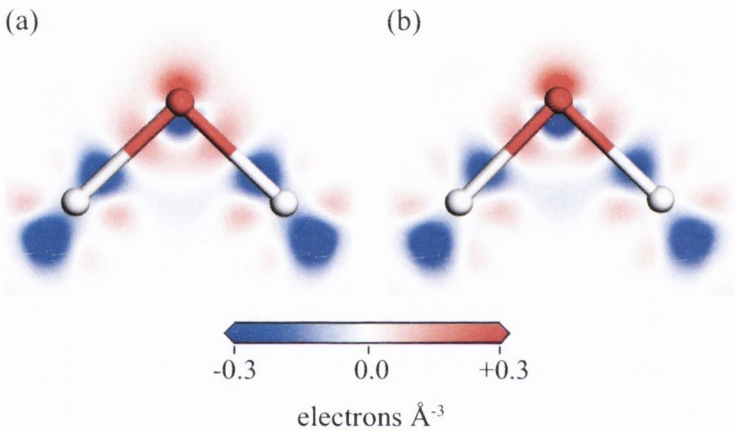


Figure 4.20: The calculated charge density difference of an adsorbed oxygen atom on the (a) Pd and (b) Pt {111} surfaces. The charge difference ranges from -0.3 (blue) to +0.3 (red) electrons $Å^{-3}$, as indicated by the scale.

The calculated PEDOS of the most stable site for O adsorption (fcc site) on the Pd and Pt surfaces are shown in Figures 4.21 (a) and (b), respectively. The electronic structure of the O adsorbate interacting with the metal surfaces is quite similar to N adsorption on Pd and Pt (Figure 4.19), as there is a range of three distinct peaks between -12 and -10 eV for O on Pd, while for O on Pt three peaks are more dispersed between -14 eV and -9.5 eV. The dispersed states from the interaction of O and Pt may be caused by the broader metal *d* band for Pt, thus causing a weaker interaction than observed for O on Pd. The occupied O 2*p* states up to E_F for both systems mix with the metal *d* bands, and their presence may account for the charge donated to the O

adsorbates for both surface. The presence of unoccupied O $2p$ states above E_F shows that the O $2p$ states are not fully occupied. E_F is lowered for the adsorption of O on Pd (-5.55 eV) compared to the pure Pd surface (-5.09 eV), and similarly for O on Pt (-5.78 eV) compared to the pure Pt surface (-5.54 eV). The lower position of E_F for O on Pd suggests that greater surface donation can occur, and may suggest a reasoning for its greater stability compared to O on Pt.

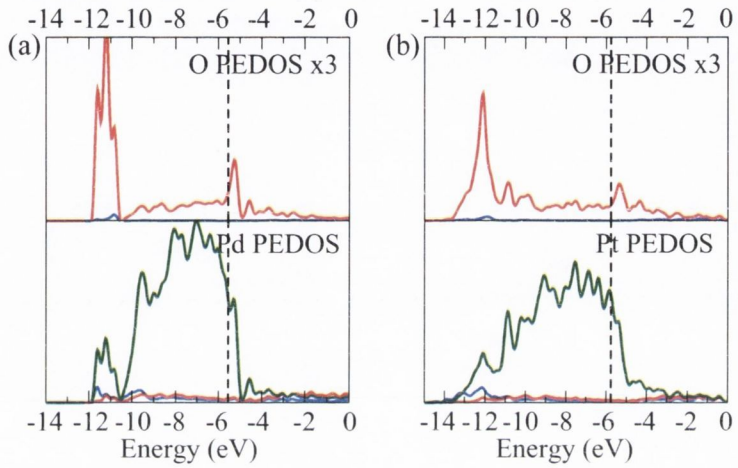


Figure 4.21: The PEDOS for oxygen adsorption on the fcc site of the (a) Pd and (b) Pt {111} surfaces. The blue, red and green lines are the s, p and d states, respectively. The E_F is indicated by the dotted line and E_{vac} is aligned to 0 eV.

4.4.5 NO adsorption modes and analysis

The adsorption of NO was investigated in a similar manner to N and O adsorption, with E_{ads}, bond lengths, and vibrational frequencies for each of the high symmetry sites, detailed in Table 4.12 for both metals. The E_{ads} values show that the top sites were found to be the least stable, with adsorption being favoured at the three fold hollow sites. The bridge site of the Pt surface was unstable for NO adsorption, with the species moving to the three fold fcc site on relaxation. Of the two three-fold hollow sites, the most stable NO adsorption mode for both Pd and Pt was found to be the fcc site, with NO on the Pd surface being more stable. The M-N and N-O bond lengths increase with increased coordination of the adsorption site. The N-O bond is elongated for the

top (0.02Å), bridge (0.05Å), and three-fold hollow sites (0.06Å), thus weakening the bond upon adsorption on both metals compared to the calculated gas phase N-O bond as indicated in Table 4.12, with the Pt-N surface bonds being longer than the Pd-N bonds. The calculated vibrational frequencies for the high symmetry sites were found to decrease with increased coordination of the adsorption site. For the most stable fcc site on Pd, the calculated vibrational frequency is in good agreement with a HREELS study by Wickham *et al.*[110]; however the calculated value is larger than other studies on Pd[133, 135] by around 40 cm^{-1}. The lower experimental vibrational frequency may be due to external influences such as thermodynamic factors or the surface concentration of NO adsorbates associated with such studies. For Pt, the calculated value is larger than HREELS and IRAS data by around 50 cm^{-1}, which may be caused by a similar reasoning. The ground state electronic configuration for gaseous NO contain spin due to an unpaired electron in the $2\pi^*$ orbital; however, all adsorption sites were found to quench the initial molecular spin of the NO molecule to zero upon interaction with the metal surface.

Surface	Site	E_{ads} (eV)	M-N (Å)	N-O (Å)	Vib (cm^{-1})
	Gas Phase	—	—	1.15	1920
Pd {111}	top	-1.09	1.82 (x1)	1.17	1846
	bridge	-1.96	1.96 (x2)	1.20	1674
	hcp	-2.25	2.03 (x3)	1.21	1583
	fcc	-2.29	2.03 (x3)	1.21	1578
Pt {111}	top	-0.98	1.82	1.17	1858
	bridge	(fcc site)	—	—	—
	hcp	-1.77	2.09 x 3	1.21	1566
	fcc	-1.93	2.08 x 3	1.22	1546

Table 4.12: The adsorption energies (E_{ads}), coordination number (CN), M-O and N-O bond lengths, and vibrational frequencies of NO for the gas phase and high symmetry sites of NO on the {111} surface of Pd and Pt.

The calculated Bader charges for gaseous NO, the pure Pd and Pt surfaces, and

for each of the NO adsorbates on the high symmetry sites of both metals are detailed in Table 4.13. The overall charge of the NO adsorbates is negative, increasing with increased coordination of the adsorption site, while the metal surface atoms are seen to become more positive than the pure surface atoms, indicating a loss in charge. This shows that there is charge transfer from the metal surface to the NO adsorbates, with the overall donated charge being similar for both surfaces. The breakdown of the Bader charges for the individual atoms of the adsorbate on each of the adsorption sites show that the N atom is less positive, and the O atom is less negative than the corresponding charges of the gaseous NO species. The N atom of the adsorbate is seen to become less positive while the O atom of the adsorbate less negative, with the increased coordination of the adsorption site on Pd. For Pt, the charge on the N atom decreases similarly to that on Pd however, the charge on the O atom increases with increased coordination of the adsorption site. The N atom becoming less positive than the N atom of the gaseous species indicates that it gains charge, while the O becoming less negative than the O of the gaseous species indicates that it loses charge. This is seen to be more pronounced on Pd than on Pt for the most stable fcc site, as the N atom gains 0.5 e and O loses 0.18 e on Pd, whereas on Pt this is a gain of 0.45 e and a loss of 0.11 e for N and O, respectively. The N atom of the adsorbate gaining charge from both surfaces is greater than the charge lost by the metal surface atoms, and O atom losing charge compared to the charge of the gaseous species, shows that the charge transfer process from both metal surfaces to the NO adsorbates is more complicated than direct charge transfer.

To visualise the charge transfer process from the metal surface to the NO adsorbates, the charge difference plot for NO adsorption on the most stable fcc site is shown in Figure 4.22. The plots show that charge is lost from the surface, while the NO adsorbates gain charge, confirming the overall charge donation process from the surface to the NO adsorbate as indicated by the overall Bader charges. The plots also indicate that the N surface atom gains considerable charge as indicated by the breakdown of the Bader charges, while the O atom loses charge in the direction of the N-O bond but gains charge perpendicular to the bond. This shows considerable change in the σ and

	Species	NO	N charge	O charge	M charge
	NO^+	+1	+1.21	-0.21	—
	NO	0	+0.53	-0.53	—
	NO^-	-1	+0.10	-1.10	—
	Pd {111}	—	—	—	-0.03
	Pt {111}	—	—	—	-0.04
Pd	top	-0.11	+0.35	-0.46	+0.22 (x1)
	bridge	-0.25	+0.10	-0.35	+0.15 (x2)
	hcp	-0.32	+0.05	-0.36	+0.12 (x3)
	fcc	-0.33	+0.03	-0.35	+0.13 (x3)
Pt	top	-0.13	+0.24	-0.37	+0.30 (x1)
	bridge	—	(fcc)	—	—
	hcp	-0.31	+0.05	-0.36	+0.10 (x3)
	fcc	-0.34	+0.08	-0.42	+0.13 (x3)

Table 4.13: The calculated Bader charges for NO in the gas phase and (b) adsorption site on the Pd and Pt {111} surface. The Bader charges for the Pd and Pt surface atoms of the adsorption sites are also included.

π systems, indicating that there is rearrangement of the electronic structure of the NO adsorbate when interacting with both metals.

To further analyse the redistribution of charge upon adsorption, a schematic of the molecular orbital (MO) diagram, the calculated electronic structure of gaseous NO, and of the most stable fcc sites for Pd and Pt are shown in Figure 4.23. The valence MO's of NO in increasing energy are; 3σ, $4\sigma^*$, 1π, 5σ, $2\pi^*$ and $6\sigma^*$, as shown in the MO diagram (Figure 4.9 (a)). The position of the occupied $4\sigma^*$, 5σ and 1π molecular orbitals for gaseous NO are shown in Figure 4.9(b) relative to the vacuum level, with the 3σ too low in energy (around -30 eV) to be observed on the plot. The calculated electronic structure for gaseous NO places the 5σ orbital higher in energy than the generally accepted arrangement of valence MO's shown in the schematic. A neutral NO molecule contains 11 valence electrons, with the highest occupied molecular orbital (HOMO) being a single electron in the doubly degenerate $2\pi^*$ molecular orbital, allowing NO

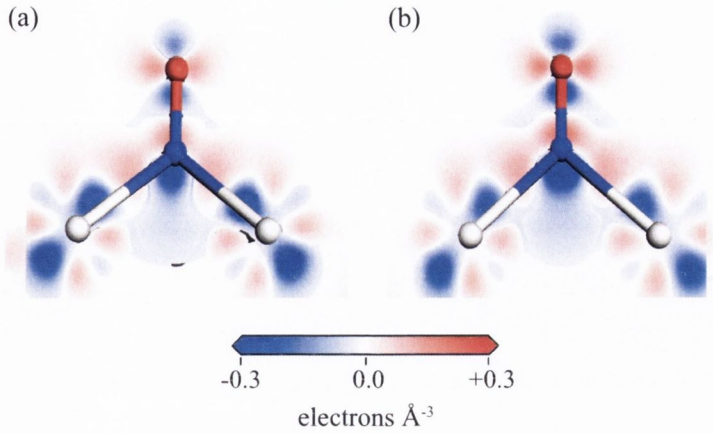


Figure 4.22: The calculated charge difference between the adsorbed NO species on the (a) Pd and (b) Pt {111} surfaces. The charge difference ranges from -0.3 (blue) to +0.3 (red) electrons Å^{-3}, as indicated by the scale.

to be a strong π acceptor. NO^+ has no unpaired electrons in this orbital, with a calculated HOMO being the 5σ, and NO^- has two unpaired electrons in the $2\pi^*$ and is iso-electronic with O_2. The nature of the MO's do not vary significantly with charge state. The $4\sigma^*$ has a strong contribution from N $2s$, O $2s$ and O $2p$ states, while the 5σ is composed of N $2p$ and O $2p$ with a small contribution from the N $2s$ states. The 1π and $2\pi^*$ are composed of a mixture of N $2p$ and O $2p$ states with a greater contribution from the O $2p$ to the 1π and a greater contribution from the N $2p$ to the $2\pi^*$.

The changes in the electronic structure of the NO adsorbate when interacting with the most stable fcc site on Pd and Pt is shown in Figures 4.23 (a) and 4.23 (b), respectively, which can be compared to the calculated PEDOS for gaseous NO (Figure 4.9 (b)). The valence band (VB) and conduction band (CB) for the NO adsorbate is similar on both surfaces, with all orbitals showing a decrease in energy relative to the corresponding orbitals of gaseous NO. The $4\sigma^*$ orbital of both adsorbates gains N $2p$ states, with a greater amount gained for NO on Pt. The 5σ orbital, which is above the 1π orbital for gaseous NO, is lower in energy than the 1π orbital, due to a stabilisation of this orbital when interacting with the metal surface, but to a greater extent on Pd. From this interaction, the 5σ orbital loses N $2s$ states while gaining O $2s$ character. As the 5σ orbital is stabilised so close in energy to the 1π, it is difficult to distinguish

between these orbitals on the PEDOS plots; however, the orbitals can be separated by the O $2s$ states as the π orbital cannot have $2s$ state contributions from symmetry considerations. The 1π orbital thus has contributions from the N and O $2p$ orbitals similar to gaseous NO. The distributions however, change from being O $2p$ dominated similar to gaseous NO to being N $2p$ dominated for the NO adsorbate on both surfaces. There is a dramatic change in the $2\pi^*$ orbital of the adsorbate when interacting with the Pd and Pt metal d bands. This orbital is split between occupied and unoccupied states, similar to gaseous NO; however, the contribution to the occupied states are primarily from the O $2p$ states with minor N $2p$ states, whereas for the gaseous NO this is quite an even mix. The unoccupied states have large contributions from both N and O $2p$ states. The position of E_F for the NO adsorbate system, is lowered on Pd to -5.44 eV and on Pt to -5.86 eV compared to the pure Pd (-5.09 eV) and Pt (-5.54 eV) surfaces.

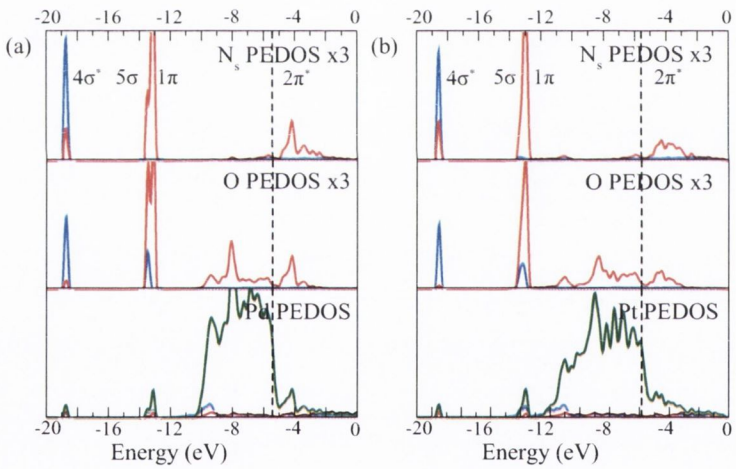


Figure 4.23: The calculated PEDOS for the most stable NO adsorption modes at the fcc site of the (a) Pd and (b) Pt {111} surfaces. The blue, red and green lines indicate the s, p and d states, respectively. The dotted line indicates the position of E_{F} and the highest occupied molecular orbital. The Evac of each graph is aligned to 0 eV.

To quantify the changes of the electronic structure for the NO adsorbate on Pd and Pt, the approximate percentage contributions of the N and O $2s/p$ states to each of the MO's for gaseous NO and NO adsorbed on the fcc site of both metals, were obtained by integration of the PEDOS and are detailed in Table 4.14. The $4\sigma^*$ orbitals are seen to gain N $2s/p$ states for NO on Pd (12/14%) and Pt (10/18%) while losing O $2s/p$

states. The opposite occurs for the 5σ orbital, as O $2s/p$ contributions increase for the NO adsorbate on Pd (6/2%) and Pt (11/4%). This shows that the $4\sigma^*$ orbital becomes more N in character while the 5σ orbital becomes more O in character when NO interacts with the metal surfaces. The change in composition of the $4\sigma^*$ orbital is similar on both surfaces, while for the 5σ orbital of NO on Pd, the increase in O $2s$ states is not as significant, and also contains 7% more N $2p$ character than NO on Pt, due to the extra stabilisation of this orbital on Pd. For gaseous NO, the higher energy π orbitals show an O dominance for the 1π orbital and N dominance for the $2\pi^*$ orbital. On adsorption of the NO molecule with Pd and Pt, this dominance to the π orbitals changes as the 1π orbital becomes more N $2p$ dominated, while the $2\pi^*_{\text{occ}}$ becomes more O $2p$ dominated; however the N/O $2p$ contributions to the $2\pi^*_{\text{unocc}}$ remain the same as gaseous NO. The interaction with the metal surfaces causes the $2\pi^*_{\text{occ}}$ orbital to have an enhanced contribution from the O $2p$ states of 44% and 39% for NO on Pd and Pt, repectively with the N $2p$ contributions to this orbital reducing by similar amounts.

The analysis of the Bader charges, the charge density difference plots, the PEDOS and the changes in the orbital contributions indicates that there is a complex change to the electronic structure for NO adsorption on the Pd and Pt surfaces. Bader analysis for NO adsorption on the most stable fcc site on both surfaces show that charge is donated from Pd and Pt to the NO adsorbates, where the breakdown of the charges indicate that the surface bound N atom gains charge while the O atom loses charge. This is seen by the charge difference plots, which also indicate that a complex electronic rearrangement of the σ and π systems occur upon adsorption of the NO molecule on both metal surfaces. The donated charge to the NO adsorbates would be expected to directly occupy the anti-bonding $2\pi^*$ orbital; however, the PEDOS plots show that the interaction of the occupied contributions to this orbital with the metal d band is primarily with O $2p$ states, where N $2p$ states are notably absent. This is caused by the redistribution of electron density within the N-O bond as the lower orbitals are stabilised containing a greater contribution from the N atom, while the higher orbitals contains contributions from the O atom. The interaction of the $2\pi^*$ orbital with the metal d

	$NO_{(g)}$				
States	$4\sigma^*$	5σ	1π	$2\pi^*_{occ}$	$2\pi^*_{unocc}$
N_s	40	11	0	0	0
N_p	0	40	34	56	59
O_s	33	1	0	0	0
O_p	27	48	66	44	41
	NO_{ads} on Pd {111}				
States	$4\sigma^*$	5σ	1π	$2\pi^*_{occ}$	$2\pi^*_{unocc}$
N_s	52	0	0	0	0
N_p	14	43	58	14	60
O_s	30	7	0	0	0
O_p	4	50	42	86	40
	NO_{ads} on Pt {111}				
States	$4\sigma^*$	5σ	1π	$2\pi^*_{occ}$	$2\pi^*_{unocc}$
N_s	50	0	0	0	0
N_p	18	36	65	17	59
O_s	30	12	0	0	0
O_p	2	52	35	83	41

Table 4.14: The percentage contributions of N_s, N_p, O_s and O_p states to the molecular orbitals of gas phase NO and NO adsorbed on the fcc site of the Pd and Pt {111} surfaces. The $2\pi^*_{occ}$ and $2\pi^*_{unocc}$ refers to the occupied and unoccupied states, respectively, for the $2\pi^*$ orbital of the NO molecule.

band reduces the N states, and stabilises the N-O anti-bonding interaction transferring electron density onto the O atom through the π system. The charge transfer to the molecule is redistributed within the N-O bond with some back donation from the O atom to the N atom through the σ interaction. This gives rise to the excess density located on the N atom that is not fully accounted for by the loss of density from the metal surface atoms, and the loss of charge from the O atom. The NO adsorbate is more stable on the Pd surface as this mechanism of electron redistribution is more pronounced, since the σ system is more stabilised and the N atom gains more charge

than on Pt, which may be attributed to the higher value of E_F.

4.4.6 NO_2 adsorption modes and analysis

The NO_2 molecule can adsorb on the Pd and Pt surfaces in four different modes; μ-nitrito (N and O bound to the surface), O-O'nitrito (O and O bound to the surface), O-nitrito (single O bound to surface), and N-nitro (N bound to surface). As mentioned previously, only the first three of these are investigated here across the four high symmetry adsorption sites as the N-nitro mode was previously found to be unstable on the Pt {111} surface.[94] For NO_2 adsorption on Pd and Pt, all possible combinations of each mode orientated across the different adsorptions sites were tested, with the most stable configuration shown in Figure 4.24. This was found to be the μ-nitrito configuration with N and O atoms bonded offset from top sites across a bridge site on both surfaces. The associated E_{ads}, molecular bond distances and angles for these configurations on Pd and Pt are provided in Table 5.6, along with the molecular bond distances and angles for gaseous NO_2. There is a negligible difference of 0.01 eV between the E_{ads} of both adsorption modes, indicating that they have similar stabilities on both metal surfaces. Molecular NO_2 is expected to have a spin due to its unpaired electron; however, for both NO_2 adsorption modes, the spin of the adsorbate is zero due to quenching by the metal surface.

The calculated bond lengths and angles for the most stable μ-nitrito modes on both surfaces are very similar with minor differences. The bond parallel to the surface (N_s-O_s) is longer than the N-O bond perpendicular to the surface, with both bonds being lengthened upon adsorption on the metal surfaces, relative to gaseous NO_2. This indicates that the elongation of the N_s-O_s bond weakens the bond from the interaction with Pd and Pt.

The calculated asymmetric, symmetric and bending vibrational modes for the μ-nitrito mode were determined to be 1520 cm^{-1} (1588 cm^{-1}), 999 cm^{-1} (1011 cm^{-1}) and 746 cm^{-1} (739 cm^{-1}) on Pd (Pt). HREELS studies for NO_2 on the clean Pd {111} surface have characterised the μ-nitrito configuration by assigning vibrational frequen-

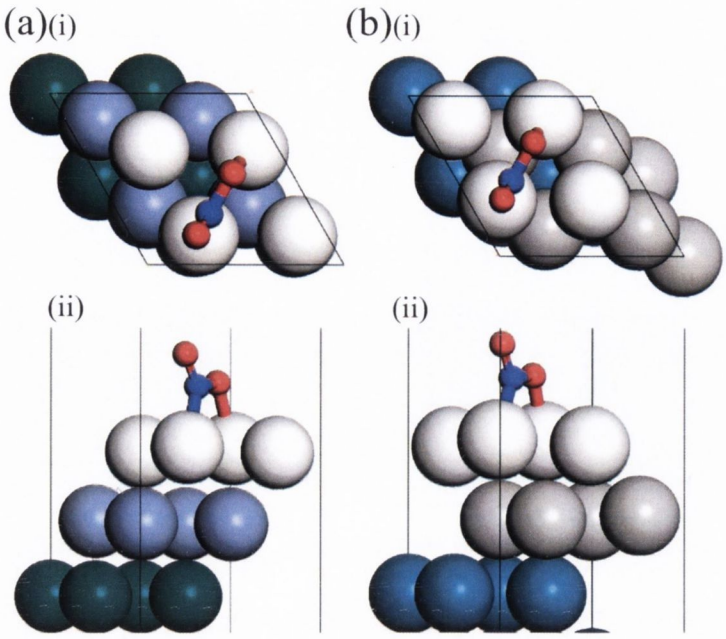


Figure 4.24: The most stable μ-nitrito mode on the (a) Pd and (b) Pt {111} surface. Both the (i) top and (ii) side view are shown for clarity.

cies of 1545 cm^{-1}, 1170 cm^{-1}, and 790 cm^{-1},[110] and for the clean Pt {111} surface as 1560 cm^{-1}, 1180 cm^{-1}, and 795cm^{-1},[111] to the asymmetric, symmetric and bending modes, respectively. These vibrational bands have also been supported by density functional theory (DFT) studies.[94, 97] The experimental vibrational bands for NO_2 on the clean Pd and Pt {111} surfaces are close to the calculated values of this study suggesting that the μ-nitrito mode is that observed on the Pd and Pt surfaces.

Surface	N	O	E_{ads} (eV)	O_s - N_s (Å)	N_s-O (Å)	O-N-O (°)
$NO_{2\,(g)}$	-	-	-	1.21	1.21	133.73
Pd {111}	top	top	-1.25	1.36	1.23	118.03
Pt {111}	top	top	-1.26	1.35	1.23	118.43

Table 4.15: The calculated bond lengths and angles for gaseous NO_2. The E_{ads}, adsorption site for N and O, the calculated bond connected to the surface (O_s-N_s), the N-O bond away from the surface (N_s-O) and the adsorbed NO_2 bond angle for most stable μ-nitrito adsorption mode on the Pd and Pt {111} surfaces. The subscript 's' donates the atom bound to the surface.

The calculated Bader charges for the gaseous NO_2 species, the pure Pd and Pt

surfaces and the most stable μ-nitrito adsorption modes are detailed in Table 4.16. Overall, the Bader charges show that the NO_2 molecules on the metal surfaces are more negative than neutral NO_2 indicating a gain in charge, while the metal surface atoms are more positive than the pure surfaces showing a decrease in charge. It is therefore observed that charge is donated from the metal surfaces to the μ-nitrito adsorbates with the NO_2 molecule on the Pd surface gaining a bit more charge (0.02 e) than on Pt. The breakdown of the individual charges for the N and O atoms of the adsorbates indicates that the N atom becomes less positive, while the surface bound O atom (O_s) becomes more negative relative to the Bader charges of the N and O atoms of gaseous NO_2. The O atom not bound to both surfaces has lost some charge (0.02 e) relative to that of gaseous NO_2. The N atom of the adsorbate becoming less positive and the O_s atom becoming more negative indicates that these atoms gain charge; however the gain of charge is not evenly distributed across both atoms. The N atom is seen to gain charge of 0.26 e and 0.27 e, while the O_s atom gains 0.11 e and 0.10 e, on Pd and Pt, respectively. The excess charge gained by the N atoms is not accounted for by the loss of charge by the metal atom, and the gain in charge for the O_s is less than that lost by the metal atoms, while the unbound O atom loses charge. This suggests that direct charge donation to the NO_2 molecule is over simplified, and some kind of electronic redistribution must be occurring upon interaction of the NO_2 molecule with the metal surfaces.

To visualise the redistribution of charge for the adsorption of the NO_2 molecule on Pd and Pt, the charge difference plots are shown in Figure 4.25. These plots show that the N_s and O_s atoms for the NO_2 adsorbate on the metal surface gains charge, while the metal surface atoms lose charge along the bond axis, supporting the Bader charges. There are also regions of decreasing and increasing charge density on the atoms of the NO_2 adsorbates. These regions indicate that that there is considerable change in the σ and π systems of the NO_2 molecule upon interaction with the metal surfaces, indicating that there is a redistribution of charge.

In order to further analyse the charge distribution of the NO_2 adsorbate when inter-

	Species	NO_2	N	O	O	*M*
(a)	NO_2^+	+1	+0.93	+0.03	+0.04	-
	NO_2	0	+0.73	-0.34	-0.39	-
	NO_2^-	-1	+0.38	-0.69	-0.69	-
	Pd {111}	—	—	—	—	-0.03
	Pt {111}	—	—	—	—	-0.04
(b)	μ-nitrito on Pd	-0.35	+0.47*	-0.45*	-0.37	+0.16 x2
	μ-nitrito on Pt	-0.33	+0.48*	-0.44*	-0.37	+0.17, +0.18

* atom bonded to surface

Table 4.16: The calculated Bader charges for NO_2 in the (a) gas phase and the pure Pd and Pt surfaces. (b) The Bader charges for the μ nitrito adsorption mode on the Pd and Pt {111} surfaces, along with the charge of the metal surface atoms bonded to the adsorbates.

acting with the Pd and Pt surfaces, the calculated PEDOS for the most stable μ-nitrito adsorption modes are shown in Figure 4.26. The valence MO's for the adsorbates are labelled in a similar manner to the MO diagram and calculated PEDOS for gaseous NO_2, shown in Figure 4.12 (a) and (b) respectively.

There appears to be a change in the electronic structure of gaseous NO_2 on adsorption and interaction with the Pd and Pt metal surfaces. The electronic structure of the μ-nitrito adsorbates are similar on both surfaces, and all the orbitals are seen to be stabilised and lowered in energy relative to E_{vac}. On adsorption, the 6σ orbital appears to gain N $2p$ states, with the 1π and 7σ still being a mix of N/O $2p$ states. The 1π orbital, which is above the 7σ for gaseous NO_2, is stabilised to below the 7σ orbital, and both orbitals become N dominated when interacting with the Pd and Pt surfaces. For both NO_2 adsorbates, the top of the VB becomes dominated by O $2p$ states that interact with the metal d bands and mix with a negligible amount of N $2p$ states. This region is a mixing of the $2\pi^{\text{nb}}$ and occupied states of the $3\pi^*$ orbitals by comparing to gaseous NO_2 and the MO diagram, that are smeared across an energy range up to E_{F} from the interaction with the metal d band. The N $2p$ contributions to the $3\pi^*$ orbital are diminished with respect to the same region on the gaseous NO_2 PEDOS. The CB

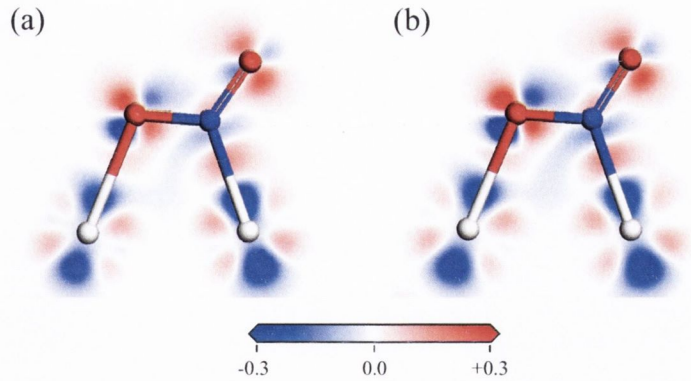


Figure 4.25: The calculated charge density difference of the most stable NO_2 adsorption mode on the (a) Pd and (b) Pt {111} surfaces. The charge difference ranges from -0.3 (blue) to +0.3 (red) electrons Å^{-3} as indicated by the scale.

for gaseous NO_2 appears to be O $2p$ dominated, and on adsorption the N/O $2p$ state distribution changes becoming N $2p$ dominated. For both NO_2 adsorbates, the E_F of the system is lowered compared to the pure Pd and Pt surfaces by a similar amount (-1.01 eV) indicating charge transfer from the surface to the adsorbate.

To quantify the changes in the NO_2 electronic structure upon adsorption, the percentage contributions of the N and O $2s/p$ states to the molecular orbitals of gaseous NO_2, and the μ-nitrito adsorption modes on Pd and Pt, were obtained by integration of the PEDOS and are detailed in Table 4.17. As the 7σ and 1π orbitals are so close in energy that it is hard to distinguish between them for the gaseous NO_2 species, as seen on the PEDOS plot, the N/O $2s/p$ contributions to these orbitals are group together in the Table. For both adsorbates, the $2\pi^{nb}$ and $3\pi^*_{occ}$ orbitals mix at the top of the valence band as seen in the PEDOS due to smearing from the interaction with the metal d band, making it difficult to distinguish between the N/O $2s/p$ contributions to these orbitals. The contributions are thus approximated by taking the percentage of states at a similar energy range to that of the analogous orbitals of the gaseous species.

The N/O $2s/p$ state percentage contributions to the orbitals show a considerable change in the electronic structure of the NO_2 molecule on adsorption and interaction with the Pd and Pt surfaces, relative to gaseous NO_2. The percentage contributions to orbitals of both μ-nitrito modes are however, very similar with small deviations in their

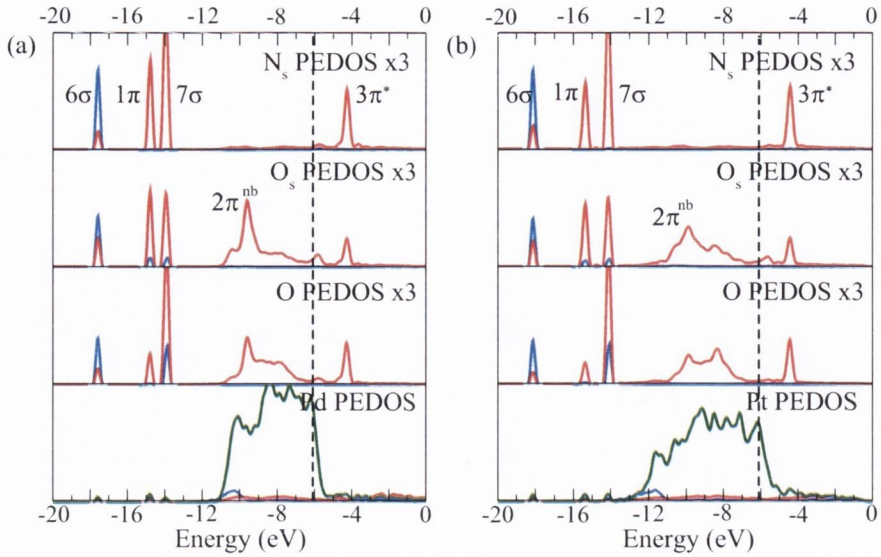


Figure 4.26: The calculated PEDOS for the most stable μ-nitrito on the (a) Pd and (b) Pt {111} surfaces. The N/O PEDOS shown is for the single atom species of the adsorbates while the Pd and Pt PEDOS is for the top surface atoms. The subscript 's' indicates an atom bound directly to the surface. The blue, red and green lines are the s, p and d states. The E_F is indicated by the dotted line for the adsorption modes and the highest occupied state of the gaseous species. The E_{vac} for the adsorbates on both surfaces is aligned to 0eV.

respective electronic structures on Pd and Pt. On adsorption, the 6σ orbital gains N $2s/p$ character, with contributions from the O_s atom remaining the same, while losing O $2p$ states from the O atom directed away from the surface. The $7\sigma/1\pi$ systems of both adsorbates appear to be relatively unchanged compared to gaseous NO_2. The higher π orbitals are O dominated similar to gaseous NO_2; however on adsorption the contributions to the $2\pi^{nb}$ shift towards the surface bound atoms, while there is a considerable shift from N contributions (around -20%) to contribution from the unbound O atom (around +20%) to the occupied states of the $3\pi^*$ orbital. The reverse occurs for the unoccupied states of the $3\pi^*$ orbital, which loses O $2p$ state contributions and gains contributions from the N atom.

The analysis of the Bader charges, the charge density difference plots, and the changes in the orbital contributions shows that there is a complex change to the electronic structure for NO_2 adsorption on Pd and Pt. The overall Bader charges indicate that there is charge transfer from Pd and Pt to the μ-nitrito adsorbates; however the

	$NO_{2\,(g)}$				
States	6σ	$7\sigma/1\pi$	$2\pi^{nb}$	$3\pi^*_{occ}$	$3\pi^*_{unocc}$
N $2s$	27	0	0	8	7
N $2p$	1	38	0	24	27
O $2s$	21	4	0	0	0
O $2p$	15	27	50	34	33
O $2s$	21	4	0	0	0
O $2p$	15	27	50	34	33
	μ-nitrito on Pd				
States	6σ	$7\sigma/1\pi$	$2\pi^{nb}$	$3\pi^*_{occ}$	$3\pi^*_{unocc}$
N_s $2s$	34	0	0	1	7
N_s $2p$	7	39	3	7	23
O_s $2s$	21	3	1	1	2
O_s $2p$	12	24	55	38	39
O $2s$	20	6	0	0	2
O $2p$	6	28	41	53	27
	μ-nitrito on Pt				
States	6σ	$7\sigma/1\pi$	$2\pi^{nb}$	$3\pi^*_{occ}$	$3\pi^*_{unocc}$
N $2s$	34	0	0	1	8
N $2p$	10	37	6	6	18
O_s $2s$	21	3	2	0	3
O_s $2p$	11	24	55	39	45
O_s $2s$	19	7	0	0	2
O_s $2p$	5	29	37	54	24

Table 4.17: The approximate percentage contributions of N $2s$, N $2p$, O $2s$ and O $2p$ states to the molecular orbitals of gas phase NO_2 and the μ-nitrito adsorption modes on the Pd and Pt {111} surfaces.

breakdown of the individual charges suggests that there is a rearrangement of the σ and π bonding within the adsorbate, which can also be seen on the charge difference plots. The lower energy orbitals are stabilised with a shift in their N/O contributions for both adsorbates. These orbitals contain a greater contribution from the surface bound atoms of the both adsorbates through interaction with Pd and Pt relative to gaseous NO_2,

with greater contribution from the N atom. The higher π orbitals are dominated by O $2p$ states for gaseous NO_2 and both adsorbates, with a shift in density from the N atom to the unbound O atom, increasing the O atom contribution to the occupied states of the $3\pi^*$ orbital. The opposite occurs for the unoccupied states of the $3\pi^*$ orbital, which indicates that the N/O $2p$ states become empty/filled from the interaction with the metal surfaces.

The mechanism of charge transfer from the surface to the adsorbates is similar for both μ-nitrito adsorbates as they have similar electronic structures; however it is more complicated than direct charge donation to the occupied states of the anti-bonding orbital. The electronic redistribution within the molecules allows the N_s and O_s $2s/p$ states to the 6σ and $2\pi^{nb}$ orbitals to increase through stabilisation of these orbitals by interaction with the metal surfaces. The N_s $2p$ state and the O $2p$ state of the unbound O atom, contributions to the occupied states of $3\pi^*$ orbital, decrease and increase, respectively; however the charge on the unbound O atom remains the same as the gaseous NO_2 species. This can be explained by the electronic redistribution and stabilisation of the 1π orbital to below the 7σ orbital, which in turn decreases the N $2p$ contributions to the higher $3\pi^*_{occ}$ orbital. The interaction of the NO_2 molecule with the Pd and Pt surface, stabilises the anti-bonding orbital $3\pi^*$ interaction between N and O, transferring the electron density to the unbound O atom of the adsorbate in a similar manner to that observed for NO adsorption. This transfers electron density back to the N_s atom through the 6σ orbital accounting for the increased charge of the N atom relative to gaseous NO_2. This suggests that the orientation of the μ-nitrito adsorption mode on the metal surface, treats the adsorbate/surface interaction and the adsorbate bonding in a similar manner to a NO adsorbate with an extended bond to an O atom.

4.4.7 Decomposition profile

The calculated energies for each step of the NO_x decomposition pathway on the Pd and Pt {111} surfaces are detailed in Table 4.18. The energetics of each step were calculated using the energies of the most stable adsorption modes for N, O, NO and NO_2 on Pd

and Pt, and the energies of their respective gaseous species. The most stable adsorption mode for N_2 and O_2 on Pd and Pt are not presented as their orientations and charge interactions are similar to that on Rh (Figures 4.13 and 4.14); however their energies are calculated in a similar manner, and used within the decomposition profile to provide a clearer understanding for their formation and removal from the {111} surface of Pd and Pt. The calculated energies for each step of the dissociation of NO_x on the Rh surface can also be summarised graphically in Figure 4.27.

		Reaction Step	Pd (eV)	Pt (eV)
(a)	(i)	$NO_{2(g)} \rightarrow NO_{2(ads)}$	-1.25	-1.26
	(ii)	$NO_{2(ads)} \rightarrow NO_{(ads)} + O_{(ads)}$	-1.21	-0.13
	(iii)	$NO_{(ads)} + O_{(ads)} \rightarrow N_{(ads)} + 2O_{(ads)}$	+0.99	+1.24
	(iv)	$N_{(ads)} + 2O_{(ads)} \rightarrow \frac{1}{2}N_{2(ads)} + 2O_{(ads)}$	-0.88	-0.68
	(v)	$\frac{1}{2}N_{2(ads)} + 2O_{(ads)} \rightarrow \frac{1}{2}N_{2(g)} + 2O_{(ads)}$	-0.15	-0.23
	(vi)	$\frac{1}{2}N_{2(g)} + 2O_{(ads)} \rightarrow \frac{1}{2}N_{2(g)} + O_{2(ads)}$	+1.78	+1.16
	(vii)	$\frac{1}{2}N_{2(g)} + O_{2(ads)} \rightarrow \frac{1}{2}N_{2(g)} + O_{2(g)}$	+0.93	+0.13
(b)	(i)	$NO_{(g)} \rightarrow NO_{(ads)}$	-2.28	-1.93
	(ii)	$NO_{(ads)} \rightarrow N_{(ads)} + O_{(ads)}$	+0.99	+1.24
	(iii)	$N_{(ads)} + O_{(ads)} \rightarrow \frac{1}{2}N_{2(ads)} + O_{(ads)}$	-0.88	-0.68
	(iv)	$\frac{1}{2}N_{2(ads)} + O_{(ads)} \rightarrow \frac{1}{2}N_{2(g)} + O_{(ads)}$	-0.15	-0.23
	(v)	$\frac{1}{2}N_{2(g)} + O_{(ads)} \rightarrow \frac{1}{2}N_{2(g)} + \frac{1}{2}O_{2(ads)}$	+0.89	+0.58
	(vi)	$\frac{1}{2}N_{2(g)} + \frac{1}{2}O_{2(ads)} \rightarrow \frac{1}{2}N_{2(g)} + \frac{1}{2}O_{2(g)}$	+0.46	+0.07

Table 4.18: The calculated energies for each step of the (a) NO_2 and (b) NO decomposition pathways on the Pd and Pt {111} surfaces.

The overall calculated energy for $NO_{(g)}$ and $NO_{2(g)}$ to $N_{2(g)}$ + $O_{2(g)}$ was calculated to be -0.95 eV, and +0.22 eV, respectively. The calculated energy for the overall $NO_{(g)}$ process is very close to the experimental value (-0.94 eV); however for NO_2 this is not as accurate to the experimental value (-0.35 eV) due to the overestimated DFT-calculated binding energy of O_2 with respect to experiment.[361–365]

The calculated dissociation energy for NO_2 is exothermic on both surfaces, with the breakdown being much more favourable on Pd. The drive to breakdown NO_2 on

Pd is more favourable as NO and O are much more stable on Pd than Pt. The facile breakdown of NO_2 on Pd is observed experimentally at low temperatures, while the relatively lower energy for this step on Pt suggests that the NO_2 molecule can exist on the Pt surface without favouring dissociation. As the energy is considerably lower on Pt, the reverse reaction which is the oxidation of NO; $NO_{(ads)}+O_{(ads)} \rightarrow NO_{2(ads)}$ (+0.13 eV) can also occur. This may have implications in NSR technologies, as the oxidation of NO for the formation of NO_2 on the surface is suggested to be important for NO_x adsorbers, as NO_2 forms a surface nitrate (NO_3^-) which subsequently leads to N_2 formation.[25, 367, 370]

The dissociation of NO is more difficult than NO_2 on both surfaces, as it is endothermic and thus requiring energy. The unfavourable breakdown of NO can be attributed to the endothermic adsorption of N ad-atoms on both surfaces, so that the drive to break the NO bond is not as favourable as observed for rhodium. The energy required to breakdown NO is less on Pd as the O atoms are more stable than on Pt, while the NO dissociation energy on Pt is close to its adsorption energy. This may explain the issues with the {111} surface of Pt not being able to break down NO, and the observed desorption from the surface at low temperatures before any dissociation can occur.[142–144] Although the energy to breakdown NO on Pd is lower than on Pt, energy is required for this step indicating that the dissociation of NO on Pd will occur at high temperatures as observed experimentally. The difficulty with breaking down NO on both surfaces may cause the formation and release of N_2O during the *de*NO_x process, which is a problem associated with these metals.

The N and O dissociation products from NO_x molecules can form N_2 and O_2 on the surface, which are then desorbed from the metal surface to their respective gaseous species. The formation of N_2 and its subsequent removal from both surfaces to the gaseous species is exothermic. The formation of N_2 on the surface is more favoured on Pd, while the removal to the gaseous species is easier on Pt. This indicates that it is easier to form N_2 on Pd, while its desorption is more facile from the Pt {111} surface. The difficulty with removing the dissociation products from the {111} surface

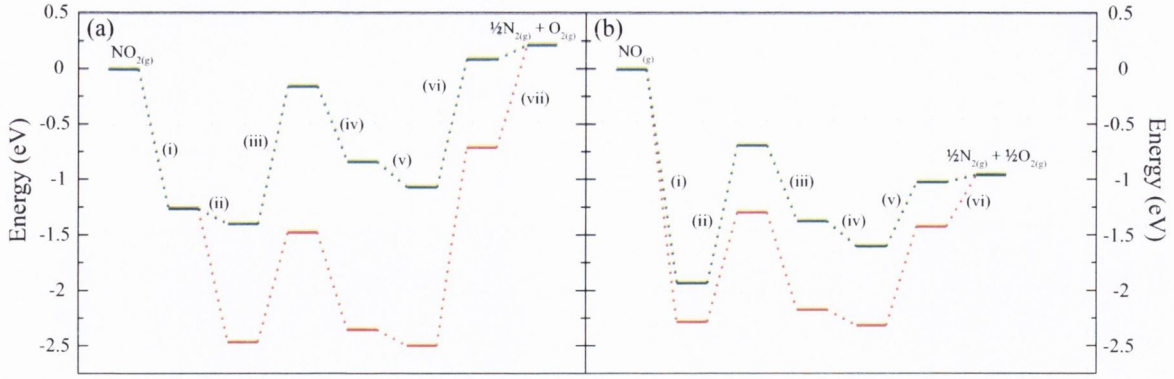


Figure 4.27: The calculated energies for the dissociation profile of (a) NO_2 and (b) NO on the Pd and Pt {111} surfaces. The red and green lines indicate the Pd and Pt dissociation pathways, respectively. The labels (i) - (vi) relate to the different steps of the profiles outlined in Table 4.18.

of Pd and Pt lies with the formation and desorption of O_2, in particular its formation. A large energy is required to form O_2 on both surfaces, especially on Pd, with the subsequent removal of O_2 from Pd also being larger than on Pt. The larger energies for these steps on Pd is caused by the relatively larger adsorption energy of O on the {111} surface of Pd, indicating that it is more stable than on Pt and strongly binds to Pd. It therefore may be necessary to use a reductant such as CO, H_2 or hydrocarbon in the reaction mixture during the *de*NO$_x$ process for Pd metal to easily remove the O atoms from the surface, in a similar manner to rhodium. The removal of O atoms in such a way from the metal surfaces will allow easy regeneration of the catalyst and assist in further breakdown of NO$_x$. For lean-*de*NO$_x$, the strong interaction of O with the Pd surfaces would allow activation of the hydrocarbon, forming a $C_xH_yO_z$ intermediate species, which has been suggested to assist in the lean-*de*NO$_x$ process.[369–371] The strong adsorption of O atoms with the Pd surface may saturate it under these conditions, blocking the sites for further breakdown of NO$_x$ and reducing its efficiency. The concentration of surface bound O atoms affects the energy to remove them as the energy is seen to be doubled when the stoichiometry of O is two. Although the formation of O_2 requires a large energy on Pt, its desorption from the surface is relatively easy in particular from the breakdown of NO. This suggests that a reductant may not be needed for Pt if there is a low energy barrier leading to the formation of O_2.

4.4.8 Discussion

The most stable adsorption sites for N, O and NO_x were determined on the {111} surface of Pd and Pt. For NO adsorption this was found to be the three-fold fcc site on both surfaces with NO being more stable on Pd. The NO adsorbate favouring the same site as N and O will lead to competition for surface sites among these species, or they will occupy unfavourable sites at higher coverages. This will hinder further NO adsorption or dissociation and deactivate Pd and Pt at higher concentrations. Indeed this is observed experimentally as NO desorption at higher coverages occurs on both metals, and dissociation is hindered until the N and O atoms are removed.

There are two proposed mechanisms for charge donation from a metal surface to an adsorbate; (1) the Blyholder model[93] and (2) the more recently proposed allylic configuration.[100–104] The Blyholder model suggests direct charge transfer from the metal surface to the LUMO of the adsorbate, while charge is transferred back from the HOMO of the adsorbate to the metal surface. The Blyholder model has been used to support charge interactions with NO adsorbates on metal surfaces;[94–98] however if direct donation to the anti-bonding $2\pi^*$ orbital is the mechanism as suggested previously,[95, 96] then both N and O $2p$ state contribution to this orbital should be observed for this orbital in the valence band. Previous studies have not separated out the N and O contributions to the $2\pi^*$ orbital. The allylic configuration established by XPS for CO and N_2 on metal surfaces, proposes that the σ interaction of the adsorbate with the metal surface is stabilised in the bonding region, while the anti-bonding region is stabilised by reducing the interaction of the π^* orbital with the metal d band. This is suggested to form a non-bonding state at the top of the valence band referred to as $\widetilde{d}_\pi$.

The electronic structure of the most stable NO and NO_2 adsorbates on the {111} surface of Pd and Pt were characterised using Bader charge analysis, charge difference plots and PEDOS. The Bader charge analysis indicates that there is an overall charge donation from both surfaces to the NO_x adsorbates, with the charge difference plots

showing a considerable change to the σ and π systems upon interaction of the adsorbates with the metal surfaces. The interaction of the NO_x molecules with the Pd and Pt surfaces causes a redistribution of electron density within the both adsorbates. For NO this interaction stabilises the N-O $2\pi^*$ anti-bonding orbital, reducing the N $2p$ contribution to this orbital, and transferring the donated electron density from the metal surface to the O atom. The mechanism for charge donation is more pronounced on Pd than on Pt, as the N atom is seen to have a greater charge, and the O atom loses more charge, relative to gaseous NO. This may be explained by the greater stability of the 5σ orbital and higher E_F on Pd that interacts more favourably with the N atom, thus allowing the NO adsorbate to be more stable on Pd than on Pt. The E_{ads} and electronic structure for the NO_2 adsorbate on Pd and Pt are similar with minor differences between them. A similar stabilisation of the $3\pi^*$ orbital is observed for the interaction of the NO_2 molecule with the Pd and Pt surface, indicating that the NO_2 adsorbate behaves like an NO molecule with an elongated bond to an O ad-atom. The absence of N $2p$ contributions to this orbital can been seen at the top of the valence band. Direct donation to the π^* orbital is therefore shown not occur, suggesting that the Blyholder model does not hold for NO_x adsorption on the {111} surface of Pd and Pt. The electronic rearrangement of the σ and π systems, along with the stabilisation of the anti-bonding orbitals would suggest that a more complicated mechanism is occurring, similarly to that proposed by the allylic configuration. The electronic structure for NO_x on these metals is closely related to the allylic configuration as; (1) the 5σ for NO, and 1π for NO_2 are greatly stabilised with Rh compared to gaseous NO_x, and (2) the $2/3\pi^*$ orbitals are stabilised and dominated by O $2p$ states at the top of the valence band. This can be linked to the non-bonding electron pair, which interacts with the metal d states giving the $\widetilde{d}_\pi$ band, as observed for N_2 and CO. A recent DFT study[105] also supports the allylic configuration as the mechanism for charge interactions for NO on the {100} surface of Pt, in a similar manner to our observations in this work.

4.5 Conclusion

The adsorption modes for N, O, N_2, O_2 and NO_x adsorbates on the {111} surface of rhodium, palladium and platinum were investigated to identify the most stable mode for each species using DFT with the PBE functional. Once the most stable adsorption mode was determined for each, their electronic interactions with the {111} surfaces were examined using Bader calculations, charge difference plots, PEDOS and percentage contributions of the individual states to the MOs. The atomic N species adsorbed exothermically at the three-fold hcp site on Rh, while it adsorbed endothermically on the Pd and Pt surfaces at the three-fold fcc sites. The O adsorbates where found to adsorb exothermically at the fcc site on all three metals, the largest adsorption energy is associated with Rh, followed by Pd and the lowest adsorption energy calculated on Pt. Bader charges and charge difference plots indicated that the N and O adsorbates gained density from the metal surfaces forming anionic $N^{\delta-}$ and $O^{\delta-}$ on the three surfaces, with the greatest charge donation from rhodium indicating a stronger interaction, and thus lower adsorption energies.

The most stable adsorption mode for NO was found to be the hcp site on Rh and the fcc site on Pd and Pt, with the trend for E_{ads} in order of largest energy being Rh > Pd > Pt. For NO_2, the μ-nitrito configuration with the N and O surface atoms bonded to two top sites across a bridge site was calculated to be the most stable adsorption mode on all three surfaces with the trend for E_{ads} being similar to NO adsorption. Bader analysis, charge difference and PEDOS plots show that there is an overall charge donation from all three surfaces to the NO and NO_2 adsorbates, with the greatest charge donation associated with Rh, and Pd/Pt donating similar charges to the NO_x adsorbates. The breakdown of the Bader charges indicate that the Rh surface donates more charge to the N atoms of the NO_x adsorbates than Pt, while for Pd the N charge of NO is similar; however there is more charge on the O atom for the NO adsorbate on Rh. The greater charge on the N atom for the NO_x molecules is reflected in the greater occupation of the N $2p$ states by comparing the occupations of the adsorbates on all

three surfaces.

The interaction of the NO_x adsorbates with the {111} surface of Rh, Pd and Pt, leads to a redistribution of electron density within the molecules and a stabilisation of the orbitals. For NO, this causes a stabilisation of 5σ orbital, significantly lowering it in energy, to a greater extent on Rh than either Pd or Pt, and also a stabilisation of the $2\pi^*$ anti-bonding orbital. The stabilisation of the N-O anti-bonding π^* orbital reduces the N contribution and transfers electron density to the O atom. The mechanism observed for NO_2 on the Rh surface, stabilises the $3\pi^*$ anti-bonding orbital in a similar manner indicating that NO_2 behaves like an NO adsorbate with an elongated bond to an O ad-atom. The electronic structure of the NO_x molecules can be related to the recently proposed allylic configuration, as the lower bonding orbitals are seen to be greatly stabilised, and the anti-bonding π^* orbitals being also stabilised with an O $2p$ dominance. The stabilised π^* anti-bonding orbital is split with the occupied π^* being O $2p$ dominated and the unoccupied states being N $2p$ dominated for the NO_x adsorbates. This model is consistent with the $\widetilde{d}_\pi$ combination associated with the allylic configuration.

The calculated energy profile for the $deNO_x$ process were determined from the most stable adsorption mode for each species on each surface, and their respective gaseous species, and are shown together in Figure 4.28.

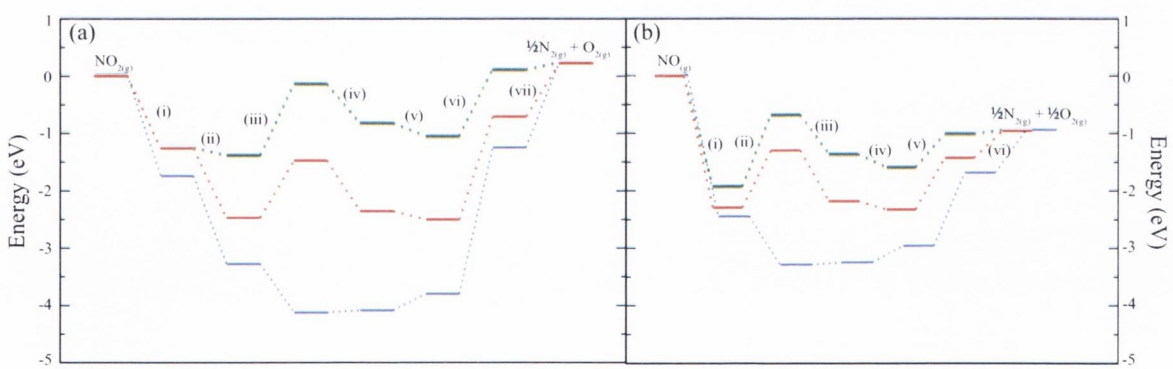


Figure 4.28: The calculated energies for the dissociation profile of (a) NO_2 and (b) NO on the Rh, Pd and Pt {111} surfaces. The blue, red and green lines indicate the Rh, Pd and Pt dissociation pathways, respectively. The labels (i) - (vi) relate to the different steps of the profiles outlined in Tables 4.9 and 4.18.

The breakdown of NO_x on the Rh surface is exothermic, while the breakdown of NO is endothermic on Pd and Pt. This shows that the breaking of the NO bond is favourable on Rh, and can explain its greater reductive properties over the other two metals. The exothermic breakdown of NO can be attributed to the exothermic adsorption of N atoms on Rh, whereas these adsorb endothermically on Pd and Pt. This drives forward the reaction to break NO and form its subsequent products. The favourable interaction of Rh metal with N and NO can be attributed to the higher E_F of Rh than either Pd and Pt, allowing easier charge donation to the adsorbates.

The subsequent removal of N and O atoms to N_2 and O_2 gases from the Rh surface is endothermic. The formation and removal of N_2 is exothermic on Pd and Pt, indicating these metals are more likely to form and remove N_2 gas than Rh. For all three metals, the formation of O_2 and its subsequent removal requires a large energy and thus extremely difficult. The large energy barrier required to remove O_2 adsorbates to their respective gaseous species is due to the large adsorption energy of O adsorbates on the Rh and Pd surfaces, while this is not as difficult on Pt. The more thermodynamical removal of gaseous species from Pd and Pt indicates their important; (1) in the TWC, Rh carries out the reduction while they remove the gases and (2) in lean-*de*NO_x for N_2 formation. The Rh {111} surface appears to be an efficient *de*NO_x catalyst due to its ease at breaking the NO bond and interaction with N atoms, indicating that any possible candidates for *de*NO_x would have to retain these qualities.

Chapter 5

Comparative DFT study of the *de*NO_x chemistry on the Rh low index and stepped surfaces

5.1 Introduction

The active metals in *de*NO_x technologies are not perfect crystalline structures, and have a mixture of surface facets on the crystal edge that interact with molecules in the gas phase. The {111} surface is the most thermodynamically stable surface and hence the most expressed on the crystalline structures; however, the metal catalysts can have other low index surfaces such as the {110} and {100} exposed at the crystal edge. These low index surfaces are more open than the close packed {111} metal surface, which make them more catalytically active to interact with gaseous species. Additionally to the presence of different surfaces at the termination of the crystalline structure, the exposed metal surfaces are not entirely flat. These can posses defects such as steps and kinks that act as active sites to enhance the ability of the surface to interact with different gases. The *de*NO_x chemistry of these lower index surfaces and a step on the {111} surface of Rh metal will need to be investigated in order to understand their ability at *de*NO_x.

Investigating the *de*NO$_x$ chemistry on the low index and stepped surface is carried out in a similar manner to that previously examined on the Rh, Pd and Pt {111} surfaces. The lowest energy adsorption mode for N, O, N_2, O_2 and NO$_x$ species are determined by examining all the possible configurations on the Rh {100} and {110} surfaces, and the Rh {443} stepped surface. Detailed analysis will be then carried out on the most stable adsorption mode, and their electronic structure on the surface will be elucidated. Their energies, along with the energies of the molecules in the gas phase, will be used to build up a decomposition profile on the surfaces, determining which will be the most catalytically active for *de*NO$_x$ chemistry.

5.2 Rh {100} and {110} surfaces

The METADISE code was used to generate the Rh {100} and {110} surfaces slabs from the relaxed bulk metal. From previous work on the {111} surfaces, a 7 layered slab with a vacuum gap of 15Å was found to be sufficient for convergence, and used for these surfaces. The metal surfaces were then expanded to a p(2x2) structure, and relaxed using a Γ-centred k-point sampling density grids of 8x8x1 and 6x8x1 for the Rh {100} and {110} surfaces, respectively, to be consistent with the k-point sampling density of the metal bulk. The surfaces were relaxed using a plane wave energy cut-off of 400 eV, and they were deemed converged when the forces acting on the atoms were reduced to less than 0.01 eV/Å. The relaxed Rh {100} and {110} p(2x2) surfaces are shown in Figure 5.1 with the high symmetry adsorption sides labelled and the layers coloured white (top) and yellow (second layer) to distinguish between the layers. The {100} surface has a and b vectors of similar length providing a cubic structure, while the {110} surface has an a vector of similar length with a longer b vector giving it a rectangular shape. The lattice positions of the atoms for the {100} surface are more closely packed than the atomic positions for the {110} surface. The {110} surface thus has more space among the surface atoms with longer metal bonds in the a vector direction, giving rise to a 'long bridge' adsorption site. The surface energies of the {100}

and {110} surfaces were calculated to be 2.41 and 2.46 j/m^2, respectively, indicating that the {100} surface is more stable.

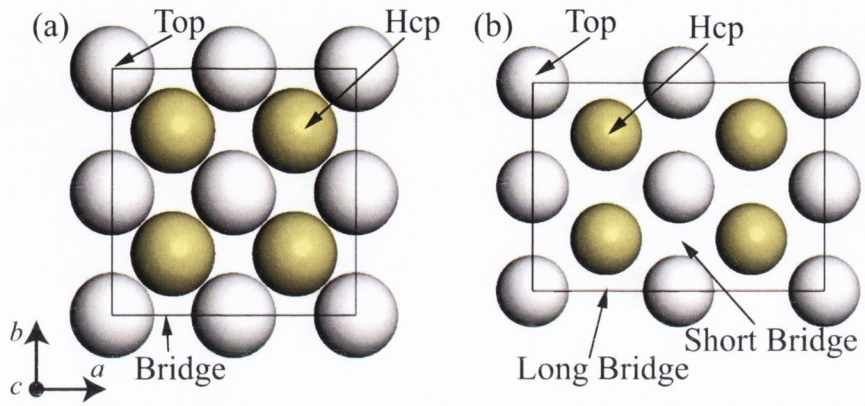


Figure 5.1: The structure of the Rh (a) {100} and (b) {110} surfaces with the high symmetry sites labelled. The top (white) and second (yellow) layers are coloured for clarity.

The PEDOS was calculated for each of the Rh {100} and {110} surfaces, and shown in Figures 5.2 (a) and (b), respectively. The PEDOS for the top most layer atoms and the inner slab (bulk) were separated out to show and differences in their electronic structures from the different coordination environments. Both PEDOS plots show that the VB up to E_F and the CB beyond, are made up mostly by Rh 4d states with a minor mixing of Rh s and p states. The surface PEDOS is different to the PEDOS of the bulk for both Rh {100} and {110}, with the major difference being at the top of the VB, where the surface has a higher concentration of Rh 4d states. The bulk PEDOS of the Rh {100} and {110} slabs are quite similar; however the PEDOS of the top layer is different, as the Rh {110} surface contains more concentrated Rh 4d states around E_F than the analogous region for Rh {100}. The Rh {110} surface has a higher E_F (-4.57 eV) than the Rh {100} surface (-4.90 eV), suggesting that charge transfer to any adsorbates on the Rh {100} surface is perhaps easier than the {110} surface due to the lower E_F and thus the larger workfunction. Bader charge analysis was carried out on the Rh {100} and {110} surfaces, and the charges of the top layer surface atoms than interact with the adsorbates, were calculated to be -0.03 and -0.04, respectively.

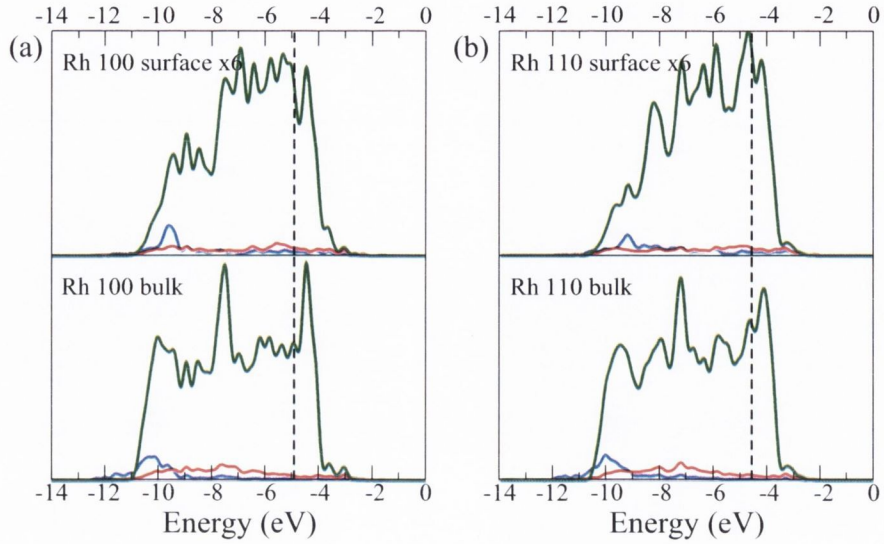


Figure 5.2: The PEDOS of the Rh (a) {100} and (b) {110} surfaces and the inner bulk layers. The dotted line indicates the position of E_F and the graphs are aligned to E_{vac} at 0 eV. The *s*, *p* and *d* states are indicated by the blue, red and green lines, respectively.

5.2.1 N adsorption and analysis

The adsorption of N on the high symmetry sites of the Rh {100} and {100} surfaces was investigated to determine the most stable adsorption mode on each surface. The CN, E_{ads}, Rh-N bond distance, and Bader charges for N adsorption on each of the sites for the two surfaces are detailed in Table 5.1 for each of the relaxed structures shown in Figure 5.3. The Rh-N bond distance is seen to increase with increased coordination of the adsorption site, with the calculated E_{ads} relative to gaseous N_2 showing a similar trend for the {100} surface. The E_{ads} values indicate that N adsorption is found to be less stable and adsorbs endothermically on the top and bridge site of the {100} surface, and the top, long bridge and hcp sites of the {110} surface. N adsorption on the four coordinated hcp site and the two coordinated short bridge site is exothermic and the most stable adsorption modes for N on the Rh {100} and {110} surfaces, respectively, with the hcp site on the Rh {100} being more stable. The metal surfaces were found to quench the atomic spin to 0 for all adsorption modes on each surface.

The Bader analysis was carried for all the adsorption sites on each surface, with

Surface	Site	CN	E_{ads} (eV)	Rh-N (Å)	N charge	Rh charge
{100}	Top	1	+1.34	1.66 (x1)	-0.37	+0.32 (x1)
	Bridge	2	+0.11	1.81 (x2)	-0.56	+0.27 (x2)
	Hcp	4	-0.52	2.03 (x4)	-0.82	+0.21 (x2), +0.14 (x2)
{110}	Top	1	+1.17	1.65 (x1)	-0.43	+0.42 (x1)
	Short Bridge	2	-0.14	1.80 (x2)	-0.57	+0.19 (x2)
	Long Bridge	2	+0.32	1.83 (x2)	-0.58	+0.25 (x2)
	Hcp	4	+0.49	1.90 (x1), 2.31 (x4)	-0.78	+0.27 (x1), +0.12 (x4)

Table 5.1: The adsorption energies (E_{ads}), coordination number (CN), M-N bond lengths and Bader charges for the different nitrogen adsorption modes on the Rh {100} and {110} surfaces. The number of bonds for each adsorbate on a high symmetry site is also included.

the charges of the N adsorbates and the Rh surface atoms that they are bonded to, detailed in Table 5.1. The Bader charges of the N adsorbates increase with increased coordination of the adsorption sites, with the charges for the Rh surface bound atoms decreasing. The charges indicate that for all adsorption modes, the N adsorbate become more negative than atomic N, gaining charge and forming $N^{\delta-}$ species, while the Rh surface atoms become more positive, losing charge. This shows that charge is transferred from the Rh surfaces to the N adsorbates. The most stable hcp adsorption site donates the greatest charge to the N adsorbate on the {100} surface, suggesting its greater stability over the other adsorption sites. For the {110} surface, the most stable short bridge site does not donate the greatest charge, as the five coordinate hcp is seen to donate the greatest charge due to the greater number of bonded Rh atoms. The reasoning for the short bridge being more stable must be due to the Rh-N bonds being ideal and the Rh surface atoms losing the least amount of charge.

To illustrate the charge transfer process, the charge difference plots for the most stable adsorption sites on the Rh {100} and {110} surfaces are shown in Figures 5.4 (a) and (b), respectively. The red regions show an increase in charge while the blue regions show a decrease in charge. These indicate that the N adsorbate on both surfaces gains charge, while the Rh surface atoms lose charge. The plots thus show that charge is

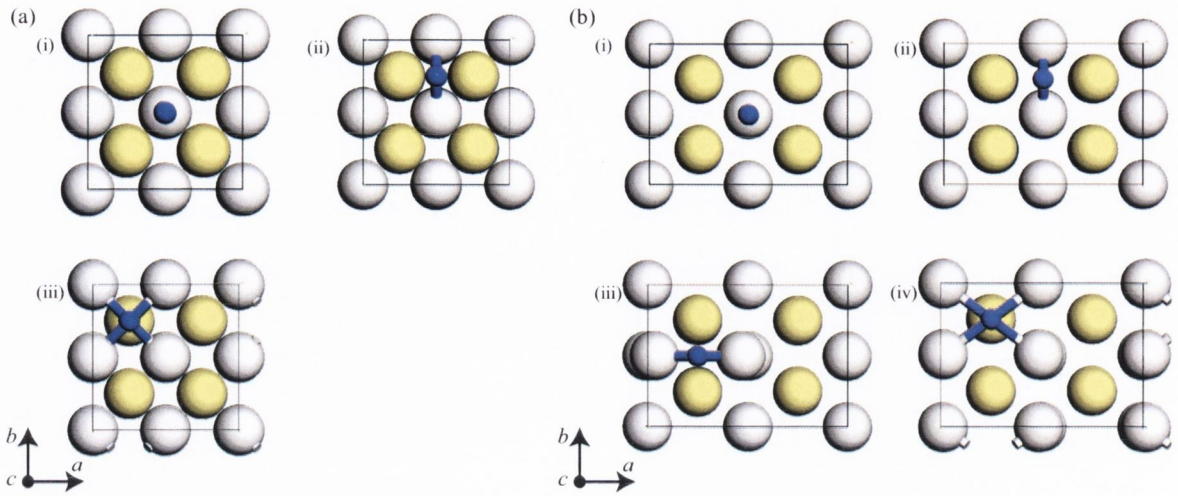


Figure 5.3: (a) The adsorption of N on the Rh {100} surface, at the (i) top, (ii) bridge and (iii) hcp sites. (b) N adsorption is also shown for {110} surface, on the (i) top, (ii) short bridge, (iii) long bridge and (iv) hcp sites. The blue sphere shows the N adsorbate, while the Rh surface layers are coloured for clarity.

transferred from the Rh surface to the N adsorbates, confirming the calculated Bader charges.

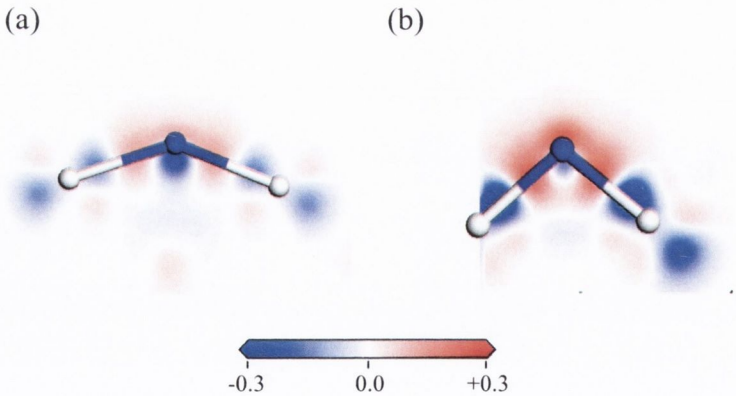


Figure 5.4: The charge difference plot for the most stable N adsorption site on the Rh (a) {100} and (b) {110} surfaces. The charge difference ranges from -0.3 (blue) to +0.3 (red) electrons Å^{-3}, as indicated by the scale.

The calculated PEDOS plots for the most stable N adsorption modes on the Rh {100} and {110} surfaces are shown in Figure 5.5. The plots show that the VB and CB are primarily a mixture of N $2p$ states and Rh $4d$ with some contributions from N $2s$ states and Rh s/p states. The plots show that there are large N $2p$ peaks at the bottom

of the VB, with N $2p$ states extended up to E_F and into the CB for both surfaces. For the {100} surface, the peak structure at the both of the VB is a large doublet while for the {110} surface the peak structure is a triplet. The N $2p$ states up to E_F are present from the occupation of N $2p$ states from the charge donation process, with the presence of states in the CB indicating that the N states are not fully occupied. The CB for N on the {100} surface contains a lesser amount of states than N on the {110} surface, which is due to the greater charge donation from the {100} surface to the N adsorbate.

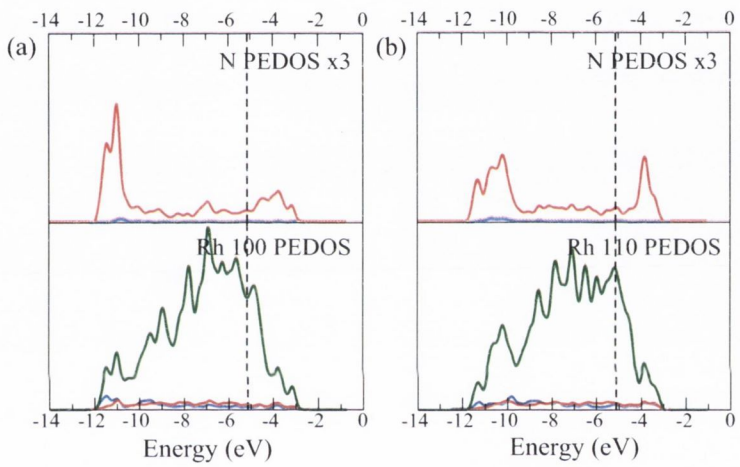


Figure 5.5: The PEDOS for N adsorption on the Rh (a) {100} and (b) {110} surfaces. The dotted line indicates the position of E_{F} and the graphs are aligned to E_{vac}. The s, p and d states are indicated by the blue, red and green lines, respectively.

5.2.2 O adsorption and analysis

The adsorption of O on the Rh {100} and {110} surfaces was carried out in a similar manner to N adsorption. The details of the CN, E_{ads}, Rh-O bond distances are given in Table 5.2 for the stable structure shown in Figure 5.6. For all O adsorbates the Rh-O bond is seen to increase with increasing coordination number of the adsorption site. The E_{ads} are calculated relative to gaseous O_2 and are seen also follow this trend for the Rh {100} surface; however for the Rh {110} surface the two coordinate bridge sites are seen to be more stable than the top and hcp sites. All the E_{ads} are seen to be exothermic and favoured on both surfaces with the hcp and short bridge being the

most stable adsorption modes on the Rh {100} and {110} surfaces, respectively. Of the most stable adsorption modes, the short bridge adsorption mode on the {110} surface is more stable. The metal surfaces are found to quench the atomic spin to 0 for all adsorption sites.

Surface	Site	CN	E_{ads} (eV)	*Rh*-O (Å)	O charge	*Rh* charge
{100}	Top	1	-0.94	1.75 (x1)	-0.60	+0.36 (x1)
	Bridge	2	-1.89	1.90 (x2)	-0.67	+0.30 (x2)
	Hcp	4	-2.08	2.15 (x4)	-0.78	+0.17 (x4)
{110}	Top	1	-1.14	1.73 (x1)	-0.59	+0.45 (x1)
	Short Bridge	2	-2.17	1.88 (x2)	-0.66	+0.30 (x2)
	Long Bridge	2	-1.51	1.95 (x2)	-0.70	+0.25 (x2)
	Hcp	4	-1.45	1.96 (x1), 2.43 (x4)	-0.78	+0.23 (x1), +0.12 (x4)

Table 5.2: The adsorption energies (E_{ads}), coordination number (CN), *Rh*-O bond lengths and Bader charges for the different oxygen adsorption modes on the Rh {100} and {110} surfaces. The number of bonds for each adsorbate on a high symmetry site is also included.

Bader analysis was carried out for all the adsorption sites on both surfaces with the charges for the O adsorbate and the Rh surface atoms that they are bound to detailed in Table 5.2. The charges for the O adsorbate are seen to increase with increased coordination of the adsorption site, while the opposite occurs for the Rh charges. The O adsorbates are seen to become more negative than atomic O for each site indicating a gain in charge, while the Rh surface atoms are seen to become more positive than the pure surface atoms, indicating a loss in charge. This shows that charge is transferred from the Rh surface to the O adsorbates with the greatest charge donated from the hcp site on both surfaces. For the Rh {100} this is the most stable adsorption site and may explain its greater stability over the other adsorption sites, while this is not the case for the Rh {110} surface. The short bridge site on the Rh {110} may be favoured over the other adsorption sites as the Rh-O bonds are at a distance preferred by the O atoms, and the individual Rh surface atoms lose greatest charge to the O adsorbate at this site.

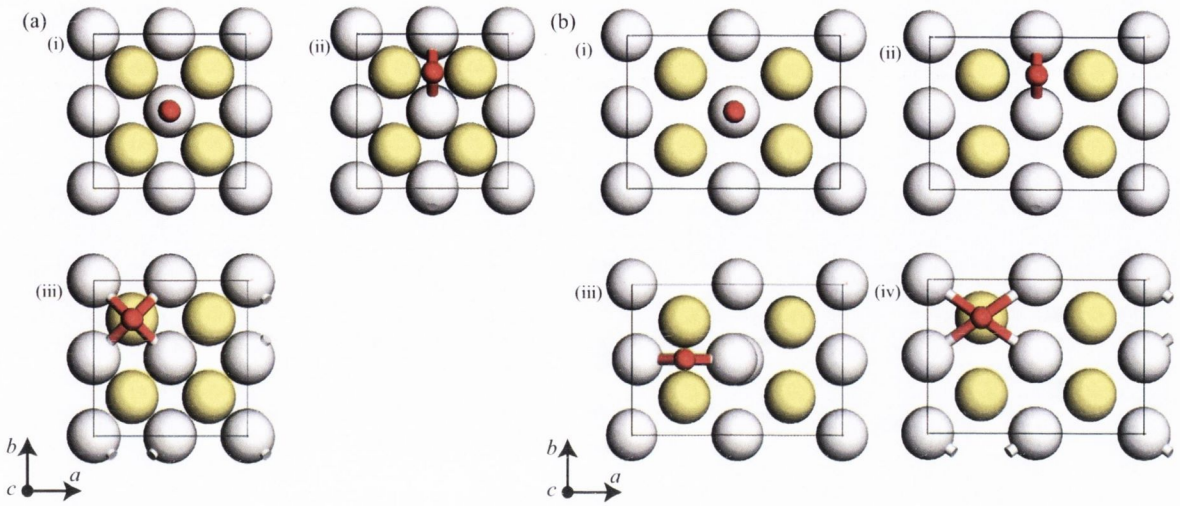


Figure 5.6: (a) The adsorption of O on the Rh {100} surface, at the (i) top, (ii) bridge and (iii) hcp sites. (b) O adsorption is also shown for {110} surface, on the (i) top, (ii) short bridge, (iii) long bridge and (iv) hcp sites. The red sphere shows the O adsorbate, while the Rh surface layers are coloured for clarity.

To illustrate the charge transfer process, the charge difference plots were determined for the most stable adsorption sites on the Rh {100} and {110} surfaces, shown in Figure 5.7. The red regions around the O adsorbate show an increase in charge, while the blue regions around the Rh surface atoms show a decrease in charge. This shows that the Rh surface donates charge to the O adsorbate forming a $O^{\delta-}$ species on the surface, and supporting the calculated Bader charges.

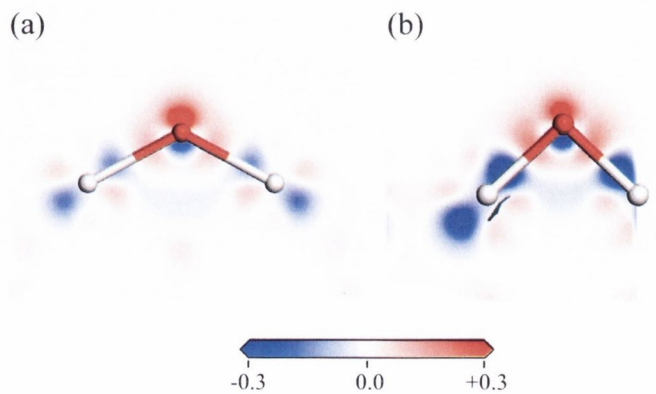


Figure 5.7: The charge difference plot for the most stable O adsorption mode on the Rh (a) {100} and (b) {110} surfaces. The charge difference ranges from -0.3 (blue) to +0.3 (red) electrons $Å^{-3}$, as indicated by the scale.

The calculated PEDOS for the most stable adsorption site on both surfaces are shown in Figure 5.8. The plots show that the VB and CB are primarily a mixture of O $2p$ states and Rh $4d$ with some contributions from O $2s$ states and Rh s/p states. The O PEDOS for adsorption on the {100} surface has a large peak at the bottom between -12 and -10 eV, and the O PEDOS for the {110} surface has a triplet peak set in a similar region on the VB. Both surfaces have occupied O $2p$ states running up to E_F that may be present due to the occupation of O $2p$ states from Rh surface charge donation to the O adsorbate. The presence of O $2p$ states in the CB indicates that the O $2p$ states are not fully filled, with the O PEDOS for the {100} system having a lesser amount compared to the CB of O on the {110} surface, due to the greater charge donated from the {100} surface.

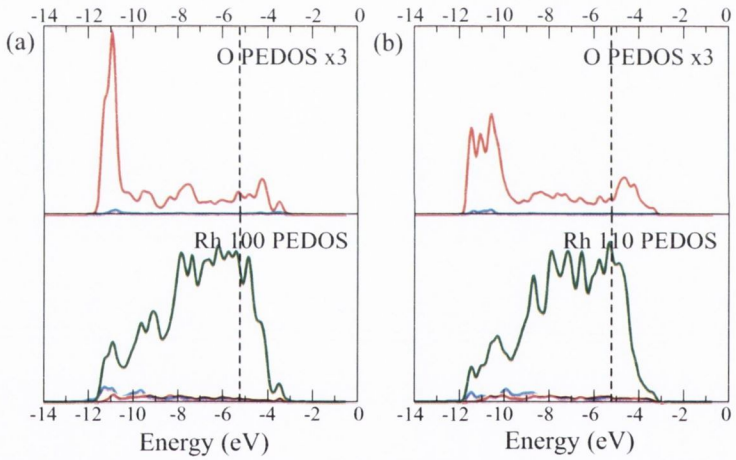


Figure 5.8: The PEDOS for O adsorption on the Rh (a) {100} and (b) {110} surfaces. The dotted line indicates the position of E_F and the graphs are aligned to E_{vac}. The s, p and d states are indicated by the blue, red and green lines, respectively.

5.2.3 NO adsorption and analysis

NO adsorption was explored on the high symmetry sites on the Rh {100} and {110} surfaces to determine the most stable adsorption mode. The E_{ads}, Rh-N and N-O bond distances, and vibrational data for each of the NO adsorption sites on both surfaces are provided in Table 5.3, for the relaxed structures that are shown in Figure 5.9. The Rh-N are seen to increase with increasing coordination of the adsorption site in

a similar manner to N adsorption, with the top site having the shortest distance and the hcp site having the longest. The N-O bond shows a similar trend, and seen to become elongated upon adsorption on the top (0.03Å), bridge (0.05Å) and hcp (0.08Å) site, relative to gaseous NO. The vibrational data show an opposite trend, with the vibrational frequencies decreasing with increasing coordination site on both surfaces. There is no sensible trend for the E_{ads} of the NO adsorbates, with the bridge being the most stable adsorption mode on the Rh {100} surface, and the short bridge site being the most stable on the {110} surface, although the top site is close in energy. Of these, the short bridge site on the {110} surface is more stable than the bridge site on the {100} surface. Molecular NO is expect to contain spin from the unpaired electron in the $2\pi^*$ orbital; however this is quenched to 0 by the interaction with the metal surfaces. The proposed tilted configuration was also tested on both surfaces, with the NO molecule relaxing back to the upright configuration. This would suggest that the tilted NO molecule on the {100} and {110} surfaces is a precursor to NO bond dissociation. The calculated vibrational frequencies are similar to the assigned vibrational bands the upright NO adsorption mode, on both surfaces.[150, 156]

Surface	Site	E_{ads} (eV)	*Rh*-N (Å)	N-O (Å)	Vib (cm^{-1})
	Gas Phase	—	—	1.15	1920
{100}	Top	-2.27	1.75 (x1)	1.18	1842
	Bridge	-2.59	1.94 (x2)	1.20	1639
	Hcp	-2.38	2.20 (x4)	1.23	1443
{110}	Top	-2.50	1.76 (x1)	1.18	1828
	Short Bridge	-2.61	1.93 (x2)	1.20	1620
	Long Bridge	-2.17	2.00 (x2)	1.20	1527
	Hcp	-1.18	2.49 (x5)	1.23	

Table 5.3: The E_{ads}, CN, *Rh*-O and N-O bond lengths, and vibrational frequencies of NO for the gas phase and high symmetry sites of NO on the Rh {100} and {110} surfaces.

The calculated Bader charges for gaseous NO (cationic, neutral, anionic), the pure

Rh surfaces, and the NO adsorbate on each of the sites for both surfaces are given in Table 5.4. The overall Bader charges for the NO adsorbates are negative, indicating charge transfer from the surface to the adsorbate which increases with increased coordination of the adsorption site. The charge transfer from each coordinated surface metal atom decreases with the coordination number, with the total transfer from the directly coordinated surface atoms not entirely accounting for the overall charge transfer; however for the top site, the overall charge is accounted for by the transferred charge. The charge gained by the adsorbates that is not accounted for by the charge lost from the bound Rh surface atoms, originates from small amounts of charge being lost from surrounding Rh atoms on the surface and subsurface layers.

	Species	NO	N charge	O charge	*M* charge
	NO^+	+1	+1.21	-0.21	—
	NO	0	+0.53	-0.53	—
	NO^-	-1	+0.10	-1.10	—
	Rh {100}	—	—	—	-0.03
	Rh {110}	—	—	—	-0.04
{100}	Top	-0.25	+0.10	-0.35	+0.29 (x1)
	Bridge	-0.35	+0.00	-0.35	+0.19, +0.14
	Hcp	-0.52	-0.05	-0.47	+0.14 (x2), +0.08 (x2)
{110}	Top	-0.21	+0.25	-0.46	+0.23 (x1)
	Short Bridge	-0.39	+0.07	-0.46	+0.17, +0.21
	Long Bridge	-0.38	+0.01	-0.39	+0.16 (x2)
	Hcp	-0.43	+0.03	-0.46	+0.10 (x1), +0.07 (x4)

Table 5.4: The calculated Bader charges for NO in the gas phase and (b) adsorption site on the Rh {100} and {110} surfaces. The Bader charges for the Pd and Pt surface atoms of the adsorption sites are also included.

The breakdown of the charges for the individual N and O atoms of the adsorbates are also detailed in Table 5.4. The charges show that for each adsorbate the N atom gains charge as it becomes less positive, while the O atoms become less negative indicating a loss of charge, compared to the neutral gaseous species. The charge gained by the

surface bound N atom appears to increase with increasing N coordination, while the O atom appears to have a similar charge for the adsorption sites of each surface, with the exception of the hcp and long bridge sites on the {100} and {110} surfaces, respectively. The greatest charge to the N atom comes from the most stable hcp site (0.58 e) on the {100} surface, with the least amount of charge lost from the O atom (0.06 e); however the bridge sites are the most stable sites for NO adsorption on the {100} and {110} surfaces, which have a lesser amount of charge donated to the N atom than the hcp site, and may be more stable due to the preferred geometric coordination similarly to N and O adsorption. The N atom gaining charge and the O atom losing charge in such a way, indicates that the mechanism for charge donation to the adsorbate is more complicated than simple direct charge transfer, in a similar manner to that observed for NO adsorption on the {111} surface. From the Bader charges it is clear that there is significant charge donation from the surface to the molecule for all of the adsorption modes, coupled with a significant redistribution of charge within the molecule leading to charge transfer from the oxygen to the nitrogen.

To illustrate the charge transfer process, Figures 5.10 a and b show the charge difference plots for NO adsorbed at the most stable adsorption sites on the {100} and {110} surfaces, respectively. The surface-bound nitrogen gains electron density (red regions), while the Rh surface atoms show a decrease in electron density (blue regions). The oxygen atom gains electron density perpendicular to the bond axis and loses electron density along the bond axis towards the nitrogen atom. This shows changes to the σ and π bonding within the molecule and supporting the complex picture of transfer and redistribution indicated by the Bader charges.

A description of the MO diagram for molecular NO, and the calculated gaseous NO is provided in Section 4.2.5. To further analyse the redistribution of charge on adsorption, the calculated PEDOS for NO adsorbed on the most stable sites of the {100} and {110} surfaces are shown in the Figure 5.11, which can be compared to gaseous NO. On adsorption, there are significant changes to the energies and composition of the orbitals with all of the orbitals reducing in energy relative to the vacuum level of gaseous NO.

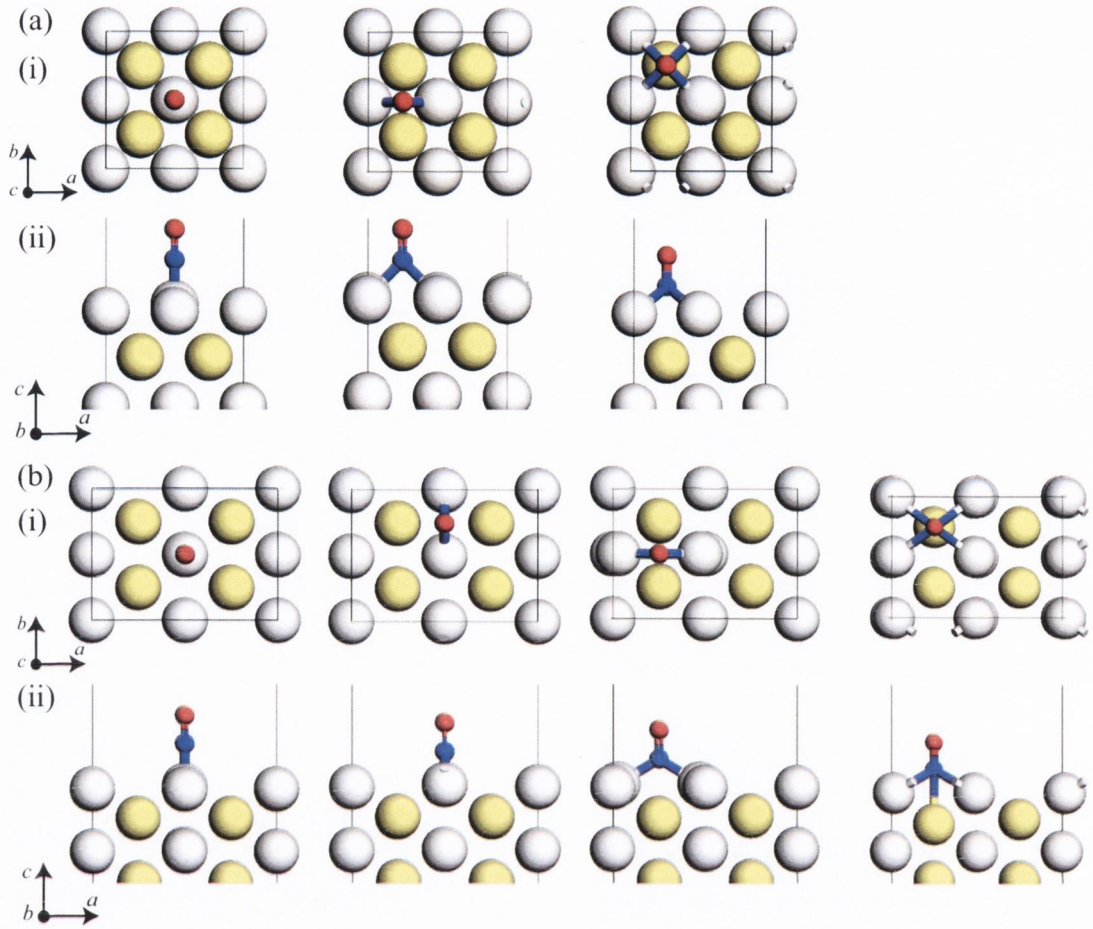


Figure 5.9: The adsorption of NO on the top, bridge and hcp sites of the Rh (a) {100} and (b) {110} surfaces. The (i) top view looking down the c-vector and (ii) side view looking along the a-vector are provided. The blue and red spheres show the N and O atoms, respectively, while the Rh surface layers are coloured for clarity.

The $4\sigma^*$ orbital gains N $2p$ contribution, while significantly losing O $2p$ contribution on both surfaces. The 5σ and 1π orbital are close in energy, with the 5σ, which is above the 1π orbital for the gaseous species, being greatly stabilised and lowered in energy to below the 1π orbital. The 1π orbital has contributions from the N/O $2p$ states similar to the gaseous species; however interaction with both surfaces has split the 1π orbital into its x and z components, with the {110} surface having greater O contributions. The contributions to the 5σ change on adsorption with an increase in the O $2s/p$ states, and thus becoming O dominated. The distribution of the lower energy orbitals, with the exception of the 5σ orbital, has changed from being O dominated for the gaseous specie to being N dominated on adsorption. The higher energy $2\pi^*$ orbital interacts

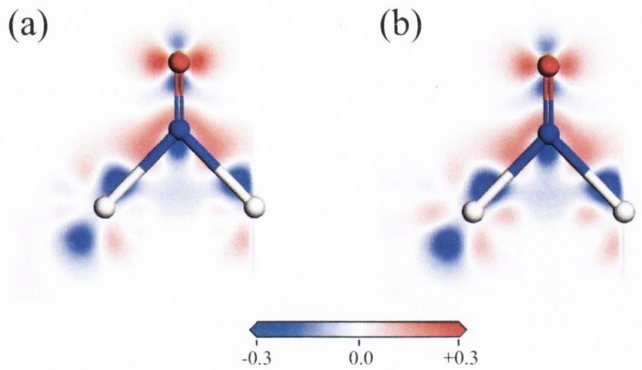


Figure 5.10: The charge difference plot for the most stable NO adsorption mode on the Rh (a) {100} and (b) {110} surfaces. The charge difference ranges from -0.3 (blue) to +0.3 (red) electrons $Å^{-3}$, as indicated by the scale.

with the Rh $4d$ band at the top of the VB, splitting it into occupied and unoccupied components around E_F. The occupied states are O dominated with some N $2p$ state contribution, while the unoccupied states of the CB are a mixture of N and O $2p$ states with a greater contribution from N.

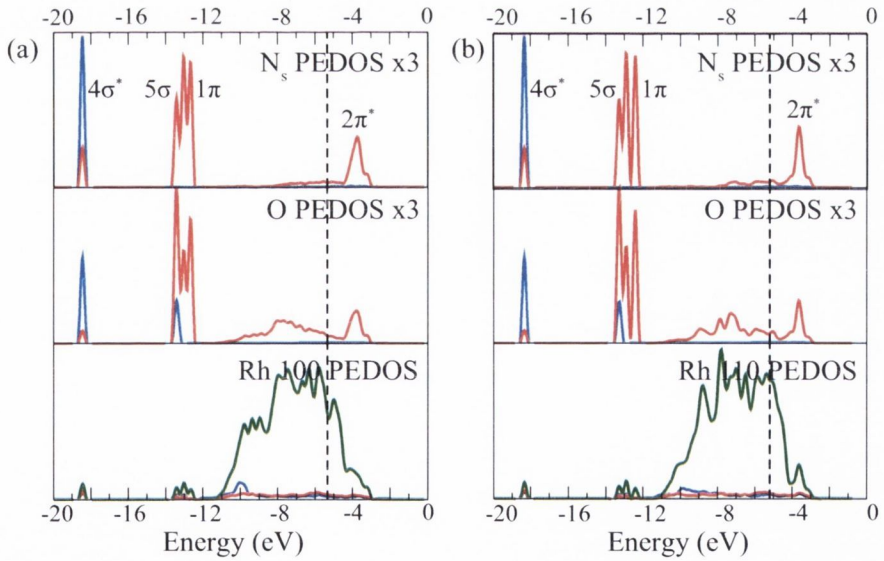


Figure 5.11: The calculated PEDOS for NO adsorption on the Rh (a) {100} and (b) {110} surfaces. The dotted line indicates the position of E_F and the graphs are aligned to E_{vac}. The s, p and d states are indicated by the blue, red and green lines, respectively.

To quantify these changes, the percentage contributions of the N $2s/p$ and O $2s/p$ states to the molecular orbitals of gas phase NO and NO adsorbed at the hcp site were

obtained by integration of the PEDOS and are detailed in Table 5.5. Comparison is only made to $NO_{(g)}$ since only minor changes are seen in the orbital character between the neutral, cationic and anionic species. The percentage contributions show that there is a redistribution and change in the electronic structure on adsorption compared to the gas phase; however, there is very little difference between the electronic structure of the NO adsorbate on the {100} and {110} surfaces. On adsorption the 4σ orbital gains N $2s/p$ character (13%/14%), while losing O $2s/p$ states (4%/23%) for NO on both surfaces. The N and O contributions to the 5σ orbital change on interacting with the surfaces, as the N $2s$ and $2p$ states reduce by 11% and 9%, respectively, while the O $2s$ and $2p$ states increase by 13% and 7%, respectively. The 1π orbital that is O dominated for gaseous NO, is N dominated on interaction with both Rh surfaces. For the higher energy $2\pi^*$ orbital, the opposite occurs for the occupied states as it significantly loses N character and becoming largely O dominated, while the unoccupied states remain N dominated.

From the analysis of the Bader charges, the charge density difference plots, the PEDOS and the changes in the orbital contributions, it is clear that there is a complex change to the electronic structure for NO adsorption on both surfaces. The overall Bader charges indicate that charge is transferred from the {100} and {110} surfaces to the NO adsorbates, with the N atoms gaining charge and the O atoms losing charge. This is seen on the charge difference plot, which also shows that that there is a complex change and redistribution to the electronic structure of the NO adsorbate, in a similar manner on both surfaces. The interaction with the metal surface stabilises the low energy orbitals, shifting them to lower energies and changing their orbital contributions. For the adsorbate, the lower energy molecular orbitals contain a greater contribution from N, while the higher energy orbitals have a greater contribution from O, reversing the effect of the greater electro-negativity of oxygen in the gas phase. This would cause the $2\pi^*$ orbital to contain a greater contribution from the O atom. The interaction of this orbital with the Rh $4d$ band splits it into occupied and unoccupied components. Charge donation to the NO adsorbate as indicated by the Bader charges is expected to occupy

	$NO_{(g)}$				
States	$4\sigma^*$	5σ	1π	$2\pi^*_{occ}$	$2\pi^*_{unocc}$
N $2s$	40	11	0	0	0
N $2p$	0	40	34	56	59
O $2s$	33	1	0	0	0
O $2p$	27	48	66	44	41
	$NO_{(ads)}$ on Rh{100}				
States	$4\sigma^*$	5σ	1π	$2\pi^*_{occ}$	$2\pi^*_{unocc}$
N $2s$	53	0	0	2	3
N $2p$	14	31	54	18	55
O $2s$	29	14	0	0	0
O $2p$	4	55	46	80	42
	$NO_{(ads)}$ on Rh{110}				
States	$4\sigma^*$	5σ	1π	$2\pi^*_{occ}$	$2\pi^*_{unocc}$
N $2s$	53	0	0	2	2
N $2p$	14	32	54	18	54
O $2s$	29	13	0	0	1
O $2p$	4	55	46	80	43

Table 5.5: The approximate percentage contributions of N $2s$, N $2p$, O $2s$ and O $2p$ states to the molecular orbitals of gas phase NO and NO adsorbed at the most stable sites of the Rh{100} and {110} surface.

the N and O states of the $2\pi^*$ orbital; however, interaction with the surface reduces the N contributions to this orbital. The $2\pi^*$ orbital is anti-bonding and the metal surface stabilises the N-O anti-bonding interaction, transferring the surface charge donation to the O atom. This effect gives rise redistribution within the NO adsorbate, allowing back-donation from the O atom to the N atom through the 5σ orbital. The charge transfer to the molecule, and the redistribution within the molecule gives rise to Bader charges which show that the nitrogen has greater charge density than the gas phase species while the oxygen atom loses charge compared to the gas phase species. There are insignificant differences in the electronic structure for NO adsorption on the two surfaces, which is also reflected in the similar E_{ads}.

5.2.4 NO_2 adsorption

The NO_2 molecule can adsorb on the Rh {100} and {110} surfaces in four different modes: μ-nitrito (N and O bound to the surface), O-O'nitrito (O and O bound to the surface), O-nitrito (single O bound to surface), and N-nitro (N bound to surface). As mentioned previously, only the first three of these are investigated here, adsorbing across the high symmetry adsorption sites. All possible orientations of each mode across the different sites were tested, with the stable configurations shown in Figure 5.12. The E_{ads} and molecular bond distances and angles for the stable configurations are provided in Table 5.6. Overall, the results show that the most stable μ-nitrito adsorption modes on the {100} and {100} surfaces indicate that N and O atoms prefer to be adsorbed at bridge positions with the surface bound atoms offset from the top sites. The adsorption of NO_2 is more stable on the {110} surface than the {100} surface, and the molecular spin of both adsorbates is zero due to quenching by the metal surface.

Surface	N	O	E_{ads} (eV)	O_s - N_s (Å)	N_s-O (Å)	O-N-O (°)
$NO_{2\,(g)}$	-	-	-	1.21	1.21	133.73
{100}	Top	Top	-1.93	1.32	1.22	118.73
{110}	Top	Top	-2.22	1.34	1.22	118.46

Table 5.6: The calculated bond lengths and angles for gaseous NO_2. The E_{ads}, adsorption site for N and O, the calculated bond connected to the surface (O_s-N_s), the N-O bond away from the surface (N_s-O) and the adsorbed NO_2 bond angle for most stable μ-nitrito adsorption mode on the Rh {100} and {110} surfaces. The subscript 's' donates the atom bound to the surface.

For the most stable μ-nitrito modes on both surfaces, Table 5.6 indicates that the bond parallel to the surface (N_s-O_s) is lengthened upon adsorption, while the N-O bond perpendicular to the surface is of a similar length to gaseous NO_2, with a reduction in the bond angle. The calculated asymmetric, symmetric and bending vibrational modes for the μ-nitrito mode on the {100} surface were determined to be 1526 cm^{-1}, 951 cm^{-1} and 749 cm^{-1}, respectively, and on the {110} surface, 1526 cm^{-1}, 897 cm^{-1}, and 738 cm^{-1}. The vibrational frequencies for the NO_2 molecule have decreased on

interaction with the metal surface with the exception of the bending mode, compared to the calculated values of 1682 cm^{-1}, 1348 cm^{-1} and 729 cm^{-1} for gaseous NO_2, which are close to the experimental values (1618 cm^{-1}, 1318 cm^{-1}, 750 cm^{-1}). The adsorption mode for NO_2 has not been detected on the low index surfaces, thus there is no experimental vibrational data for comparison.

HREELS studies of NO_2 on the clean Pd {111} surface have characterised the μ-nitrito configuration by assigning vibrational frequencies of 1545 cm^{-1}, 1170 cm^{-1}, and 790 cm^{-1},[110] and for the clean Pt {111} surface as 1560 cm^{-1}, 1180 cm^{-1}, and 795cm^{-1},[111] to the asymmetric, symmetric and bending modes, respectively, which has also been supported by density functional theory (DFT) studies.[94, 97] These bands fall within the difference between the calculated frequencies and that of the gaseous NO_2 species, suggesting that the μ-nitrito could possibly be the NO_2 adsorption mode on the low index surfaces.

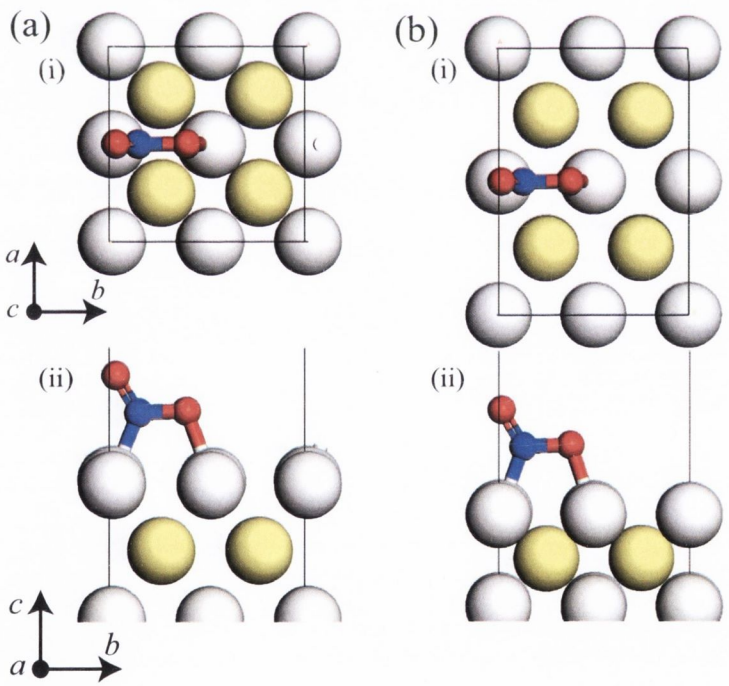


Figure 5.12: The most stable adsorption modes of NO_2 on the Rh (a) {100} and (b) {110} surfaces. The (i) top view looking down the c-vector and (ii) side view looking along the a-vector are provided. The blue and red spheres show the N and O atoms, respectively, while the Rh surface layers are coloured for clarity.

To assess the electronic interactions between NO_2 and the metal surface, the Bader

charges for the individual atoms of both μ-nitrito modes, were calculated along with the Rh surface atoms that the NO_2 molecules were bonded to, and are shown in Table 5.7. The equivalent charges for the gaseous molecules and pure Rh {111} surface are also given in Table 5.7. For both NO_2 adsorption modes the overall charge on the molecules is negative, -0.43 e for the μ-nitrito mode on the {100} surface and -0.46 e on the {110} surface. The change in overall charge of the Rh surface atoms that are directly bound to the NO_2 adsorbates are positive, indicating that there is a transfer of charge from the surface to the adsorbate. The discrepancy between the charge gained by the adsorbates and the charge lost from the Rh surface atoms that the molecules are bound to, is due to small amounts of charge being lost from surrounding Rh atoms on the surface and subsurface layers.

	Species	NO_2	N charge	O charge	O charge	Rh charge
(a)	NO_2^+	+1	+0.93	+0.03	+0.04	-
	NO_2	0	+0.73	-0.34	-0.39	-
	NO_2^-	-1	+0.38	-0.69	-0.69	-
	Rh {100}	-	-	-	-	-0.03
	Rh {110}	-	-	-	-	-0.04
(b)	μ nitrito on Rh {100}	-0.43	+0.44	-0.49*	-0.38	+0.18, +0.20
	μ nitrito on Rh {110}	-0.46	+0.40	-0.47*	-0.39	+0.18, +0.23

* O atom bonded to surface

Table 5.7: (a) The calculated Bader charges for gaseous NO_2 and the Rh surface atoms of the pure surface, and (b) for adsorbed NO_2 on the Rh {100} and {110} surfaces, and the Rh atoms they are bound to.

The Bader charges of the individual adsorbate atoms show that the N atom is less positive than the corresponding N atom of the gaseous species for both adsorption modes, with the N atom of the μ-nitrito mode on the {110} surface being the least positive. This indicates that the N atom has gained charge relative to the gaseous species, 0.31 e and 0.33 e on the {100} and {110} surfaces, respectively. The O_s atoms of both adsorption modes are more negative than the O atoms for the gaseous species, and

the unbound O atom has a charge similar to the gaseous NO_2 species (a difference of 0.01 e). For simple charge transfer, the charge lost from the surface Rh atoms would be expected to be located at the surface-bound atoms of the adsorbate. However as with NO adsorption, this is not seen to be the case, indicating that a more complex mechanism must be occurring. The charge donated from the Rh surface to the adsorbates must be coupled with a significant redistribution of the σ and π systems within the molecules to account for the gain in charge by the individual atoms of the adsorbates, in a similar manner to NO adsorption.

To visualise the charge transfer process, the charge difference is plotted for both μ-nitrito adsorption modes in Figures 5.13 (a) and (b), respectively. The charge difference plots show that for both adsorbates, all the adsorbate atoms gain charge, while the Rh surface atoms loose charge in accordance with the overall charge donation process as indicated by the Bader charges. There are however, negative regions as well as positive regions surrounding the atoms of the adsorbates suggesting that there is a significant change in the σ and π systems of the adsorbate when interacting with the metal surface. This shows that there is considerable redistribution of electron density across the adsorbates upon adsorption on the Rh surface.

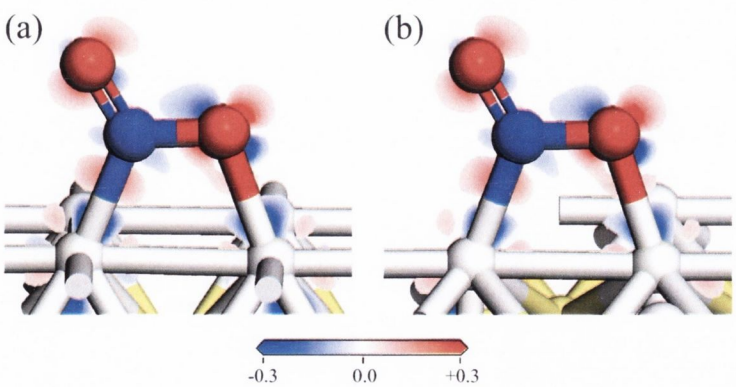


Figure 5.13: The charge difference plot for the most stable NO_2 adsorption mode on the Rh (a) {100} and (b) {110} surfaces. The charge difference ranges from -0.3 (blue) to +0.3 (red) electrons $Å^{-3}$, as indicated by the scale.

In order to further analyse the charge distribution of the NO_2 adsorbate, the electronic structure for the most stable μ-nitrito modes are shown in Figure 5.14. The

MO diagram for the valence molecular orbitals of NO_2, and the calculated PEDOS for gaseous NO_2 are shown and described in Section 4.2.6.

The electronic structure for both μ-nitrito adsorption modes are seen to be different to gaseous NO_2 due to the interaction with the Rh surface; however the characteristics of their respective electronic structures are quite similar. The low energy valence orbitals appear to be lowered in energy, relative to the gaseous species, upon interaction with the Rh surfaces. The 6σ orbital is seen to gain some additional N $2p$ contribution for both modes on interaction with the Rh surfaces, while the 7σ and 1π orbitals of the gaseous species have similar compositions to gaseous NO_2. The 1π orbital is stabilised by the surface interaction, lowering it in energy and causing it to appear lower than the 7σ orbital, which is is above for NO_2g. The top of the VB for both adsorbates primarily contains O $2p$ states, mixing with some N $2p$ states, and the Rh $4d$ band. The MO diagram and calculated PEDOS for the gaseous species shows that this region contains a mixture of the $2\pi^{\mathrm{nb}}$ and $3\pi^*$ orbitals, which interact with the Rh $4d$ band from -12 eV up to E_{F}, smearing out the N and O $2p$ states. The CB of the adsorbates contains N/O $2p$ states with a peak around -4 eV, which are the unoccupied $3\pi^*$ states.

To quantify the changes in the NO_2 electronic structure upon adsorption, the percentage contributions of the N and O $2s/p$ states to the molecular orbitals of gaseous and adsorbed NO_2 were obtained by integrating the PEDOS and are detailed in Table 5.8. As the 7σ and 1π orbitals are so close in energy, it is hard to distinguish between them for the gaseous NO_2 species, and the N/O $2s/p$ contributions to these orbitals are grouped together in the Table. For both adsorbates, the $2\pi^{\mathrm{nb}}$ and $3\pi^*_{\mathrm{occ}}$ orbitals mix at the top of the valence band, making it difficult to distinguish between their N/O $2s/p$ contributions. The contributions are thus approximated by taking the percentage of states at a similar energy range to that for the analogous orbitals of the gaseous species.

The percentage contribution values of the N/O $2s/p$ states to the molecular orbitals show a considerable change in the electronic structure of both μ-nitrito modes relative to gaseous NO_2; however there is very little difference in their percentage contributions,

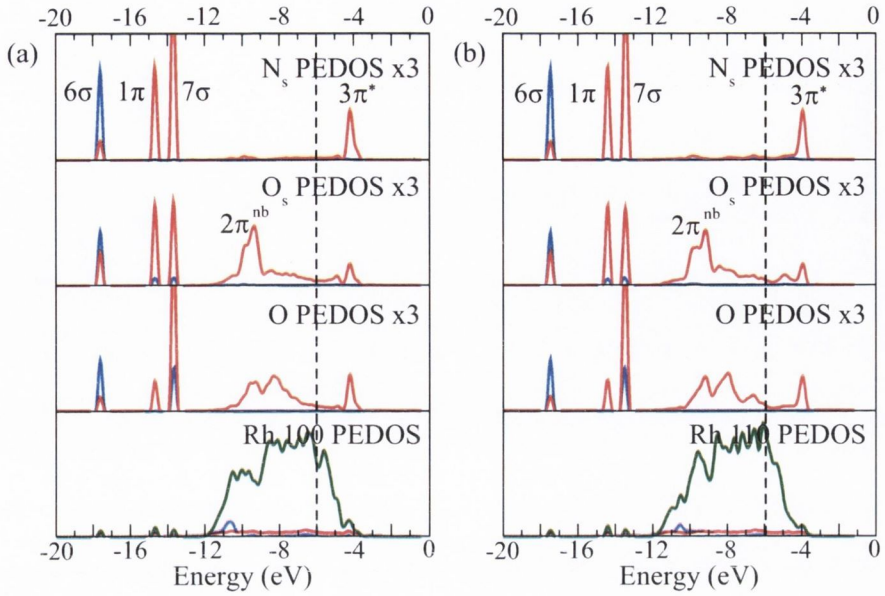


Figure 5.14: (a) Molecular orbital diagram for NO_{2g}. The PEDOS for (b) gaseous NO_2 and the most stable NO_2 adsorption modes on the Rh (c) {100} and (d) {110} surfaces. The dotted line indicates the position of E_F and the graphs are aligned to E_{vac}. The s, p and d states are indicated by the blue, red and green lines, respectively.

relative to one another. Upon adsorption, the composition of the 6σ orbital shows an increase from the N $2s/p$ states, and a considerable loss of O $2p$ states, which may indicate transfer of density from the unbound O atom to the N_s atom of both modes. The contributions to the $7\sigma/1\pi$ system of both adsorbates is relatively unaffected, indicating that either only small changes in the composition are observed, or that the redistribution of one orbital is complimentary to the other. The higher energy $2\pi^{nb}$ orbital gains N $2p$ and O_s $2p$ character while losing O $2p$ states for both adsorbates interacting with the Rh surfaces. The $3\pi^*_{occ}$ loses N $2s/p$ states, and gains O_s $2s$ states (25%) for the NO_2 adsorbate on the {100} surface, and gains O $2p$ (22%) for the NO_2 adsorbate on the {110} surface. The unoccupied states of the $3\pi^*$ orbital loses N_s $2p$ contribution, while there is an increase in the O_s contributions with the O $2p$ states decreasing in contribution to this orbital.

Overall, the stabilisation and shift to lower energies for the σ orbitals allows the μ-nitrito adsorbates to have greater N character for these orbitals, and allowing the higher orbitals to become O dominated. Although both adsorbates have similar electronic

structures when interacting with the {100} and {110} surfaces, the main difference between them is that when NO_2 adsorbs on the {100} surface there is a large increase (25%) in the O_s $2p$ contribution to the $3\pi^*$ orbital, while for NO_2 interacting with the {110} surface, there is a large increase for the O $2p$ states (22%) of the O atom not bound to the surface.

	$NO_{2\,(g)}$				
States	6σ	$7\sigma/1\pi$	$2\pi^{nb}$	$3\pi^*_{occ}$	$3\pi^*_{unocc}$
N $2s$	27	0	0	8	7
N $2p$	1	38	0	24	27
O $2s$	21	4	0	0	0
O $2p$	15	27	50	34	33
O $2s$	21	4	0	0	0
O $2p$	15	27	50	34	33
	μ-nitrito on Rh{100}				
States	6σ	$7\sigma/1\pi$	$2\pi^{nb}$	$3\pi^*_{occ}$	$3\pi^*_{unocc}$
N_s $2s$	35	0	0	1	7
N_s $2p$	7	39	5	5	19
O_s $2s$	21	2	1	1	2
O_s $2p$	12	24	60	59	44
O $2s$	20	6	0	0	2
O $2p$	5	29	34	34	26
	μ-nitrito on Rh{110}				
States	6σ	$7\sigma/1\pi$	$2\pi^{nb}$	$3\pi^*_{occ}$	$3\pi^*_{unocc}$
N $2s$	35	0	0	1	6
N $2p$	7	39	5	7	21
O_s $2s$	20	2	1	1	2
O_s $2p$	13	23	61	35	44
O_s $2s$	20	6	0	0	0
O_s $2p$	5	30	33	56	27

Table 5.8: The approximate percentage contributions of N $2s$, N $2p$, O $2s$ and O $2p$ states to the molecular orbitals of gas phase NO_2 and the μ-nitrito adsorption modes on the Rh {100} and {110} surfaces.

From the analysis of the Bader charges, the charge density difference plots, and the

changes in the orbital contributions it is clear that there is a complex change to the electronic structure on NO_2 adsorption on the {100} and {110} surfaces, in a similar manner to the {111} surface. The overall Bader charges show that there is charge transfer from the Rh surfaces to both of the adsorbates; however the breakdown of the individual charges suggests that there is a rearrangement of the σ and π bonding within the adsorbate, which can also be seen on the charge difference plots. The 6σ, 7σ and 1π orbitals are lowered in energy with a shift in their N/O contributions for both adsorbates. For both adsorption modes, these orbitals contain a greater contribution from the surface-bound atoms relative to gaseous NO_2, with an greater increase in the N $2s/p$ contributions to the 6σ orbital and a significant decrease in the O $2p$ state contribution to this orbital. The higher energy π orbitals are typically dominated by O $2p$ states, with an increase in O_s $2p$ states to the $2\pi^{nb}$ orbital and a decrease in contribution from the O atom not bound to the surface to this orbital. There is an increase in the O $2p$ states to $3\pi^*_{occ}$ orbital from the O surface bound atom for NO_2 on Rh {100} and from the unbound O atom for NO_2 on Rh {110}, relative to gaseous NO_2. The opposite occurs for the unoccupied states of the $3\pi^*$ orbital, where it is seen that the N $2p$ states decrease while the O_s $2p$ states increase to this orbital when interacting with the Rh surface.

The mechanism for charge donation to the μ-nitrito mode on both surfaces is complicated. The negative charges on the N_s and O_s atoms can be accounted for by the increase in N $2s/p$ contributions to the 6σ orbital, and N/O $2p$ contributions to the $2\pi^{nb}$ from the electronic redistribution for NO_2 on interacting with the Rh surfaces. The charge lost from the surface bound Rh atoms is transferred to the $3\pi^*$ orbital of the NO_2, with the density residing on the O_s atom for NO_2 on the {100} surface, and the O atom not bound to the surface for the {110} surface. This indicates that the charge transfer mechanism from the surface to the NO_2 adsorbate is different on both surfaces. For NO_2 on the {100} surface the surface charge transfer is directly to the surface bound O atom; however for NO_2 on {110}, the charge transfer to the O atom not bound to the surface can be explained by the stabilisation of the anti-bonding $3\pi^*$

orbital interaction between N_s and O. This reduces the N contribution and transfers the electron density donated from the surface to the unbound O atom of the adsorbate in a similar manner to that observed for NO adsorption. This is balanced by the transfer of electron density back to the N_s atom through the 6σ orbital accounting for the increased charge of the N atom, and the charge of the O atom being similar to gaseous NO_2. The more stable E_{ads} for NO_2 on the {110} surface suggests that the stabilisation of the NO anti-bonding interaction by the {110} surface, and transferring density to the unbound O atom, suggests that this electronic configuration is preferred over the electronic rearrangement of NO_2 on the {100} surface.

5.2.5 N_2 and O_2 adsorption on the Rh {100} and {110} surfaces

The most stable adsorption modes for N_2 and O_2 were explored on the Rh {100} and {110} surfaces by trialling the different molecular orientations, perpendicular and flat on the surface, across the four high symmetry adsorption sites. A number of configurations were thus examined and relaxed, with the most stable configuration for N_2 and O_2 adsorption shown in Figure 5.15. The N_2 molecule is shown to prefer adsorption perpendicular to the top site on both surface, while the preferential adsorption mode for O_2 was calculated to be flat across the small bridge on both surfaces. The E_{ads} for the most stable adsorption modes for N_2 and O_2 were calculated to be -0.61 eV and -1.75 eV, respectively, on the {100} surface, while for the {110} surface these were calculated to be -0.81 eV and -2.15 eV. The adsorption energies indicate that both molecular species are more stable on the {110} surface, with the O_2 being more stable than N_2 and both metal surfaces were found to quench the molecular spin of the adsorbate to zero. On adsorption, the molecular bonds for N_2 and O_2 were calculated to be 1.14 Å and 1.38 Å, respectively, on both surfaces, showing a lengthening and weakening from the calculated bonds for gaseous N_2 (1.12 Å) and O_2 (1.23 Å). The N-Rh bond was calculated to be 1.92 Å while for the O_2 adsorbate, the bonds were calculated to be 1.94Å at the

top site. The calculated values indicate that the O-O bond is elongated further than the N-N bond on adsorption, indicating that the O-O bond of the adsorbate becomes much weaker than the N-N when interacting with the Rh surface. Detailed analysis of the electronic structure and interactions for the most stable adsorbates on the metal surfaces are not presented, as the bond lengths are similar to that of N_2 and O_2 on the {111} surface, indicating that their electronic structures should be similar to that presented previously (Section 4.2.7)

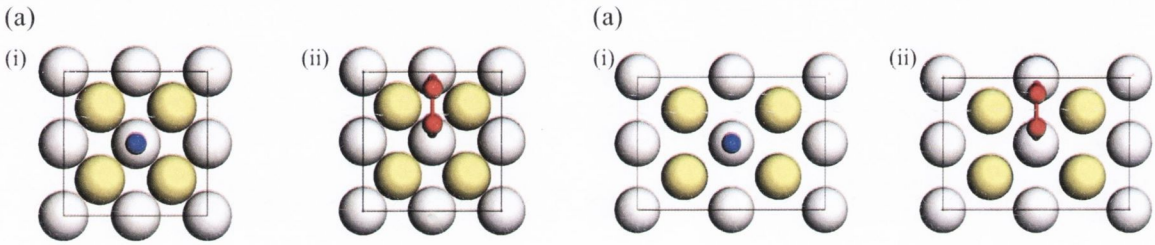


Figure 5.15: The calculated most stable adsorption modes on the Rh (a) {100} and (b) {110} surfaces for (i) N_2 and (ii) O_2. The blue and red spheres are the nitrogen and oxygen atoms, respectively, with the top (white) and second (yellow) layers coloured for clarity.

5.2.6 Decomposition Profile

The reaction energies for each process in the NO and NO_2 decomposition pathways on the Rh {100} and {110} surfaces were calculated using the energies of the most stable adsorption modes for N, O, NO, N_2, O_2 and NO_2, as detailed in Table 5.9. The decomposition pathways for NO_2 and NO on the Rh low index surfaces can also be summarised graphically, as shown in Figures 5.16 (a) and (b), respectively

The decomposition of NO_2 is exothermic on both surfaces, being more favoured on the Rh {100} surface than on the {110} surface. There is thus a greater drive to form NO+O on the {100} surface, even though the NO and O adsorbates are more stable on the {110} surface; however there is not a huge difference between the E_{ads} of NO and O on the two surfaces. The subsequent breakdown of NO is also exothermic on both surfaces, and is more favoured on the Rh {100} surface. The more favourable breakdown

		Reaction Step	{100} (eV)	{110} (eV)
(a)	(i)	$NO_{2(g)} \rightarrow NO_{2(ads)}$	-1.94	-2.22
	(ii)	$NO_{2(ads)} \rightarrow NO_{(ads)} + O_{(ads)}$	-1.56	-1.38
	(iii)	$NO_{(ads)} + O_{(ads)} \rightarrow N_{(ads)} + 2O_{(ads)}$	-0.97	-0.65
	(iv)	$N_{(ads)} + 2O_{(ads)} \rightarrow \frac{1}{2}N_{2(ads)} + 2O_{(ads)}$	+0.21	-0.27
	(v)	$\frac{1}{2}N_{2(ads)} + 2O_{(ads)} \rightarrow \frac{1}{2}N_{2(g)} + 2O_{(ads)}$	+0.31	+0.41
	(vi)	$\frac{1}{2}N_{2(g)} + 2O_{(ads)} \rightarrow \frac{1}{2}N_{2(g)} + O_{2(ads)}$	+2.41	+2.18
	(vii)	$\frac{1}{2}N_{2(g)} + O_{2(ads)} \rightarrow \frac{1}{2}N_{2(g)} + O_{2(g)}$	+1.75	+2.15
(b)	(i)	$NO_{(g)} \rightarrow NO_{(ads)}$	-2.59	-2.61
	(ii)	$NO_{(ads)} \rightarrow N_{(ads)} + O_{(ads)}$	-0.97	-0.65
	(iii)	$N_{(ads)} + O_{(ads)} \rightarrow \frac{1}{2}N_{2(ads)} + O_{(ads)}$	+0.21	-0.27
	(iv)	$\frac{1}{2}N_{2(ads)} + O_{(ads)} \rightarrow \frac{1}{2}N_{2(g)} + O_{(ads)}$	+0.31	+0.41
	(v)	$\frac{1}{2}N_{2(g)} + O_{(ads)} \rightarrow \frac{1}{2}N_{2(g)} + \frac{1}{2}O_{2(ads)}$	+1.21	+1.09
	(vi)	$\frac{1}{2}N_{2(g)} + \frac{1}{2}O_{2(ads)} \rightarrow \frac{1}{2}N_{2(g)} + \frac{1}{2}O_{2(g)}$	+0.88	+1.08

Table 5.9: The calculated energies for each step of the (a) NO_2 and (b) NO decomposition pathways on the Rh {100} and {110} surfaces.

of NO can be attributed to the more stable N ad-atoms on the {100} surface, and also there is a small difference (0.09 eV) in the O E_{ads} for both surfaces. The breakdown of NO_x is more favourable on the {100} surface than the previously examined {111} surface of the three metals. The trend for *de*NO_x on the low index surfaces is, from the surface with the most favourable energy, {100} > {111} > {110}, indicating that the closely packed {111} surface is more active for *de*NO_x than the more open {110} surface. The cause for this trend is the stability of the surface bound N ad-atoms as their relative E_{ads} follow a similar pattern, while the E_{ads} for resultant O species does not.

The formation of N_2 on the {100} surface is endothermic while N_2 formation on the {110} surface is exothermic. This indicates that N_2 formation is more favourable on the {110} surface, and that a different mechanism must be occurring than on the {100} surface. For both surfaces the removal of N_2 requires energy, which is 0.1 eV less on the {100} surface. These steps indicate that the {110} surface can form N_2, but N_2

desorption is easier from the {100} surface. Energy is also required on the {111} surface to form N_2; however the required energy is lower than the {100} surface. Similar to the {111} surface, there is a large energy required to form and remove O_2. The formation of O_2 is much more difficult on the {100} surface than on the {110} surface, while the subsequent desorption is much more favourable from the {100} surface. The formation of O_2 requires less energy on both surfaces than the {111} surface, while its removal from the {111} needs less energy than the other low index surfaces. The large energies associated with O_2 formation and desorption are due to the large E_{ads} of the O species on all three surfaces. This indicates that O is difficult to remove from rhodium metal, regardless of the surface index, and thus requires a reductant.

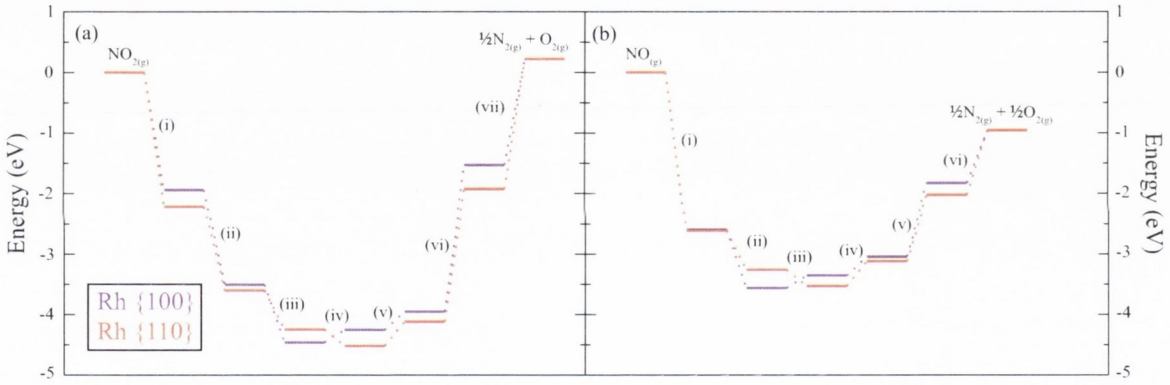


Figure 5.16: The calculated energies for the dissociation profile of (a) NO_2 and (b) NO on the Rh {100} and {110} surfaces. The purple and orange lines indicate the {100} and {110} dissociation pathways, respectively.

5.2.7 Discussion

As mentioned previously, there are two proposed mechanisms for charge donation from a metal surface to an adsorbate; (1) the Blyholder model[93] and (2) the more recently proposed allylic configuration.[100–104] A description of the Blyholder model suggesting direct charge transfer from the metal surface to the adsorbate, and the allylic configuration established by XPS for CO and N_2 on metal surfaces,[100–104] was provided in Section 4.3, and a similar discussion is not required.

The electronic structure of the most stable NO and NO_2 adsorbates on the {100} and {110} surfaces was characterised using Bader charge analysis, charge difference plots and PEDOS. The Bader charge analysis indicates that there is an overall charge donation from the surface to both adsorbates, with the charge difference plots showing a considerable change to the σ and π systems upon interaction of the adsorbates with the Rh surfaces. The interaction of NO_x molecules with the surfaces causes a redistribution of electron density within both adsorbates. For NO this interaction stabilises the N-O $2\pi^*$ anti-bonding orbital, reducing the N $2p$ contribution to this orbital, and transferring the donated electron density from Rh to the O atom. The electronic structure for NO adsorption is similar on both surfaces, which is reflected in the adsorption energies. The charge redistribution on interaction with the {100} and {110} surfaces is similar to the {111} surface, indicating that a similar charge donation mechanism occurs for NO adsorption on rhodium metal, regardless of the metal surface index. The difference in the electron structures of the NO adsorbates on the {100} and {110} to the NO adsorbate on the {111} surface can be seen in the contribution from the unbound O to the occupied states of the $2\pi^*$ orbital, and the N contribution to the $4\sigma^*$ orbital. These contributions are larger than for NO on the {111} surface, perhaps explaining the greater stability.

A similar stabilisation of the $3\pi^*$ orbital is observed for the interaction of μ-nitrito mode with both surfaces, indicating that the NO_2 adsorbate behaves like an NO molecule with an elongated bond to an O ad-atom. Similar to NO adsorption, the NO_2 adsorbate is more stable on the {100} and {110} surfaces due to the greater contribution from the unbound O atom to the occupied states of the $3\pi^*$ orbital. The absence of N $2p$ contributions to this orbital can been seen at the top of the valence band. Direct donation to the π^* orbital is therefore shown not occur, suggesting that the Blyholder model does not hold for NO_x adsorption on the Rh {111} surface. The electronic rearrangement of the σ and π systems, along with the stabilisation of the anti-bonding orbitals would suggest that a more complicated mechanism is occurring, similarly to that proposed by the allylic configuration. The electronic structure for

NO_x on the low index surfaces is closely related to the allylic configuration as; (1) the 5σ for NO, and 1π for NO_2 are greatly stabilised on the rhodium surface compared to gaseous NO_x, and (2) the $2/3\pi^*$ orbitals are stabilised and dominated by O $2p$ states at the top of the valence band. This can be linked to the non-bonding electron pair, which interacts with the Rh $4d$ states giving the $\widetilde{d}_\pi$ band, a filled state at the top of the VB similar to N_2 and CO. This indicates that the allylic configuration can be extended to all low index surfaces of rhodium metal, suggesting that this mechanism provides a complete description of surface-adsorbates charge donations on metal surfaces.

The calculated *de*NO_x profile in this study provides an insight into the presence of low index surfaces on the catalyst surface within *de*NO_x technologies. The {100} and {110} surfaces provide different advantages for *de*NO_x chemistry. The {100} surface is a better catalyst to drive the decomposition reaction to breakdown NO, while the {110} surface is more useful for the formation of N_2. A mixture of both these surfaces on the rhodium metal catalyst would provide advantages for different steps of the *de*NO_x pathway. The selectivity of the Rh surface for producing N_2 and other organo-nitro species under rich conditions (excess fuel) may be attributed to the {110} surface. Similar to the {111} surface, the low index surfaces break the NO bond exothermically, supporting suggestions that this is the reason why Rh metal is efficient at *de*NO_x.[70, 71] In order for alternative *de*NO_x catalysts to emulate the properties of Rh metal, they would therefore have to be exothermic and favour the breaking the NO bond, while also having a strong interaction with N and O atoms. This is an important attribute of Rh metal as under rich conditions it is difficult to form N_2 in the presence of excess hydrocarbons.[367]

The strong interaction of the O ad-atoms with the low index surfaces will most likely cause the saturation of the surface with O atoms, when a high oxygen concentration is present. This will lead to deactivation of the catalyst, hindering any further *de*NO_x; however this may also be beneficial to Rh as a three-way catalyst, as the O surface species are more likely to remain in their adsorption site and unlikely to form O_2. This will allow the easy oxidation of a reductant such as CO or H_2; however under

lean conditions (excess oxygen) the excess O may inhibit NO_x breakdown, explaining why Rh can be inefficient under lean conditions.[25, 68, 367, 368] The facile removal of surface O ad-atoms from the Rh surface using a reductant such as CO or H_2 will allow regeneration of the catalyst and assist in further breakdown of NO_x. For NO_x storage-reduction catalysts, lean-trap NO_x and selective catalytic reduction of NO_x, the strong interaction of O with the surface would allow activation of fuel hydrocarbons, forming a $C_xH_yO_z$ intermediate species, which has been suggested to assist in the *de*NO_x process.[369–371]

5.3 Rh {443} stepped surface

The Rh {443} stepped surface was generated using the METADISE code in a similar way to the Rh low index surfaces. Similarly to previous generated surfaces, the slab model was employed for the Rh {443} stepped surface using 7-layers and a 15Å vacuum gap. The surface was expanded to a p(3x1) structure, and relaxed using a Γ-centred k-point sampling density grids of 5x4x1, consistent with the k-point sampling density of the metal bulk. The surfaces were relaxed using a plane wave energy cut-off of 400 eV, and they were deemed converged when the forces acting on the atoms were reduced to less than 0.01 eV/Å. The relaxed structure of the Rh {443} p(3x1) surface is shown in Figure 5.17 with the step edge and terrace indicated in Figure 5.17 (a), and all the possible high symmetry adsorption sites on the step and the terrace labelled in Figure 5.17 (b). The figure shows that the Rh {443} stepped surface adopts a {111} close packing arrangement above and below the surface step layer which is coloured white, and the top, hcp and fcc layers of the {111} terrace below the step are coloured yellow, green, and blue for clarity. The {443} surface is thus an extended {111} surface with a step present, and has four high symmetry sites (top, bridge, hcp, fcc) that will be tested to find the most stable adsorption site for each of the adsorbates (N, O, NO, NO_2). There are a number of different possible sites to be tested due to different coordination environments of each site above and below the step as labelled in the figure.

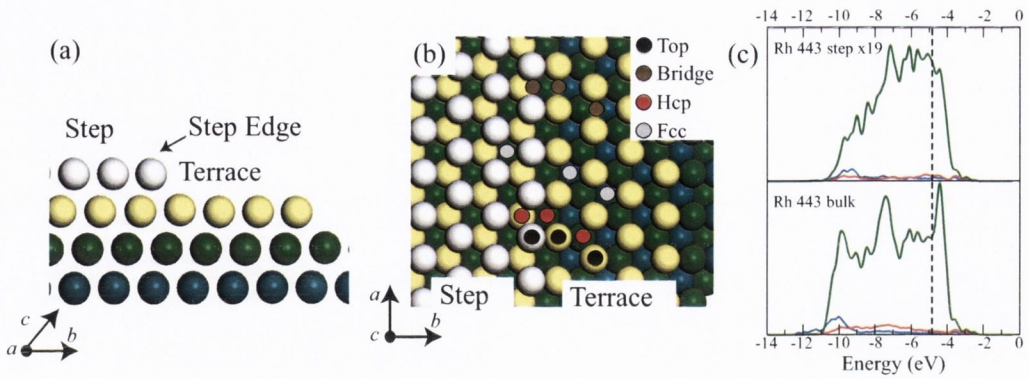


Figure 5.17: The structure of the Rh stepped {443} surface, along the (a) b-vector and (b) c-vector is indicate the position of all possible high symmetry sites that are labelled. The top (white) and second (yellow) layers are coloured for clarity. (c) The PEDOS of the Rh stepped {443} surface and the inner bulk layers. The dotted line indicates the position of E_{F} and the graph is aligned to E_{vac}. The s, p and d states are indicated by the blue, red and green lines, respectively.

The calculated PEDOS for the Rh {443} stepped surface is shown in Figure 5.17 (c). The PEDOS for the surface step is separated from the rest of the metal slab (bulk) to show its different electronic structure due to the different coordination environment of the step. Both PEDOS plots show that the VB up to E_{F} and the CB beyond, are made up mostly by Rh $4d$ states with a minor mixing of Rh s and p states. The PEDOS of the step is largely magnified compared to the slab bulk, as the number of metal atoms on the step is small in comparison to the number present in the rest of the slab. The PEDOS for the bulk has a similar electronic structure to previous slab bulks of the low index surfaces, indicating a consistency in the calculations; however, the electronic structure of the step shows that it has a high concentration of Rh $4d$ states at E_{F} that trails off towards the end of the VB around -12 eV. The position of the E_{F} relative to E_{vac} is quite similar to the Rh {100} surface and lower than the {110} surface suggesting that charge donation to the adsorbates will be similar to the Rh {100} surface.

5.3.1 N adsorption and analysis

The adsorption of N was explored on all the possible high symmetry sites above and below the step, and on the terrace of the Rh {443} stepped surface. The structures for

the most stable adsorption modes are shown in Figure 5.18, with the structures for the hcp below the step, and the top and bridge sites being absent since these relaxed to other adsorption modes. For the top and bridge sites below the step, the N adsorbate relaxed to bond with the step atoms to form a three and four coordinated adsorption mode, respectively. All other adsorption modes typically formed one, two and three coordinated adsorption modes for the top, bridge and fcc/hcp sites, respectively.

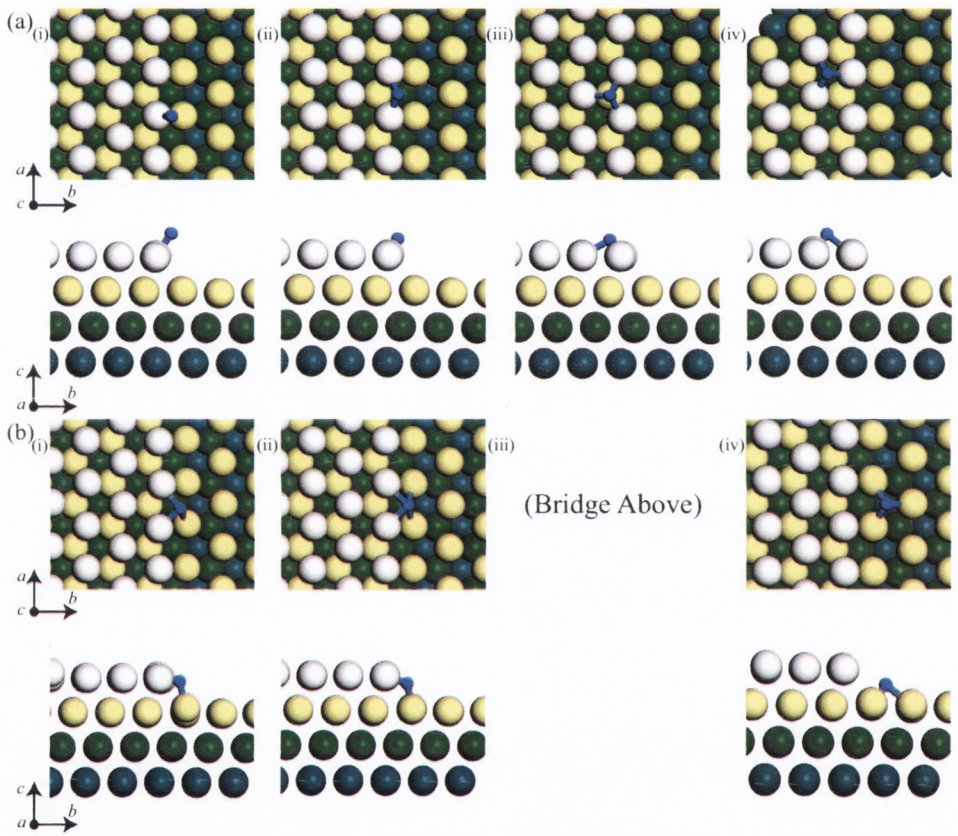


Figure 5.18: The most stable adsorption modes of N (a) above and (b) below the step, and on the (c) terrace of the Rh {443} stepped surface, at the (i) top, (ii) bridge, (iii) hcp, and (iv) fcc sites, along the c and a vectors. The blue sphere shows the N adsorbate, while the Rh surface layers are coloured for clarity.

The details of the CN, E_{ads}, and Rh-N bond distances for each of the stable adsorption modes are given in Table 5.10, with (a) above and (b) below the step, and (c) terrace corresponding to (a), (b) and (c) in the figure. The E_{ads} for N on the step are seen to increase with increase coordination of the N adsorbate, with the bond distances following a similar trend. The top site shows weak adsorption with the E_{ads} being

endothermic, while the other adsorption modes show favourable exothermic adsorption with the three-fold hollow site being the most stable adsorption mode above the step. For the N adsorbates below the step, although the adsorbates posses different coordination environments, the E_{ads} are exothermic and favoured having with each site having similar values and similar bond distances. The hcp site is unstable and relaxes to the bridge site on the step edge. N adsorption on the terrace sites posses similar bond energies and distances to the Rh {111} surface, providing evidence that the terrace is behaving in a similar manner to the {111} surface. Overall, the hcp site on the step is the most stable adsorption site for N adsorption on the Rh {443} surface, agreeing with previous work on rhodium step surfaces.[201] All adsorption sites quench the atomic spin to 0.

	Site	CN	E_{ads} (eV)	Rh-N (Å)	N charge	Rh charge
(a) Above	Top	1	+1.06	1.65 (x1)	-0.39	+0.32 (x1)
	Bridge	2	-0.23	1.80 (x2)	-0.55	+0.26 (x2)
	Hcp	3	-0.62	1.88 (x2), 1.92 (x1)	-0.65	+0.22 (x3)
	Fcc	3	-0.10	1.92 (x3)	-0.62	+0.20 (x3)
(b) Below	Top	3	-0.05	1.97 (x2), 1.88	-0.66	+0.18 (x3)
	Bridge	4	-0.04	1.98 (x2), 2.08 (x2)	-0.71	+0.15 (x4)
	Hcp	-	(bridge above)	—	—	—
	Fcc	3	-0.05	1.93 (x3)	-0.64	+0.18 (x3)
(c) Terrace	Top	-	(hcp)	—	—	—
	Bridge	-	(fcc)	—	—	—
	Hcp	3	-0.40	1.90 (x3)	-0.64	+0.21 (x3)
	Fcc	3	-0.24	1.91 (x3)	-0.63	+0.20 (x3)

Table 5.10: The adsorption energies (E_{ads}), coordination number (CN), *Rh*-N bond lengths and Bader charges for the most stable nitrogen adsorption modes (a) above and (b) below the step, and on the (c) terrace of the Rh {443} stepped surface. The number of bonds for each adsorbate on a high symmetry site is also included.

Bader analysis was carried out on the most stable adsorption modes with the calculated charges detailed in Table 5.10. For all adsorption modes, the charge of the N adsorption increases with increasing coordination of the adsorption site, and the op-

posite trend for the charges of the bound Rh atoms. The charges show that the N adsorbates gain charge, relative to atomic N, while the Rh surface atoms loose charge, becoming more positive. This shows that the N adsorbates form $N^{\delta-}$ species on all adsorption sites, indicating that charge is donated from the Rh atoms to the N adsorbates. The greatest charge donated from the least number of coordinated Rh atoms is associated with the most stable hcp site on the step. This may explain why this adsorption mode is favoured over the other stable modes.

To visualise the charge transfer process, the charge difference plot for the most stable adsorption mode was calculated and shown in Figure 5.19 (a). The plot shows that the N adsorbate gains charge (red regions) while the Rh surface atom loose charge (blue regions) upon interaction of the N atom with the surface. This confirms the Bader charges and the direction of the charge transfer process.

The PEDOS was calculated for the most stable adsorption mode for N on the Rh {443} stepped surface and shown in Figure 5.19 (b). The VB and CB are primarily made up of a mixture of N $2p$ and Rh $4d$ states, with minor contributions from the N $2s$ states and Rh s/p states. The bottom of the VB between -12 and -10 eV has two large N $2p$ peaks that interact with a larger peak at the bottom of the Rh $4d$ band. There are occupied N $2p$ states up to E_F that interact with the Rh $4d$ band. These are present from the surface charge donation to the N adsorbate. The presence of N $2p$ states in the conduction band indicates that they are not fully occupied.

5.3.2 O adsorption and analysis

The adsorption of O was investigated in a similar manner to N adsorption with the most stable adsorption modes for O above and below the step and on the terrace shown in Figure 5.20. The structures for the top, bridge and hcp site below the step are absent as these structures relaxed to the bridge site on the step edge. The top and bridge sites on the terrace also relaxed to hcp and fcc sites, respectively, as seen for N adsorption. All the other adsorption modes relaxed to the desired configurations as shown in the figure.

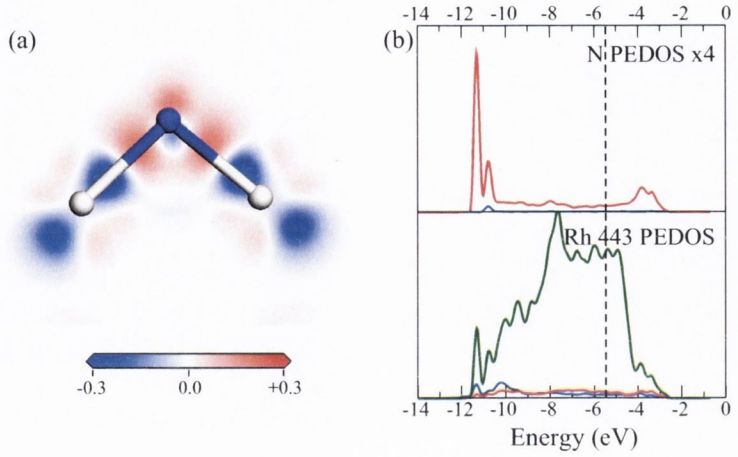


Figure 5.19: (a) The charge difference plot for the most stable N adsorption site on the Rh {443} stepped surface. The charge difference ranges from -0.3 (blue) to +0.3 (red) electrons $Å^{-3}$, as indicated by the scale. (b) The PEDOS for the most stable N adsorption mode on the Rh {443} stepped surface. The dotted line indicates the position of E_F and the graphs are aligned to E_{vac}. The *s*, *p* and *d* states are indicated by the blue, red and green lines, respectively.

The CN, E_{ads}, and Rh-O bond distances are detailed in Table 5.11, with the details for the unstable adsorption modes absent as they relaxed to different configurations. The adsorption of O on the step shows that all E_{ads} are exothermic and favoured, with the top and fcc site having similar E_{ads}, and the bridge site on the step edge being the most stable. The Rh-O bond distances are seen to increase with coordination of the O adsorbate. For O adsorption below the step, the top, bridge and hcp sites are unstable, relaxing to the bridge site on the step edge, indicating its strong affinity for O adsorption, while the adsorption on the fcc site is exothermic and favoured. The most stable site for O being the step edge supports previous work on rhodium stepped surfaces.[201] Similar to N adsorption, the E_{ads} for O adsorption on the terrace are similar to E_{ads} for that on the flat {111} surface, indicating that the terrace closely represents the {111} surface.

Bader charge analysis was carried out on the stable adsorption modes for O adsorption on the Rh {443} stepped surface, and are detailed in Table 5.11. Similar to N adsorption, the charges on the O adsorbate increase with increasing coordination of the adsorption site, while there is an opposite trend for the Rh atoms. The negative charges

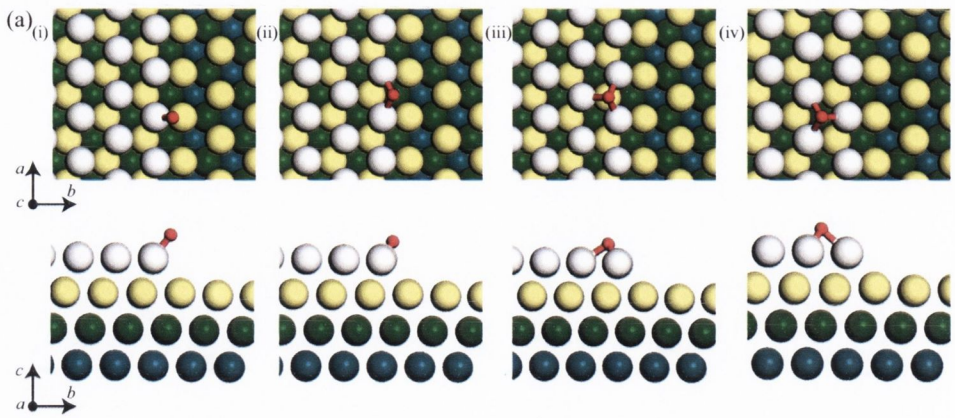


Figure 5.20: The most stable adsorption modes of O (a) above and (b) below the step, and on the (c) terrace of the Rh {443} stepped surface, at the (i) top, (ii) bridge, (iii) hcp, and (iv) fcc sites, along the *c* and *a* vectors. The red sphere shows the O adsorbate, while the Rh surface layers are coloured for clarity.

of the O adsorbate relative to atomic O, show that the O adsorbates gain charge forming $O^{\delta-}$ species on the surface for all adsorption modes, while the Rh atoms become more positive relative to the pure surface, indicating a loss in charge. This shows that charge is donated from the surface to the O adsorbates. For the most stable bridge site on the step edge, the O adsorbate gains considerable charge while the surface bound Rh atoms lose more charge than the Rh atoms of the three-fold coordination sites, perhaps elucidating its preferred configuration over the other modes.

To visualise the charge transfer process, the charge difference plot for the most stable adsorption mode was determined and shown in Figure 5.21 (a). The plot shows that the O adsorbate gains charge (red regions) while the Rh surface atom loose charge (blue regions) upon interaction of the O atom with the surface. This confirms the Bader charges and the direction of the charge transfer process.

The PEDOS was calculated for the most stable O adsorption mode on the Rh {443} surface, and is shown in Figure 5.21 (b). The VB and CB are a mixing of O 2*p* states with Rh 4*d* states, and smaller contributions from O 2*s* states and Rh *s*/*p* states. The O states are low in energy with the VB extending to -14 eV, and at the bottom of the VB there are 3 large O 2*p* peaks that interacting with the bottom of the Rh 4*d* band. The presence of O 2*p* states up to E_F that interact with the Rh 4*d* band indicate the

	Site	CN	E_{ads} (eV)	Rh-O (Å)	O charge	Rh charge
(a) Above	Top	1	-1.33	1.73 (x1)	-0.56	+0.37 (x1)
	Bridge	2	-2.65	1.88 (x2)	-0.65	+0.28 (x2)
	Hcp	3	-2.21	1.97 (x2), 2.05 (x1)	-0.72	+0.23 (x3)
	Fcc	3	-1.33	2.00 (x2), 2.03 (x1)	-0.71	+0.22 (x2), +0.17 (x1)
(b) Below	Top	-	(Bridge above)	—	—	—
	Bridge	-	(Bridge above)	—	—	—
	Hcp	-	(Bridge above)	—	—	—
	Fcc	3	-1.77	2.01 (x3)	-0.71	+0.19 (x3)
(c) Terrace	Top	-	(hcp)	—	—	—
	Bridge	-	(fcc)	—	—	—
	Hcp	3	-1.97	1.99 (x3)	-0.70	+0.21 (x2), +0.19 (x1)
	Fcc	3	-2.05	2.00 (x3)	-0.70	+0.20 (x3)

Table 5.11: The adsorption energies (E_{ads}), coordination number (CN), *Rh*-O bond lengths and Bader charges for the most stable oxygen adsorption modes (a) above and (b) below the step, and on the (c) terrace of the Rh {443} stepped surface. The number of bonds for each adsorbate on a high symmetry site is also included.

occupation of states due to charge donation from the surface, and O $2p$ states in the CB shows that these states are not fully filled.

5.3.3 NO adsorption and analysis

NO adsorption was explored above and below the step, and the terrace of the Rh {443} stepped surface, and the stable adsorption modes are shown in Figure 5.22. The structures for the adsorption on the top, bridge and fcc site below the step, and the top and bridge site on the terrace are absent since these were found to be unstable, relaxing to the structures indicated on the figure. The top and bridge sites were found to relaxed off the step edge, while the three-fold hcp and fcc sites relaxed to the desired configuration. The adsorption of NO on the top site below the step was found to form a bond with the step edge and the O atom of the molecule directed away from the step. Adsorption on the hcp and fcc sites of the flat terrace relaxed to the same configuration.

The CN, E_{ads}, Rh-N, N-O bond distances and vibrational frequencies for the stable

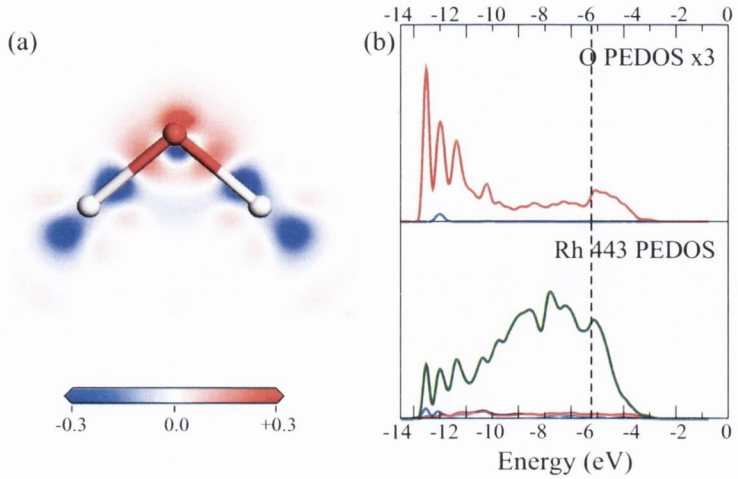


Figure 5.21: (a) The charge difference plot for the most stable O adsorption site on the Rh {443} stepped surface. The charge difference ranges from -0.3 (blue) to +0.3 (red) electrons Å^{-3}, as indicated by the scale. (b) The PEDOS for the most stable O adsorption mode on the Rh {443} stepped surface. The dotted line indicates the position of E_{F} and the graphs are aligned to E_{vac}. The *s*, *p* and *d* states are indicated by the blue, red and green lines, respectively.

adsorption modes are detailed in Table 5.12. The bond distance of the coordinated N atom of the adsorbate is seen to increase with increased coordination of the adsorption site, with the N-O bond being elongated by 0.03Å (top), 0.06Å (bridge), and 0.07Å (fcc/hcp) upon adsorption relative to gaseous NO; however for the top site below the step, the N-O bond is lengthened by 0.05Å. The most stable NO adsorption mode on the Rh {443} stepped surface is the bridge site on the step edge. Its preference over other adsorption sites close to the step as the bridge, hcp and fcc relaxing to this configuration, indicates a strong affinity for NO adsorption on the step edge. All adsorption sites were found to quench the molecular spin of the NO adsorbate to zero.

Bader analysis was carried out on the stable NO adsorption modes on the Rh {443} surface, with the charges detailed in Table 5.13. The overall Bader charges show that the NO adsorbates are negative, gaining density from the interaction with the Rh {443} surface, where the charge donation increases with increased coordination of the N atom. The charge lost from the individual Rh surface atoms follows an opposite trend as seen in the table. The overall charge transfer for the top and bridge sites is accounted for by the coordinated Rh surface atoms, with the three-fold hollow sites

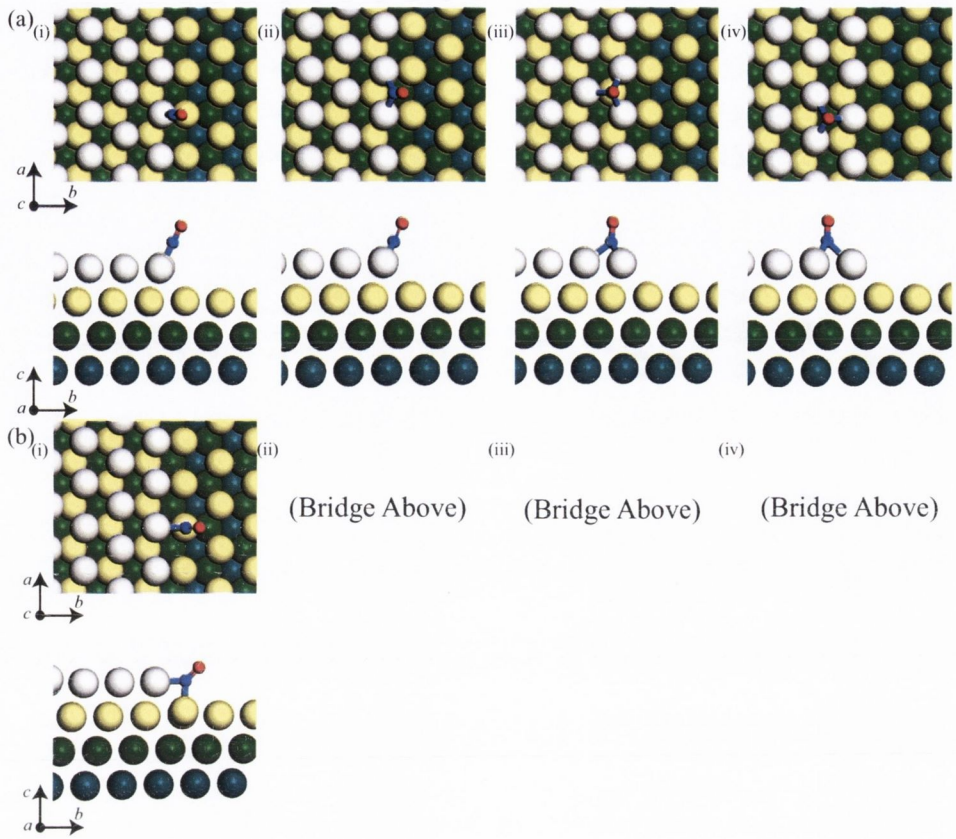


Figure 5.22: The most stable adsorption modes of NO (a) above and (b) below the step, and on the (c) terrace of the Rh {443} stepped surface, at the (i) top, (ii) bridge, (iii) hcp, and (iv) fcc sites, along the c and a vectors. The blue and red spheres show the N and O atoms, respectively, while the Rh surface layers are coloured for clarity.

only accounting for 75% of the charge transferred. The remaining 25% of charge gained from the adsorbates may perhaps come from Rh atoms on the surface/step donating smaller amounts of charge.

The breakdown of the charges for the N and O atoms of the adsorbates show that the coordinated N atom gains charge as it less positive for the low coordinated top and bridge sites, gaining $0.36\,e$ and $0.48\,e$ respectively, and negative for the three-coordinated hcp and fcc sites, gaining $0.61\,e$ and $0.57\,e$, relative to gaseous NO. The O atom loses similar charge ($0.13\,e$) for all adsorbates, relative to gaseous NO. The N atom gaining charge and the O atom losing charge in such a way suggests that there is significant redistribution of charge within the adsorbate when interacting with the Rh {443} stepped surface. For the most stable adsorption mode, the bridge site on the

Surface	Site	E_{ads} (eV)	*Rh*-N (Å)	N-O (Å)	Vib (cm^{-1})
	Gas Phase	—	—	1.15	1920
(a) Above	Top	-2.56	1.76 (x1)	1.18	1817
	Bridge	-2.83	1.93 (x2)	1.21	1610
	Hcp	-2.69	2.01 (x2), 2.05 (x1)	1.22	1493
	Fcc	-2.39	2.04 (x3)	1.22	1516
(b) Below	Top	-2.35	1.95 (x2)	1.20	1605
	Bridge	(bridge above)	—	—	—
	Hcp	(bridge above)	—	—	—
	Fcc	(bridge above)	—	—	—
(c) Terrace	Top	(hcp)	—	—	—
	Bridge	(fcc)	—	—	—
	Hcp	-2.49	2.02 (x3)	1.22	
	Fcc	-2.44	2.03 (x3)	1.22	

Table 5.12: The adsorption energies (E_{ads}), coordination number (CN), *Rh*-N and N-O bond lengths, and vibrational frequencies of NO for the gas phase and high symmetry sites of NO (a) above and (b) below the step, and the (c) terrace of the Rh {443} stepped surface.

step, the N atom gains the most charge of the low coordinated adsorption sites; however not to the same extent as the three-fold hollow sites. The bridge site on the step edge may be more stable as the N atom prefers to remain slightly positive, with the Rh surface atoms donating more charge than the other adsorption sites. Further analysis of the most stable bridge site will be carried out to examine the charge redistribution for the NO molecule when interacting with the step edge.

The charge difference plot was calculated for the most stable NO adsorption mode to illustrate the redistribution of charge for the NO adsorbate interacting with the Rh surface step, shown in Figure 5.23 (a). The plot shows that the NO molecule gains charge (red regions) while the Rh surface atoms lose charge (blue regions) supporting the Bader charges. This shows that charge is donated from the Rh step to the NO adsorbate on the bridge site. The charge difference plot also shows that the O atom loses charge along the bond axis towards the N atom, indicating that O atom donates

	Species	NO	N charge	O charge	M charge
	NO^+	+1	+1.21	-0.21	—
	NO	0	+0.53	-0.53	—
	NO^-	-1	+0.10	-1.10	—
	Rh {443} step	—	—	—	-0.04
	Rh {443} terrace	—	—	—	-0.03
(a) Above	Top	-0.23	+0.17	-0.40	+0.21 (x1)
	Bridge	-0.36	+0.05	-0.41	+0.16 (x2)
	Hcp	-0.48	-0.08	-0.40	+0.13 (x3)
	Fcc	-0.44	-0.04	-0.40	+0.11, +0.13 (x2)
(b) Below	Top	-0.35	+0.06	-0.41	+0.16 (x2)
	Bridge	(bridge above)	—	—	—
	Hcp	(bridge above)	—	—	—
	Fcc	(bridge above)	—	—	—
(c) Terrace	Top	(hcp)	—	—	—
	Bridge	(fcc)	—	—	—
	Hcp	-0.46	-0.06	-0.40	+0.13 (x2)
	Fcc	-0.45	-0.06	-0.39	+0.13 (x2)

Table 5.13: The calculated Bader charges for NO in the gas phase and the adsorption sites (a) above and (b) below the step, and on (c) the terrace of the Rh {443} stepped surface. The Bader charges for the Rh surface atoms of the adsorption sites are also included.

charge back to the N atom, accounting for the greater charge on the N atom that is not donated by the Rh surface atoms.

To further assess the electronic structure for the most stable NO adsorption mode on the Rh step, the PEDOS was calculated and shown in Figure 5.23 (b). The MOs for the NO adsorbate is labelled in a similar manner to the MO diagram and calculated PEDOS for gaseous NO (Figure 5.9). The adsorption of NO on the bridge site at the step edge lowers the energy of all MOs relative to gaseous NO. The 5σ orbital, that is above the 1π orbital for gaseous NO, is stabilised and lowered in energy to below the 1π orbital on interaction with the Rh step. The $4\sigma^*$ orbital gains N $2s$ and $2p$ states, while losing O $2p$ states. The 5σ orbital in the gas phase is N dominated and on interaction

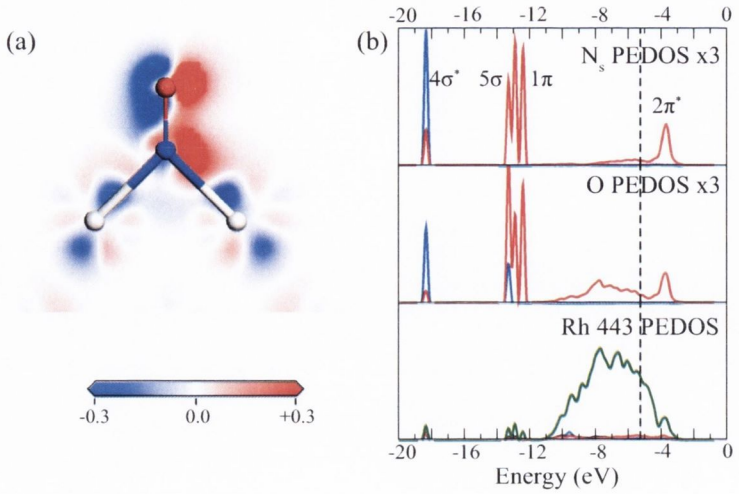


Figure 5.23: (a) The charge difference plot for the most stable NO adsorption site on the Rh {443} stepped surface. The charge difference ranges from -0.3 (blue) to +0.3 (red) electrons Å^{-3}, as indicated by the scale. (b) The PEDOS for the most stable NO adsorption mode on the Rh {443} stepped surface. The dotted line indicates the position of E_F and the graphs are aligned to E_{vac}. The *s*, *p* and *d* states are indicated by the blue, red and green lines, respectively.

with the Rh step becomes O dominated from the stabilisation to below the 1π orbital. Similar to gaseous NO, the 1π orbital is a mixture of N and O $2p$ states, which is N dominated and split into its x and y components. The higher 2π orbital is split into occupied and unoccupied components from the interaction of the Rh $4d$ band at the top of the VB. The occupied component of the $2\pi^*$ orbital is O dominated, while the unoccupied states at the bottom of the CB are N dominated. The interaction with the Rh $4d$ states reverses the N/O dominated character observed in the gas phase.

The percentage contributions of the N and O states to the MOs are detailed in Table 5.14 and compared to the N/O percentage contributions to the gaseous NO species, to examine the redistribution of charge when interacting with the Rh step. There is a significant redistribution within the σ orbitals as the $4\sigma^*$ orbital becomes N dominated, while the 5σ orbital becomes O dominated on interaction with the Rh step. A similar mechanism occurs for the higher 1π and $2\pi^*_{occ}$ orbitals, as they are N and O dominated, respectively, while the N/O contributions to the unoccupied states of the $2\pi^*$ orbital is similar to gaseous NO.

	$NO_{(g)}$				
States	$4\sigma^*$	5σ	1π	$2\pi^*_{occ}$	$2\pi^*_{unocc}$
N $2s$	40	11	0	0	0
N $2p$	0	40	34	56	59
O $2s$	33	1	0	0	0
O $2p$	27	48	66	44	41
	$NO_{(ads)}$ on Rh{443}				
States	$4\sigma^*$	5σ	1π	$2\pi^*_{occ}$	$2\pi^*_{unocc}$
N $2s$	53	0	0	2	2
N $2p$	13	31	54	17	53
O $2s$	30	14	0	0	1
O $2p$	4	55	46	81	44

Table 5.14: The approximate percentage contributions of N $2s$, N $2p$, O $2s$ and O $2p$ states to the molecular orbitals of gas phase NO and NO adsorbed at the most stable sites of the Rh{443} stepped surface.

From the analysis of the Bader charges, the charge density difference plots, the PEDOS and the changes in the orbital contributions, it is clear that there is a complex change to the electronic structure for the most stable NO adsorption mode on the step edge. Analysis of the bridge site on the step edge shows that the interaction of the NO molecule with the step stabilises the MOs, causing both a lowering of the energy and a shift in the orbital contributions. For the adsorbate, the $4\sigma^*$ and 1π orbitals contain a greater N contribution, while the 5σ and $2\pi^*_{occ}$ orbitals have a greater O contribution. The strong interaction of the $2\pi^*$ orbital with the Rh $4d$ band splits it into occupied and unoccupied parts. The $2\pi^*$ orbital is anti-bonding and the interaction with the step reduces the N contributions to the occupied part, indicating that the mechanism of stabilisation is to reduced the anti-bonding interaction and transfer electron density onto the oxygen atom. This gives rise to charge transfer to the NO adsorbate with a charge redistribution within the molecule. The Bader charges show that the coordinated N atom has greater charge density than the gas phase species, while O loses charge. The charge is lost by a back donation from the O atom through the $4\sigma^*$ and 1π orbitals to the N atom, accounting for its greater charge.

5.3.4 NO_2 adsorption and analysis

The adsorption of NO_2 was investigated in a similar manner to N, O and NO on the Rh {443} stepped surface, with the different NO_2 adsorption modes (μ-nitrito, O-O'-nitrito, O-nitrito) explored across the high symmetry sites above and below the step, and on the terrace of the Rh {443} stepped surface. The most stable structure for the μ-nitrito, O-O'-nitrito and O-nitrito adsorption modes are shown in Figure 5.24. For each adsorption mode, the NO_2 molecule was found to be most stable at the bridge site on the step edge with N and O atoms bonded offset from top sites for the μ-nitrito and O-O'-nitrito, while the O atom sits in the bridge site for the O-nitrito mode. The most stable NO_2 adsorbate of the μ-nitrito and O-O'-nitrito adsorption modes can be seen to adsorb at a tilted angle off the step edge, and the O-nitrito mode adsorbs perpendicular to the step edge, as seen in the figure.

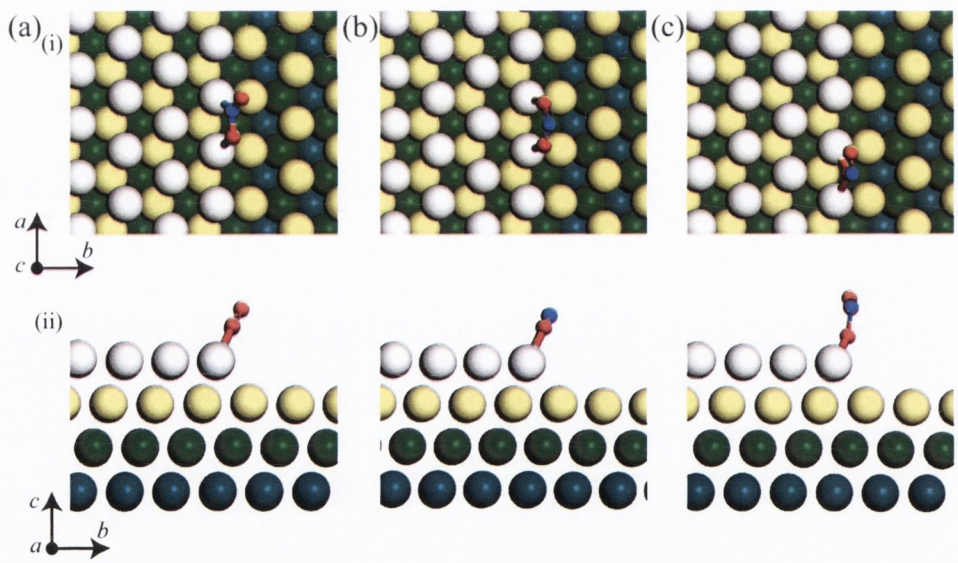


Figure 5.24: The most stable adsorption modes (a) μ-nitrito, (b) O-O'-nitrito and (c) O-nitrito adsorption modes on the Rh {443} stepped surface, along the (i) *c* and (ii) *a* vectors. The blue and red spheres show the N and O atoms, respectively, while the Rh surface layers are coloured for clarity.

The E_{ads}, bond lengths and angles for the most stable NO_2 adsorption modes are detailed in Table 5.15, along with the calculated details for gaseous NO_2. The μ-nitrito mode is seen to be the most stable of the adsorption modes, with the O-nitrito being

the least stable adsorption mode. For the μ-nitrito adsorption mode, the bond parallel to the surface (N_s-O_s) can be seen to become elongated relative to gaseous NO_2 on adsorption at the step edge, while the bond directed away from the step edge (N_s-O) is at a similar length to gaseous NO_2. Both N-O bonds for the O-O'-nitrito mode are elongated on interaction with the step edge, and also the bond perpendicular to the step edge for the O-nitrito mode is also elongated. The bond angle of all the NO_2 adsorption modes is greatly decreased compared to the gas phase, with the O-nitrito mode showing the greatest decrease. Molecular NO_2 is expected to contribute spin to the system from the unpaired electron in its HOMO; however this is quenched to 0 by the Rh step. As the μ-nitrito mode is clearly the most stable adsorption mode, analysis of its electronic structure will be carried to examine its interaction with the Rh step edge.

Configuration	Site	Site	E_{ads} (eV)	O-N (Å)	N-O (Å)	O-N-O (°)
$NO_{2\,(g)}$	-	-	-	1.21	1.21	133.73
μ-nitrito	Top	Top[1]	-2.67	1.33	1.22	118.42
O-O'-nitrito	Top	Top[1]	-2.22	1.27	1.27	118.04
O-nitrito	Fcc	top[2]	-1.56	1.47	1.19	112.70

[1] molecule across bridge site
[2] N-O bond directed to top site

Table 5.15: The calculated bond distance and angle of gaseous $NO_{2\,(g)}$. The E_{ads}, the calculated N-O bonds and angles for the most stable (a) μ-nitrito, (b) O-O'-nitrito and (c) O-nitrito adsorption modes on the Rh {443} stepped surface. The subscript 's' denotes the surface bound atom on the Rh {111} surface.

The calculated vibrational frequencies of the most stable μ-nitrito mode at the bridge site on the step edge are, 1497 cm^{-1}, 948 cm^{-1} and 745 cm^{-1} for the asymmetric, symmetric and bending modes, respectively. There is very little experimental evidence to describe the adsorption of NO_2 on the step edge; however the experimental detection of co-adsorbed NO and O on the step edge suggests that fast dissociation kinetics may be occurring.[67, 203–205]

Bader analysis was carried out for the most stable μ-nitrito mode at the bridge site on the step edge, with the calculated charges detailed in Table 5.16, along with the charges for gaseous NO_2 in its cationic, neutral and anionic forms, and the charges for the Rh {443} step atoms. The overall charge of the NO_2 adsorbate is negative, while the Rh step atoms are positive suggesting charge transfer from the Rh step to the molecule; however this only accounts for 85% of the charge gained by the NO_2 molecule. The charges for the individual atoms indicate that the surface bound N and O atoms of the NO_2 adsorbate gain 0.31 e and 0.15 e, respectively, while the O atom not bound to the step has a similar charge (-0.01 e difference) to the O atom of gaseous NO_2. The charge gained by the N atom is greater than, while the charge gained by the O atom is less than the charge lost from the Rh step atoms. This interaction and 85% of the charge transferred to the NO_2 adsorbate being accounted for by the Rh step atoms, suggested that simple direct charge transfer from the Rh step to the NO_2 molecule is not occurring and a more complicated mechanism is present.

	Species	NO_2	N charge	O charge	O charge	Rh charge
(a)	NO_2^+	+1	+0.93	+0.03	+0.04	-
	NO_2	0	+0.73	-0.34	-0.39	-
	NO_2^-	-1	+0.38	-0.69	-0.69	-
	Rh {443} step	—	—	—	—	-0.04
(b)	μ nitrito on Rh {443}	-0.47	+0.42	-0.49*	-0.40	+0.18 (x2)

* O atom bonded to surface

Table 5.16: (a) The calculated Bader charges for gaseous NO_2 and the Rh surface atoms of the pure step and terrace, and (b) for adsorbed NO_2 on the Rh {443} step, and the Rh step atoms it is bound to.

To examine the charge interaction of the NO_2 molecule with the Rh step edge, the charge difference plot was calculated and shown in Figure 5.25. The charge difference plot shows that the NO_2 adsorbate gains charge (red regions) and the Rh step atoms lose charge (blue regions). This indicates that charge is donated from the step to the NO_2 molecule supporting the Bader charges. The plot also shows that there is charge

lost from the atoms on the NO_2 atoms along the bond axis, suggesting that there is a change in the σ and π systems of the adsorbate. There is thus a redistribution of charge within the adsorbate from the interaction of the NO_2 with the Rh step. This may account for the extra charge on the N atom and loss in charge on the O atom that is not accounted for by surface donation.

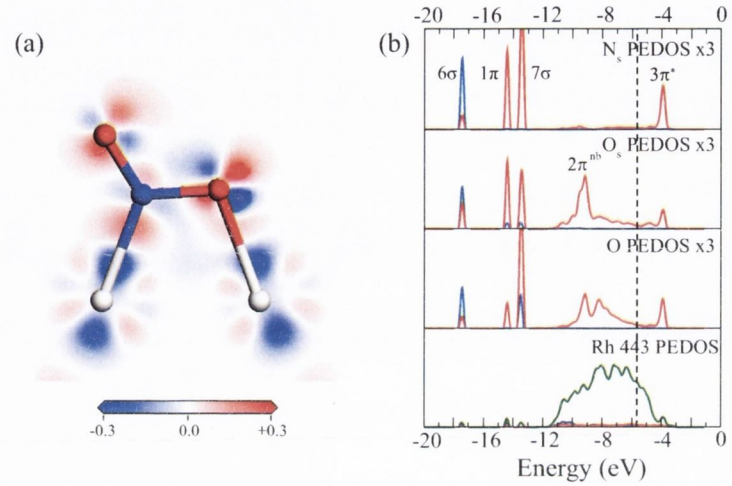


Figure 5.25: (a) The charge difference plot for the most stable NO_2 adsorption site on the Rh {443} stepped surface. The charge difference ranges from -0.3 (blue) to +0.3 (red) electrons $Å^{-3}$, as indicated by the scale. (b) The PEDOS for the most stable NO_2 adsorption mode on the Rh {443} stepped surface. The dotted line indicates the position of E_F and the graphs are aligned to E_{vac}. The s, p and d states are indicated by the blue, red and green lines, respectively.

The calculated PEDOS for the most stable μ-nitrito mode on the Rh step edge is shown in Figure 5.25 (b), to examine its electronic structure and charge redistribution. The MO diagram and calculated electronic structure for gaseous NO_2 are given in Figure 4.12, for comparison.

The PEDOS for NO_2 on the Rh step shows a similar electronic structure to NO_2 adsorption on the flat low index surfaces. On adsorption, all the MOs are stabilised and lowered in energy relative to the position of the MOs for gaseous NO_2, with the 1π orbital being greatly stabilised to below the 7σ orbital. The 6σ orbital gains N $2p$ states, while losing O contributions on interaction of the NO_2 molecule with the Rh step. The composition of the $7\sigma/1\pi$ orbital appears to be N dominated for the NO_2, the reverse of gaseous NO_2, while the $2\pi*^{nb}$ and $3\pi^*_{occ}$ orbitals are O dominated. The $3\pi^*$ orbital of

the NO_2 orbital is expected to contain N contributions from the gained charge; however this is not the case. The bottom of the CB is also N dominated, suggesting that simple charge donation to this orbital does not occur, and charge redistribution must be the mechanism, as observed on the low index surfaces.

To further assess and quantify the redistribution of the charge for the NO_2 molecule interacting with the Rh step, the approximate percentage contributions of the N/O $2s/p$ states to the MOs are detailed in Table 5.17, along with the percentage contributions to gaseous NO_2 for comparison. As the 7σ and 1π orbitals are so close in energy, it is hard to distinguish between them for the gaseous NO_2 species, and the N/O $2s/p$ contributions to these orbitals are grouped together in the table. For both adsorbates, the $2\pi^{nb}$ and $3\pi^*_{occ}$ orbitals mix at the top of the valence band, making it difficult to distinguish between their N/O $2s/p$ contributions. The contributions are thus approximated by taking the percentage of states at a similar energy range to that for the analogous orbitals of the gaseous species.

On adsorption, the 4σ orbital of the NO_2 molecule appears to gain N $2s/p$ states (8/6%) and lose O $2p$ states (10%) from the O atom not bound to the surface, while the O_s atom remains relatively unchanged. The contributions to the $7\sigma/1\pi$ system of the NO_2 adsorbate is also relatively unaffected, indicating that either only small changes in the composition are observed, or that the redistribution of one orbital is complimentary to the other. The $2\pi^{nb}$ appears to become dominated by O_s states by gaining O $2p$ character (10%) when the NO_2 molecule interacts with the Rh step, while gaining 4% N $2p$ character. For the $3\pi^*$ orbital of the NO_2 adsorbate, the O $2p$ occupied states of the O atom not bound to the surface gains 25%, while the orbital significantly loses N character with the unoccupied states of the $3\pi^*$ are dominated by O_s states. The changes to the orbital composition on adsorption of the NO_2 orbital at the Rh step shows considerable charge redistribution across the adsorbate with changes to the higher π orbitals, with the lower orbitals being N dominated.

Analysis of the Bader charges, the charge density difference plots, and the changes in the orbital contributions show that there is a complex change to the electronic structure

	$NO_{2\,(g)}$				
States	6σ	$7\sigma/1\pi$	$2\pi^{nb}$	$3\pi^{*}_{occ}$	$3\pi^{*}_{unocc}$
N $2s$	27	0	0	8	7
N $2p$	1	38	0	24	27
O $2s$	21	4	0	0	0
O $2p$	15	27	50	34	33
O $2s$	21	4	0	0	0
O $2p$	15	27	50	34	33
	μ-nitrito on Rh{443}				
States	6σ	$7\sigma/1\pi$	$2\pi^{nb}$	$3\pi^{*}_{occ}$	$3\pi^{*}_{unocc}$
N_s $2s$	35	0	0	1	6
N_s $2p$	7	39	4	6	17
O_s $2s$	21	2	1	0	2
O_s $2p$	13	24	60	34	46
O $2s$	19	6	0	0	0
O $2p$	5	29	35	59	29

Table 5.17: The approximate percentage contributions of N $2s$, N $2p$, O $2s$ and O $2p$ states to the molecular orbitals of gas phase NO_2 and the μ-nitrito adsorption mode on the Rh {443} stepped surface.

of the NO_2 molecule when interacting with the step edge of the Rh {443} surface. The overall Bader charges indicate that there is charge transfer from the Rh step to the NO_2 adsorbate; however the breakdown of the individual charges suggests that there is a rearrangement of the σ and π bonding within the adsorbate, which can also be seen on the charge difference plots. The 6σ, 7σ and 1π orbitals are stabilised and lowered in energy relative to the energies for the MOs of gaseous NO_2. These orbitals are dominated by N states, with an greater increase in the N $2s/p$ contributions to the 6σ orbital relative to gaseous NO_2, which may account for the increased charge on the N atom. The higher energy π orbitals are typically dominated by O $2p$ states, with a significant increase in the O_s $2p$ states to the $2\pi^{nb}$ orbital and in O contribution to the $3\pi^{*}$occ orbital for the unbound O atom, relative to gaseous NO_2. As the O_s contributions to the orbitals, excluding the $2\pi^{nb}$, are relatively unaffected relative to gaseous NO_2, the increase in charge on the O_s atom can be associated with the increased

contribution to the $2\pi^{nb}$ orbital from the redistribution of charge due to the interaction with the Rh step. The charge of the O atom not bound to Rh has a similar charge to gaseous NO_2; however its contributions to the $3\pi^*_{occ}$ orbital significantly increases (25%), along with a decrease in its contributions to the 6σ (10%) and $2\pi^{nb}$ (15%) orbitals.

The interaction of the NO_2 molecule with the Rh surface, stabilises the anti-bonding $3\pi^*$ orbital interaction between N_s and O, reduces the N contribution and transfers the electron density donated from the surface to the unbound O atom of the adsorbate in a similar manner to that observed for NO adsorption. This is balanced by the transfer of electron density back to the N_s atom through the 6σ orbital, and to the O_s atom through the $2\pi^{nb}$ orbital, accounting for the increased charge of the surface bound atoms. This suggests that the orientation of the μ-nitrito adsorption mode on the Rh surface, treats the adsorbate/surface interaction and the adsorbate bonding in a similar manner to a NO adsorbate with an extended bond to an O atom, as observed with the Rh low index surfaces.

5.3.5 Decomposition Profile

The reaction energies for each process in the NO and NO_2 decomposition pathways on the Rh {443} surface were calculated using the energies of the most stable adsorption modes for N, O, NO and NO_2, and their respective gaseous species, and detailed in Table 5.18. The overall decomposition pathways for NO_2 and NO can also be summarised graphically, as shown in Figures 5.26 (a) and (b), respectively.

The calculated reaction energies show that the adsorption and the subsequent breakdown of NO_x is exothermic on the Rh {443} stepped surface. The dissociation of NO_2 to NO and O is favourable (-1.61 eV), with the large drive to form the dissociation products being a result of the large E_{ads} of NO and O. The subsequent reduction of NO to N and O also has an energy of -1.38 eV to form the products. This energy is not as large as the dissociation of NO_2 as N atoms are not as stable as NO on the step. The profile for the step indicates that the breakdown of NO_x is energetically more favourable than the flat low index surfaces of rhodium. This shows that the step

	Reaction Step	Energy (eV)
(a)	$NO_{2(g)} \rightarrow NO_{2(ads)}$	-2.67
	$NO_{2(ads)} \rightarrow NO_{(ads)} + O_{(ads)}$	-1.61
	$NO_{(ads)} + O_{(ads)} \rightarrow N_{(ads)} + 2O_{(ads)}$	-1.38
	$N_{(ads)} + 2O_{(ads)} \rightarrow \frac{1}{2}N_{2(g)} + O_{2(g)}$	+5.88
(b)	$NO_{(g)} \rightarrow NO_{(ads)}$	-2.82
	$NO_{(ads)} \rightarrow N_{(ads)} + O_{(ads)}$	-1.38
	$N_{(ads)} + O_{(ads)} \rightarrow \frac{1}{2}N_{2(g)} + \frac{1}{2}O_{2(g)}$	+3.24

Table 5.18: The energies for each step of the (a) NO_2 and (b) NO decomposition pathways on the Rh {443} stepped surface.

defect on the {111} surface enhances the catalytic reduction of NO_x, as observed by experiment.[190, 193, 194]

The combination and desorption of the atomic N and O atoms to gaseous N_2 and O_2 is an endothermic process, requiring a large amount of energy for both pathways. Comparing to other profiles developed for the low index surfaces, the formation of O_2 and subsequent desorption from the step edge is the probably cause of the large energy requirement. The large energy required to remove O_2 is perhaps caused by the strong bind of O atoms to the step edge, in a similar manner to the low index surfaces. There is a need to remove the O ad-atoms as these prefer the same adsorption sites as NO and will block subsequent NO_x breakdown. A reductant is thus needed to remove surface-bound O atoms from the Rh step edge, in a similar manner to other surfaces of rhodium metal.

5.3.6 Discussion

The electronic structure of the most stable NO and NO_2 adsorbates on the Rh {443} surface was characterised using Bader charge analysis, charge difference plots and PE-DOS. The Bader charge analysis indicates that there is an overall charge donation from the surface to both adsorbates, with the charge difference plots showing a considerable

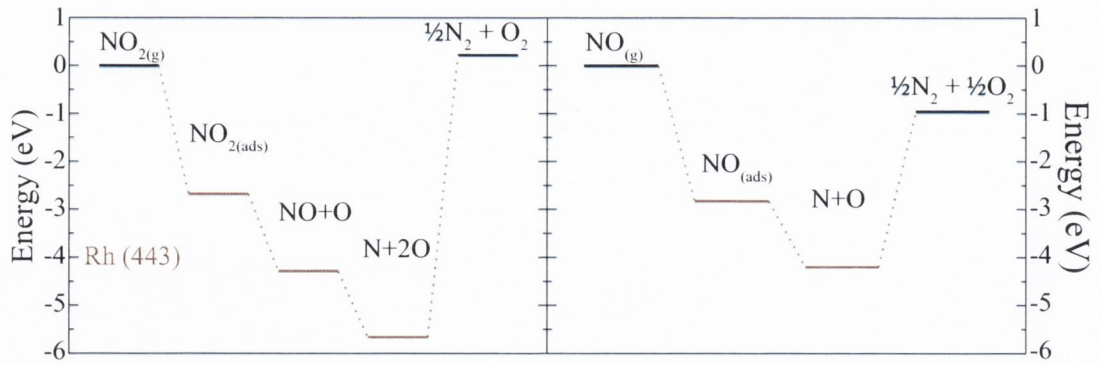


Figure 5.26: The calculated energies for the dissociation profile of (a) NO_2 and (b) NO on the Rh {443} stepped surface.

change to the σ and π systems upon interaction of the adsorbates with the Rh surface. The interaction of NO_x molecules with the Rh step causes a redistribution of electron density within both adsorbates. For NO this interaction stabilises the N-O $2\pi^*$ anti-bonding orbital, reducing the N $2p$ contribution to this orbital, and transferring the donated electron density from Rh to the O atom. A similar stabilisation of the $3\pi^*$ orbital is observed for the interaction of μ-nitrito mode with the Rh surface, indicating that the NO_2 adsorbate behaves like an NO molecule with an elongated bond to an O ad-atom. The absence of N $2p$ contributions to this orbital can been seen at the top of the valence band. Direct donation to the π^* orbital is therefore shown not occur, suggesting that the Blyholder model does not hold for NO_x adsorption on the Rh {111} surface. The electronic rearrangement of the σ and π systems, along with the stabilisation of the anti-bonding orbitals would suggest that a more complicated mechanism is occurring, similarly to that proposed by the allylic configuration. The electronic structure for NO_x on Rh is closely related to the allylic configuration as on the step edge, in a similar manner to NO_x adsorption on the low index planes of rhodium metal. The NO adsorption mode on the step edge having a greater stability over the low index surfaces can be attributed to the splitting of the 1π orbital on interaction with the step, and greater charge donation which is reflected in the increase contribution of the O atom to the occupied states of the $3\pi^*$ orbital.

The calculated decomposition profile shows that the breakdown of NO_x is much more

energetically favourable than the low index surfaces. This indicates that the defect step is more active towards *de*NO_x than the flat surfaces, enhancing the catalytic properties of the {111} surface. The defect step as a more active site than a flat surface has also been suggested experimentally,[190, 193, 194] and the step structure chosen for this study appears to be more active than previous structures.[81, 188] Similar to other rhodium surfaces, O atoms will saturate the step edge and are particularly detrimental to further NO_x reduction as the O atoms prefer a similar adsorption site to NO. This would lead to deactivation of the step, and a reductant is required.

5.4 Conclusion

The adsorption modes for N, O, N_2, O_2 and NO_x adsorbates on the {100}, {110} and {443} surfaces of rhodium were investigated to identify the most stable mode for each species using DFT with the PBE functional. Once the most stable adsorption mode was determined for each, their electronic interactions with the surfaces were examined using Bader calculations, charge difference plots, PEDOS and percentage contributions of the individual states to the MOs. The atomic N species adsorbed exothermically at the hollow site of the {100} and {443} surface, while it adsorbed on the short bridge site of the {110} surface. The O adsorbates where found to adsorb exothermically at the bridge site on the {100} and {110} surfaces, and at the step edge on the {443} surface. The N and O adsorbates were found to be more stable on the {443} surface than either of the other low index surfaces. N adsorption is more stable on the {100} surface than the {110} surface, while the reverse is true for O adsorption. Bader charges and charge difference plots indicated that the N and O adsorbates gained density from the metal surfaces forming anionic $N^{\delta-}$ and $O^{\delta-}$ on the three surfaces, with the greatest charge donation from the step indicating a stronger interaction, and thus lower adsorption energies.

The most stable adsorption mode for NO was found to be the bridge site on both the {100} and {110} surfaces, while the step edge was the preferential adsorption site

for NO on the {443} surface of Rh. The trend for E_{ads} in order of largest energy being {443} > {100} > {110}. For NO_2, the μ-nitrito configuration with the N and O surface atoms bonded to two top sites across a bridge site was calculated to be the most stable adsorption mode on all three surfaces with the trend for E_{ads} being similar to NO adsorption. Bader analysis, charge difference and PEDOS plots show that there is an overall charge donation from all three surfaces to the NO and NO_2 adsorbates, with the greatest charge donation associated with the stepped surface of Rh.

The interaction of the NO_x adsorbates with the three surfaces leads to a redistribution of electron density within the molecules and a stabilisation of the orbitals. For NO, this causes a stabilisation of 5σ orbital, significantly lowering it in energy, and also a stabilisation of the $2\pi^*$ anti-bonding orbital. The stabilisation of the N-O anti-bonding π^* orbital reduces the N contribution and transfers electron density to the O atom. The mechanism observed for NO_2 on the Rh surface, stabilises the $3\pi^*$ anti-bonding orbital in a similar manner indicating that NO_2 behaves like an NO adsorbate with an elongated bond to an O ad-atom. The electronic structure of the NO_x molecules on all three surfaces can be related to the recently proposed allylic configuration, as the lower bonding orbitals are seen to be greatly stabilised, and the anti-bonding π^* orbitals being also stabilised with an O $2p$ dominance. The stabilised π^* anti-bonding orbital is split with the occupied π^* being O $2p$ dominated and the unoccupied states being N $2p$ dominated for the NO_x adsorbates. This model is consistent with the $\widetilde{d}_\pi$ combination associated with the allylic configuration. This indicates that the allylic configuration can be extended to all low index surfaces of rhodium metal, suggesting that this mechanism provides a complete description of surface-adsorbates charge donations on metal surfaces.

The calculated energy profile for the *de*NO_x process were determined from the most stable adsorption mode for each species on each surface, and their respective gaseous species. The breakdown of NO_x on the three surfaces is exothermic, with the energetically most favourable breakdown being associated with the step surface. The trend for the breakdown of NO_x with the most favourable first is; {443} > {100} > {111}

> {110}. The stepped surface being the most active for *de*NO_x is due to the greater stability of N and O species, driving the reaction to the dissociation products. This shows that defect sites such as steps on the flat surfaces enhance the breaking of the NO bond on rhodium metal. Of the four rhodium surfaces under investigation, the {110} surface is the least active for *de*NO_x; however the formation of N_2 is exothermic on this surface, while it is endothermic on the others. This indicates that a mixture of {100}/{111} surfaces with the {110} surface will provide the most active combination for the reduction and easy removal of N_2.

For all three metals, the formation of O_2 and its subsequent removal requires a large energy and thus extremely difficult. The large energy barrier required to remove O_2 adsorbates to their respective gaseous species is due to the large adsorption energy of O adsorbates on all low index surfaces of Rh. The strongly bound O atoms will saturate the surface, blocking sites for subsequent NO_x breakdown and deactivating the catalyst. In particular for the step on the {111} surface, as there is competition between O and NO for preferential adsorption at the step edge. This indicates that Rh metal would become deactivated under high O_2 concentrations, and thus not effective for lean-*de*NO_x. The strongly bound O atoms will therefore have to be removed by a reductant during the redox process.

Chapter 6

Effect of Rh cluster size on *de*NO_x

6.1 Introduction

The active metal catalysts that are utilised in *de*NO_x technologies form small metal clusters that are dispersed, and impregnated on oxide supports such as CeO_2 and γ-Al_2O_3. The metal clusters expose low index surfaces at their terminated crystal edge, and as the {111} surface is the most thermodynamically stable surface, it is likely to be the most expressed surface on the metal clusters under thermodynamic control. Metal clusters are not uniform in size across the oxide support, and therefore the size of their surface facets vary. The variation of the size of the surface and cluster facets will affect their catalytic properties and behaviour to interact with gases, and consequently the reactions that take place on the cluster surface. It is therefore necessary to examine the effect of varying the size of the {111} surface of the cluster facet, on the *de*NO_x chemistry of Rh metal. The adsorption of N, O and NO adsorbates on the Rh clusters was explored in a similar manner to the adsorption on the Rh low index surfaces, to determine the most stable adsorption modes on each of the clusters. The electronic structure for the most stable adsorption mode will be determined and their energies used to build a decomposition profile.

6.2 Rh$_n$ clusters (n = 10, 20, 35, 56)

The metal clusters were generated by cutting {111} surfaces of varying size from the relaxed structure of the Rh {111} surface so that the atoms are already in their relaxed positions. The {111} surface of the metal cluster was varied by adding a row of atoms to the surface from 3 to 6 rows, producing Rh clusters containing 10, 20, 35 and 56 atoms. The Rh_{10}, Rh_{20}, Rh_{35} and Rh_{56} metal clusters were place in cubic unit cells with dimensions of 15 x 15 x 20Å, 20 x 20 x 22Å, 22 x 22 x 24Å, and 25 x 24 x 26Å, respectively, so that their neighbouring images under periodic boundary conditions where sufficiently far apart that no interactions occurred. The structures were relaxed using a Γ-centred k-point of 1x1x1 and a plane wave energy cut-off of 400 eV. The structures were deemed converged when the forces acting on the atoms were reduced to less than 0.01 eV/Å. The relaxed structures for the Rh clusters are shown in Figure 6.1, with the {111} surface being expanded from 4.91Å to 13.52Åfor the Rh_{10} to Rh_{56} clusters, respectively. The layers are coloured for clarity in a similar manner to the low index surfaces, with the adsorption sites being easily identified, as top/bridge (white), hcp (yellow) and fcc (green). The number of possible adsorption sites to be explored increases with increasing size of the Rh clusters.

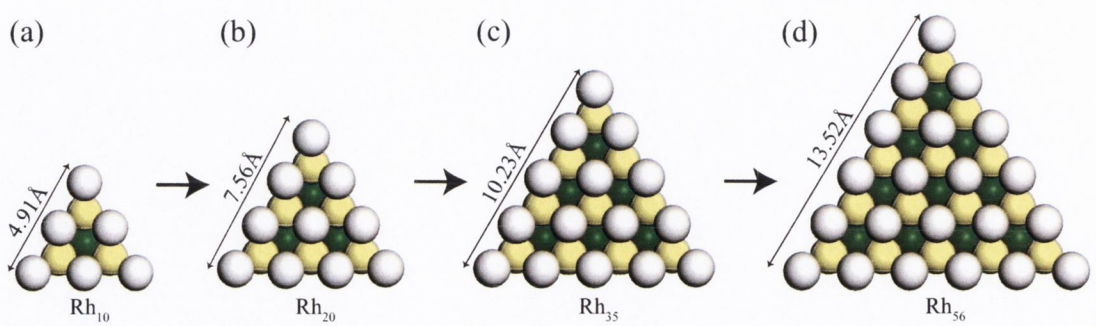


Figure 6.1: The relaxed structures of the Rh clusters with varying the size of the {111} surface for (a) Rh_{10}, (b) Rh_{20}, (c) Rh_{35} and (d) Rh_{56} metal clusters. The top (white), second (yellow) and third (green) layers are coloured for clarity allowing identification of top/bridge (white), hcp (yellow) and fcc (green) high symmetry adsorption sites.

As the Rh clusters have terminated edges, they would be expected to have a number of unpaired electrons at the edges of the metal clusters since the metal atoms are not fully coordinated. The ground state electronic structure of the metal clusters was therefore explored by examining the electronic spin of each metal cluster. The metal clusters were constrained to an initial large spin during relaxation. After a number of ionic steps their electronic spin was released and then relaxed to their lowest energy electronic arrangement providing the ground state spin. For the Rh_{10} cluster the ground state spin was determined to be 2, however, for the other clusters the ground state spins were determined have higher spin integers, and thus a number of different spins were tested for each metal cluster to ensure that the obtained spin was the lowest energy electronic arrangement. The energies for the different tested spins are shown in Figure 6.2. The graph shows that there are a number of local minima, and the global minimum of a spin of 14, 19 and 8 for Rh_{20}, Rh_{35} and Rh_{56} clusters, respectively. The graph shows that the lowest energy spins increase with increasing cluster size up to Rh_{35}, with a much lower spin for the largest Rh_{56} cluster.

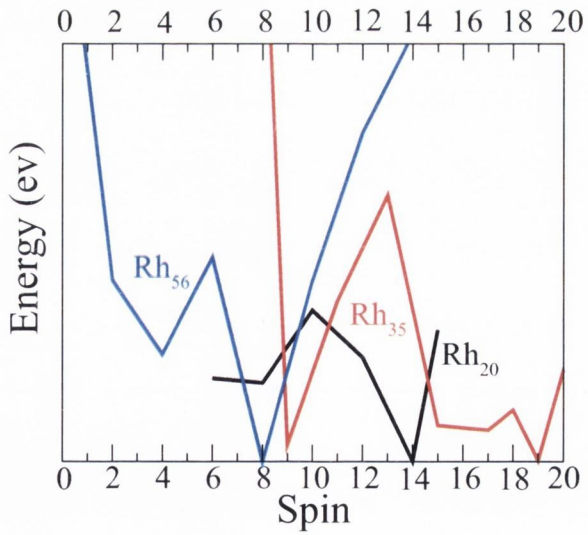


Figure 6.2: The energies for the different spins of the Rh_n (n = 20, 35, 56) metal clusters.

The calculated PEDOS for the lowest energy electronic configuration of the Rh_n clusters is shown in Figure 6.3. The graphs show both spin up and spin down contribu-

tions to the VB and CB, which are dominated by Rh 4*d* states with minor contributions from Rh *s/p* states for each of the metal clusters. The calculated PEDOS for the Rh_{10} cluster shows that there is an energy gap in the states around -7 eV, and also between the top of the VB and bottom of the CB. For the Rh_{20} cluster, the energy gap closes around -6 eV with the energy gap between the VB and CB also becoming smaller. On approaching the Rh_{35} and Rh_{56} clusters, both energy gaps disappear. This shows that the electronic structure of the smaller clusters is molecular in nature, while as the cluster size increases they become more metallic in nature with the band gap disappearing. The largest Rh cluster has a electronic structure similar to the extended crystalline Rh {111} surface, indicating that the cluster size is sufficiently large and approaching a metal surface. The position of the E_F is seen to increase with increasing cluster size, from -3.69 eV to -3.09 eV for Rh_{10} to Rh_{56}, respectively.

6.3 N, O and NO adsorption on Rh_n clusters

6.3.1 N adsorption

N adsorption was explored for all the possible adsorption sites on each of the Rh_n clusters to determine the lowest energy adsorption mode. The number of configurations for each of the four types of adsorption site increases with increasing Rh cluster size. For example, the Rh_{10} nanoparticle has one kind of hcp and fcc site to test, the Rh_{20} nanoparticle has two kinds of hcp site and one fcc site, while the Rh_{35} nanoparticle has three kinds of hcp and two fcc, and the Rh_{56} nanoparticle has three hcp and three fcc sites. Nitrogen was placed on all possible adsorption sites and relaxed to determine the lowest energy adsorption mode for each cluster. The most stable adsorption sites were determined to be a three-fold hcp site at the corner of the Rh_{10}, Rh_{35} and Rh_{56} clusters, while preferential N adsorption occurs at the low coordinated bridge edge site on the Rh_{20}, as shown in Figure 6.4.

The associated CN, E_{ads}, spin and bond lengths for the most stable N adsorption sites on each of the Rh clusters are detailed in Table 6.1. The E_{ads} increases from the

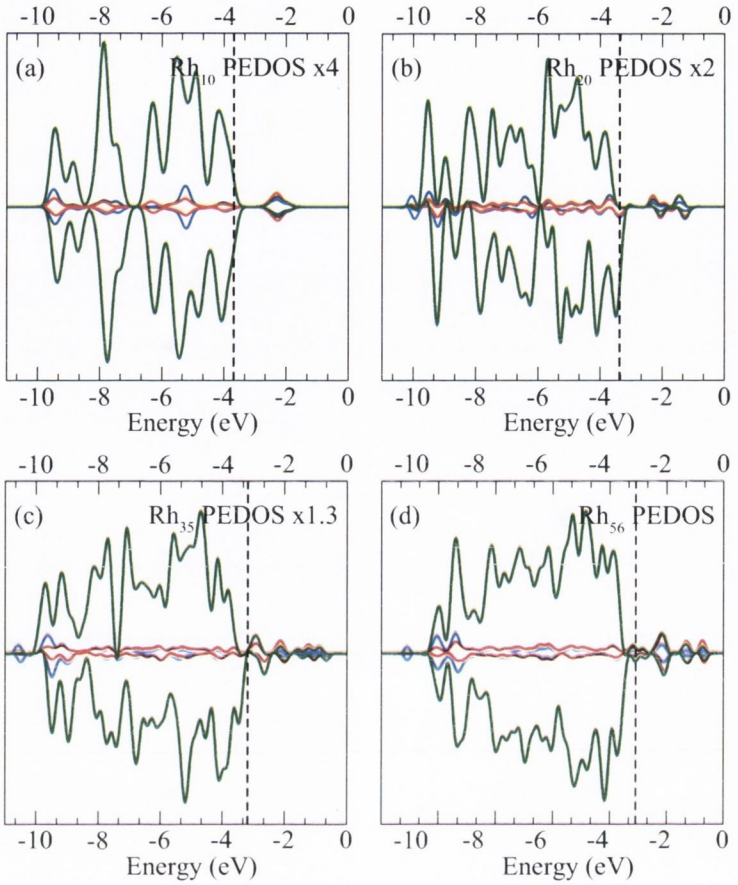


Figure 6.3: The calculated PEDOS of the lowest energy electronic configuration for the (a) Rh_{10}, (b) Rh_{20}, (c) Rh_{35} and (d) Rh_{56} metal clusters. The graphs are scaled relative to to the largest Rh cluster, with E_F indicated by the dotted line and each graph aligned to their respective E_{vac}'s. The *s*, *p* and *d* states are indicated by the blue, red and green lines, respectively.

Rh_{10} to the Rh_{20} cluster, and progressively decreases to Rh_{56}, with N adsorption having the most stable adsorption mode on the bridge site edge of the Rh_{20} cluster. This energy is around 0.30 eV more stable than the bridge sites of the other Rh clusters. The hcp site on the middle of the Rh_{56} cluster has an adsorption energy of -0.33 eV which is similar to the calculated adsorption energy of the most stable hcp adsorption site on the extended Rh {111} surface. This indicates that the Rh_{56} cluster size is approaching the behaviour of a {111} surface.

The spin for N adsorption on the Rh clusters has no trend, and the spin for N on the Rh_{10} reduces by 1 from the clean Rh_{10} cluster. The spin of the system decreases for N on the Rh_{20} and Rh_{35} clusters compared to their respective clean clusters. The spin of

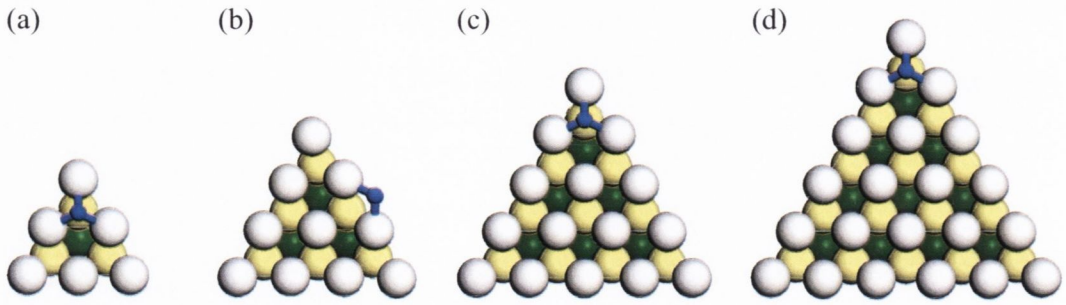


Figure 6.4: The most stable N adsorption modes on the (a) Rh_{10} (b) Rh_{20} (c) Rh_{35} and (d) Rh_{56} clusters. The nitrogen atoms are the blue spheres with the Rh atoms coloured by the different layers.

the system for N adsorption on the Rh_{56} cluster however, increases from the pure Rh_{56} cluster showing that more electrons become unpaired when N interacts with the cluster surface. All Rh-N bond lengths for the three-fold hcp sites are quite similar, with the bond length being shorter for the low coordinated bridge edge site for N adsorption on Rh_{20}.

Rh cluster	Site	CN	E_{ads} (eV)	Spin	Rh-N (Å)	N Charge	Rh Charge
Rh_{10}	hcp corner	3	-0.531	1	1.87 (x3)	-0.61	+0.32 (x2), +0.14
Rh_{20}	bridge edge	2	-0.844	11	1.80 (x2)	-0.60	+0.33 (x2)
Rh_{35}	hcp corner	3	-0.630	16	1.86 (x3)	-0.59	+0.23 (x2), +0.18
Rh_{56}	hcp corner	3	-0.537	11	1.87 (x3)	-0.61	+0.24 (x2), +0.17

Table 6.1: The most stable adsorption site, CN, E_{ads}, spin, Rh-N bond length, and N and Rh charges for the N adsorption on the Rh_n clusters.

The Bader charges (Table 6.1) show that the N adsorbates are more negative than atomic N, indicating that charge transfer to the N adsorbates. The charges show that the Rh surface atoms on the bridge site lose the most charge to the adsorbates, suggesting a stronger interaction than on the other clusters, and thus a more stable adsorption energy. The charge transfer process to the adsorbate can also be seen by the calculated charge difference plots, shown in Figure 6.5. The smaller Rh_{10} cluster have regions of gain/loss on other Rh atoms on the clusters which show that their electronic structure is influenced by the N adsorption, whereas for the larger clusters (Rh_{35} and Rh_{56}) on

the Rh atoms that are bound to the N atom are effected.

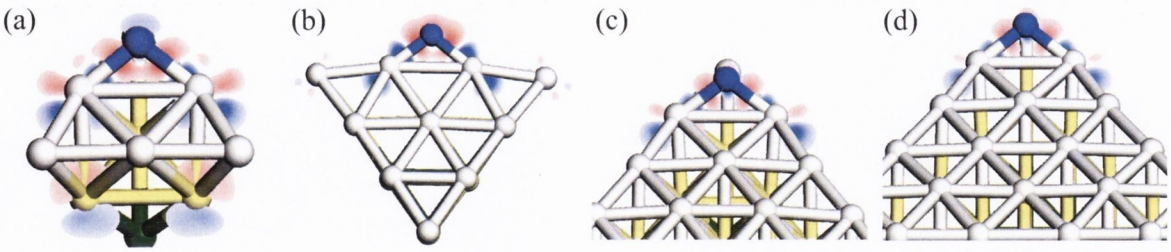


Figure 6.5: The charge difference plot for the most stable N adsorption modes on the (a) Rh_{10} (b) Rh_{20} (c) Rh_{35} and (d) Rh_{56} clusters. The charge difference ranges from -0.3 (blue) electrons/Å^3 to +0.3 (red) electrons/Å^3.

The PEDOS (Figure 6.6) shows that the VB and CB for each N adsorption site is dominated by a mixing of N $2p$ and Rh $4d$ states with smaller contributions from N $2s$ and Rh s/p states. The occupied N $2s$ states are too low in energy to be observed on the PEDOS plots. The band gaps observed for the smaller clusters (Rh_{10} and Rh_{20}) are not present from the N adsorption on these clusters. For the hcp sites on the Rh_{10}, Rh_{35} and Rh_{56} nanoparticles, there appears to be a N $2p$ peak from -12 to -10 eV which changes for the different cluster size. The lower energy peak of the two appears to change with increasing cluster size, being largest on the large clusters suggesting a difference in the bonding of the N adsorbates. The presence of N $2p$ states up to E_F and into the CB are quite similar on the Rh_{10}, Rh_{35} and Rh_{56} clusters from similar charge donation from the cluster to the N adsorbate. The electronic structure for N adsorption on the Rh_{20} cluster is different due to the different coordination environment of the adsorption mode. There are a number of N $2p$ peaks from -12 to -6 eV that are not observed on the other plots. These interact with the Rh $4d$ band, and there are states present up to E_F from charge donation to the adsorbate from the cluster. The presence of N $2p$ states on all plots indicate that the N states are not fully filled.

6.3.2 O adsorption

The most stable O adsorption modes on the Rh_n clusters is the bridge site on the cluster edge as shown in Figure 6.7. The most stable adsorption mode being similar on all Rh

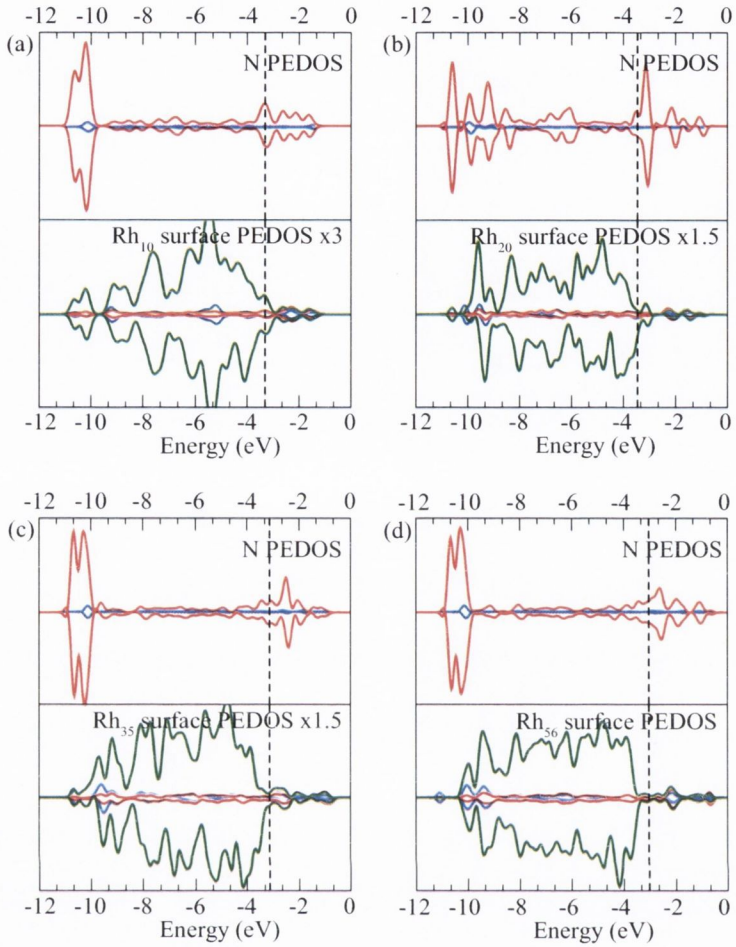


Figure 6.6: The calculated PEDOS for the most stable N adsorption modes on the (a) Rh_{10} (b) Rh_{20} (c) Rh_{35} and (d) Rh_{56} clusters. The PEDOS for the top Rh surface layer is shown in each plot with the *s*, *p* and *d* states shown by the blue, red and green lines, respectively. Each plot is aligned to E_{vac} at 0 eV with the position of E_F indicated by the dotted line. The Rh_{10-35} surface PEDOS are scaled relative to the Rh_{56} PEDOS, while the N PEDOS are all on the same scale.

clusters indicates that O will favour being on the edge of the cluster regardless of the cluster size.

The CN, E_{ads}, spin, and Rh-O bond distances of the most stable adsorption modes on each of the Rh clusters are detailed in Table 6.2. Comparing the adsorption energies shows that oxygen adsorption is more stable on the Rh_{20} cluster than the other clusters. The spin of the system for O adsorption on the Rh_{10} is unchanged to the spin of the bare Rh_{10} cluster, with the spin of the system for O adsorption on the other clusters decreasing relative to their respective bare clusters. The Rh-O bond distances are seen

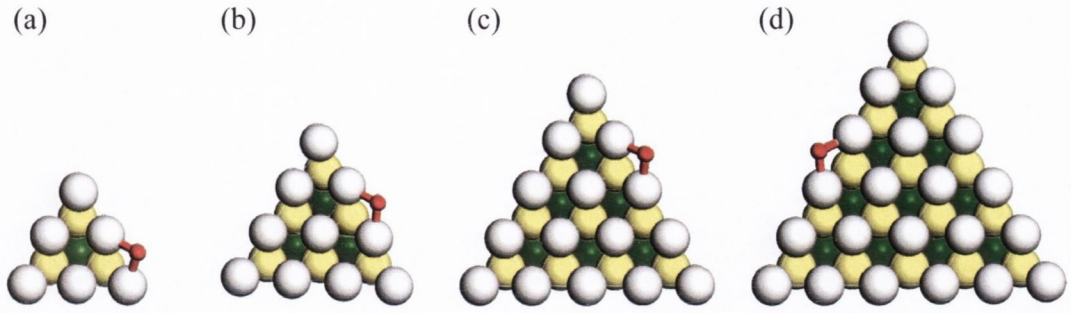


Figure 6.7: The most stable oxygen adsorption modes on the (a) Rh_{10} (b) Rh_{20} (c) Rh_{35} and (d) Rh_{56} clusters. The oxygen atoms are the red spheres with the Rh atoms coloured by the different layers, similarly to the clean clusters.

to be within a range of 0.07Å as O favours similar adsorption sites on the Rh_n clusters. Similar to N adsorption, the adsorption energy for the fcc site on the Rh_{56} is similar in energy to the most stable fcc site for O adsorption on the Rh {111} surface, showing that the Rh cluster size is approaching the properties of the extended surface.

Rh cluster	Site	CN	E_{ads} (eV)	Spin	Rh-O (Å)	O Charge	Rh Charge
Rh_{10}	bridge edge	2	-2.13	2	1.92, 1.89	-0.67	+0.25, +0.40
Rh_{20}	bridge edge	2	-2.82	10	1.87 (x2)	-0.70	+0.35 (x2)
Rh_{35}	bridge edge	2	-2.24	13	1.93, 1.86	-0.69	+0.36, +0.20
Rh_{56}	bridge edge	2	-2.34	6	1.89 (x2)	-0.70	+0.25 (x2)

Table 6.2: The adsorption site, CN, E_{ads}, spin, Rh-N bond length, and N and Rh charges for the most stable O adsorption modes on the Rh_n clusters.

Bader charges (Table 6.2) show that the O adsorbates gain charge relative to atomic O, showing charge transfer from the Rh cluster, with all adsorption sites donating a similar charge. The Rh surface atoms for the most stable O adsorption site on the Rh_{20} cluster lose the most charge to the adsorbate, indicating a stronger interaction and it being more stable than the other bridge edge sites on the different Rh clusters. The charge donation from the Rh clusters to the O adsorbates can be seen on the calculated charge difference plots (Figure 6.8).

The calculated PEDOS (Figure 6.9) shows that the VB and CB for all PEDOS plots are dominated by a mixture of O $2p$ and Rh $4d$ states with small contributions from

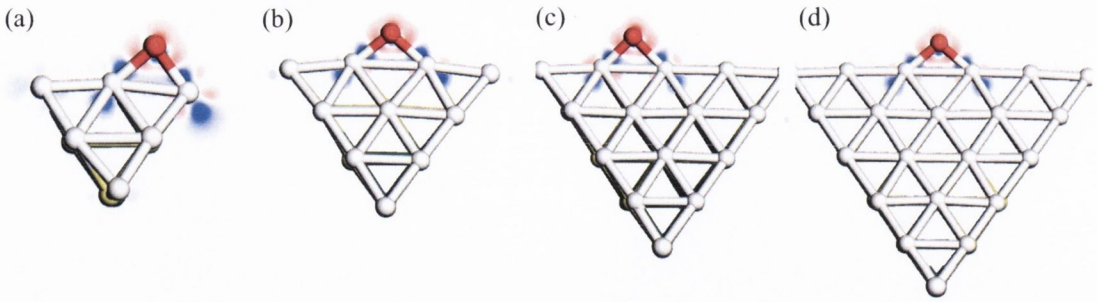


Figure 6.8: The charge difference plot for the most stable oxygen adsorption modes on the (a) Rh_{10} (b) Rh_{20} (c) Rh_{35} and (d) Rh_{56} clusters. The charge difference ranges from -0.3 (blue) electrons/Å^3 to +0.3 (red) electrons/Å^3.

O 2*s* states and Rh *s*/*p* states. The electronic structure of the VB and CB are quite similar for O adsorption on all Rh clusters. There is a range of peaks around -11 to -8 eV at the bottom of the VB for each system, which appears to have a greater O 2*p* contribution for O adsorption on the Rh_{20} cluster than on the other clusters. The O 2*p* states from -8 eV up to E_F the have greater contributions spread over the energy range to the VB for O adsorption on the Rh_{10}, Rh_{35} and Rh_{56} clusters, while for O on Rh_{20} there are two peaks around -7 eV and E_F. For all Rh clusters, the O 2*p* states up to E_F that interact with the Rh 4*d* band are filled from charge donation to the O adsorbate; however, the presence of O 2*p* states in the CB indicates that the O states are not fully filled.

6.3.3 NO adsorption

The most stable NO adsorption modes on the Rh clusters are shown in Figure 6.10. NO prefers the three-fold hcp site at the corner on the Rh_{10}, Rh_{35}, and Rh_{56} clusters, while preferential NO adsorption occurs offset from the top site located at the corner of the Rh_{20} cluster as shown in Figure 6.10 (b). This site is 0.30-0.50 eV more stable than on the other clusters, indicating that there must be some difference in the electronic structure to change the adsorption site preference.

The CN, E_{ads}, spin, Rh-N and N-O bond distances, and vibrational data for the most stable adsorption modes on the Rh clusters are detailed in Table 6.3, along with

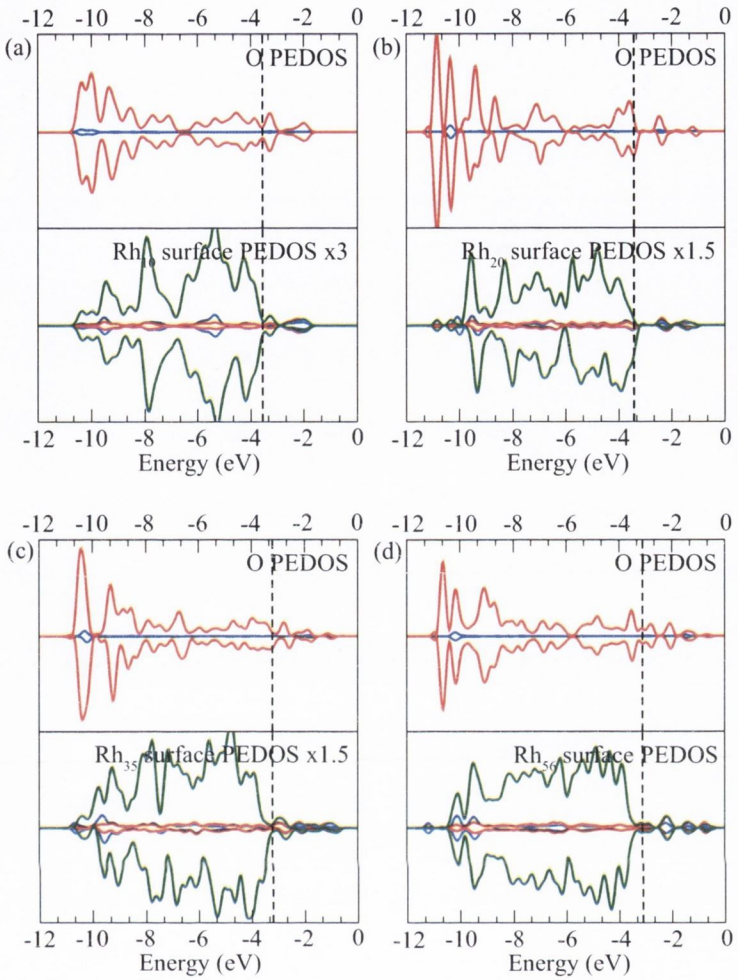


Figure 6.9: The calculated PEDOS for the most stable O adsorption modes on the (a) Rh_{10} (b) Rh_{20} (c) Rh_{35} and (d) Rh_{56} clusters. The PEDOS for the top Rh surface layer is shown in each plot with the *s*, *p* and *d* states shown by the blue, red and green lines, respectively. Each plot is aligned to the vacuum energy at 0 eV with the position of the fermi level indicated by the dotted line.

the details for gaseous NO. The E_{ads} are seen to decrease with increasing Rh cluster size, with NO being most stable on the Rh_{10} cluster. The system spin for NO adsorbed on Rh_{10} and Rh_{56} is found to decrease by 1 relative to the pure clusters, while the system spin remains unchanged for the Rh_{35} cluster. The system spin for the NO adsorbate on the Rh_{20} cluster appears to increase relative to the bare cluster. The bond lengths for the coordinated N atom on the Rh clusters are longer for the three-fold hcp site than the top site, and has similar lengths regardless of cluster size. The N-O bond length is seen to increase by 0.04Å and 0.08Å when interacting with the top and hcp sites,

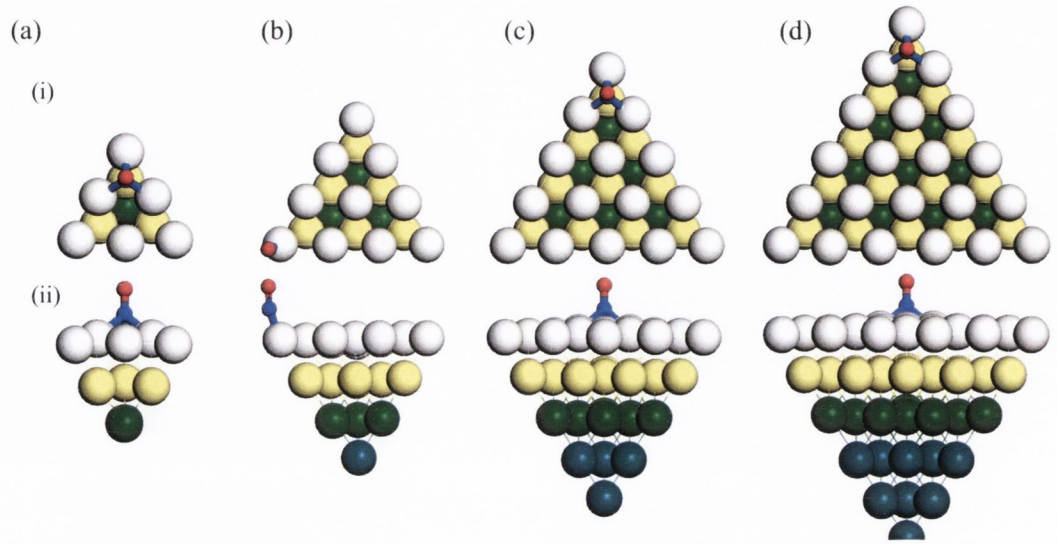


Figure 6.10: The most stable NO adsorption modes on the (a) Rh_{10} (b) Rh_{20} (c) Rh_{35} and (d) Rh_{56} clusters, along the (i) *c*- and (ii) the *b*-vectors. The N and O atoms are the blue and red spheres, respectively, with the Rh atoms coloured by the different layers, similarly to the bare clusters.

respectively, on the Rh clusters, relative to gaseous NO. The vibrational frequencies are seen to have an opposite trend with their values decreasing with increasing Rh cluster size for the hcp site, and the top site on the Rh_{20} cluster has a larger calculated value due to the lower coordination of the site.

Rh cluster	Site	CN	E_{ads} (eV)	Spin	Rh-N (Å)	N-O (Å)	Vib (cm^{-1})
	Gas Phase	—	—	—	—	1.15	1920
Rh_{10}	hcp corner	3	-2.92	1	2.00 (x2), 1.96	1.23	1624
Rh_{20}	top corner	1	-2.87	15	1.75 (x1)	1.19	1783
Rh_{35}	hcp corner	3	-2.82	19	2.02 (x2), 1.93	1.23	1482
Rh_{56}	hcp corner	3	-2.77	7	2.01 (x2), 1.94	1.23	

Table 6.3: The adsorption site, CN, E_{ads}, spin, Rh-N and N-O bond lengths, and vibrational data for the most stable NO adsorption modes on the Rh_n clusters.

Bader charge (Table 6.4) indicate that charge is donated from the adsorption site to the NO adsorbate on each cluster, with the largest donation from the hcp site which is similar on the Rh_{10}, Rh_{35} and Rh_{56} clusters. The charge of the NO adsorbate on the

Rh_{20} is not as large since the adsorbate is coordinated to less Rh atoms. The Rh surface atoms that are bound to the NO adsorbates are seen to become more positive relative to the charges for the bare clusters, indicating a loss in charge to the NO adsorbate which decreases with increasing cluster size. The breakdown of the charges for the atoms of the NO adsorbates show that the coordinated N atom becomes negative gaining charge from the hcp site of the Rh_{10}, Rh_{35} and Rh_{56} clusters, while the coordinated N atom on the Rh_{20} cluster gains charge becoming less positive relative to gaseous NO, but not to the same extent. The O atom of the NO adsorbates on each of the Rh clusters has lost charge relative to gaseous NO, with the greatest charge being lost from NO on the largest cluster. The overall charge for NO on Rh_{56} is balanced however, by the N atom gaining more charge than that observed on the other clusters. The N atom gaining charge and the O atom losing charge in such a way indicates that the mechanism for charge transfer is similar to that observed on the crystalline Rh surfaces in previous chapters. There is thus significant charge donation from the surface to the molecule for all of the adsorption modes, coupled with a significant redistribution of charge within the molecule leading to charge transfer from the oxygen to the nitrogen.

	Species	NO	N charge	O charge	*Rh* charge
	NO^+	+1	+1.21	-0.21	—
	NO	0	+0.53	-0.53	—
	NO^-	-1	+0.10	-1.10	—
Rh_{10}	hcp corner	-0.49	-0.05	-0.44	+0.27 (x2), +0.12
Rh_{20}	top corner	-0.24	+0.25	-0.49	+0.20 (x1)
Rh_{35}	hcp corner	-0.49	-0.05	-0.44	+0.18 (x3)
Rh_{56}	hcp corner	-0.49	-0.07	-0.42	+0.15 (x2), +0.20

Table 6.4: The calculated Bader charges for NO in the (a) gas phase and (b) adsorption site on the Rh_n clusters.

The calculated charge difference plots for the most stable NO adsorption modes on the Rh clusters (Figure 6.11), show that on interaction of the NO adsorbate with the Rh_{20-56} clusters there is charge donation to the adsorbates with redistribution of charge

within the adsorbate, as indicated by the Bader charges. For the Rh_{10} cluster there is significant redistribution of charge across the cluster when interacting with the NO adsorbate. This suggests that a stronger interaction with the Rh cluster occurs, and a greater redistribution of charge than on the other clusters due to a lower number of cluster Rh atoms.

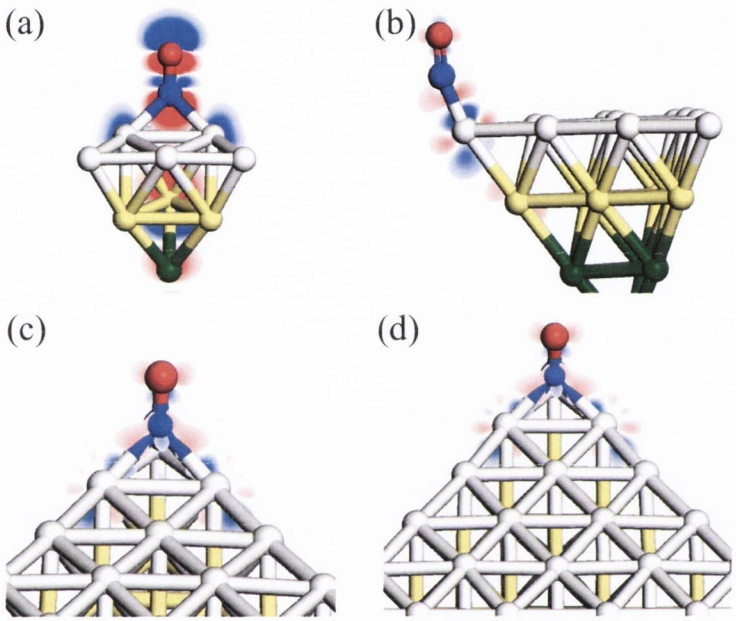


Figure 6.11: The charge difference plot for the most stable NO adsorption modes on the (a) Rh_{10} (b) Rh_{20} (c) Rh_{35} and (d) Rh_{56} nanoparticles. The charge difference ranges from -0.3 (blue) electrons/Å^3 to +0.3 (red) electrons/Å^3.

The calculated PEDOS for NO on the Rh_n clusters are given in Figure 6.12. The valence molecular orbitals of a gaseous NO molecule, and the molecular orbital diagram are shown in previous chapters (Figure 4.9 (a)). The orbitals are labelled in a similar manner for the NO molecule on the Rh clusters, relative to their respective E_{vac}. The position of the orbitals are at a lower energy to that of the calculated electronic structure for gaseous NO (Figure 4.9 (b)) due to their stabilisation when interacting with the Rh clusters. The 5σ orbital, which is above the 1π for gaseous NO, is significantly lowered in energy to below the 1π orbital for the NO adsorbate on all clusters.

The VB and CB contain a mixture of N and O $2s/p$ states and Rh $4d$ states, with minor contributions from Rh s/p states. On interaction with the Rh clusters, the $4\sigma^*$

orbital gains N $2p$ character, while losing O $2p$ character compared to the gaseous species. The N/O contributions to this orbital are seen to decrease within increasing Rh cluster size. The 5σ orbital is lowest in energy when interacting with the Rh_{20} clusters, while for the other clusters it overlaps in energy with the 1π orbital. The N/O contributions to this orbital decrease for the NO molecule interaction with the large Rh_{35} and Rh_{56} clusters. The 1π orbital is at a similar energy on all clusters with the N/O $2p$ contributions decreasing with increasing cluster size. The higher 2π orbital is split into occupied and unoccupied contributions when interacting with the Rh $4d$ band at the top of the VB. For all clusters, the O $2p$ states provide the greatest contribution to the occupied states of this orbital, while the unoccupied component is dominated by N $2p$ states. Similarly to the other orbitals, the N and O contributions to the 2π orbital decrease with increasing Rh cluster size.

The approximate percentage contributions for the most stable NO adsorption modes on the Rh clusters (Table 5.5) were calculated in a similar way to the low index surfaces of Rh. The N and O $2s/p$ contributions to the different orbital are similar for the Rh_{10}, Rh_{35} and Rh_{56} clusters since these have a similar adsorption site. The contributions to the orbitals of the NO molecule on the Rh_{20} cluster are different due to the different preferential adsorption site, with the exception of contributions to the 4σ orbital which are similar for all clusters. The 5σ orbital is O dominated for all clusters with the O s and p contributions increasing with increasing cluster size, whereas the N $2p$ contributions decrease with increasing cluster size. The largest changes occur fot the π system with the changing cluster size. The 1π system is N dominated and $2\pi^*_{occ}$ is O dominated for the NO molecule on the hcp site; however for the NO adsorbate on the top site of the Rh_{20} cluster there is a change in the dominant contributions to the 1π orbital with less O $2p$ contribution to the $2\pi^*_{occ}$ than on the other clusters. The contributions to the $2\pi^*_{unocc}$ appear to be similar on all clusters.

Comparing the orbital contributions to the NO adsorbate on the Rh clusters to the gas phase species shown in previous sections, there is considerable electronic rearrangement of the σ and π systems, similarly to the extended metal surfaces. The electronic

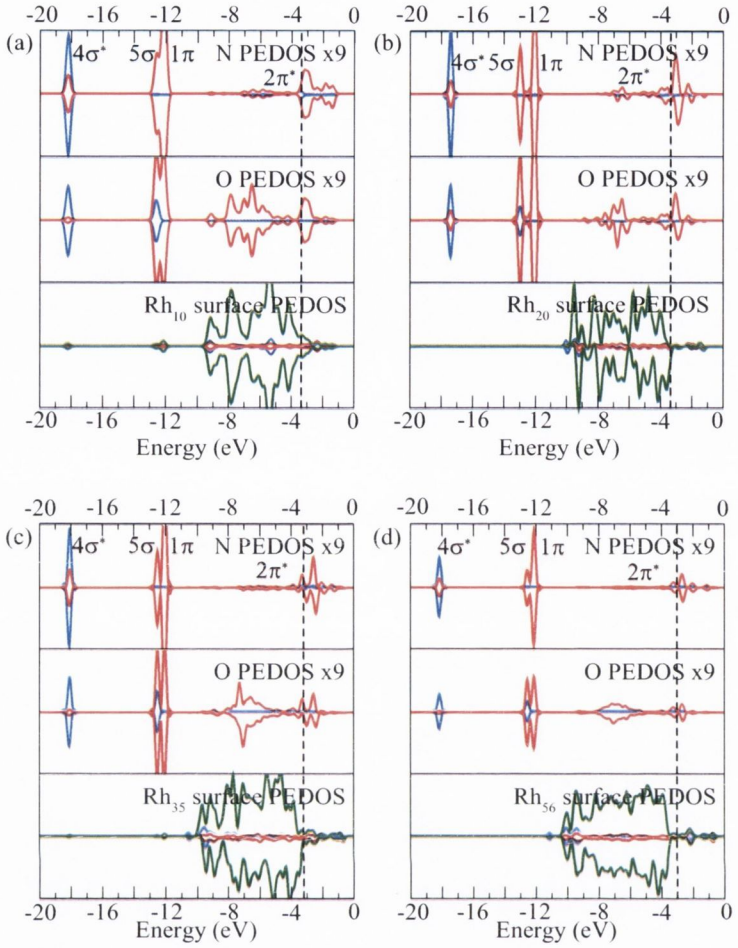


Figure 6.12: The calculated PEDOS for the most stable NO adsorption modes on the (a) Rh_{10} (b) Rh_{20} (c) Rh_{35} and (d) Rh_{56} clusters. The PEDOS for the top Rh surface layer is shown in each plot with the *s*, *p* and *d* states shown by the blue, red and green lines, respectively. Each plot is aligned to E_{vac} at 0 eV with the position of E_{F} indicated by the dotted line.

structure for NO on the Rh_n clusters is closely related to the allylic configuration, in a similar manner to NO_x adsorption on the low index planes of rhodium metal.

In comparison to the extended metal {111} surface of rhodium, the N and O contributions to the σ system of the NO adsorbate on the clusters is similar to the NO adsorbate on the Rh {111} surface. The difference between the clusters and extended surface lies in the interaction of the NO π system with the metal Rh atoms. The contributions to the 1π orbital are O dominanted for the adsorption on the Rh clusters, whereas for the extended metal Rh surface the 1π orbital is N dominated. For the $2\pi^*_{occ}$ orbital, the orbital is O $2p$ dominated on both metal clusters and the extended metal

(a)	$NO_{(ads)}$ on Rh_{10}					(b)	$NO_{(ads)}$ on Rh_{20}				
States	$4\sigma^*$	5σ	1π	$2\pi^*_{occ}$	$2\pi^*_{unocc}$	States	$4\sigma^*$	5σ	1π	$2\pi^*_{occ}$	$2\pi^*_{unocc}$
N $2s$	52	0	0	2	4	N $2s$	52	0	0	3	2
N $2p$	16	40	61	14	56	N $2p$	11	36	45	25	57
O $2s$	30	11	1	0	0	O $2s$	29	11	0	1	0
O $2p$	2	49	38	84	40	O $2p$	8	53	55	71	41
(c)	$NO_{(ads)}$ on Rh_{35}					(d)	$NO_{(ads)}$ on Rh_{56}				
States	$4\sigma^*$	5σ	1π	$2\pi^*_{occ}$	$2\pi^*_{unocc}$	States	$4\sigma^*$	5σ	1π	$2\pi^*_{occ}$	$2\pi^*_{unocc}$
N $2s$	52	1	0	1	5	N $2s$	51	1	0	1	5
N $2p$	11	29	62	12	55	N $2p$	15	30	54	11	49
O $2s$	29	16	0	0	0	O $2s$	32	16	0	0	1
O $2p$	8	54	38	87	40	O $2p$	2	53	46	88	45

Table 6.5: The approximate percentage contributions of N $2s$, N $2p$, O $2s$ and O $2p$ states to the molecular orbitals of NO adsorbed at the most stable sites of the (a) Rh_{10}, (b) Rh_{20}, (c) Rh_{35} and (d) Rh_{10} clusters.

surface; however the greater O contribution to this orbital is observed for the NO on the clusters than NO on the metal surface. This indicates that the greater adsorption energies on the metal clusters is due to the greater occupation of the O orbitals than the metal surface. The unoccupied states of the $2\pi^*$ are similar on the clusters and the metal surface. The adsorption of NO is most stable on the Rh_{10} cluster due to the greater contribution of the N atom to the 5σ and 1π orbitals.

6.3.4 Decomposition Profile

The calculated energies for each step of the NO decomposition pathway on the Rh_n clusters are detailed in Table 6.6, with the energies for the breakdown of NO on the Rh {111} surface also shown for comparison. Only the breakdown of NO was examined as this was shown previously to be the rate determining step during the *de*NO_x process, and more important than the easier breakdown of NO_2. The energetics of each step for NO dissociation were calculated using the energies of the most stable adsorption modes for N, O, and NO on the Rh_n clusters, and the energies of their respective gaseous

species. The calculated energies for each step of the dissociation of NO_x on the Rh surface can also be summarised graphically in Figure 6.13.

Reaction Step	Rh_{10}	Rh_{20}	Rh_{35}	Rh_{56}	Rh {111}
$NO_{(g)} \rightarrow NO_{(ads)}$	-2.94	-2.90	-2.85	-2.79	-2.46
$NO_{(ads)} \rightarrow N_{(ads)} + O_{(ads)}$	-0.67	-1.73	-0.98	-1.04	-0.84
$N_{(ads)} + O_{(ads)} \rightarrow \frac{1}{2}N_{2(g)} + \frac{1}{2}O_{2(g)}$	+2.66	+3.67	+2.88	+2.87	+4.36

Table 6.6: The calculated energies for the dissociation profile of NO on the Rh_n (n = 10, 20, 35, 56) clusters, and the extended Rh {111} surface with all values given in eV.

The breakdown of NO is the most energetically favourable on the Rh_{20} cluster, and least favourable on the Rh_{10} cluster, even though its adsorption is more stable. Comparing the energies to the Rh {111} surface, it is seen that the breakdown of NO on the clusters, with the exception of the Rh_{10} cluster, is more favourable than on the extended {111} surface. The trend for the breakdown of NO with the most energetically favourable being first is; $Rh_{20} > Rh_{56} > Rh_{35} >$ Rh {111} $> Rh_{10}$, indicating that the reduction of NO decreases with decreasing cluster size, with the exception of the most catalytically active Rh_{20} cluster. The breakdown of NO being more favourable on the Rh_{20} cluster can be explained by the N and O decomposition products being more stable on the Rh_{20} cluster than on the other cluster. This drives the reaction to dissociation, as indicated on the previously examined extended low index surfaces. Apart from the Rh_{10} cluster, the decomposition of NO is more favourable on the Rh_{20-56} clusters than on the extended low index surfaces, and the stepped surface with the decomposition data shown in previous chapters. The Rh_n clusters are more catalytically active towards *de*NO_x than the extended surfaces. This shows that the breakdown of NO is cluster size dependent, and the 'special' case of transition metal clusters with s^1 valence shells being highly active is observed in this study for *de*NO_x on Rh.[259, 260, 262, 264, 265, 278]

The removal of N_2 and O_2 from the clusters is difficult with a large energy requirement on each in a similar manner to the Rh {111} surface. The Rh_{20} cluster requires the most energy to remove the N and O ad-atoms, since they are more stable on this

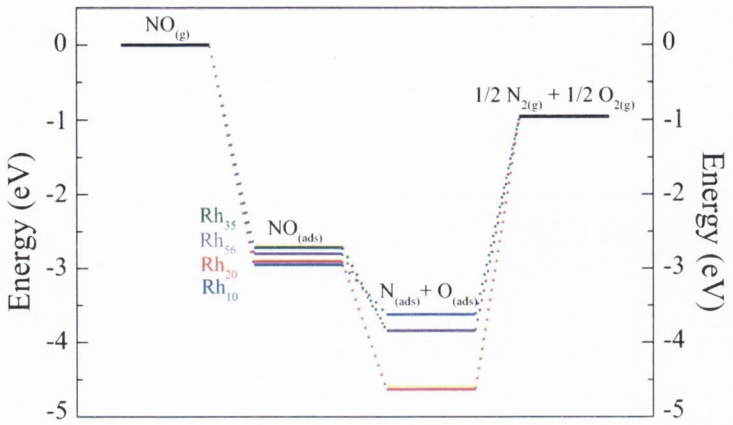


Figure 6.13: The calculated energies for the dissociation profile of (a) NO_2 and (b) NO on the Rh_n (n = 10, 20, 35, 56) clusters. The blue, red, purple and green lines show the dissociation pathways for the Rh_{10}, Rh_{20}, Rh_{35} and Rh_{56} clusters, respectively.

cluster. The Rh_{10} cluster requires the least amount of energy to remove the dissociation products, which is also less favourable for NO dissociation. The large energy required to remove these dissociation products from the Rh_n clusters can be attributed to the large adsorption energy of O atoms, with the energy on the extended surface larger due to the greater stability of O atoms. The O ad-atoms saturating the Rh_n clusters will block sites for any further NO_x breakdown, and thus poisoning the catalyst. The Rh_n cluster becoming saturated over time by O atoms is observed experimentally as the formation of $[Rh_xO_y]^+$ rhodium oxide are detected which inhibit any further NO decomposition.[276] The Rh cluster being more favourable for $de\mathrm{NO}_x$ than the extended surface and requiring less energy to remove the dissociation products, shows that they are a superior catalyst than large extended planes of Rh metal.

6.4 NO barrier on the Rh_{20} cluster

The adsorption of NO and energy to form N and O atoms was investigated in the previous section on the Rh_n clusters. The decomposition profile, built from the most stable adsorption modes, showed the energies from one step of the $de\mathrm{NO}_x$ process to another; however they did not indicate the energy barrier (activation energy) required to break the molecular bonds. As the $de\mathrm{NO}_x$ process was found to be most favourable

on the Rh_{20} cluster, the energy barriers to breakdown NO on the Rh_{20} cluster was explored using the climbing nudged elastic band (cNEB) method.

6.4.1 Co-adsorption

The starting and end points for the cNEB method are required to anchor the calculation and allow the images to relax relative to these points. For the initial starting points, the most stable adsorption modes for the NO (molecular species) obtained in the previous section are used; however for the end points, the co-adsorption of the N+O for the breakdown of NO are needed. The lowest energy configuration for the co-adsorption modes are obtained by exploring all possible combinations of each species on the different adsorption sites for the Rh_{20} cluster. For example, the O adsorbate was fixed at its most stable adsorption mode on the Rh_{20} cluster (the bridge site on cluster edge), while N adsorption was varied across the different adsorption sites to obtain the energies for the different configurations. This was reversed for N at its most stable adsorption mode while the O species was varied across the different adsorption sites.

The calculated configurations for the most stable N+O co-adsorption on the Rh_{20} cluster are shown in Figure 6.14. For both configurations, each of the adsorbed species prefer the bridge site on the cluster edge, where for N and O this is the same as single atomic adsorption on the Rh_{20} cluster.

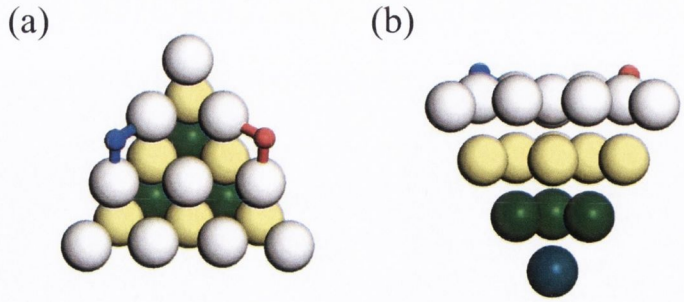


Figure 6.14: The most stable adsorption configuration for the co-adsorption of N+O on the Rh_{20} cluster, along the (a) *c*- and (b) *b*- vectors. The blue and red spheres are the N and O atoms, respectively, with the top layers of the Rh_{20} cluster coloured for clarity.

The details of the E_{ads}, spin and bond lengths for the most stable configurations for the co-adsorption N+O are given in Table 6.7. The calculated bond lengths for the co-adsorption of N+O on the Rh cluster are within 0.02 Å of the single N and O adsorbates on the cluster. For the co-adsorption of N+O, the overall spin is more than the spin of the N and O adsorption on the cluster, and one less than the spin of the pure Rh_{20} cluster.

Config.	Site	E_{ads} (eV)[1]	Spin[2]	Rh-N (Å)	Rh-O (Å)
N + O	Edge	-4.18	13	1.79	1.86

Table 6.7: The calculated E_{ads}, Spin, and bond distances for the most stable co-adsorption configurations of N+O on the Rh_{20} cluster.

The Bader charges indicated that the N (-0.59) and O (-0.69) species gained electron density from the Rh atoms, indicating charge transfer from the Rh_{20} species to the adsorbate, forming anionic species. The charge gained from each of the adsorbates and the charge lost from the Rh surface atoms which they are bound to is similar to that observed for the single adsorbed species on the Rh_{20} cluster. The PEDOS of each species is similar to the single adsorbed species on the Rh_{20} cluster, and therefore is not shown. Similar Bader charges and PEDOS shows that the charge interactions between the N, O and NO adsorbates with the Rh_{20} cluster do not change when another species is also adsorbed on the cluster.

The reaction pathway for the breakdown of NO on the Rh_{20} cluster leading to the most stable co-adsorption configuration for N and O is shown in Figure 6.15. The energies for each step of the pathway are shown relative to the most stable NO adsorption mode on the Rh_{20} cluster. The transition state is activated by tilting down the NO molecule so that it lies flat on the cluster, with the N atom bound to a bridge site and the O atom bound to a top site. The movement of the NO molecule in such a way has an energy barrier of 0.75 eV, elongating the bond to 1.28Å compared to the gas phase species (1.17Å). The calculated energy barrier is significantly lower than the calculated

value for NO decomposition on the {111} surface across the bridge and top sites after adsorption onto the hcp site. The barrier is however, greater by +0.2 eV compared to the barrier to NO breakdown through the weak top site intermediate. This suggests the breakdown of NO on the Rh cluster is much easier than the {111} surface of Rh after NO adsorption on the hcp site; however a further investigation is required to see if the NO molecule may also go through a weak intermediate on the Rh cluster to reduce the energy barrier.

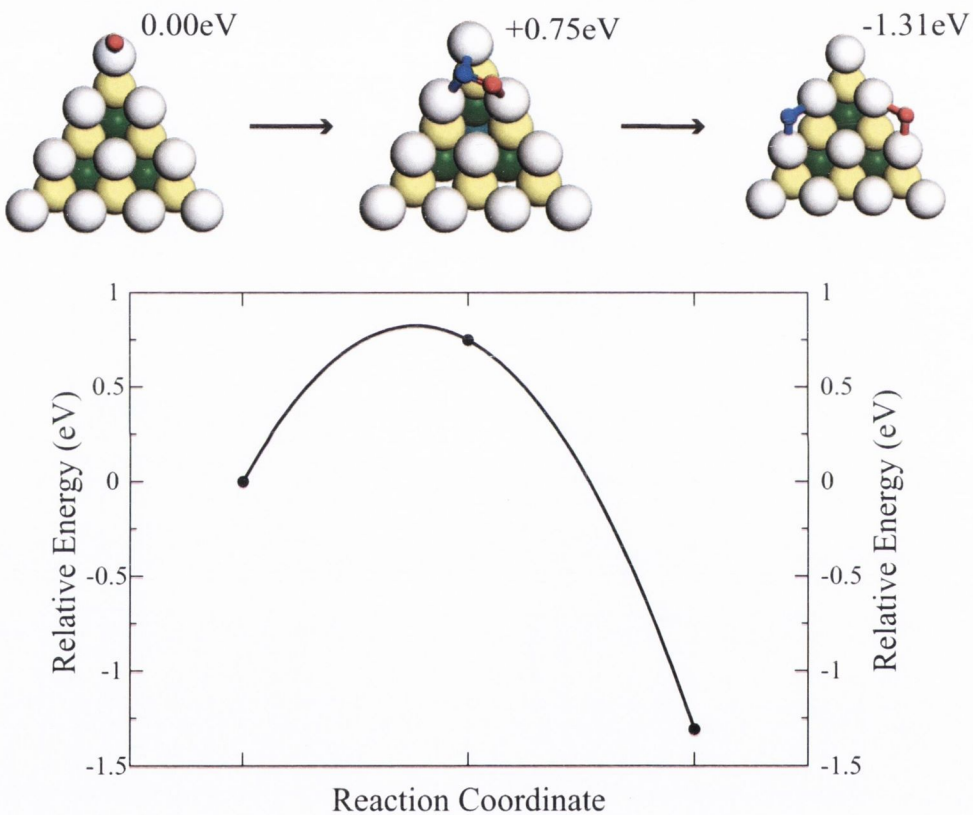


Figure 6.15: The reaction pathway for the decomposition of NO → N+O on the Rh_{20} cluster. The blue and red spheres are the N and O atoms, respectively, with the top layers of the Rh_{20} cluster coloured for clarity. The energy profile for the breakdown of NO is also shown.

6.5 Conclusion

The adsorption modes for N, O, and NO adsorbates on the Rh_n clusters were investigated to identify the most stable mode for each species using DFT with the PBE

functional. Once the most stable adsorption mode was determined for each, their electronic interactions with the {111} surfaces on each cluster was examined using Bader calculations, charge difference plots, PEDOS and percentage contributions of the individual states to the MOs. The atomic N species adsorbed exothermically at the three-fold hcp site on Rh_{10}, Rh_{35} and Rh_{56} clusters, while preferential adsorption occurred at the bridge edge site on the Rh_{20} cluster, with the greatest stability associated with the Rh_{20} cluster. The O adsorbates where also found to adsorb exothermically at the bridge edge site on all three metals, and the largest adsorption energy is associated with Rh_{20}, similar to N adsorption. Bader charges and charge difference plots indicated that the N and O adsorbates gained density from the metal surfaces forming anionic $N^{\delta-}$ and $O^{\delta-}$ on the three surfaces, with the greatest charge donation from Rh_{20} indicating a stronger interaction, and thus lower adsorption energies. The most stable adsorption mode for NO was found to be the hcp site on the Rh_{10}, Rh_{35} and Rh_{56} clusters, with the top site at the corner of the cluster preferred on the Rh_{20} species.

The trend for E_{ads} for the different adsorbates with varying cluster size is shown in Figure 6.16, indicating that N and O adsorption are much more stable than on the other clusters. The NO molecule is becoming less stable with increasing cluster size.

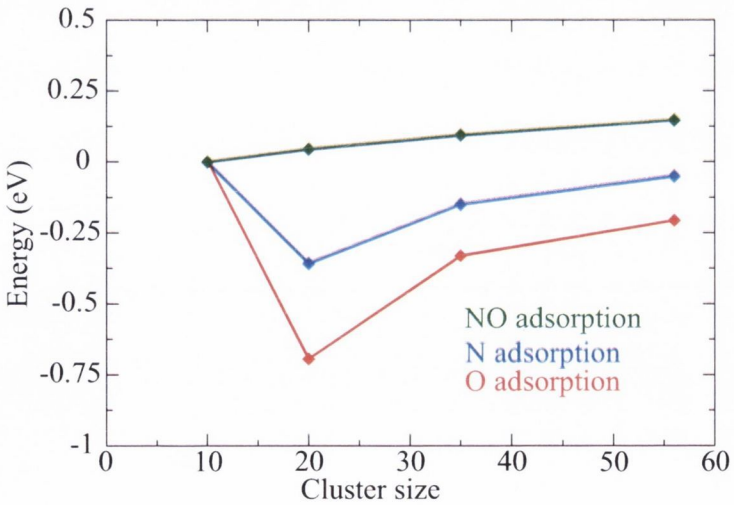


Figure 6.16: The trends for the adsorption energies of the N (blue), O (red) and NO (green) species on the Rh_n clusters.

Bader analysis, charge difference and PEDOS plots show that there is an overall charge

donation from all clusters to the NO adsorbate. The interaction of the NO adsorbates with the {111} surface of Rh_n, leads to a redistribution of electron density within the molecules and a stabilisation of the orbitals. The electronic structure of the NO on the Rh_n clusters can be related to the recently proposed allylic configuration, as the lower bonding orbitals are seen to be greatly stabilised, and the anti-bonding π^* orbitals being also stabilised with an O $2p$ dominance, in a similar manner to the Rh {111} surface. This model is consistent with the $\widetilde{d}_\pi$ combination associated with the allylic configuration. The electronic interactions with the Rh_n clusters are seen to be similar to the extended rhodium metal surfaces, further supporting the allylic configuration.

The NO decomposition profile for the Rh_n clusters was calculated from the energies of the most stable adsorption modes, and their respective gaseous species. The energetics show that the breakdown of NO is most favourable on the Rh_{20} clusters, with the NO dissociation energy decreasing with decreasing cluster size. The Rh_{20} cluster being the most favourable size for NO dissociation is due to the greater stability of N and O on the cluster than on the other clusters. This drives the dissociation reaction towards forming the N and O products. The breakdown of NO is more favourable on the clusters than the Rh {111} surface indicating that the clusters are more favourable for *de*NO$_x$. The subsequent removal of N and O from the surface of the cluster requires a large energy on all cluster sizes, similarly to the extended low index surfaces. This is attributed to the large adsorption energy of O atoms on the Rh_n clusters, which are difficult to remove. This is observed experimentally as Rh_xO_y complexes are found to form due to the dissociation on the metal clusters.[276] Similarly to other Rh surfaces, a reductant is required to remove O bound species. The energy barrier to break the NO bond is significantly lower than NO adsorption on the Rh {111} surface, suggesting that the breakdown on the cluster is much faster and facile than the extended {111} surface.

Chapter 7

Preliminary results for the chemical reduction of NO_x on the Rh {111} surface

7.1 Introduction

The mechanism for *de*NO_x on Rh is uncertain, as the breakdown of NO_x to N and O atoms can proceed through two intermediate transition structures, an N_2O_2 dimer or N_2O and O on the surface. These transition structures can be formed from two NO molecules reacting directly to form the N_2O_2 dimer, or when one NO molecule breaks up on the surface and the N atom moves to form N_2O with another NO molecule on the metal surface. The work outlined in this chapter will examine both possible pathways to show the lowest energy transition structure that is most likely to occur on the Rh {111} surface.

The chapter will provide preliminary calculations for the reduction of NO_x on the Rh {111} surface. The activation energy barriers for adsorption and NO_x dissociation on the Rh {111} surface. The activation energy barriers for the movement of N, O and NO across the Rh {111} surface will then be calculated to show which species is more likely to move during the *de*NO_x process, and also to compare the energy barriers for the

Rh {111} surface to Pd and Pt {111} surfaces. The competing pathways through the intermediates during the *de*NO_x process will be also examined, in order to determine the lowest energy pathway. All these calculations were carried out using the cNEB method on an expanded {111} p(3x3) surface. The expanded surface is required for the cNEB calculations so that more adsorption sites are available for the species to move and interact on the surface, and also to ensure that the image cells do not interact with one another under periodic boundary conditions.

7.2 NO_x adsorption and bond dissociation on the Rh {111} surface

The molecules in the gas phase was used as a starting point, and the most stable adsorption modes for NO_x on the Rh {111} surface were used as the end points to calculate the energy barriers to adsorption. For the gas phase starting points, the molecules were held fixed in the c-vector direction above the surface slab, and the bonds were relaxed in the ab-plane. The cNEB method was then used between the relaxed gaseous species and the most stable molecular adsorption mode.

In order to calculate the energy barriers to molecular bond breaking on rhodium, the most stable adsorption modes for each of the molecular species were used as a starting point. For the end points, the co-adsorption of the N+O and NO+O for the breakdown of NO and NO_2, respectively, are needed. The lowest energy configuration for the co-adsorption modes are obtained by exploring all possible combinations of each species on the different adsorption sites for the {111} surface of Rh.

7.2.1 NO_2 bond breaking

The most stable adsorption mode for NO_2 on the {111} surface was calculated previously to be the μ-nitrito mode across a bridge site, with the surface bound N and O atoms offset from top sites. This adsorption mode is used as the starting point for the

cNEB calculations to determine the bond dissociation energy, and as an end point for NO_2 adsorption on to the surface. The end point for the cNEB method was explored by examining the co-adsorption configurations for NO and O on the different combinations of surface sites. The most stable co-adsorption configurations for NO and O were calculated to be the NO_{fcc}+O_{fcc} and the NO_{hcp}+O_{fcc} combinations with E_{ads} of -3.25 eV and -3.27 eV, respectively, relative to the energy of NO_2. The adsorption energies are within 0.02 eV, and therefore both their bond dissociation pathways will need to be examined in detail to see which is more favourable.

The calculated NO_2 bond dissociation pathways, from gaseous NO_2 leading to the two different combinations are shown in Figure 7.1, with the energies shown relative to gaseous NO_2. There is no adsorption barrier for NO_2 from the gas phase onto the surface, as the energy profile proceeds decreases in energy to adsorption.

The bond dissociation pathway for the NO_{hcp}+O_{fcc} combination is shown in Figure 7.1 (a). The NO_2 molecule proceeds through a weakly bound intermediate (Figure 7.1 a(i)) where the N atom is bound to the top site (N-nitro mode) which requires 0.41 eV to form, leading to the breaking of the NO bond. All other images for this reaction pathway (Figure 7.1 a) shows NO and O movement across the surface to the most stable configuration and the barriers to this diffusion will be discussed later in the chapter. The energy require to form the N-nitro mode shows the rate limiting step for the breaking of the NO_2 molecule to NO_{hcp} and O_{fcc}.

For the bond dissociation pathway leading to NO_{fcc}+O_{fcc} combination, the NO_2 adsorbate is activated by the NO and O moving in opposite directions, twisting the NO_2 molecule and 0.11 eV less stable than the NO_2 adsorbate. The calculated transition state shown in Figure 7.1 b(iii) indicates further elongation of the NO bond parallel to the surface from 1.33Å to 1.64Å, leading to the breaking of the NO bond parallel to the surface, with an energy barrier of 0.71 eV. The resultant NO and O are present at bridge sites before adsorbing into the three-fold hollow sites.

The cNEB calculations indicate that the most energetically favourable pathway for NO_2 dissociation on the {111} surface of rhodium is through a weak intermediate

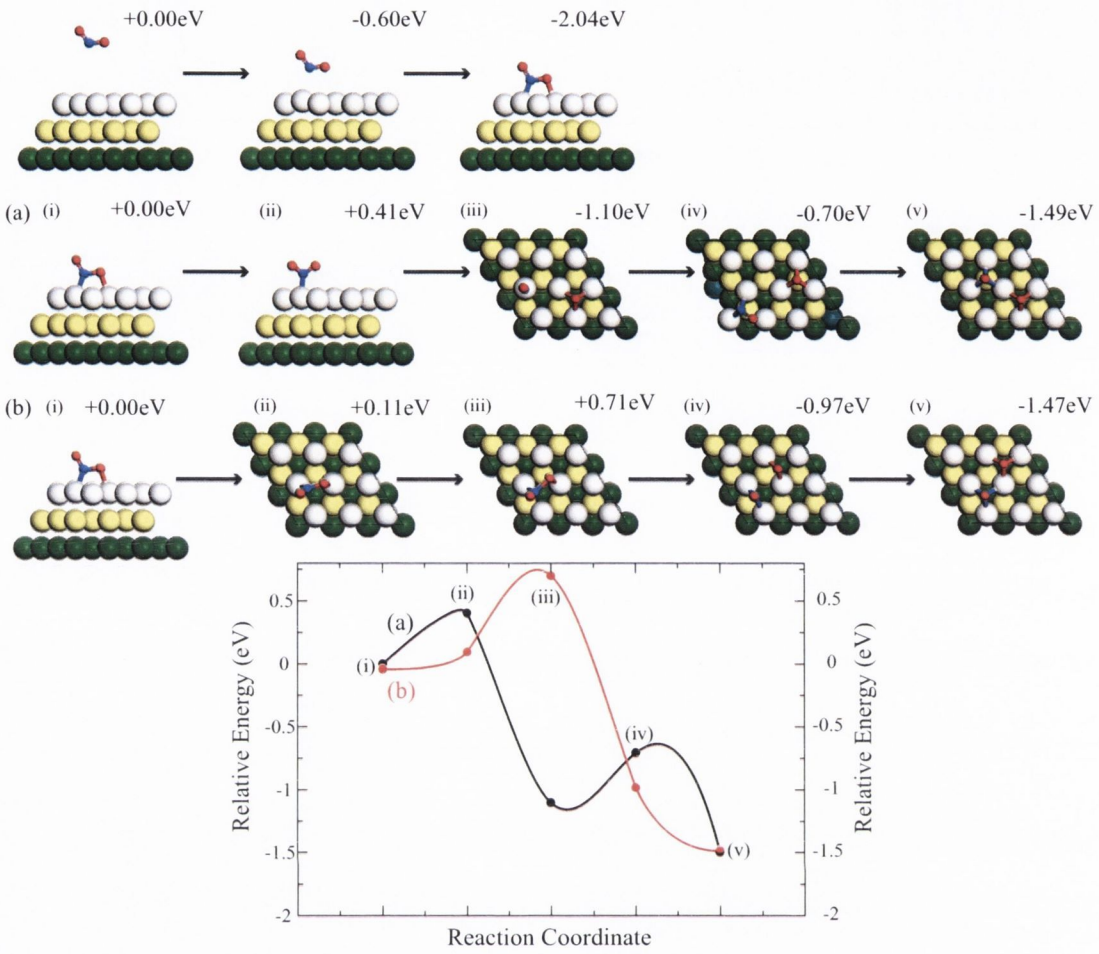


Figure 7.1: The reaction pathway from NO_2 in the gas phase above the surface leading to NO_2 bond dissociation on the {111} surface of rhodium, leading to the (a) NO_{hcp}+O_{fcc} and (b) NO_{fcc}+O_{fcc} combinations. The energy for each step is shown relative to $NO_{(2ads)}$, and the energy profile is also shown. The blue and red spheres are the N and O atoms, respectively, and the layers of the rhodium metal slab are coloured for clarity.

(Figure 7.1 a(i)) at the top site. The calculated energy barrier is 0.30 eV than across the bridge site, with the transition state shown in Figure 7.1 b(iii). The resultant species are seen to diffuse across top (NO species) and bridge sites (O species) before finishing in the three-fold hollow sites.

7.2.2 NO bond breaking

The NO bond dissociation pathways were carried out in a similar manner to N_2 and O_2. The most stable adsorption mode for NO on the {111} surface of Rh was calculated to

be the three-fold hcp adsorption site. The co-adsorption of N and O was investigated to determine the lowest energy configuration for the dissociation products, and the most stable adsorption modes are shown in Figure 7.2. Similar to N_2 and O_2, the nearest neighbour N_{hcp}+O_{fcc} combination relaxed to form molecular NO on the hcp site, and is thus not shown in the figure. The calculated Rh-N and Rh-O bond lengths are of a similar length to the single atomic adsorbed species, as calculated previously on the {111}p(2x2) surface. The most stable configuration for the combination of N and O on the {111} surface is when N is adsorbed at the hcp site and O at the fcc site, each side of the top site. This configuration for the N and O adsorbates will be used as the end point for the NO bond dissociation pathway; however the adsorption at two hcp sites and two fcc sites are also quite similar in energy. Although these two combinations at the 2xfcc and 2xhcp sites are similar in energy, the N_{fcc}+O_{fcc} combination is less likely to occur as both N and NO prefer the hcp site. The combination of N_{hcp}+O_{fcc} will be used as as the end point to examine the NO bond dissociation pathway across the bridge site.

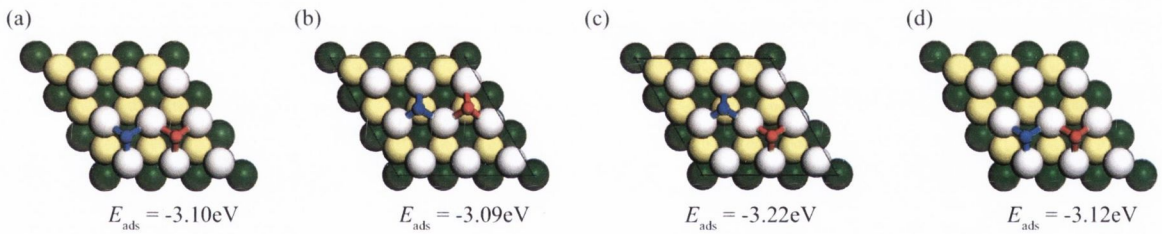


Figure 7.2: The most stable configurations for the co-adsorption of N and O atoms at the (a) fcc + fcc, (b) hcp + hcp, (c) hcp + fcc and (d) fcc + fcc sites on the {111} surface of Rhodium. The E_{ads} associated with each configuration is also shown relative to gaseous NO. The blue and red spheres are the N and O atoms, respectively, and the layers of the Rhodium surface are coloured for clarity.

The pathway to be examined for the NO bond dissociation is directly from the NO gaseous species, as shown in Figure 7.3. The energy for each step of the reaction pathway is shown relative to gaseous NO. From the gaseous species, there is no barrier to adsorption as the energy decreases to adsorption, and the calculated pathway adsorbs NO on to the top site, which then tilts down to the surface, with both N and O atoms

bonded to the surface and the NO bond lengthening by 0.07Å, relative to the calculated gaseous species (1.17Å). This weakens the NO bond leading to dissociation with an energy barrier of 0.50 eV, and the movement of N across the top site settling in the hcp site. The reaction profile indicates that the NO adsorption on the top site provides a weak intermediate precursor, facilitating dissociation rather than adsorption on to the most favourable hcp site. The NO bond dissociation at the hcp site is requires examination as this is the most stable site.

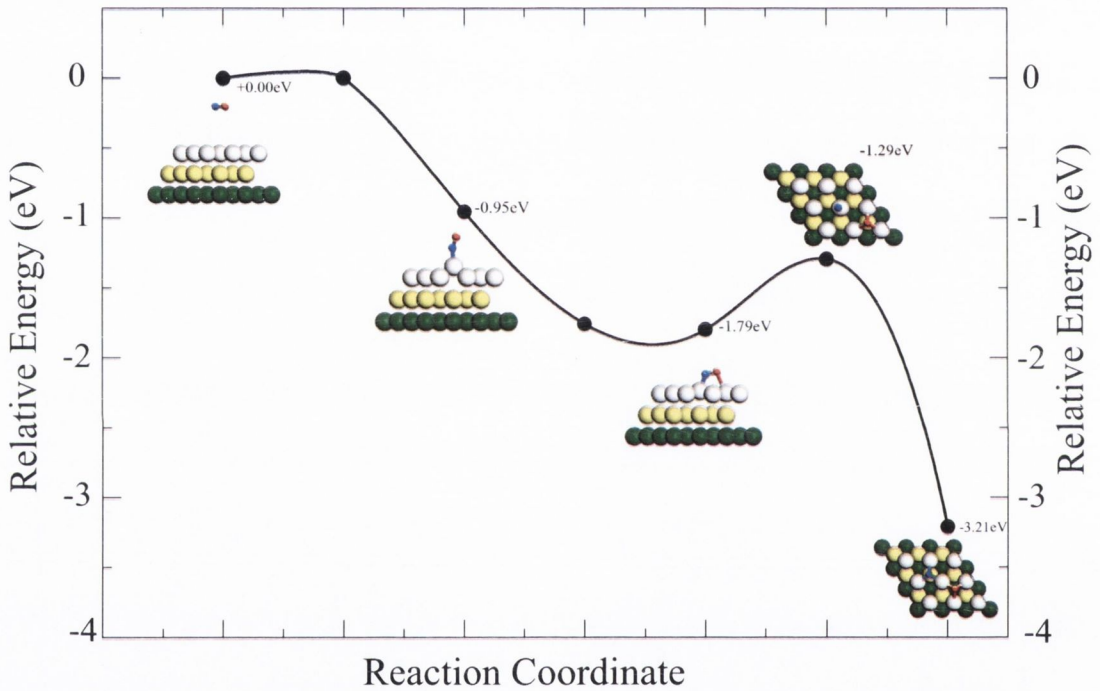


Figure 7.3: The reaction pathway from the gas phase leading to NO bond dissociation on the {111} surface of rhodium. The energy for each step is shown relative to the energy of gaseous NO above the metal surface. The blue and red spheres are the N and O atoms for NO, and the layers of the rhodium metal slab are coloured for clarity.

The NO bond dissociation for NO adsorption at the hcp site is shown in Figure 7.4, with the energies shown for each step relative to NO in the gas phase above the metal slab. There is no barrier to direct adsorption on to the hcp site. The figure shows the NO bond dissociation across the (a) top and (b) bridge sites, to compare which is more favourable. The NO bond is elongated from 1.17Å (NO_g) to 1.76 for the transition state (Figure 7.4 (a)ii) with the O atom bound to the top site, which indicates

an energy barrier of 1.98 eV across the top site, and the O atom proceeds across the top site, adsorbing into the fcc site. The dissociation of the NO across the bridge site is shown in Figure 7.3 (b). The transition state structure (Figure 7.4 (b)ii) shows that the NO adsorbate tilts down for both N and O bound to a bridge site, with an elongated NO bond of 1.71Å. The barrier to dissociation across the bridge site is 1.50 eV, with the N and O atoms settling back into the two hcp sites. This configuration is less stable than the combination of N and O at the hcp and fcc sites. Diffusion of the O atom for the N_{hcp}-O_{hcp} configuration may occur from the hcp site, leading to the resulting N_{hcp}-O_{fcc} configuration.

The dissociation of NO with the presence of O on the surface from NO_2 dissociation was also investigated, with the calculated pathway shown in Figure 7.5. The transition state (Figure 7.5 ii) shows that the bond dissociation occurs across the bridge site, with both N and O atoms bound to the surface in a similar manner to that observed for NO dissociation across the bridge site (Figure 7.4 (b)). The NO bond is lengthened from 1.22Å for adsorbed NO to 1.79Åacross the bridge site, weakening the N-O bond and facilitating dissociation with an energy barrier of 0.23 eV, which is much lower than the previously calculated barriers across the top and bridge sites. This indicates that the presence of O on the surface enhances the dissociation of NO. Bader charges for the transition state show that there is an increase in electron density for the NO molecule adsorbed on the surface, compared to a single NO adsorbate. This suggests that the O atom donates charge through the Rh atom into the NO bond, facilitating dissociation.

The calculated pathways for NO dissociation at the hcp site, indicate that the NO bond is elongated, weakened and dissociated. The calculated energy barriers indicate that dissociation across the bridge site is easier by 0.5 eV, suggesting that this is the more favourable pathway when NO is adsorbed at the hcp site. The cNEB calculation directly from gaseous NO leading to NO dissociation indicates that the bond dissociation proceeds through a weakly bound intermediate at the top site, and a weak precursor adsorbed across the bridge site. The energy barrier to NO bond dissociation

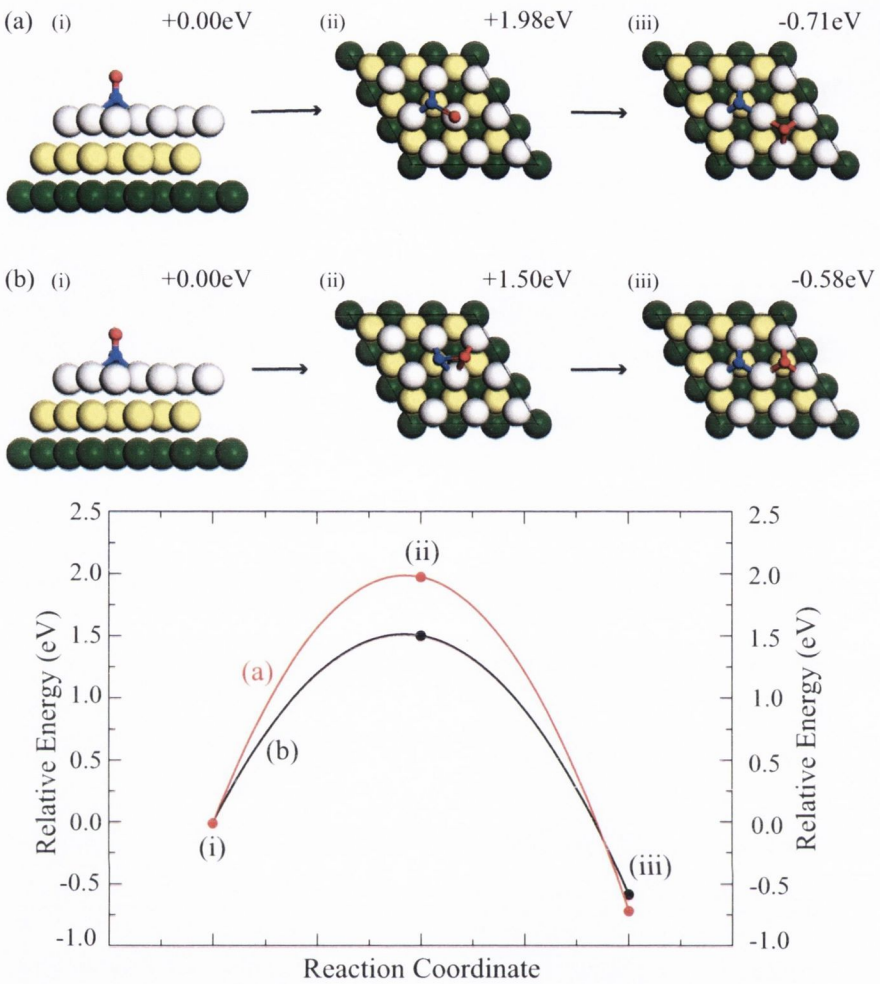


Figure 7.4: The reaction pathway from NO in the gas phase above the surface leading to NO bond dissociation on the {111} surface of rhodium, across the (a) bridge site and (b) the top site. The energy for each step is shown relative to gaseous NO. The blue and red spheres are the N and O atoms for NO, and the layers of the rhodium metal slab are coloured for clarity.

is calculated to 1-1.5 eV less than that for NO dissociation from the most stable hcp site, suggesting that this reaction pathway is more favourable. This is the more favourable mechanism to NO bond dissociation on a clean {111} surface of rhodium. If adsorption does occur at the hcp site, the energy barriers are relatively high, which indicates that the mechanism for direct NO dissociation must be more complicated, requiring further investigation. The presence of O on the Rh surface is shown to reduce the energy barrier, making dissociation of NO on the Rh surface more easier. This would suggest that once tightly bound O adsorbs on the surface, then a Rh_xO_y complex facilitates more

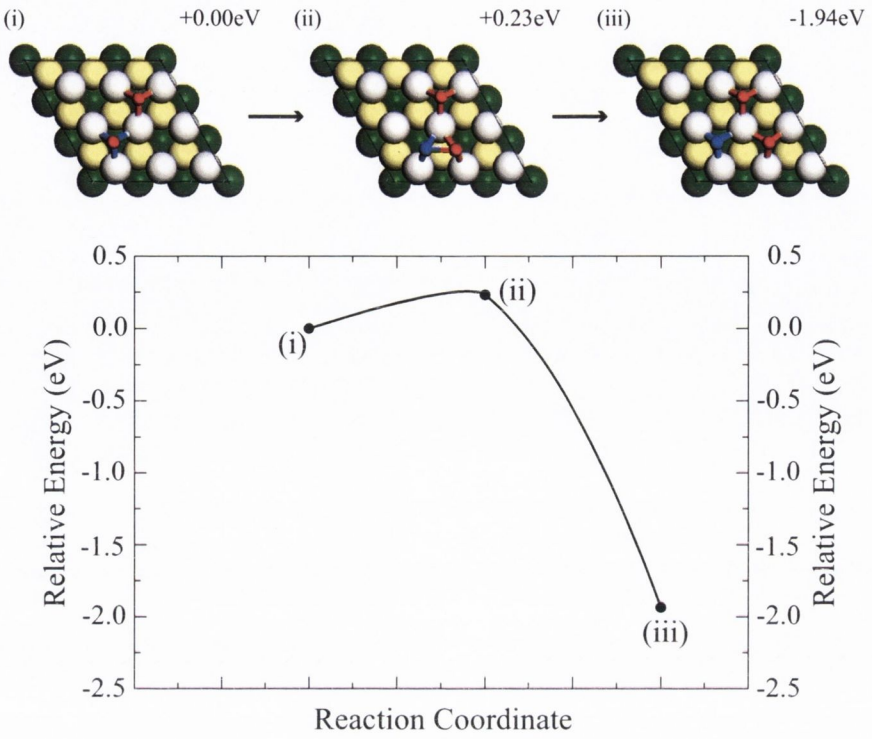


Figure 7.5: The reaction pathway for the dissociation of NO + O → N + 2O. The energy for each step is shown relative to gaseous NO_2. The blue and red spheres are the N and O atoms, respectively, and the layers of the rhodium metal slab are coloured for clarity.

facile dissociation than a clean surface.

7.2.3 Discussion

The pathway for the dissociation of NO and NO_2 was shown to proceed through a weakly bound intermediate on the top site. For NO, the precursor for dissociation was lying flat on the bridge site with an energy barrier of 0.50 eV to break the NO bond. This would suggest that once NO_2 adsorbs to the surface, or once the weak intermediate is formed, then decomposition occurs with an energy barrier of 0.40 eV which is less than the dissociation of NO by 0.10 eV. The fast dissociation of NO_2 would explain the lack of experimental detection of any NO_2 species on the Rh surface. The larger barrier for NO dissociation is expected, as this is identified during the *de*NO_x process as the rate limiting step.

The subsequent breakdown of NO when O is present was also examined leading to N

and 2O on the surface. The barrier for NO dissociation with O present on the surface, significantly reduces the NO bond dissociation barrier by 1.28 eV compared to when NO is adsorbed on the surface and breakdown occurs across the bridge site (Figure 7.4 (b)). The energy barrier for NO dissociation when O is present is lower by 0.17 eV compared to the more favourable NO dissociation pathway through the weak NO intermediate at the top site. The lowering of the NO dissociation barrier is caused by O present on the surface, pushing density into the NO bond and facilitating dissociation. This may suggest that strongly bound O species on the surface may activate NO dissociation on Rh and explain its ease at breaking the NO bond. The formation of a Rh_2O_3 species on the support has been suggest to assist in the reduction of NO_x;[374] however further experimental support is lacking in examining rhodium oxide as a mechanism for NO dissociation. Although the presence of O atoms reduces the barrier to NO dissociation, the subsequent formation of N_2 and O_2 would be difficult, in particular with strongly bound O ad atoms, suggesting a different mechanism is more likely. Additionally, the presence of N_2O detected during the decomposition of NO as an intermediate also suggests evidence for a different mechanism which needs to be examined in detail.

7.3 Atomic and molecular diffusion on the Rh, Pd and Pt {111} surfaces

The N, O and NO species were adsorbed at each of the four high symmetry sites (fcc, top, hcp, bridge) on the {111} surface for the starting and end points of the cNEB calculations. For each of these species to diffuse across the {111} surface, they can proceed from a hollow site across a top or bridge site. To fully investigate the N, O and NO diffusion pathways, three different pathways are explored across the high symmetry sites, fcc to top, top to hcp, and hcp to fcc as illustrated in Figure 7.6.

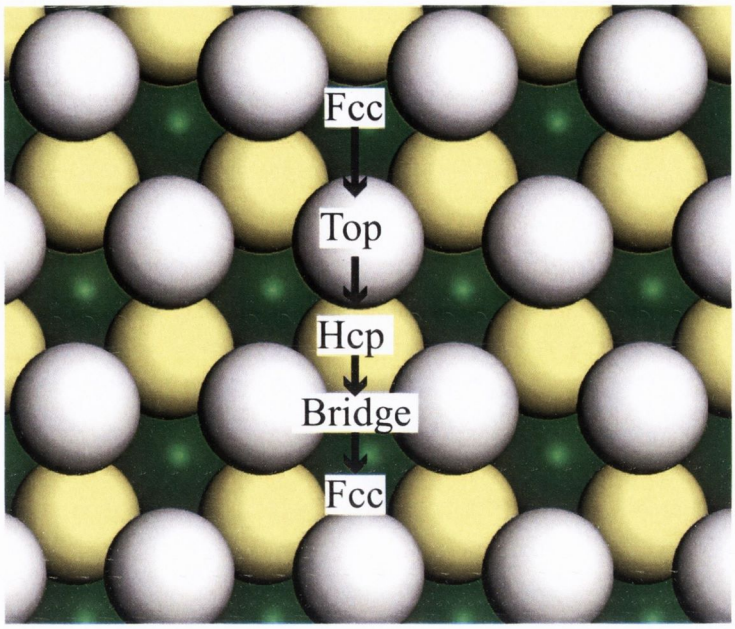


Figure 7.6: The structure of the Rh {111} surfaces with the diffusion pathways to be tested for N, O and NO across the high symmetry adsorption sites which are labelled. The top (white) and second (yellow) layers are coloured for clarity.

7.3.1 N diffusion

The N adsorbates on the four sites of the metal {111} p(3x3) surfaces were to have similar bond lengths and the hcp being the most stable site, as seen for N adsorption on the metals {111} p(2x2) surfaces. The diffusion of N is found to proceed through a similar pathway on all three {111} surfaces, across the four high symmetry points as depicted in Figure 7.6. The bond lengths are seen to increase with increased coordination of the N adsorbate on all surfaces in a similar manner to that observed previously N adsorption on the p(2x2) surfaces. The reaction profile for the change in energy with respect to the change in coordination of the N adsorbate across each of the {111} surfaces is shown in Figure 7.7, with the energies for each of the structures on the pathway shown relative to the starting fcc site. The energy required for the movement of N from the fcc site to the top site is less on Rh (2.27 eV), greater on Pt (2.36 eV) and the greatest on Pd (2.69 eV). The energy required to pass from the hcp site through the bridge site to the fcc site is 0.67 eV, 0.69 eV and 0.65 eV on Rh, Pd and Pt, respectively. This indicates that the energy barrier is the smallest on Pt and greatest on Pd.

The energy barrier for N across the bridge site is significantly less than over the top site on all three surfaces. This indicates that N is more likely to move across the bridge sites than the top site on all three {111} surfaces. The barrier to diffusion across the bridge site is smallest on Pt by 0.02 eV over Rh and 0.04 eV more than Pd, indicating that the diffusion of N is easier on Pt than the other metals.

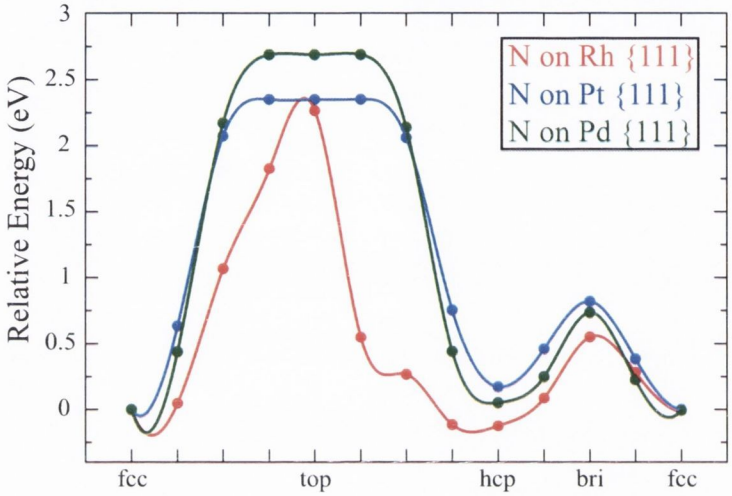


Figure 7.7: The energy versus reaction coordinate profile of N diffusion across adsorption sites on the Rh, Pt and Pd {111} surfaces. The red, blue and green lines are the profiles for N diffusion on Rh, Pd and Pt, respectively. The energies are relative to the starting fcc site of their respective surfaces.

7.3.2 O diffusion

The diffusion of O across the {111} surfaces of Rh, Pd and Pt was carried out in a similar manner to N diffusion. The reaction profile for the O adsorbate across each of the {111} surfaces is shown in Figure 7.8, with the energies for each of the structures on the pathway shown relative to the starting fcc site. The fcc site is the most stable adsorption site for O on all three {111} surfaces, and thus the lowest point on the energy profile for Rh, Pd and Pt. For O diffusion over the top site, the energy barrier is quite similar on Pt (1.41 eV) and Rh (1.43 eV) with a larger energy required to get over this site on Pd (1.67 eV). O diffusion across the bridge site from one hollow site (hcp) to the other (fcc) requires the greatest amount of energy on Pt (0.57 eV), a similar amount of

energy on Pd (0.53 eV) and the least on Rh (0.50 eV).

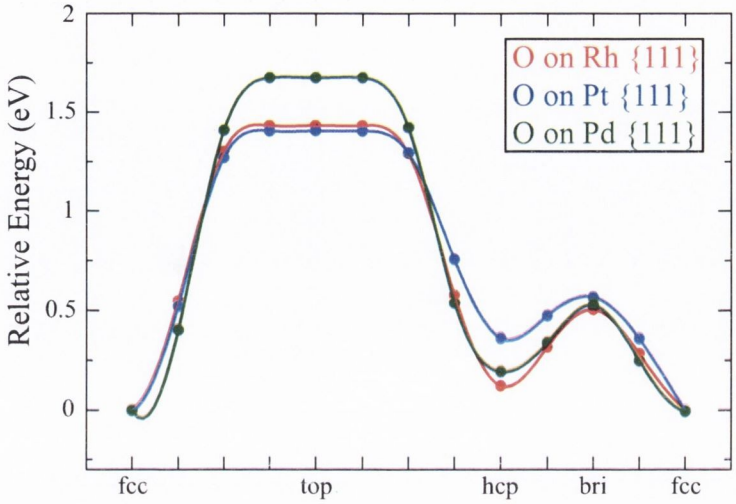


Figure 7.8: The energy versus reaction coordinate profile of O diffusion across adsorption sites on the Rh, Pt and Pd {111} surfaces. The red, blue and green lines are the profiles for O diffusion on Rh, Pd and Pt, respectively. The energies are relative to the starting fcc site of their respective surfaces.

The energy profile for O diffusion across the Rh, Pd and Pt {111} surfaces shows that the energy barrier to get over the top site is significantly larger than the bridge site on all three surfaces. This indicates that the movement of O across the {111} surface of Rh, Pd and Pt is more likely to proceed across the bridge site from hollow site to hollow site, in a similar manner to N diffusion. The calculated activation energy required to diffuse across the bridge site is less on Rh than on either Pt or Pd, indicating that diffusion is faster across the Rh {111} surface.

7.3.3 NO diffusion

The N and O bond lengths are similar to that for NO adsorption on the {111}-p(2x2) surfaces. The diffusion of NO is found to proceed through a similar pathway on the Pd and Pt surfaces, to that seen for N and O diffusion; however on the Rh {111} surface, from the top site to the hcp site the NO molecule prefers to go through the fcc site as a intermediate before settling in the hcp site. The N bond lengths coordinated to the surfaces, and the N-O bond length for the NO molecule are seen to increase with

increasing coordination on all surfaces in a similar manner to NO adsorption previously explored on the p(2x2) surfaces.

The reaction profile for the change in energy with respect to the change in site across each of the {111} surfaces is shown in Figure 7.9, with the energies for each of the structures on the pathway shown relative to the starting fcc site. For NO diffusion on Pd, the energy profile shows that the energy barrier across the top (1.18 eV) and the bridge sites (0.35 eV) is much higher in energy that on the Pt and Rh surfaces. The energy profile for NO diffusion on Pt and Rh is more complex. The energy profile indicates that there is a barrier to breaking the N bonds from surface on Rh and Pt (0.6 eV). Once the coordination of the N atom is reduced from three (fcc site) to one (top site), the energy is lowered on both surfaces. On the Pt surface, the energy to get over the top site rises to 0.78 eV while on the Rh surface this lowers to 0.45 eV indicating that diffusion across the top site on Rh is easier. Proceeding from the top site to the hcp site, there is again a similar energy barrier to form the N-M bonds when going from a coordinate of one to a three on Pt. On Rh however, the energy is down hill to the hcp site as the diffusion of NO on Rh goes through the fcc site as an intermediate step before settling in the hcp site. This indicates that the calculation finds a lower point than the transition state it is supposed to find. These results for NO diffusion on Rh going from the top to the hcp site appear to be spurious and require further investigation. Similar to N and O diffusion, the energy barrier across the bridge site is much lower on Rh (0.17 eV) and Pt (0.18 eV) than across the top site of these metals, indicating that NO diffusion is easier across the bridge site. On Rh however, once the Rh-N bond is broken from a coordination of three to one then the energy is downhill to the hcp site. The energy required to go from a coordination of three to one remains higher than across the bridge site.

7.3.4 Discussion

The diffusion of N, O and NO was examined on the {111}-p(3x3) surfaces of Rh, Pd and Pt using DFT calculations with the PBE exchange correlation functional and the

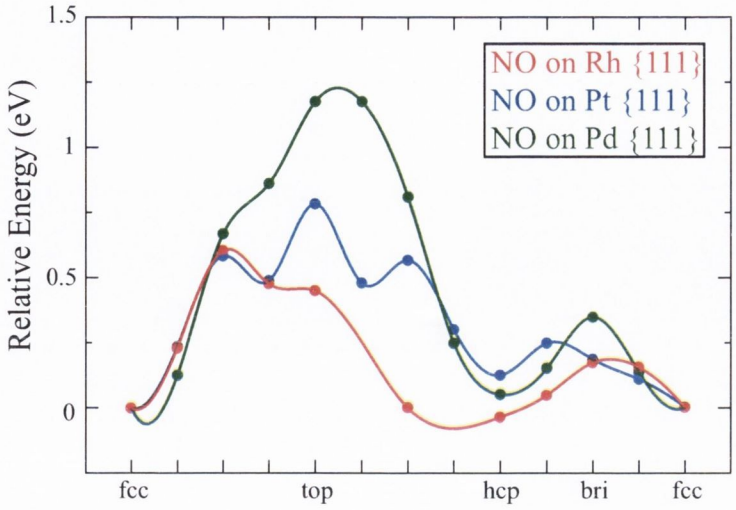


Figure 7.9: The energy versus reaction coordinate profile of NO diffusion across adsorption sites on the Rh, Pt and Pd {111} surfaces. The red, blue and green lines are the profiles for O diffusion on Rh, Pd and Pt, respectively. The energies are relative to the starting fcc site of their respective surfaces.

cNEB approach. The calculations show that the diffusion pathway structure across the top and bridge sites for N and O on the three surfaces is similar, with the calculated energy barriers indicating that diffusion is easier across the bridge site for both species on each surface. The diffusion for both N is easier across the Pt and for O is it easier across Rh. Comparing the N and O energy barriers, O diffusion is much more facile by around 0.30 eV on all three surfaces. This indicates that O is more likely to move across the surfaces than N atoms, where the slow diffusion of N has been observed by TPD experiments.[287] The recombination of N atoms to form N_2 at low temperatures would therefore be difficult by movement of N atoms across the surface, which at higher temperature is seen to occur. This may explain why a higher coverage of N atoms are required on the metals surfaces before any low temperature N_2 desorption is detected.[295] The high coverage of N atoms are said to form N islands on the metal surface, and recombination occurs *via* a reaction between N+N atoms within molecular islands, assisting in the low temperature formation of N_2.[294]

Oxygen atoms are thermodynamically more stable on the Rh, Pd and Pt surfaces and are known to saturate the surface, blocking sites for further NO_x decomposition, in

particular on Rh and Pd. A reductant such as H_2 or CO is thus require to remove the strongly bond O ad-atoms at low temperatures; however once high enough temperatures are reached to move O atoms on the surface during the reaction process, then diffusion is quite rapid. The fast diffusion of O atoms on the metal surfaces is observed experimental as at temperatures between 800-1000K, as O_2 is seen to form and desorb quite easily from the metal surfaces.[375 379] The formation of O_2 and subsequent desorption from Pt is attributed to kinetic effects, as studied by TPD experiments.[377] The formation of O_2 or CO_2 is important to the redox cycle to regeneration the catalyst after $de\mathrm{NO}_x$. The easier movement of O over N, leads to easier oxidation of CO or O_2 formation as the O atoms are more likely to move forming the products as observed by experimental Auger and X-ray spectroscopy,[380] and PM-IRAS.[381]

The diffusion of NO on the three metals is more likely to occur across the bridge site than the top site. Comparing molecular NO diffusion to atomic N and O, the energy barriers across the bridge site are lower by 0.4-0.5 eV than N, and 0.02-0.2 eV than O. This indicates that NO diffusion is much easier on the metal surfaces, in particular on Rh and Pt. This would assist in the oxidation of NO to NO_2 as an important intermediate for lean-$de\mathrm{NO}_x$ for SCR and NSR technologies.[382, 383] The diffusion of NO across Rh is more facile than Pd and Pt metals, and this may assist in it possessing better reductive properties. The suggested mechanism for NO reduction *via* the combination of N and NO to form the N-NO intermediate is more likely to occur with the surface diffusion of NO to N. For the dimer mechanism where two NO molecules combine to form the N_2O_2 complex, both NO molecules can easily diffuse across the metal surface to form $(NO)_2$ dimers. This in contrast to previous suggestions that the NO molecule breaks on the surface, and the N atoms diffuse across the surface to the NO molecule to form the N-NO intermediate to N_2 formation.[297, 308] A Monte Carlo simulations by Bustos *et al.*[300, 301] examined Eley-Rideal behaviour and Langmuir-Hinshelwood mechanisms between N and NO suggesting that the Eley-Rideal behaviour is more probable, where NO in the gas phase adsorbs on to N atoms to form the N-NO intermediate. The presence of surface N islands was said to hinder any diffusion of

adsorbed species, ruling out the Langmuir-Hinshelwood mechanism. The calculated energy barriers suggest that NO diffusion is facile on a clean Rh {111} surface, and the Langmuir-Hinshelwood mechanism is a possible mechanism where NO is more likely to diffuse to adsorbed N atoms.

7.4 Reaction pathways and intermediates

The mechanism for the breakdown of NO on the clean {111} surface of rhodium is in considerable debate. Experimental and theoretical studies have indicated that the breakdown of NO proceeds through a N_2O intermediate; however the precursor to this intermediate is not clear. The formation of N_2O can occur through two possible pathways; (1) an N-NO precursor, where one NO molecule is dissociated and the resulting N atom combines with surface bound NO or (2) a $(NO)_2$ dimer precursor, where the two NO molecules combine to form N_2O_2 on the surface. The former precursor is said to occur on the Rh {111} surface by experimental studies;[297] however the $(NO)_2$ dimer is said to be a weak precursor on Ag, Cu and the step of Pt, leading to N_2O formation.[72, 316, 324] More recently DFT studies have indicated the possibility of the $(NO)_2$ dimer precursor leading to N_2O formation;[318] however the complete mechanism was not examined. Both pathways need to be examined in detail.

7.4.1 The adsorption of N_2O, N_2O_2 on the Rh {111} surface

The intermediate formation after NO_x adsorption and diffusion on the Rh {111} surface needs to be examined to provide a more complete picture of the reduction process on the surface. The possible orientations for the N_2O_2 dimer and N_2O species to be examined are shown in Figure 7.10 (a) and (b), respectively. Each of these orientations were explored across each of the adsorption sites on the surface, producing a large number of configurations to be tested. All possible configurations were calculated, and the most stable adsorption modes for N_2O_2 and N_2O are shown in Figure 7.10 (c), along with the associated adsorption energies. The preferred adsorption mode for N_2O_2 has not been

observed on other metals surfaces, as on Pt the orientation shown in Figure 7.10 (a) (i) is preferred,[316, 331] while the orientation in Figure 7.10 (a) (iii) is observed on Ag.[336] There are two possible adsorption modes for N_2O that are similar in energy, with the adsorption mode shown in Figure 7.10 (c) (i) shown previously to be the most stable mode for N_2O but with a much weaker E_{ads}.[304] Both N_2O adsorption modes shown, will need to be examined during the decomposition pathway due to their closeness in energy. All molecular bond lengths are seen to increase from the gas phase species when interacting with the surface, while the bond angles are found to decrease. The molecular spin is completely quenched to 0 by the surface, as seen previously for NO and NO_2.

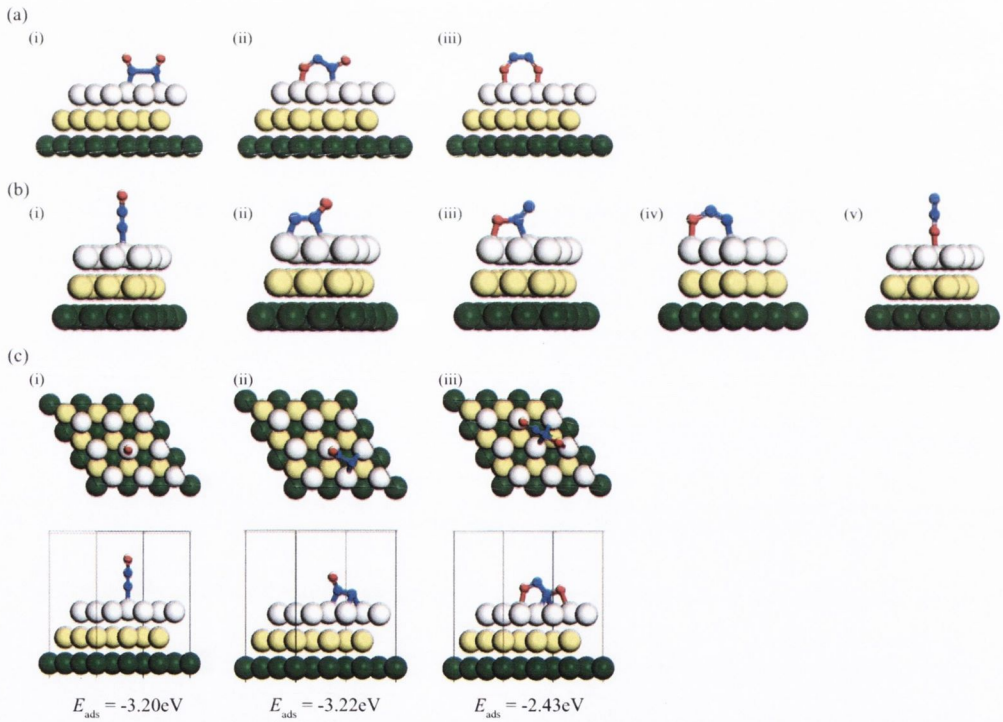


Figure 7.10: The possible orientations for (a) N_2O_2 and (b) N_2O to be examined on the Rh {111} surface. (c) The most stable adsorption modes for (i)-(ii) N_2O and (iii) N_2O_2 with the E_{ads} also shown. The blue and red spheres are the N and O atoms, respectively, and the layers of the rhodium metal slab are coloured for clarity.

The complete *de*NO_x profile on the Rh {111} surface will require the most stable configurations of NO + N + O, N_2O + O, N_2 + 2O, and N_2 + O_2 for the different stages of the reaction mechanisms on the surface. To reduce the number of combinations

to test, the most stable adsorption modes for each species were used to test different adsorption site combinations on the {111} surface. The most stable co-adsorption configuration for each step outlined above are shown in Figure 7.11, along with the E_{ads} for each mode relative to the gaseous species. All the bond lengths and angles were found to be similar to the adsorption of a single species on the surface, and the molecular spins were quenched by the metal surface.

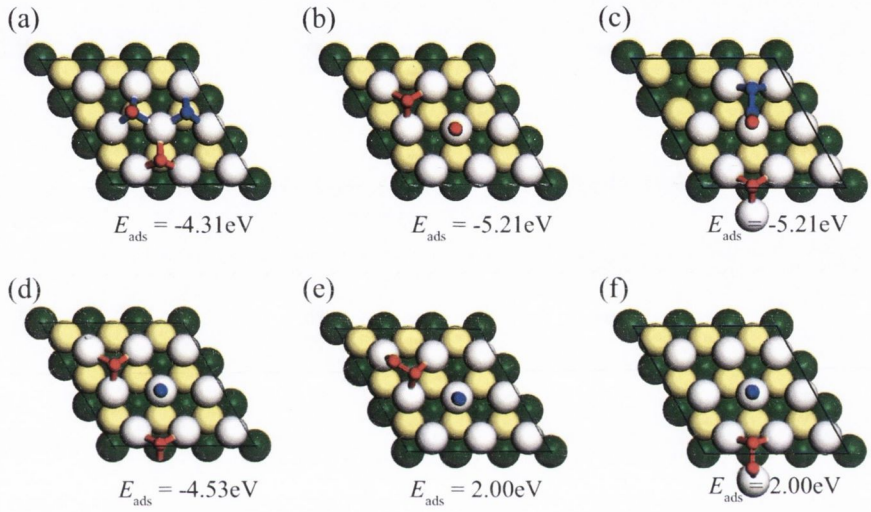


Figure 7.11: The most stable adsorption co-adsorption configurations for (a) NO + N + O, (b)/(c) N_2O + O, (d) N_2 + 2O, and (e)/(f) N_2 + O_2 on the {111} surface of rhodium. The blue and red spheres are the N and O atoms, respectively, and the layers of the rhodium metal slab are coloured for clarity.

7.4.2 Preliminary results for the intermediate formation during *de*NO_x

The adsorption of two NO molecules at two hcp sites were used as the starting point for the cNEB calculations to determine the precursor to N_2O formation. These were found to have similar bond lengths to single NO adsorption on the surface, and the molecular spin was also quenched to 0 by the metal surface. All energies for the decomposition pathways are shown relative to the two NO molecules on the Rh {111} surface.

The reaction mechanism for the formation of the N_2O_2 dimer on the Rh {111} surface is shown in Figure 7.12, along with the subsequent breakdown leading to N_2O

formation. The reaction mechanism indicates that the two NO molecules move towards one another across the surface by a Langmuir-Hinshelwood type mechanism, with the diffusion costing energy. This leads to the formation of the N_2O_2 dimer with a energy barrier of 2.14 eV to make the N-N bond, which then relaxes to the most stable adsorption mode for N_2O_2. The N_2O_2 complex is then activated to the neighbouring top site before elongating the NO bond to 1.69Å facilitating the breaking of the bond with an energy barrier of 0.69 eV, leading to a weak N_2O + O combination. This N_2O orientation on the surface then moves to form the most stable adsorption mode for N_2O bonded straight down on a top site. There is an energy barrier of 0.43 eV to break the NO bond on the most stable N_2O complex, giving the N_2 + 2O configuration which is more stable than the N_2 and O_2 co-adsorption on the surface. The removal of N_2 from the surface has a barrier of 0.91 eV with O atoms remaining on the surface. These can be removed by either a reductant such as CO or H_2, or if the temperature is high enough they can diffuse to form O_2.

The reaction pathway for the N-NO precursor to N_2O formation is shown in Figure 7.13, with the energies for each step relative to two adsorbed NO molecules. The pathway (a) leads through one NO breaking its bond with an energy barrier of 0.66 eV leading to a more stable NO + N + O configuration, than two NO molecules on the surface. The formation of the N_2O adsorbate and subsequent breakdown to either N_2 + 2O or N_2 + O_2 lead to questionable results, and require further investigation. This reaction pathway will require further detail to examine and determine the reaction intermediate and energy barrier for the bond breaking mechanism.

The pathway leading to the formation of the N_2O configuration perpendicular to the surface and bonded at the top site is shown in Figure 7.13 (b). The cNEB calculation indicates that the pathway proceeds through a N_2O_2 dimer, with the O-N bonded to the surface and the N-N=O bond away from the surface. The molecular bonds for this complex are seen to be elongated relative to the gaseous species, and the energy barrier to forming this complex, breaking the N-O bond on the surface and forming N_2O is 2.55 eV. This energy barrier is much larger than the N_2O_2 dimer pathway shown

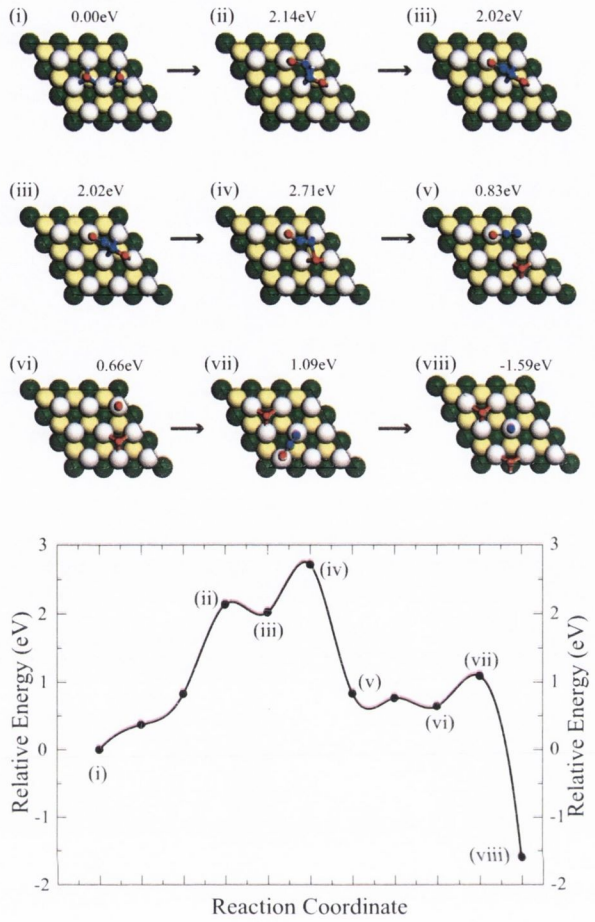


Figure 7.12: The reaction mechanism for the formation of N_2O_2 leading to N_2O formation and subsequent decomposition to N_2. The blue and red spheres are the N and O atoms, respectively, and the layers of the rhodium metal slab are coloured for clarity.

in Figure 7.12, as there are many steps involved. This mechanism requires further attention to describe the mechanism in more detail to breakdown the pathway into a number of detailed steps.

The breakdown of N_2O can proceed by two competing pathways shown in Figure 7.13 (c) and (d). The cNEB calculation indicates that desorption of the N_2O adsorbate can occur with a energy barrier of 0.44 eV, which can then break the N-O bond to form O_2 on the surface with the surface O adsorbate. The N_2O bond breaking can occur with a similar energy barrier (0.43 eV) leading to N_2 + 2O, where the N_2 molecule can subsequently desorb from the surface. Both of these steps require further investigation to provide a more detailed description of the pathways.

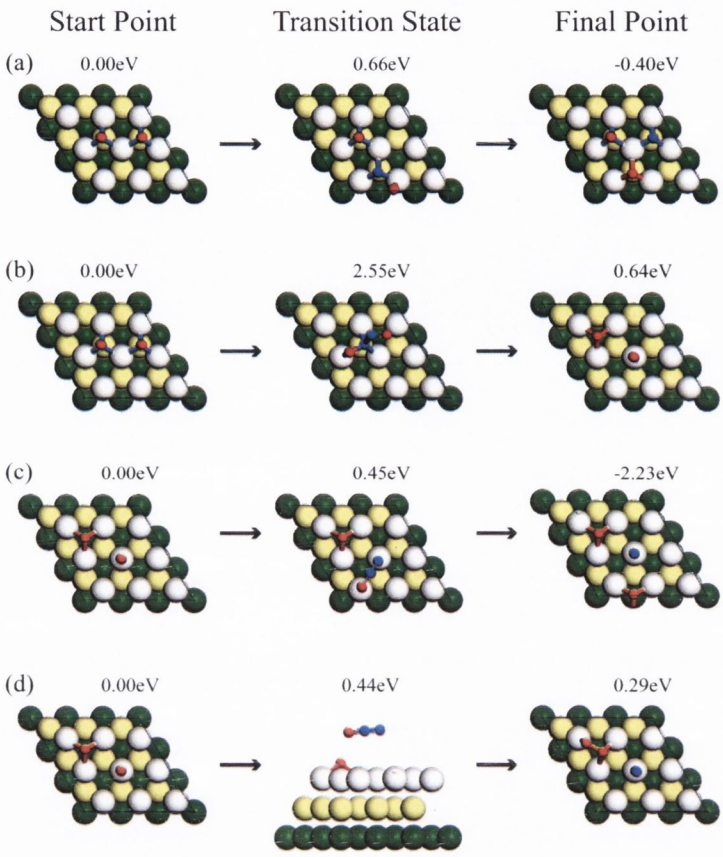


Figure 7.13: The reaction mechanism for the N-NO precursor to N_2O formation and subsequent decomposition to N_2. (a) The pathway for the breaking of the NO bond leading to the flat stable N_2O configuration and (b) the pathway leading to the straight down N-top site N_2O configuration. The blue and red spheres are the N and O atoms, respectively, and the layers of the rhodium metal slab are coloured for clarity.

7.5 Discussion

The reaction pathways leading to the formation of N_2O and its subsequent breakdown was examined on the {111} p(3x3) surface of rhodium. The mechanism through the N_2O_2 dimer was calculated, and found that its formation on the surface is difficult, with a large energy barrier (2eV) to forming the N-N bond. Once the N_2O_2 dimer is formed, then the energy barrier leading to subsequent breaking of the N-O bond is not as large, forming N_2O + O on the surface. The breaking of an NO molecule on the surface when another NO is present on the surface requires less energy, leading to the NO+N+O configuration which is more stable than 2NO. There is thus a large energy requirement

to proceed from this configuration and form the N_2O + O adsorbate on the surface, than proceeding through the N_2O_2 dimer. This indicates that once the weakly bound N_2O_2 dimer is formed then the dissociation on the surface is more energetically favourable than proceeding through the more stable NO+N+O configuration. A reaction pathway leading to the formation of an N_2O_2 with a lower energy barrier is perhaps possible, and a more detailed description of the pathway is required and different mechanisms trialled, to provide a much clear description of the mechanism for N_2O formation.

The calculated reaction pathways indicate that the energy barrier for the breaking of the NO bond for the N_2O intermediate is relatively low. The more favoured pathway is to form the N_2 + 2O configuration on the surface rather than the less stable combination of N_2 + O_2 on the surface. This indicates that the difficulty with rhodium metal lies with the formation of O_2, and surface adsorbed O atoms are preferred at low temperatures. These ad-atoms can be remove by using a reductant during the redox reaction. The cNEB calculations indicate that the desorption of N_2O from the Rh surface is a competing mechanism to the dissociation of N_2O which may explain the experimental detection of gaseous N_2O in the reaction mixture at low temperatures. The cNEB calculations also indicate that there is a barrier to desorption of N_2 from the rhodium surface.

7.6 The energy barriers to N_2 and O_2 bond formation

7.6.1 Energy barrier to forming the N_2 bond

The most stable adsorption mode for N_2 on the Rh {111} surface was calculated to be a N-terminating σ-bonded complex, along the surface normal and bonded to a single top site. This adsorption mode was used as the starting point for the cNEB method to calculate the energy barrier to bond dissociation. For the end point of the cNEB, the co-adsorption of N on the Rh {111} surface needs to be investigated to determine the

most stable configuration for two N atoms on the surface. The calculated stable configurations for the co-adsorption of N are shown in Figure 7.14. The nearest neighbour N_{fcc}+N_{hcp} combination was tested, which relaxed to a N_2 adsorbate on the surface due to the close proximity of the two N ad-atoms. All calculated Rh-N bond lengths for the adsorption modes are similar to single N adsorption on the Rh {111} surface. The E_{ads} for each configuration is also given in the figure and calculated relative to gaseous N_2. The N_{fcc}+N_{fcc} combinations is seen to the be the least stable, while the adsorption of N at the next nearest neighbour (nnn) hcp sites (Figure 7.14 (c)) is the most stable. This is likely to be the end point to test the pathway for N_2 bond dissociation; however the combinations of N adsorption at the mixed hcp and fcc sites (Figure 7.14 (a)) and at the nearest neighbour (nn) hcp sites (Figure 7.14 (b)) are within 0.1-0.2 eV of the most stable configuration, prompting these combinations to be also tested as end points.

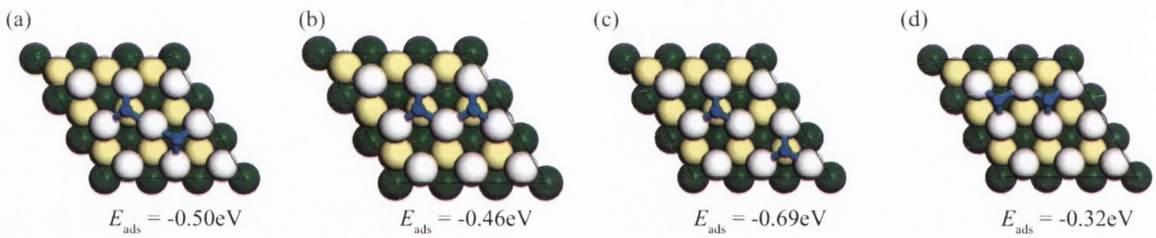


Figure 7.14: The most stable configurations for the co-adsorption of two N atoms at the (a) hcp + fcc, (b) hcp + hcp-nn, (c) hcp + hcp-nnn and (d) fcc + fcc sites on the {111} surface of Rhodium. The E_{ads} associated with each configuration is also shown relative to gaseous N_2. The blue spheres are the N atoms and the layers of the Rhodium surface are coloured for clarity.

The different pathways for the N_2 bond dissociation between the most stable N_2 adsorption mode and the different configurations for the co-adsorption of N on the Rh {111} surface in Figure 7.15. The energies shown in the figure for the calculated transition states and the different co-adsorption modes are given relative to the energy of the N_2 adsorption adsorption mode. The transition state, requires a large amount of energy to move the N_2 adsorbate into a flat configuration, elongating the N_2 adsorbate bond from 1.13 Å to 1.76 Å. The large energy requirement to subsequently form N_2 bond across a top site is calculated to be 2.23 eV. The calculated pathways for other

co-adsorption configurations leading to N_2 formation are still ongoing and is required to provide a clearer picture of the N_2 bond formation mechanism.

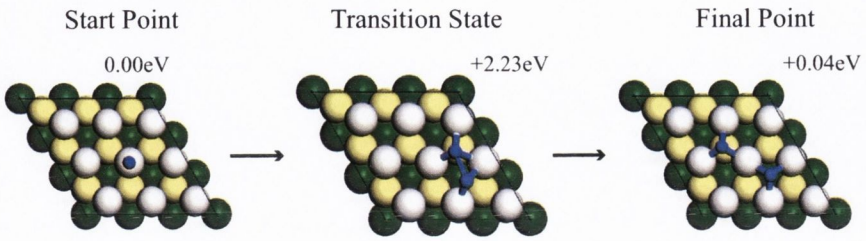


Figure 7.15: The reaction pathway for the N_2 bond dissociation from the most stable N_2 adsorption mode to the stable configuration for the co-adsorption of N atoms at the (a) hcp + fcc, (b) hcp + hcp-nn, and (c) hcp + hcp-nnn site combinations. The energy (eV) for each step and end point is labelled, and are calculated relative to the energy of the N_2 adsorption mode.

7.6.2 The energy barrier for O_2 bond formation

The most stable adsorption mode for O_2 on the {111} surface of Rh was calculated to be a flat π bonded complex from a top site across a hcp hollow to a bridge site. This adsorption mode was used as the starting point for the cNEB method to calculate the energy barrier to bond dissociation. For the end point of the cNEB, the co-adsorption of two O atoms on the Rh {111} surface needs to be investigated to determined the most stable configuration on the surface. The calculated stable configurations for the co-adsorption of O are shown in Figure 7.16, with the Rh-O bond lengths being similar to single atomic O on the {111} surface. The nearest neighbour O_{fcc}+O_{hcp} combination was tested, which relaxed to a O_2 adsorbate on the surface due to the close proximity of the two O ad-atoms. The E_{ads} for each configuration is also given in the figure and calculated relative to gaseous O_2. The most stable configuration for co-adsorption of two O atoms on the surface is the next nearest neighbour (nnn) fcc sites (Figure 7.16 (b)) with the least stable configuration being mixture of hcp and fcc sites beside the top site (Figure 7.16 (a)), and adsorption at two hcp sites (Figure 7.16 (d)). The adsorption of O at two nearest neighbour fcc sites is within 0.1 eV of the most stable site and will also be examined as a possible pathway for O_2 bond dissociation.

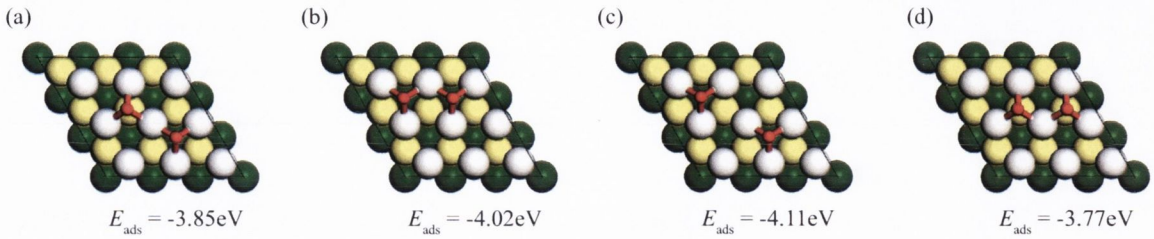


Figure 7.16: The most stable configurations for the co-adsorption of two O atoms at the (a) hcp + fcc, (b) fcc + fcc-nn, (c) fcc + fcc-nnn and (d) hcp + hcp sites on the {111} surface of Rhodium. The E_{ads} associated with each configuration is also shown relative to gaseous N_2. The blue spheres are the N atoms and the layers of the Rhodium surface are coloured for clarity.

The calculated pathway for the O_2 bond formation, between the most stable O_2 adsorption mode and the O_{fcc} + O_{fcc} configurations on the Rh {111} surface, are shown in Figure 7.17. The energies shown in the figure for the calculated transition state, and the different co-adsorption modes are given relative to the energy of the O_2 adsorption adsorption mode. Although the configuration shown in Figure 7.16 (c) is more stable than that shown in Figure 7.16 (b) relative to gaseous O_2, both co-adsorption configurations have the same energy relative to the most stable O_2 adsorption mode. The transition state was calculated to be an upright O_2 complex on a bridge site which is 0.80 eV less stable than the most stable adsorption mode. This transition state appears to indicate that the reaction profile between the start and end points contains many minima. The pathway therefore requires more detail to provide a clearer picture of the bond formation mechanism. Other pathways are still ongoing, such as the formation of an O_2 bond across the bridge sites leading to the nn O_{fcc}+O_{fcc} combination.

7.6.3 Discussion

The bond formation pathways and energy barriers was calculated for N_2, O_2 and NO_x adsorbates on the Rh {111} surface. For both N_2 and O_2 the bond dissociation pathways leading to the most stable configurations for nnn N_{hcp}+N_{hcp} and O_{fcc}+O_{fcc} combinations are difficult with high activation energy. Pathways across the bridge sites require further investigation to elucidate their full bond formation mechanism. From the calculated

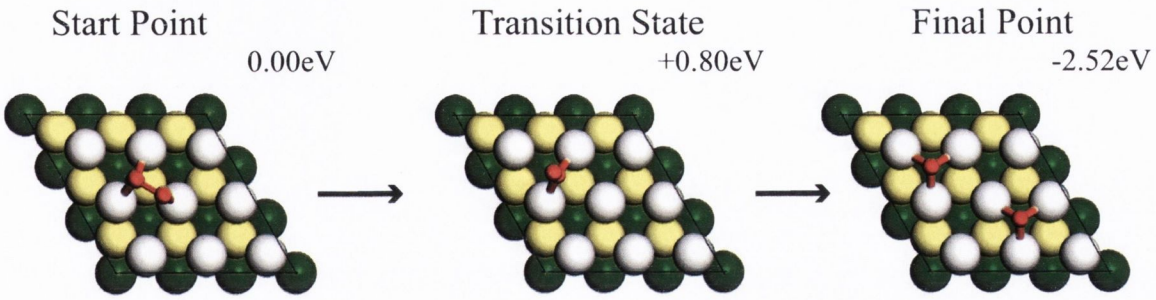


Figure 7.17: The reaction pathway for the O_2 bond formation from the most stable O_2 adsorption mode to the stable configuration for the co-adsorption of O atoms at the (a) fcc + fcc-nn, and (b) fcc + fcc-nnn site combinations. The energy (eV) for each step and end point is labelled, and are calculated relative to the energy of the O_2 adsorption mode.

transition states for N_2 and O_2, the energy to form N_2 bond is much larger than O_2, indicating that forming the N_2 bond is much more difficult. This is not surprising as the triple NN bond is much stronger than O_2. This would suggest that the recombination of N + N leading to N_2 is difficult, and a more complicated process must be occurring at low temperatures on the {111} surface of rhodium. This shows that energy is required to get the N atoms to diffuse and recombine for the higher temperature route to N_2 formation. For O_2, the O atoms are very stable on the surface; however once the temperature is high enough to move the O atoms, then the O_2 bond formation is not as difficult.

7.7 Conclusion

The bond breaking pathways for NO_x was investigated on the Rh {111} surface. For the bond dissociation of NO_x on the Rh surface, a number of pathways were considered from the gas phase. Both NO and NO_2 were found to prefer a pathway involving a weak intermediate precursor bound to a top site, that facilitated dissociation. If the molecules adsorbed into their most stable configurations on the Rh surface, then dissociation across a bridge site was calculated to be the lowest energy pathway. The dissociation of NO_2 leads to resultant dissociation products, NO + O on the surface.

The subsequent breakdown of the resultant NO was found to occur across the bridge site with a much lower barrier than that observed for NO on the clean surface. This indicates that the presence of O on the surface reduces the energy barrier, facilitating NO dissociation on Rh.

The reaction pathways for the diffusion were also investigated on the {111} surface of rhodium. The calculated diffusion pathways for N, O and NO indicate that all species prefer to move across the bridge site on each surface. The energy barrier across the bridge site for the diffusion of NO is the lowest, indicating that this species is the most mobile on the metal surface, followed by O diffusion and the energy barriers for N diffusion are the largest. Of the three metal surfaces tested (Rh, Pd and Pt) Pt metal exhibits the lowest N diffusion barriers showing that each species are able to move across Pt more easily than on either Pd or Rh, and Rh displays the lowest barrier for O diffusion.

The different pathways leading to N_2O formation was also investigated on the Rh {111} surface. The calculated pathways showed that the formation of the N_2O_2 dimer is difficult; however, once the dimer is formed then the NO bond is easier to break leading to N_2O formation. The second pathway involving the breaking of an NO molecule leading to the NO+N+O combination on the surface has a much lower barrier than the formation of the N_2O_2 dimer. This combination on the surface is highly stable, and energy is required to form the N_2O species on the surface for the end point on this pathway. Further exploration of other possible pathways are required to provide a clearer insight to the mechanism leading to N_2O formation, dissociation and subsequent formation of N_2 and O_2.

There is a large energy required to form the N_2 and O_2 bonds on the surface; however, the mechanism for bond formation to proceed through a weakly bound intermediate across two bridge sites requires further attention to provide more detail on the bond formation mechanism. This will elucidate a clearer description of N_2 and O_2 on the Rh surface.

Chapter 8

Conclusions

8.1 Conclusion

The fundamental aim of this thesis was to understand the catalytic properties of rhodium metal for *de*NO_x applications using a computational approach. Density functional theory using the PBE functional was employed in VASP to investigate all the possible adsorption modes of N, O, N_2, O_2 and NO_x adsorbates on the {111} surface of rhodium, palladium and platinum. Once the most stable adsorption modes for each species was determined, detailed analysis of the electronic structure was carried out using Bader analysis, charge difference and PEDOS plots, and the N/O state contributions to the molecular orbitals of the adsorbates. The overall Bader charges indicated that charge donation occurred from the metal surfaces to all adsorbates, with the charge difference plots shown a considerable change in the σ and π systems of the molecular adsorbates. The interaction of the NO_x adsorbates with the {111} surface of Rh, Pd and Pt, leads to a redistribution of electron density within the molecules and a stabilisation of the orbitals. For NO, this causes a stabilisation of 5σ orbital, significantly lowering it in energy, to a greater extent on Rh than either Pd or Pt, and also a stabilisation of the $2\pi^*$ anti-bonding orbital. The stabilisation of the N-O anti-bonding π^* orbital reduces the N contribution and transfers electron density to the O atom. The mechanism observed for NO_2 on the Rh surface, stabilises the $3\pi^*$ anti-bonding orbital in a similar manner indicating that NO_2 behaves like an NO adsorbate with an elongated bond to an O ad-atom. The electronic structure of the NO_x molecules can be

related to the recently proposed allylic configuration, as the lower bonding orbitals are seen to be greatly stabilised, and the anti-bonding π^* orbitals being also stabilised with an O $2p$ dominance. The stabilised π^* anti-bonding orbital is split with the occupied π^* being O $2p$ dominated and the unoccupied states being N $2p$ dominated for the NO_x adsorbates. This model is consistent with the $\widetilde{d}_\pi$ combination associated with the allylic configuration.

The calculated energy profile for the $de\mathrm{NO}_x$ process were determined from the most stable adsorption mode for each species on each surface, and their respective gaseous species. The breakdown of NO_x on the Rh surface is exothermic, while the breakdown of NO is endothermic on Pd and Pt. This shows that the breaking of the NO bond is favourable on Rh, and can explain its greater reductive properties over the other two metals. The exothermic breakdown of NO can be attributed to the exothermic adsorption of N atoms on Rh, whereas these adsorb endothermically on Pd and Pt. This drives forward the reaction to break NO and form its subsequent products. The favourable interaction of Rh metal with N and NO can be attributed to the higher E_F of Rh than either Pd and Pt, allowing easier charge donation to the adsorbates. The subsequent removal of N and O atoms to N_2 and O_2 gases from the Rh surface is endothermic. The formation and removal of N_2 is exothermic on Pd and Pt, indicating these metals are more likely to form and remove N_2 gas than Rh. For all three metals, the formation of O_2 and its subsequent removal requires a large energy and thus extremely difficult. The large energy barrier required to remove O_2 adsorbates to their respective gaseous species is due to the large adsorption energy of O adsorbates on the Rh and Pd surfaces, while this is not as difficult on Pt. This indicates that a reductant is required to remove the O ad-atoms from the Rh and Pd surfaces.

Chapter 5 examined the adsorption modes for N, O, N_2, O_2 and NO_x adsorbates on the {100}, {110} and {443} surfaces of rhodium were investigated in a similar manner to the {111} surface. The trend for the E_ads of NO adsorption in order of largest energy being {443} > {100} > {110}, and a similar the trend was observed for NO_2. Bader analysis, charge difference and PEDOS plots show that there is an overall charge

donation from all three surfaces to the NO and NO_2 adsorbates, with the greatest charge donation associated with the stepped surface of Rh. The interaction of the NO_x adsorbates with the three surfaces leads to a redistribution of electron density within the molecules and a stabilisation of the orbitals. The mechanism for stabilisation of the N-O anti-bonding π^* orbital which reduces the N contribution and transfers electron density to the O atom, is similar to that observed on the {111} surfaces. The electronic structure of the NO_x molecules on all three surfaces can be related to the recently proposed allylic configuration which is consistent with the $\widetilde{d}_\pi$ combination associated with the allylic configuration. This indicates that the allylic configuration can be extended to all low index surfaces of rhodium metal, suggesting that this mechanism provides a complete description of surface-adsorbates charge donations on metal surfaces.

The calculated energy profile for the $de\mathrm{NO}_x$ process were determined from the most stable adsorption mode for each species on the {100}, {110} and {443} surfaces, and their respective gaseous species. The breakdown of NO_x on the three surfaces is exothermic, with the energetically most favourable breakdown being associated with the step surface. The trend for the breakdown of NO_x with the most favourable first is; {443} > {100} > {111} > {110}. The stepped surface being the most active for $de\mathrm{NO}_x$ is due to the greater stability of N and O species, driving the reaction to the dissociation products. This shows that defect sites such as steps on the flat surfaces enhance the breaking of the NO bond on rhodium metal. Of the four rhodium surfaces under investigation, the {110} surface is the least active for $de\mathrm{NO}_x$; however the formation of N_2 is exothermic on this surface, while it is endothermic on the others. This indicates that a mixture of {100}/{111} surfaces with the {110} surface will provide the most active combination for NO_x reduction and easy removal of N_2.

For all three metals, the formation of O_2 and its subsequent removal requires a large energy and thus extremely difficult. The large energy barrier required to remove O_2 adsorbates to their respective gaseous species is due to the large adsorption energy of O adsorbates on all low index surfaces of Rh. The strongly bound O atoms will saturate the surface, blocking sites for subsequent NO_x breakdown and deactivating

the catalyst. In particular for the step on the {111} surface, as there is competition between O and NO for preferential adsorption at the step edge. This indicates that Rh metal would become deactivated under high O_2 concentrations, and thus not effective for lean-*de*NO_x. The strongly bound O atoms will therefore have to be removed by a reductant during the redox process.

Chapter 6 investigated the effect of varying the {111} surface and size of Rh_n clusters for *de*NO_x applications. The NO molecule was found to becoming less stable with increasing cluster size and Bader analysis, charge difference and PEDOS plots showed that there was an overall charge donation to the NO adsorbates. The interaction of the NO adsorbates with the {111} surface of Rh_n, leads to a redistribution of electron density within the molecules and a stabilisation of the orbitals, in a similar manner to the extended low index surfaces. The electronic interactions with the Rh_n clusters are seen to be similar to the extended rhodium metal surfaces, further supporting the allylic configuration. The NO decomposition profile for the Rh_n clusters was calculated from the energies of the most stable adsorption modes, and their respective gaseous species. The energetics show that the breakdown of NO is most favourable on the Rh_{20} clusters, with the NO dissociation energy decreasing with decreasing cluster size. The Rh_{20} cluster being the most favourable size for NO dissociation is due to the greater stability of N and O on the cluster than on the other clusters. This drives the dissociation reaction towards forming the N and O products. The subsequent removal of N and O from the surface of the cluster requires a large energy on all cluster sizes. This is attributed to the large adsorption energy of O atoms on the Rh_n clusters, which are difficult to remove. This is observed experimentally as Rh_xO_y complexes are found to form due to the dissociation on the metal clusters.[276] Similarly to other Rh surfaces, a reductant is required to remove O bound species.

The final chapter of results (chapter 7) examines the reaction pathways for the diffusion, bond breaking and reaction mechanisms were investigated on the {111} surface of rhodium. The calculated diffusion pathways for N, O and NO indicate that all species prefer to move across the bridge site on each surface, with the NO molecule being the

most mobile species. Pt metal exhibits the lowest diffusion barriers showing that each species are able to move across Pt more easily than on either Pd or Rh. The bond breaking pathways for N_2, O_2 and NO_x were investigated on the Rh {111} surface. There is a large energy required to form the N_2 and O_2 bonds on the surface across the top site; however, the mechanism for bond dissociation appears to proceed through a weakly bound intermediate across two bridge sites. For the bond dissociation of NO_x on the Rh surface, a number of pathways were considered from the gas phase. Both NO and NO_2 were found to prefer a pathway involving a weak intermediate precursor bound to a top site, that facilitated dissociation. If the molecules adsorbed into their most stable configurations on the Rh surface, then dissociation across a bridge site was calculated to be the lowest energy pathway. The dissociation of NO_2 leads to resultant dissociation products, NO + O on the surface. The subsequent breakdown of the resultant NO was found to occur across the bridge site with a much lower barrier than that observed for NO on the clean surface. This indicates that the presence of O on the surface reduces the energy barrier, facilitating NO dissociation on Rh.

The different pathways leading to N_2O formation was also investigated on the Rh {111} surface. The calculated pathways showed that the formation of the N_2O_2 dimer is difficult; however, once the dimer is formed then the NO bond is easier to break leading to N_2O formation. The second pathway involving the breaking of an NO molecule leading to the NO+N+O combination on the surface has a much lower barrier than the formation of the N_2O_2 dimer. This combination on the surface is highly stable, and energy is required to form the N_2O species on the surface for the end point on this pathway. This indicates that if a possible low energy pathway exists using the N_2O_2 dimer, then this is the mechanism leading to the N_2O formation on the {111} surface of Rh. The exploration of a possible low energy pathway is required to provide a clearer insight to the mechanism leading to N_2O formation.

8.2 Future research

The calculated mechanisms describing the N_2 and O_2 bond dissociations in this body of work provide a basis for further exploration of competing mechanism that may occur. The possibility of a weak intermediate bound across a hollow site to two bridge sites needs to be examined for both pathways, as the calculated pathways across a top site are too high in energy. The pathways leading to N_2O formation also need considerable more attention. The saddle points between structures are calculated and shown, but a more indept description of the pathways are required to fully show the reaction mechanisms. The formation of the N_2O_2 dimer on the surface is difficult due to the large energy required to form the N-N bond; however once the dimer is formed the pathway is energetically favourable. This would encourage further calculations into other possible mechanisms leading to the dimer formation to provide further insight into a low energy pathway, possibly by an Eiley-Rideal mechanism.

The research conducted in this thesis indicated that rhodium metal is an efficient $de\mathrm{NO}_x$ catalyst from the favourable interaction with nitrogen. Alternative catalysts would have to exhibit a similar interaction with nitrogen to behave in a similar manner to rhodium. The favourable interaction with nitrogen would enhance the breaking of the NO bond, an important step during the $de\mathrm{NO}_x$ process that rhodium carries out well. Another area to examine for alternative $de\mathrm{NO}_x$ catalysts, is the use of bimetallics. These have interesting properties from the manipulation of the electronic structure and mixing in the valence band to interact with the gaseous species in a number of ways. Bimetallics open up the possibility of various combinations to test, producing a large number of permutations that could replace the traditional Rh/Pt bimetallic used in TWCs. A number of studies wish to use precious metal free catalysts as these have the potential to be more cost effective and more thermodynamically more stable, withstanding large temperatures. Such catalysts would be Zeolites, metal-oxides and spinel complexes. There are a number of possiblities for next generation $de\mathrm{NO}_x$ technologies.

References

[1] M. C. Payne, M. P. Teter, D. C. Allan, T. A. Arias and J. D. Joannopoulos, *Rev. Mod. Phys.*, 1992, **64**, 1045–1097.

[2] M. L. Bell and Davis, *Devra Lee. Reassessment of the Lethal London Fog of 1952: Novel Indicators of Acute and Chronic Consequences of Acute Exposure to Air Pollution*, Environmental Health Perspectives, 2001.

[3] A. Whittaker, K. BruB, T. Jones, R. Maynard and R. Richards, *Science of The Total Environment*, 2004, **334335**, 435 – 445.

[4] R. Schwartz Cowan, *A Social History of American Technology*, Oxford University Press, 1997.

[5] D. Mira-Salama, C. Grning, N. Jensen, P. Cavalli, J.-P. Putaud, B. Larsen, F. Raes and H. Coe, *Atmospheric Research*, 2008, **88**, 294 – 304.

[6] *Jones, Kay H. "Cato Institute Policy Analysis No. 168: The Truth About Ozone and Urban Smog." (1992).*

[7] Y. Jin, M. Veiga and C. Kennes, *J. Chem. Technol. Biotechnol.*, 2005, **80**, 483 – 494.

[8] C. S. Sloane, *Atmospheric Environment (1967)*, 1988, **22**, 2021 – 2031.

[9] K. G. Sexton, H. E. Jeffries, M. Jang, R. M. Kamens, M. Doyle, I. Voicu and I. Jaspers, *Inhalation Toxicology*, 2004, **16**, 107–114.

[10] A. Zanasi, M. Piattella and A. Potena, *Multidscip. Respir. M.*, 2009, **4**, 423–429.

[11] R. P. Cody, C. P. Weisel, G. Birnbaum and P. J. Lioy, *Environmental Research*, 1992, **58**, 184 – 194.

[12] A. Krupnick, *The Environment of Oil*, Springer Netherlands, 1993, vol. 17, pp. 143–177.

[13] D. Elsom, *Smog alert: managing urban air quality.*, Routledge,, 2014.

[14] J. A. Leone and J. H. Seinfeld, *Atmospheric Environment (1967)*, 1985, **19**, 437 – 464.

[15] W. Chameides, R. Lindsay, J. Richardson and C. Kiang, *Science*, 1988, **241**, 1473–1475.

[16] J. G. Calvert, *Environmental Science & Technology*, 1976, **10**, 256–262.

[17] G. Z. Whitten, H. Hogo and J. P. Killus, *Environmental Science & Technology*, 1980, **14**, 690–700.

[18] G. D'amato, *Clinical and Experimental Allergy*, 2000, **30.5**, 628–636.

[19] P. Brimblecombe, *The big smoke: a history of air pollution in London since medieval times*, Routledge, 2011.

[20] J. R. Mammarella, 25 Sep. 2001.

[21] S. J. P. Pallo, John M. and W. Schafer, 24 Aug. 1982.

[22] F. Z. Hagena, J. and D. Assanis, *SAE Technical Paper*, 2006, **01**, 1151.

[23] H. Wise and M. F. Frech, *J. Chem. Phys.*, 1952, **20**, 22–24.

[24] H. S. Glick, J. J. Klein and W. Squire, *J. Chem. Phys.*, 1957, **27**, 850–857.

[25] R. Burch, J. P. Breen and F. C. Meunier, *Appl. Catal., B*, 2002, **39**, 283–303.

[26] F. Kapteijn, J. Rodriguez-Mirasol and J. A. Moulijn, *Applied Catalysis B: Environmental*, 1996, **9**, 25 – 64.

[27] S. Tauster, *SAE Technical Paper 930250*, 1993.

[28] J. Kaspar, P. Fornasiero and M. Graziani, *Catalysis Today*, 1999, **50**, 285 – 298.

[29] R. D. Monte, P. Fornasiero, J. Kaspar, M. Graziani, J. M. Gatica, S. Bernal and A. Gmez-Herrero, *Chem. Commun*, 2000, 2167 – 2168.

[30] F. Deganello, A. Longo and A. Martorana, *Journal of Solid State Chemistry*, 2003, **175**, 289 – 298.

[31] R. D. Monte and J. Kaspar, *Catalysis Today*, 2005, **100**, 27 – 35.

[32] Y. Lui and J. Dettling, *SAE Technical Paper 930249*, 1993.

[33] R. Farrauto and R. Heck, *Catalysis Today*, 2000, **55**, 179 – 187.

[34] T. Bunluesin, R. Gorte and G. Graham, *Applied Catalysis B: Environmental*, 1998, **15**, 107 – 114.

[35] T. Bunluesin, H. Cordatos and R. Gorte, *Journal of Catalysis*, 1995, **157**, 222 – 226.

[36] M. Chen, Y. Cai, Z. Yan, K. Gath, S. Axnanda and D. W. Goodman, *Surface Science*, 2007, **601**, 5326 – 5331.

[37] G. Zafiris and R. Gorte, *Journal of Catalysis*, 1993, **143**, 86 – 91.

[38] S. Bernal, G. Blanco, J. Calvino, J. Gatica, J. Omil and J. Pintado, *Topics in Catalysis*, 2004, **28**, 31–45.

[39] M. D. Amiridis, T. Zhang and R. J. Farrauto, *Applied Catalysis B: Environmental*, 1996, **10**, 203 – 227.

[40] M. KOEBEL, M. ELSENER and T. MARTI, *Combustion Science and Technology*, 1996, **121**, 85–102.

[41] M. Koebel, M. Elsener and M. Kleemann, *Catalysis Today*, 2000, **59**, 335 – 345.

[42] P. G. Savva and C. N. Costa, *Catalysis Reviews*, 2011, **53**, 91–151.

[43] N. NOJIRI, Y. SAKAI and Y. WATANABE, *Catalysis Reviews*, 1995, **37**, 145–178.

[44] N. Topsoe, H. Topsoe and J. Dumesic, *Journal of Catalysis*, 1995, **151**, 226 – 240.

[45] E. Kikuchi and K. Yogo, *Catalysis Today*, 1994, **22**, 73 – 86.

[46] M. Koebel, M. Elsener and G. Madia, *IEC Research*, 2001, **40**, 52.

[47] C. Orsenigo, L. Lietti, E. Tronconi, P. Forzatti and F. Bregani, *Industrial & Engineering Chemistry Research*, 1998, **37**, 2350–2359.

[48] J. Li, H. Chang, L. Ma, J. Hao and R. T. Yang, *Catalysis Today*, 2011, **175**, 147 – 156.

[49] K. M, K. R, M. S and S. N, *Applied Catalysis B: Environmental*, 2005, **60**, 173–179.

[50] S. Matsumoto, *Catalysis Today*, 1996, **29**, 43 – 45.

[51] T. Szailer, J. H. Kwak, D. H. Kim, J. C. Hanson, C. H. Peden and J. Szanyi, *Journal of Catalysis*, 2006, **239**, 51 – 64.

[52] I. Malpartida, M. A. L. Vargas, L. J. Alemany, E. Finocchio and G. Busca, *Applied Catalysis B: Environmental*, 2008, **80**, 214 – 225.

[53] M. Symalla, A. Drochner, H. Vogel, S. Philipp, U. Gbel and W. Mller, *Topics in Catalysis*, 2007, **42-43**, 199–202.

[54] U. Elizundia, R. Lpez-Fonseca, I. Landa, M. Gutirrez-Ortiz and J. Gonzlez-Velasco, *Topics in Catalysis*, 2007, **42-43**, 37–41.

[55] Y. Su, K. S. Kabin, M. P. Harold and M. D. Amiridis, *Applied Catalysis B: Environmental*, 2007, **71**, 207 – 215.

[56] Q. Zhang, L. Lv, J. Zhu, X. Wang, J. Wang and M. Shen, *Catal. Sci. Technol.*, 2013, **3**, 1069–1077.

[57] S. Matsumoto, *Catalysis Today*, 2004, **90**, 183 – 190.

[58] M. Takeuchi and S. Matsumoto, *Topics in Catalysis*, 2004, **28**, 151–156.

[59] E. Corbos, M. Haneda, X. Courtois, P. Marecot, D. Duprez and H. Hamada, *Catalysis Communications*, 2008, **10**, 137 – 141.

[60] R. Büchel, S. E. Pratsinis and A. Baiker, *Applied Catalysis B: Environmental*, 2012, **113-114**, 160 – 171.

[61] S. Matsumoto, *CATTECH*, 2000, **4**, 102–109.

[62] H.-S. Roh, Y. Wang and D. King, *Topics in Catalysis*, 2008, **49**, 32–37.

[63] I. Hachisuka, H. Hirata, Y. Ikeda and S. Matsumoto, *SAE Technical Paper*, 2000, **01**, 1196.

[64] H. Hirata, I. Hachisuka, Y. Ikeda, S. Tsuji and S. Matsumoto, *Topics in Catalysis*, 2001, **16-17**, 145–149.

[65] A. Fritz and V. Pitchon, *Appl. Catal., B*, 1997, **13**, 1 – 25.

[66] V. Pârvulescu, P. Grange and B. Delmon, *Catalysis Today*, 1998, **46**, 233 – 316.

[67] F. Garin, *Applied Catalysis A: General*, 2001, **222**, 183 – 219.

[68] G. Djéga-Mariadassou, *Catal. Today*, 2004, **90**, 27 – 34.

[69] A. Srinivasan and C. Depcik, *Catalysis Reviews*, 2010, **52**, 462–493.

[70] K. C. Taylor, *Catal. Rev. - Sci. Eng.*, 1993, **35**, 457 – 481.

[71] M. Shelef and G. W. Graham, *Catal. Rev. - Sci. Eng.*, 1994, **36**, 433.

[72] W. Brown and D. King, *J. Phys. Chem. B*, 2000, **104**, 11440.

[73] P. J. Loferski, *U.S Geological Survey Minerals Yearbook*, 2012.

[74] C.-T. Kao, G. Blackman, M. V. Hove, G. Somorjai and C.-M. Chan, *Surf. Sci.*, 1989, **224**, 77 – 96.

[75] H. J. Borg, J. F. Reijerse, R. A. van Santen and J. W. Niemantsverdriet, *J. Chem. Phys.*, 1994, **101**, 10052–10063.

[76] H. Permana, K. S. Ng, C. H. Peden, S. J. Schmieg, D. K. Lambert and D. N. Belton, *J. Catal.*, 1996, **164**, 194 – 206.

[77] Y. J. Kim, S. Thevuthasan, G. S. Herman, C. H. F. Peden, S. A. Chambers, D. N. Belton and H. Permana, *Surf. Sci.*, 1996, **359**, 269 – 279.

[78] H. Xu and K. Y. Simon-Ng, *Surf. Sci.*, 1996, **365**, 779 – 788.

[79] D. Loffreda, D. Simon and P. Sautet, *J. Chem. Phys.*, 1998, **108**, 6447–6457.

[80] D. Loffreda, D. Simon and P. Sautet, *Chem. Phys. Lett.*, 1998, **291**, 15–23.

[81] D. Loffreda, D. Simon and P. Sautet, *J. Catal.*, 2003, **213**, 211 – 225.

[82] O. R. Inderwildi, D. Lebiedz, O. Deutschmann and J. Warnatz, *J. Chem. Phys.*, 2005, **122**, 154702.

[83] F. Solymosi and J. Sarkany, *Appl. Surf. Sci.*, 1979, **3**, 68 – 82.

[84] R. Dictor, *J. Catal.*, 1988, **109**, 89 – 99.

[85] J. Liang, H. P. Wang and L. D. Spicer, *J. Phys. Chem.*, 1985, **89**, 5840–5845.

[86] H. Arai and H. Tominaga, *J. Catal.*, 1976, **43**, 131 – 142.

[87] T. W. Root, G. B. Fisher and L. D. Schmidt, *J. Chem. Phys.*, 1986, **85**, 4679–4686.

[88] J. L. Gland and B. A. Sexton, *Surf. Sci.*, 1980, **94**, 355 – 368.

[89] B. Hayden, *Surf. Sci.*, 1983, **131**, 419 – 432.

[90] R. Krishnamurthy and S. S. C. Chuang, *J. Phys. Chem.*, 1995, **99**, 16727–16735.

[91] S. S. C. Chuang and C. D. Tan, *J. Catal.*, 1998, **173**, 95 – 104.

[92] C. Kao, G. Blackman, M. V. Hove, G. Somorjai and C. Chan, *Surf. Sci.*, 1989, **224**, 77 – 96.

[93] G. Blyholder, *J. Phys. Chem.*, 1964, **68**, 2772–2777.

[94] R. B. Getman and W. F. Schneider, *J. Phys. Chem. C*, 2007, **111**, 389–397.

[95] Z.-H. Zeng, J. L. F. Da Silva, H.-Q. Deng and W.-X. Li, *Phys. Rev. B*, 2009, **79**, 205413.

[96] Z.-H. Zeng, J. L. F. Da Silva and W.-X. Li, *Phys. Rev. B*, 2010, **81**, 085408.

[97] R. Getman and W. Schneider, *ChemCatChem*, 2010, **2**, 1450–1460.

[98] M. T. Koper and R. A. van Santen, *J. Electroanal. Chem.*, 1999, **476**, 64 – 70.

[99] L. W.-X. Zeng Z.-H., Da Silva J.L.F., *Phys. Chem. Chem. Phys.*, 2010, **12**, 2459–2470.

[100] A. Nilsson, M. Weinelt, T. Wiell, P. Bennich, O. Karis, N. Wassdahl, J. Stöhr and M. G. Samant, *Phys. Rev. Lett.*, 1997, **78**, 2847–2850.

[101] A. Föhlisch, M. Nyberg, P. Bennich, L. Triguero, J. Hasselström, O. Karis, L. G. M. Pettersson and A. Nilsson, *J. Chem. Phys.*, 2000, **112**, 1946–1958.

[102] A. Nilsson and L. G. M. Pettersson, *Surf. Sci. Rep.*, 2004, **55**, 49 – 167.

[103] M. Beye, T. Anniyev, R. Coffee, M. Dell'Angela, A. Föhlisch, J. Gladh, T. Katayama, S. Kaya, O. Krupin, A. Møgelhøj, A. Nilsson, D. Nordlund, J. K. Nørskov, H. Öberg, H. Ogasawara, L. G. M. Pettersson, W. F. Schlotter, J. A. Sellberg, F. Sorgenfrei, J. J. Turner, M. Wolf, W. Wurth and H. Öström, *Phys. Rev. Lett.*, 2013, **110**, 186101.

[104] M. Dell'Angela, T. Anniyev, M. Beye, R. Coffee, A. Fhlisch, J. Gladh, T. Katayama, S. Kaya, O. Krupin, J. LaRue, A. Mgelhj, D. Nordlund, J. K. Nrskov, H. berg, H. Ogasawara, H. strm, L. G. M. Pettersson, W. F. Schlotter, J. A. Sellberg, F. Sorgenfrei, J. J. Turner, M. Wolf, W. Wurth and A. Nilsson, *Science*, 2013, **339**, 1302–1305.

[105] P. S. Moussounda, M. Ndollo, T. Dintzer, J. C. M. Nkouka and F. Garin, *Phys. Scr.*, 2013, **87**, 055601.

[106] T. Root, L. Schmidt and G. B. Fisher, *Surf. Sci.*, 1983, **134**, 30–45.

[107] M. Mavrikakis, J. Rempel, J. Greeley, L. Hansen and J. Norskov, *J. Chem. Phys.*, 2002, **117**, 6737–6744.

[108] T. Jirsak, J. Dvorak and J. A. Rodriguez, *Surf. Sci.*, 1999, **436**, L683 – L690.

[109] J. A. Anderson, G. J. Millar and C. H. Rochester, *J. Chem. Soc. Faraday T.*, 1990, **86**, 571–576.

[110] D. Wickham, B. A. Banse and B. E. Koel, *Surface Science*, 1991, **243**, 83 – 95.

[111] M. Bartram, R. Windham and B. Koel, *Surface Science*, 1987, **184**, 57 – 74.

[112] M. E. Bartram, R. G. Windham and B. E. Koel, *Langmuir*, 1988, **4**, 240–246.

[113] M. E. Bartram, B. E. Koel and E. A. Carter, *Surface Science*, 1989, **219**, 467 – 489.

[114] A. R. Burns, D. R. Jennison and E. B. Stechel, *Physical Review B*, 1989, **40**, 9485–9497.

[115] D. Wickham, B. Banse and B. Koel, *Surface Science*, 1989, **223**, 82 – 100.

[116] S. Mulla, N. Chen, W. Delgass, W. Epling and F. Ribeiro, *Catalysis Letters*, 2005, **100**, 267–270.

[117] R. G. L. Schmidt and J. L. Gland, *Surface Science*, 1981, **109**, 367 – 380.

[118] H. Conrad, G. Ertl, J. Kãppers and E. Latta, *Surface Science*, 1977, **65**, 235 – 244.

[119] M. Bertolo and K. Jacobi, *Surface Science*, 1990, **236**, 143 – 150.

[120] M. Bertolo, K. Jacobi, S. Nettesheim, M. Wolf and E. Hasselbrink, *Vacuum*, 1990, **41**, 76 – 78.

[121] P. Chen and D. Goodman, *Surface Science*, 1993, **297**, L93 – L99.

[122] K. Hansen, Z. Sljivancanin, B. Hammer, E. Laegsgaard, F. Besenbacher and I. Stensgaard, *Surface Science*, 2002, **496**, 1–9.

[123] C. Hess, E. Ozensoy and D. W. Goodman, *The Journal of Physical Chemistry B*, 2003, **107**, 2759–2764.

[124] H. Ibach and S. Lehwald, *Surface Science*, 1978, **76**, 1 – 12.

[125] M. Kiskinova, G. Pirug and H. Bonzel, *Surface Science*, 1984, **136**, 285 – 295.

[126] N. Materer, A. Barbieri, D. Gardin, U. Starke, J. D. Batteas, M. A. Van Hove and G. A. Somorjai, *Physical Review B*, 1993, **48**, 2859–2861.

[127] N. Materer, A. Barbieri, D. Gardin, U. Starke, J. Batteas, M. V. Hove and G. Somorjai, *Surface Science*, 1994, **303**, 319 – 332.

[128] Q. Ge and D. King, *Chemical Physics Letters*, 1998, **285**, 15 – 20.

[129] P. Fouquet, A. P. Graham and G. Witte, *The Journal of Chemical Physics*, 2000, **112**, 7600–7605.

[130] M. Matsumoto, N. Tatsumi, K. Fukutani, T. Okano, T. Yamada, K. Miyake, K. Hate and H. Shigekawa, *Journal of Vacuum Science and Technology A: Vacuum, Surfaces and Films*, 1999, **17**, 1577–1580.

[131] M. Matsumoto, K. Fukutani, T. Okano, K. Miyake, H. Shigekawa, H. Kato, H. Okuyama and M. Kawai, *Surface Science*, 2000, **454-456**, 101 – 105.

[132] M. Matsumoto, N. Tatsumi, K. Fukutani and T. Okano, *Surface Science*, 2002, **513**, 485 – 500.

[133] R. Ramsier, Q. Gao, H. Waltenburg, K. Lee, O. Nooij, L. Lefferts and J. Y. Jr., *Surface Science*, 1994, **320**, 209 – 237.

[134] K. Thirunavukkarasu, K. Thirumoorthy, J. Libuda and C. S. Gopinath, *The Journal of Physical Chemistry B*, 2005, **109**, 13283–13290.

[135] E. Ozensoy, C. Hess and D. W. Goodman, *Topics in Catalysis*, 2004, **28**, 13–23.

[136] H. Tang and B. L. Trout, *Journal of Physical Chemistry B*, 2005, **109**, 17630–17634.

[137] V. Johanek, S. Schauermann, M. Laurin, C. S. Gopinath, J. Libuda and H. Freund, *J. Phys. Chem. B*, 2004, **108**, 14244–14254.

[138] E. Ozensoy, C. Hess and D. W. Goodman, *Journal of the American Chemical Society*, 2002, **124**, 8524–8525.

[139] E. Ozensoy, C. Hess, D. Loffreda, P. Sautet and D. Goodman, *J. Phys. Chem. B*, 2005, **109**, 5414–5417.

[140] F. Leisenberger, G. Koller, M. Sock, S. Surnev, M. Ramsey, F. Netzer, B. Kltzer and K. Hayek, *Surface Science*, 2000, **445**, 380 – 393.

[141] R. Imbihl and J. Demuth, *Surface Science*, 1986, **173**, 395 – 410.

[142] T. Lin and G. Somorjai, *Surface Science*, 1981, **107**, 573 – 585.

[143] C. Campbell, G. Ertl and J. Segner, *Surface Science*, 1982, **115**, 309 – 322.

[144] J. F. Zhu, M. Kinne, T. Fuhrmann, R. Denecke and H. P. Steinrck, *Surface Science*, 2003, **529**, 384 – 396.

[145] J. S. Villarrubia and W. Ho, *The Journal of Chemical Physics*, 1987, **87**, 750–764.

[146] M. Bowker, Q. Guo and R. Joyner, *Surface Science*, 1991, **257**, 33 – 40.

[147] P. Ho and J. White, *Surface Science*, 1984, **137**, 103 – 116.

[148] M. van Tol and B. Nieuwenhuys, *Applied Surface Science*, 1993, **67**, 188 – 197.

[149] F. Bondino, G. Comelli, A. Baraldi, E. Vesselli, R. Rosei, A. Goldoni, S. Lizzit, C. Bungaro, S. de Gironcoli and S. Baroni, *The Journal of Chemical Physics*, 2003, **119**, 12525–12533.

[150] J. S. Villarrubia, L. J. Richter, B. A. Gurney and W. Ho, *Journal of Vacuum Science & Technology A*, 1986, **4**, 1487–1490.

[151] V. Schmatloch and N. Kruse, *Surface Science*, 1992, **269/ 270**, 488 – 494.

[152] D. L. Vuckovic, S. A. Jansen and R. Hoffmann, *Langmuir*, 1990, **6**, 732–746.

[153] M.-H. Tsai and K. C. Hass, *Phys. Rev. B*, 1995, **51**, 14616–14625.

[154] D. Loffreda, F. Delbecq, D. Simon and P. Sautet, *The Journal of Chemical Physics*, 2001, **115**, 8101–8111.

[155] K. Tian, X.-Y. Tu and S.-S. Dai, *Surf. Sci.*, 2007, **601**, 3186–3195.

[156] G. Cautero, C. Astaldi, P. Rudolf, M. Kiskinova and R. Rosei, *Surface Science*, 1991, **258**, 44 – 54.

[157] A. Baraldi, V. Dhanak, M. Kiskinova and R. Rosei, *Applied Surface Science*, 1994, **78**, 445 – 456.

[158] A. Baraldi, V. Dhanak, G. Comelli, K. Prince and R. Rosei, *Surface Science*, 1993, **293**, 246 – 253.

[159] A. Morgante, D. Cvetko, A. Santoni, K. Prince, V. Dhanak, G. Comelli and M. Kiskinova, *Surface Science*, 1993, **285**, 227 – 236.

[160] D. Liao, K. Glassford, R. Ramprasad and J. Adams, *Surface Science*, 1998, **415**, 11 – 19.

[161] A. Siokou, R. van Hardeveld and J. Niemantsverdriet, *Surface Science*, 1998, **402-404**, 110 – 114.

[162] M. M. M. Jansen, O. Caniaz, B. E. Nieuwenhuys and J. W. H. Niemantsverdriet, *Langmuir*, 2010, **26**, 16239–16245.

[163] M. J. P. Hopstaken and J. W. Niemantsverdriet, *Journal of Vacuum Science and Technology A*, 2000, **18**, 1503–1508.

[164] M. J. P. Hopstaken and J. W. Niemantsverdriet, *The Journal of Physical Chemistry B*, 2000, **104**, 3058–3066.

[165] E. Shustorovich and A. T. Bell, *Surface Science*, 1993, **289**, 127 – 138.

[166] W. Oed, B. D. atsch, L. Hammer, K. Heinz and K. M. aller, *Surface Science*, 1988, **207**, 55 – 65.

[167] J. Mercer, P. Finetti, F. Leibsle, R. McGrath, V. Dhanak, A. Baraldi, K. Prince and R. Rosei, *Surface Science*, 1996, **352-354**, 173 – 178.

[168] A. Baraldi, J. Cerdá, J. M. Gago, G. Comelli, S. Lizzit, G. Paolucci and R. Rosei, *Phys. Rev. Lett.*, 1999, **82**, 4874–4877.

[169] A. G. Norris, F. Schedin, G. Thornton, V. R. Dhanak, T. S. Turner and R. McGrath, *Phys. Rev. B*, 2000, **62**, 2113–2117.

[170] D. L. Vuckovic, S. A. Jansen and R. Hoffmann, *Langmuir*, 1990, **6**, 732–746.

[171] V. Schmatloch, I. Jirka and N. Kruse, *Surface Science*, 1993, **297**, L100 – L103.

[172] C. Peden, D. Belton and S. Schmieg, *Journal of Catalysis*, 1995, **155**, 204 – 218.

[173] G. Herman, C. Peden, S. Schmieg and D. Belton, *Catalysis Letters*, 1999, **62**, 131–138.

[174] G. Comelli, S. Lizzit, P. Hofmann, G. Paolucci, M. Kiskinova and R. Rosei, *Surface Science*, 1992, **277**, 31 – 42.

[175] V. R. Dhanak, K. C. Prince, R. Rosei, P. W. Murray, F. M. Leibsle, M. Bowker and G. Thornton, *Phys. Rev. B*, 1994, **49**, 5585–5590.

[176] G. Comelli, V. Dhanak, M. Kiskinova, N. Pangher, G. Paolucci, K. Prince and R. Rosei, *Surface Science*, 1992, **260**, 7 – 13.

[177] M. Gierer, H. Over, G. Ertl, H. Wohlgemuth, E. Schwarz and K. Christmann, *Surface Science*, 1993, **297**, L73 – L78.

[178] V. Schmatloch, I. Jirka, S. Heinze and N. Kruse, *Surface Science*, 1995, **331333, Part A**, 23 – 29.

[179] P. W. Murray, G. Thornton, M. Bowker, V. R. Dhanak, A. Baraldi, R. Rosei and M. Kiskinova, *Phys. Rev. Lett.*, 1993, **71**, 4369–4372.

[180] P. Murray, F. Leibsle, G. Thornton, M. Bowker, V. Dhanak, A. Baraldi, M. Kiskinova and R. Rosei, *Surface Science*, 1994, **304**, 48 – 58.

[181] K. Imamura, H. Horino, I. Rzeżnicka, I. Kobal, A. Kokalj, Y. Ohno, B. E. Nieuwenhuys, A. Hiratsuka and T. Matsushima, *Surface Science*, 2004, **566-568, Part 2**, 1076 – 1081.

[182] V. P. Zhdanov and T. Matsushima, *Surface Science*, 2005, **583**, 253 – 264.

[183] I. I. Rzeźnicka, Y. Ma, G. Cao and T. Matsushima, *The Journal of Physical Chemistry B*, 2004, **108**, 14232–14243.

[184] X. J. Shen, H. Kwak, D. Mocuta, A. M. Radojevic, S. Smadici and R. M. Osgood, *Phys. Rev. B*, 2001, **63**, 165403.

[185] S. Smadici, D. Mocuta and R. M. Osgood, *Phys. Rev. B*, 2004, **69**, 035415.

[186] J. E. Ortega, M. Ruiz-Osés and J. Kuntze, *Phys. Rev. B*, 2005, **72**, 195416.

[187] S. Payne, H. Kreuzer, W. Frie, L. Hammer and K. Heinz, *Surface Science*, 1999, **421**, 279 – 295.

[188] N. Janssen, A. Cholach, M. Ikai, K. Tanaka and B. Nieuwenhuys, *Surface Science*, 1997, **382**, 201 – 213.

[189] E. H. G. Backus, A. Eichler, M. L. Grecea, A. W. Kleyn and M. Bonn, *The Journal of Chemical Physics*, 2004, **121**, 7946–7954.

[190] B. Hammer, *Faraday Discuss.*, 1998, **110**, 323–333.

[191] B. Hammer, *Surface Science*, 2000, **459**, 323 – 348.

[192] Z.-P. Liu and P. Hu, *Journal of the American Chemical Society*, 2003, **125**, 1958–1967.

[193] L. A. DeLouise and N. Winograd, *Surface Science*, 1985, **159**, 199 – 213.

[194] R. Wolf, J. Bakker and B. Nieuwenhuys, *Surface Science*, 1991, **246**, 135 – 140.

[195] D. Castner, B. Sexton and G. Somorjai, *Surface Science*, 1978, **71**, 519 – 540.

[196] F. Esch, A. Baraldi, C. Comelli, S. Lizzit, M. Kiskinova, P. D. Cobden and B. E. Nieuwenhuys, *The Journal of Chemical Physics*, 1999, **110**, 4013–4019.

[197] S. Liepold, N. Elbel, M. Michl, W. Nichtl-Pecher, K. Heinz and K. Müller, *Surface Science*, 1990, **240**, 81 – 84.

[198] H. Hendrickx and B. Nieuwenhuys, *Surface Science*, 1986, **175**, 185 – 196.

[199] O. R. Inderwildi, D. Lebiedz, O. Deutschmann and J. Warnatz, *ChemPhysChem*, 2005, **6**, 2513–2521.

[200] S. González, D. Loffreda, P. Sautet and F. Illas, *The Journal of Physical Chemistry C*, 2007, **111**, 11376–11383.

[201] J. Rempel, J. Greeley, L. B. Hansen, O. H. Nielsen, J. K. Nrskov and M. Mavrikakis, *J. Phys. Chem. C*, 2009, **113**, 20623–20631.

[202] S. Dahl, A. Logadottir, R. C. Egeberg, J. H. Larsen, I. Chorkendorff, E. Törnqvist and J. K. Nørskov, *Phys. Rev. Lett.*, 1999, **83**, 1814–1817.

[203] P. Granger, J. Lecomte, L. Leclercq and G. Leclercq, *Applied Catalysis A: General*, 2001, **208**, 369 – 379.

[204] G. Comelli, V. Dhanak, M. Kiskinova, K. Prince and R. Rosei, *Surf. Sci. Rep.*, 1998, **32**, 165–231.

[205] F. Zaera, S. Wehner, C. S. Gopinath, J. L. Sales, V. Gargiulo and G. Zgrablich, *The Journal of Physical Chemistry B*, 2001, **105**, 7771–7774.

[206] M. B. Knickelbein, *Annual Review of Physical Chemistry*, 1999, **50**, 79–115.

[207] T. L. Haslett, K. A. Bosnick and M. Moskovits, *The Journal of Chemical Physics*, 1998, **108**, 3453–3457.

[208] E. A. Rohlfing, D. M. Cox, A. Kaldor and K. H. Johnson, *The Journal of Chemical Physics*, 1984, **81**, 3846–3851.

[209] S. Yang and M. B. Knickelbein, *The Journal of Chemical Physics*, 1990, **93**, 1533–1539.

[210] E. K. Parks, T. D. Klots and S. J. Riley, *The Journal of Chemical Physics*, 1990, **92**, 3813–3826.

[211] M. B. Knickelbein, S. Yang and S. J. Riley, *The Journal of Chemical Physics*, 1990, **93**, 94–104.

[212] M. B. Knickelbein and S. Yang, *The Journal of Chemical Physics*, 1990, **93**, 5760–5767.

[213] B. Collings, D. Rayner and P. Hackett, *International Journal of Mass Spectrometry and Ion Processes*, 1993, **125**, 207 – 214.

[214] K. Athanassenas, D. Kreisle, B. Collings, D. Rayner and P. Hackett, *Chemical Physics Letters*, 1993, **213**, 105 – 110.

[215] K. J. Taylor, C. L. PettietteHall, O. Cheshnovsky and R. E. Smalley, *The Journal of Chemical Physics*, 1992, **96**, 3319–3329.

[216] D. G. Leopold and W. C. Lineberger, *The Journal of Chemical Physics*, 1986, **85**, 51–55.

[217] J. Ho, K. M. Ervin and W. C. Lineberger, *The Journal of Chemical Physics*, 1990, **93**, 6987–7002.

[218] M. Gausa, G. Ganteför, H. Lutz and K. Meiwes-Broer, *International Journal of Mass Spectrometry and Ion Processes*, 1990, **102**, 227 – 237.

[219] H. Kietzmann, J. Morenzin, P. S. Bechthold, G. Ganteför and W. Eberhardt, *The Journal of Chemical Physics*, 1998, **109**, 2275–2278.

[220] R. Whetten, D. Cox, D. Trevor and A. Kaldor, *Surface Science*, 1985, **156, Part 1**, 8 – 35.

[221] I. M. L. Billas, J. A. Becker, A. Châtelain and W. A. de Heer, *Phys. Rev. Lett.*, 1993, **71**, 4067–4070.

[222] K. Holczer, O. Klein, G. Grüner, J. D. Thompson, F. Diederich and R. L. Whetten, *Phys. Rev. Lett.*, 1991, **67**, 271–274.

[223] F. Liu, S. N. Khanna and P. Jena, *Phys. Rev. B*, 1991, **43**, 8179–8182.

[224] M. E. Geusic, M. D. Morse and R. E. Smalley, *The Journal of Chemical Physics*, 1985, **82**, 590–591.

[225] M. D. Morse, M. E. Geusic, J. R. Heath and R. E. Smalley, *The Journal of Chemical Physics*, 1985, **83**, 2293–2304.

[226] L. Song, A. Eychmueller, R. J. St. Pierre and M. A. El-Sayed, *The Journal of Physical Chemistry*, 1989, **93**, 2485–2490.

[227] Y. Hamrick, S. Taylor, G. W. Lemire, Z.-W. Fu, J.-C. Shui and M. D. Morse, *The Journal of Chemical Physics*, 1988, **88**, 4095–4098.

[228] Y. M. Hamrick and M. D. Morse, *The Journal of Physical Chemistry*, 1989, **93**, 6494–6501.

[229] M. R. Zakin, R. O. Brickman, D. M. Cox and A. Kaldor, *The Journal of Chemical Physics*, 1988, **88**, 3555–3560.

[230] P. Schnabel, M. P. Irion and K. G. Weil, *The Journal of Physical Chemistry*, 1991, **95**, 9688–9694.

[231] M. P. Irion and P. Schnabel, *The Journal of Physical Chemistry*, 1991, **95**, 10596–10599.

[232] S. W. Buckner, J. R. Gord and B. S. Freiser, *The Journal of Chemical Physics*, 1988, **88**, 3678–3681.

[233] J. Alford, P. Williams, D. Trevor and R. Smalley, *International Journal of Mass Spectrometry and Ion Processes*, 1986, **72**, 33 – 51.

[234] M. P. Irion, A. Selinger and R. Wendel, *International Journal of Mass Spectrometry and Ion Processes*, 1990, **96**, 27 – 47.

[235] C. Berg, T. Schindler, A. Lammers, G. Niedner-Schatteburg and V. E. Bondybey, *The Journal of Physical Chemistry*, 1995, **99**, 15497–15501.

[236] P. Radi, G. von Helden, M. Hsu, P. Kemper and M. Bowers, *International Journal of Mass Spectrometry and Ion Processes*, 1991, **109**, 49 – 73.

[237] T. H. Upton, W. A. Goddard III and C. F. Melius, *Journal of Vacuum Science & Technology*, 1979, **16**, 531–536.

[238] R. C. Baetzold and R. E. Mack, *The Journal of Chemical Physics*, 1975, **62**, 1513–1520.

[239] R. Messmer, C. T. Jr. and K. Johnson, *Chemical Physics Letters*, 1975, **36**, 423 – 426.

[240] N. Rösch and D. Menzel, *Chemical Physics*, 1976, **13**, 243 – 256.

[241] M. Castro and D. R. Salahub, *Phys. Rev. B*, 1994, **49**, 11842–11852.

[242] M. Castro, C. Jamorski and D. R. Salahub, *Chemical Physics Letters*, 1997, **271**, 133 – 142.

[243] H. Grönbeck and A. Rosén, *The Journal of Chemical Physics*, 1997, **107**, 10620–10625.

[244] H. Kietzmann, J. Morenzin, P. S. Bechthold, G. Ganteför, W. Eberhardt, D.-S. Yang, P. A. Hackett, R. Fournier, T. Pang and C. Chen, *Phys. Rev. Lett.*, 1996, **77**, 4528–4531.

[245] H.-J. Fan, C.-W. Liu and M.-S. Liao, *Chemical Physics Letters*, 1997, **273**, 353 – 359.

[246] K. Raghavan, M. S. Stave and A. E. Depristo, *Chemical Physics Letters*, 1988, **149**, 89 – 94.

[247] K. Raghavan, M. S. Stave and A. E. DePristo, *The Journal of Chemical Physics*, 1989, **91**, 1904–1917.

[248] M. S. Stave and A. E. DePristo, *The Journal of Chemical Physics*, 1992, **97**, 3386–3398.

[249] N. N. Lathiotakis, A. N. Andriotis, M. Menon and J. Connolly, *EPL (Europhysics Letters)*, 1995, **29**, 135.

[250] D. J. Wales and L. J. Munro, *The Journal of Physical Chemistry*, 1996, **100**, 2053–2061.

[251] R. Smalley, *In Comparision of Ab initio Quantum Chemistry with Experiment for Small Molecules*, Dordrecht, The Netherlands: Reidel, 1985, pp. 53 – 65.

[252] A. Kaldor, D. Cox, D. Trevor and M. Zakin, *Zeitschrift für Physik D Atoms, Molecules and Clusters*, 1986, **3**, 195–204.

[253] A. Kaldor, D. Cox and M. Zakin, *In Evolution of Size Effects In Chemical Dynamics*, New York: Wiley, 1988, vol. 60, pp. 211 – 261.

[254] V. A. Spasov, T. H. Lee, J. P. Maberry and K. M. Ervin, *The Journal of Chemical Physics*, 1999, **110**, 5208–5217.

[255] V. A. Spasov, T.-H. Lee and K. M. Ervin, *The Journal of Chemical Physics*, 2000, **112**, 1713–1720.

[256] V. A. Spasov, Y. Shi and K. M. Ervin, *Chemical Physics*, 2000, **262**, 75 – 91.

[257] S. P. Walch and C. W. Bauschlicher, *The Journal of Chemical Physics*, 1985, **83**, 5735–5742.

[258] C.-X. Su, D. A. Hales and P. B. Armentrout, *The Journal of Chemical Physics*, 1993, **99**, 6613–6623.

[259] W. A. de Heer, *Rev. Mod. Phys.*, 1993, **65**, 611–676.

[260] M. Brack, *Rev. Mod. Phys.*, 1993, **65**, 677–732.

[261] S. Krückeberg, G. Dietrich, K. Lützenkirchen, L. Schweikhard, C. Walther and J. Ziegler, *The Journal of Chemical Physics*, 1999, **110**, 7216–7227.

[262] P. Armentrout, *Annual Review of Physical Chemistry*, 2001, **52**, 423–461.

[263] X. Wu and A. K. Ray, *The Journal of Chemical Physics*, 1999, **110**, 2437–2445.

[264] K. Clemenger, *Phys. Rev. B*, 1985, **32**, 1359–1362.

[265] T. P. Martin, T. Bergmann, H. Goehlich and T. Lange, *The Journal of Physical Chemistry*, 1991, **95**, 6421–6429.

[266] Y. Jinlong, F. Toigo and W. Kelin, *Phys. Rev. B*, 1994, **50**, 7915–7924.

[267] Z.-Q. Li, J.-Z. Yu, K. Ohno and Y. Kawazoe, *Journal of Physics: Condensed Matter*, 1995, **7**, 47.

[268] B. V. Reddy, S. K. Nayak, S. N. Khanna, B. K. Rao and P. Jena, *Phys. Rev. B*, 1999, **59**, 5214–5222.

[269] C.-H. Chien, E. Blaisten-Barojas and M. R. Pederson, *The Journal of Chemical Physics*, 2000, **112**, 2301–2307.

[270] C. Barreteau, R. Guirado-López, D. Spanjaard, M. C. Desjonquères and A. M. Oleś, *Phys. Rev. B*, 2000, **61**, 7781–7794.

[271] F. Aguilera-Granja, J. L. Rodríguez-López, K. Michaelian, E. O. Berlanga-Ramírez and A. Vega, *Phys. Rev. B*, 2002, **66**, 224410.

[272] L. Wang and Q. Ge, *Chemical Physics Letters*, 2002, **366**, 368 – 376.

[273] T. Futschek, M. Marsman and J. Hafner, *Journal of Physics: Condensed Matter*, 2005, **17**, 5927.

[274] M. J. Piotrowski, P. Piquini, L. Candido and J. L. F. Da Silva, *Phys. Chem. Chem. Phys.*, 2011, **13**, 17242–17248.

[275] J. L. F. Da Silva, M. J. Piotrowski and F. Aguilera-Granja, *Phys. Rev. B*, 2012, **86**, 125430.

[276] M. S. Ford, M. L. Anderson, M. P. Barrow, D. P. Woodruff, T. Drewello, P. J. Derrick and S. R. Mackenzie, *Phys. Chem. Chem. Phys.*, 2005, **7**, 975–980.

[277] M. L. Anderson, M. S. Ford, P. J. Derrick, T. Drewello, D. P. Woodruff and S. R. Mackenzie, *The Journal of Physical Chemistry A*, 2006, **110**, 10992–11000.

[278] D. Harding, M. S. Ford, T. R. Walsh and S. R. Mackenzie, *Phys. Chem. Chem. Phys.*, 2007, **9**, 2130–2136.

[279] G. Kummerlöwe and M. K. Beyer, *International Journal of Mass Spectrometry*, 2005, **244**, 84 – 90.

[280] C. Berg, M. Beyer, U. Achatz, S. Joos, G. Niedner-Schatteburg and V. E. Bondybey, *The Journal of Chemical Physics*, 1998, **108**, 5398–5403.

[281] I. Balteanu, O. P. Balaj, B. S. Fox-Beyer, P. Rodrigues, M. T. Barros, A. M. C. Moutinho, M. L. Costa, M. K. Beyer and V. E. Bondybey, *Organometallics*, 2004, **23**, 1978–1985.

[282] G. Albert, C. Berg, M. Beyer, U. Achatz, S. Joos, G. Niedner-Schatteburg and V. E. Bondybey, *Chemical Physics Letters*, 1997, **268**, 235 – 241.

[283] C. Adlhart and E. Uggerud, *The Journal of Chemical Physics*, 2005, **123**, 214709.

[284] I. Balteanu, O. P. Balaj, M. K. Beyer and V. E. Bondybey, *International Journal of Mass Spectrometry*, 2006, **255-256**, 71 – 75.

[285] M. J. Piotrowski, P. Piquini, Z. Zeng and J. L. F. Da Silva, *The Journal of Physical Chemistry C*, 2012, **116**, 20540–20549.

[286] D. Belton and S. Schmieg, *Journal of Catalysis*, 1993, **144**, 9 – 15.

[287] M. Aryafar and F. Zaera, *Journal of Catalysis*, 1998, **175**, 316 – 327.

[288] T. Root, L. Schmidt and G. B. Fisher, *Surface Science*, 1985, **150**, 173 – 192.

[289] T. W. Root, G. B. Fisher and L. D. Schmidt, *The Journal of Chemical Physics*, 1986, **85**, 4687–4695.

[290] S. B. Schwartz, G. B. Fisher and L. D. Schmidt, *The Journal of Physical Chemistry*, 1988, **92**, 389–395.

[291] C. H. F. Peden, D. W. Goodman, D. S. Blair, P. J. Berlowitz, G. B. Fisher and S. H. Oh, *The Journal of Physical Chemistry*, 1988, **92**, 1563–1567.

[292] V. P. Zhdanov and B. Kasemo, *Surface Science Reports*, 1997, **29**, 31 – 90.

[293] V. P. Zhdanov and T. Matsushima, *Surface Science*, 2007, **601**, 2373 – 2377.

[294] F. Zaera and C. S. Gopinath, *The Journal of Chemical Physics*, 1999, **111**, 8088–8097.

[295] C. S. Gopinath and F. Zaera, *Journal of Catalysis*, 1999, **186**, 387 – 404.

[296] C. S. Gopinath and F. Zaera, *The Journal of Physical Chemistry B*, 2000, **104**, 3194–3203.

[297] F. Zaera and C. S. Gopinath, *Chemical Physics Letters*, 2000, **332**, 209 – 214.

[298] F. Zaera and C. S. Gopinath, *Journal of Molecular Catalysis A: Chemical*, 2001, **167**, 23 – 31.

[299] C. S. Gopinath and F. Zaera, *Journal of Catalysis*, 2001, **200**, 270 – 287.

[300] V. Bustos, C. S. Gopinath, R. Unac, F. Zaera and G. Zgrablich, *The Journal of Chemical Physics*, 2001, **114**, 10927–10931.

[301] V. Bustos, R. Unac, F. Zaera and G. Zgrablich, *The Journal of Chemical Physics*, 2003, **118**, 9372–9379.

[302] F. Zaera and C. S. Gopinath, *Phys. Chem. Chem. Phys.*, 2003, **5**, 646–654.

[303] S. Wehner, M. T. Paffett and F. Zaera, *The Journal of Physical Chemistry B*, 2004, **108**, 18683–18692.

[304] J.-F. Paul, J. Pérez-Ramírez, F. Ample and J. M. Ricart, *The Journal of Physical Chemistry B*, 2004, **108**, 17921–17927.

[305] A. Kokalj and T. Matsushima, *The Journal of Chemical Physics*, 2005, **122**, 034708.

[306] T. Matsushima, *The Journal of Physical Chemistry C*, 2007, **111**, 6422–6427.

[307] T. Kondo, M. Sakurai, T. Matsushima and J. Nakamura, *The Journal of Chemical Physics*, 2010, **132**, 134704.

[308] D. N. Belton, C. L. Dimaggio, S. J. Schmieg and K. Y. S. Ng, *Journal of Catalysis*, 1995, **157**, 559 – 568.

[309] I. Nakai, H. Kondoh, T. Shimada, M. Nagasaka, R. Yokota, K. Amemiya, H. Orita and T. Ohta, *The Journal of Physical Chemistry B*, 2006, **110**, 25578–25581.

[310] Y.-L. Zhao, M. D. Bartberger, K. Goto, K. Shimada, T. Kawashima and K. N. Houk, *Journal of the American Chemical Society*, 2005, **127**, 7964–7965.

[311] M. D. Lim, I. M. Lorkovic and P. C. Ford, *Inorganic Chemistry*, 2002, **41**, 1026–1028.

[312] K. Goto, Y. Hino, T. Kawashima*, M. Kaminaga, E. Yano, G. Yamamoto, N. Takagi and S. Nagase, *Tetrahedron Letters*, 2000, **41**, 8479 – 8483.

[313] L. Ignarro, *Nitric Oxide, Biology, and Pathobiology*, Academic Press: San Diego, 2000.

[314] W. A. Brown, P. Gardner and D. A. King, *The Journal of Physical Chemistry*, 1995, **99**, 7065–7074.

[315] T. R. Ward, R. Hoffmann and M. Shelef, *Surf. Sci.*, 1993, **289**, 85 – 99.

[316] R. Burch, S. Daniells and P. Hu, *J. Chem. Phys.*, 2004, **121**, 2737–2745.

[317] I. Nakai, H. Kondoh, T. Shimada, R. Yokota, T. Katayama, T. Ohta and N. Kosugi, *The Journal of Chemical Physics*, 2007, **127**, 024701.

[318] I. Nakai, H. Kondoh, T. Shimada, M. Nagasaka, R. Yokota, T. Katayama, K. Amemiya, H. Orita and T. Ohta, *The Journal of Physical Chemistry C*, 2009, **113**, 13257–13265.

[319] W. J. Dulmage, E. A. Meyers and W. N. Lipscomb, *Acta Crystallographica*, 1953, **6**, 760–764.

[320] C. E. Dinerman and G. E. Ewing, *The Journal of Chemical Physics*, 1970, **53**, 626–631.

[321] L. Krim and N. Lacome, *The Journal of Physical Chemistry A*, 1998, **102**, 2289–2296.

[322] J. Suzanne, J. P. Coulomb, M. Bienfait, M. Matecki, A. Thomy, B. Croset and C. Marti, *Phys. Rev. Lett.*, 1978, **41**, 760–763.

[323] I. Nandhakumar, Z. Li, R. Palmer and R. Amos, *Surface Science*, 1995, **329**, 184 – 192.

[324] W. A. Brown, R. K. Sharma, D. A. King and S. Haq, *The Journal of Physical Chemistry*, 1996, **100**, 12559–12568.

[325] C. M. Kim, C.-W. Yi and D. W. Goodman, *The Journal of Physical Chemistry B*, 2002, **106**, 7065–7068.

[326] I. Zakharov, A. Suvorin, A. Kolbasin and O. Zakharova, *Journal of Structural Chemistry*, 2007, **48**, S147–S159.

[327] W. A. Brown, P. Gardner, M. P. Jigato and D. A. King, *The Journal of Chemical Physics*, 1995, **102**, 7277–7280.

[328] C. I. Carlisle and D. A. King, *The Journal of Physical Chemistry B*, 2001, **105**, 3886–3893.

[329] M. P. Jigato, V. Termath, P. Gardner, N. Handy, D. King, S. Rassias and M. Surman, *Molecular Physics*, 1995, **85**, 619–633.

[330] M. P. Jigato, D. A. King and A. Yoshimori, *Chemical Physics Letters*, 1999, **300**, 639 – 644.

[331] R. Burch, S. Daniells and P. Hu, *J. Chem. Phys.*, 2002, **117**, 2902–2908.

[332] A. L. L. East, *The Journal of Chemical Physics*, 1998, **109**, 2185–2193.

[333] H. A. Duarte, E. Proynov and D. R. Salahub, *The Journal of Chemical Physics*, 1998, **109**, 26–35.

[334] R. Sayós, R. Valero, J. M. Anglada and M. González, *The Journal of Chemical Physics*, 2000, **112**, 6608–6624.

[335] M. Tobita, S. A. Perera, M. Musial, R. J. Bartlett, M. Nooijen and J. S. Lee, *The Journal of Chemical Physics*, 2003, **119**, 10713–10723.

[336] Z.-P. Liu, S. J. Jenkins and D. A. King, *Journal of the American Chemical Society*, 2004, **126**, 7336–7340.

[337] A. R. Leach, *Molecular Modelling: Principles and Applications*, Prentice Hall, 2001.

[338] C. J. Cramer, *Essentials of Computational Chemistry*, Wiley, 2004.

[339] P. Hohenburg and W. Kohn, *Physics Review*, 1964, **136**, B864.

[340] W. Kohn and L. J. Sham, *Phys. Rev.*, 1965, **140**, A1133–A1138.

[341] F. Bloch, *Z. Phys. A: Hadrons Nucl*, 1919, **57**, 545.

[342] D. Ceperley and B. Alder, *Phys. Rev. Lett.*, 1980, **45**, 566.

[343] S. Vosko, L. Wilk and M. Nusair, *Can. J. Phys.*, 1980, **58**, 1200.

[344] A. D. Becke, *Phys. Rev. A*, 1988, **38**, 3098.

[345] J. P. Perdew and Y. Wang, *Physical Review B*, 1992, **45**, 13244–13249.

[346] J. P. Perdew, K. Burke and M. Ernzerhof, *Phys. Rev. Lett.*, 1996, **77**, 3865.

[347] H. J. Monkhorst and J. D. Pack, *Phys. Rev. B*, 1976, **13**, 5188–5192.

[348] A. Baldereschi, *Physical Review B*, 1973, **7**, 2697.

[349] G. Kresse and J. Furthmuller, *Comp. Mater. Sci.*, 1996, **6**, 15–50.

[350] G. Kresse and D. Joubert, *Phys. Rev. B*, 1999, **59**, 1758–1775.

[351] G. Kresse and J. Hafner, *Phys. Rev. B*, 1994, **49**, 14251–14271.

[352] G. Kresse and J. Furthmüller, *Phys. Rev. B*, 1996, **54**, 11169–11186.

[353] R. F. W. Bader, *Atoms in Molecules - A Quantum Theory*, Oxford University Press, Oxford, United Kingdom, 1990.

[354] G. Henkelman, A. Arnaldsson and H. Jónsson, *Comp. Mater. Sci.*, 2006, **36**, 354 – 360.

[355] E. Sanville, S. D. Kenny, R. Smith and G. Henkelman, *J. Comput. Chem.*, 2007, **28**, 899 – 908.

[356] W. Tang, E. Sanville and G. Henkelman, *J. Phys.: Condens. Matter*, 2009, **21**, 084204.

[357] H. J. G Henkelman, BP Uberuaga, *The Journal of Chemical Physics*, 2000, **113**, 9901 – 9904.

[358] H. J. G Henkelman, *The Journal of chemical physics*, 2000, **113**, 9978 – 9985.

[359] F. D. Murnaghan, *Proc. Natl. Acad. Sci. U. S. A.*, 1944, **30**, 244–247.

[360] E. Owen and E. Yates, *Philos. Mag.*, 1933, **16**, 606.

[361] B. G. Johnson, P. M. W. Gill and J. A. Pople, *J. Chem. Phys.*, 1993, **98**, 5612–5626.

[362] L. A. Curtiss, K. Raghavachari, P. C. Redfern and J. A. Pople, *J. Chem. Phys.*, 1997, **106**, 1063.

[363] B. Hammer, L. B. Hansen and J. K. NÃrskov, *Phys. Rev. B*, 1999, **59**, 7413.

[364] M. Nolan, S. C. Parker and G. W. Watson, *Surf. Sci.*, 2005, **595**, 223–232.

[365] D. O. Scanlon, A. Walsh, B. J. Morgan, M. Nolan, J. Fearon and G. W. Watson, *J. Phys. Chem. C*, 2007, **111**, 7971–7979.

[366] J. J. Carey, J. Allen, B. M.E and W. G.W., *J. Phys. Chem. C*, 2014, **(preparation)**, year.

[367] M. Wojciechowska and S. Lomnicki, *Clean Prod. and Proc.*, 1999, **1**, 237 – 247.

[368] G. Djéga-Mariadassou, F. Fajardie, J. F. Tempere, J. M. Manoli, O. Touret and G. Blanchard, *J. Mol. Catal. A: Chem.*, 2000, **161**, 179–189.

[369] H. Hamada, Y. Kintaichi, M. Sasaki, T. Ito and M. Tabata, *Appl. Catal., A*, 1991, **75**, L1 – L8.

[370] G. R. Bamwenda, A. Ogata, A. Obuchi, J. Oi, K. Mizuno and J. Skrzypek, *Appl. Catal., B*, 1995, **6**, 311 – 323.

[371] M. Sasaki, H. Hamada, Y. Kintaichi and T. Ito, *Catal. Lett.*, 1992, **15**, 297–304.

[372] Y. Waseda, K. Hirata and M. Ohtani, *High Temperatures-High Pressures*, 1975, **7**, 221.

[373] C. Nagabushana and K. Krishna, *Canadian Journal of Physics*, 1964, **42**, 1336.

[374] M. Adamowska, A. Krzto, M. Najbar, J. Camra, G. Djga-Mariadassou and P. D. Costa, *Applied Catalysis B: Environmental*, 2009, **90**, 535 – 544.

[375] D. Castner and G. Somorjai, *Applications of Surface Science*, 1980, **6**, 29 – 38.

[376] T. Matsushima, *Surface Science*, 1985, **157**, 297 – 318.

[377] D. H. Parker, M. E. Bartram and B. E. Koel, *Surface Science*, 1989, **217**, 489 – 510.

[378] B. A. Banse and B. E. Koel, *Surface Science*, 1990, **232**, 275 – 285.

[379] E. Putna, J. Vohs and R. Gorte, *Surface Science*, 1997, **391**, L1178 – L1182.

[380] M. Chen, Y. Cai, Z. Yan, K. Gath, S. Axnanda and D. W. Goodman, *Surface Science*, 2007, **601**, 5326 – 5331.

[381] F. Gao, S. McClure, Y. Cai, K. Gath, Y. Wang, M. Chen, Q. Guo and D. Goodman, *Surface Science*, 2009, **603**, 65 – 70.

[382] L. Olsson, B. Westerberg, H. Persson, E. Fridell, M. Skoglundh and B. Andersson, *The Journal of Physical Chemistry B*, 1999, **103**, 10433–10439.

[383] S. Salasc, M. Skoglundh and E. Fridell, *Applied Catalysis B: Environmental*, 2002, **36**, 145 – 160.